1-1-1991

Structural failure analysis of Calumet Harbor breakwater

Rama Krishna Challa
Iowa State University

Structural failure analysis of Calumet Harbor breakwa

by

Rama K. Challa

A Thesis Submitted to the
Graduate Faculty in Partial Fulfillment of the
Requirements for the Degree of
MASTER OF SCIENCE

Department: Civil and Construction Engineering
Major: Structural Engineering

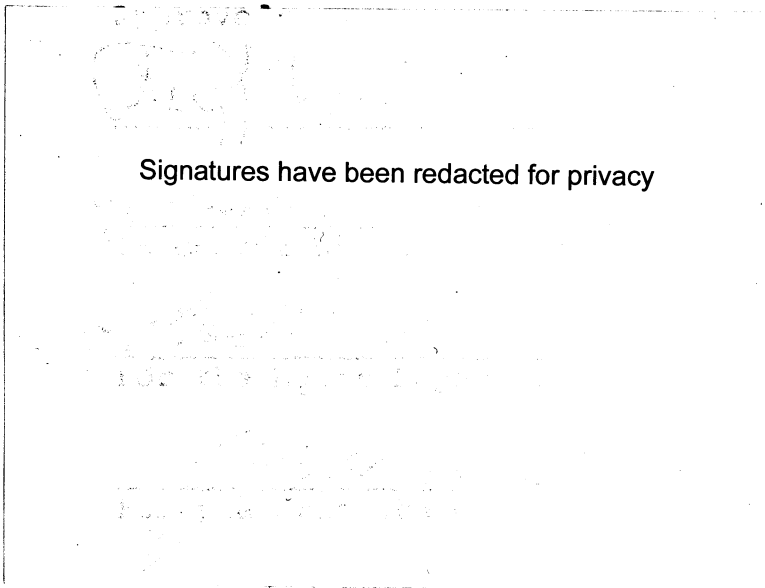

Iowa State University
Ames, Iowa

1991

TABLE OF CONTENTS

	PAGE
LIST OF FIGURES	v
LIST OF TABLES	xvii
ABSTRACT	xx
CHAPTER 1. INTRODUCTION	1
1.1 Background	1
1.2 Objectives and Scope of Work	9
1.3 Literature Survey	14
CHAPTER 2. FIELD INSTRUMENTATION	17
2.1 Background	17
2.2 Field Instrumentation	17
CHAPTER 3. FATIGUE TESTS	31
3.1 Introduction	31
3.2 Test Procedure	31
3.3 Discussion of Results	33
CHAPTER 4. EVALUATION OF FORCES ON THE STRUCTURE	39
4.1 Introduction	39
4.2 Burns Harbor Data	39
4.3 Evaluation of Force Field on the Structure	45
4.4 Determination of the Wave Pressures	46
4.5 Determination of the Forces on the Breakwater	52

CHAPTER 5. DATA ANALYSIS AND COMPARISON OF FIELD DATA 66

5.1 Data Analysis 66

5.2 Processing of the Data 67

5.3 Correlation of the Finite Element Data with the Field Data 73

CHAPTER 6. FAILURE ANALYSIS AND FATIGUE EVALUATION 102

6.1 Introduction 102

6.2 Potential Failure Modes of the Structure 102

6.3 Fatigue Life Evaluation 104

6.4 Limitations in Analysis 115

6.5 Rehabilitation Alternatives 116

CHAPTER 7. SUMMARY, CONCLUSIONS AND RECOMMENDATIONS 117

7.1 Summary 117

7.2 Conclusions 119

7.3 Recommendations for Further Study 120

CHAPTER 8. REFERENCES 123

ACKNOWLEDGEMENTS 125

APPENDIX A 126

A.1 Field Instrumentation - Phase II Operations 126

A.2 Recorded data of Phase II Operations 133

A.3 Field Instrumentation - Phase I Operations 134

A.4 Recorded data of Phase I Operations 139

A.5 Diagnostic Tests 161

APPENDIX B 168

B.1 Fatigue Tests - Equipment 168

B.2 Fatigue Tests - Discussion of Measured Parameters 171

B.3 Fatigue Tests - Discussion of Failure Mechanism 174

APPENDIX C 177

C.1 Bivariate Histograms 177

C.2 Typical Calculations Using the Cnoidal Wave Theory 177

C.3 Equivalent Stress Analysis Method 194

APPENDIX D 201

D.1 SAS Analysis Results 201

D.2 Hoop Force Range Variation with Elevation 201

APPENDIX E 231

E.1 Computer Programs 231

LIST OF FIGURES

PAGE

Chapter 1:

Fig. 1.1 Location of Calumet Harbor breakwater 2

Fig. 1.2 Sectional elevation and plan view of breakwater Cells 3

Fig. 1.3 View towards northwest end of breakwater indicating failed cells 5

Fig. 1.4 View towards southeast end of breakwater indicating failed cells 5

Fig. 1.5 Photograph of the failed cells during a reconnaissance survey 6

Fig. 1.6 Plan view of a cell indicating split piles at a Y -Intersection 6

Fig. 1.7 View of the structure towards the south east end indicating settled capstones 7

Fig. 1.8 Photograph of rubble mound created at cells 115, 116 and 117 8

Fig. 1.9 Overall solution approach 10

Fig. 1.10 Individual areas of effort in the study 10

Chapter 2:

Fig. 2.1 Schematic diagram of instrumentation scheme 18

Fig. 2.2 Location of strain gauges on the instrumented cells 20

Fig. 2.3 Layout of instrumentation cable network 21

Fig. 2.4 Underwater welder surfacing for a tool during welding operation 21

Fig. 2.5 Fixing of cables to capstones 22

Fig. 2.6 Final stages of the Installation operation 22

Fig. 2.7 View of the substation during installation and testing of communications system 23

Fig. 2.8a Typical data segment (Strain Gauges 1,3,4,5) 26

Fig. 2.8b Typical data segment (Strain Gauges 6,7,8,9) 27

Fig. 2.8c Typical data segment (Strain Gauges 10,12,13) 28

Fig. 2.9 Wave gauge being installed at site by the Corps of Engineers personnel 29

Chapter 3:

Fig. 3.1 Test set up indicating the MTS loading frame. Load input is by hydraulic load cells at either end of the system 32

Fig. 3.2 Quantities measured during testing 34

Fig. 3.3 Trace of the target specimen during testing 34

Fig. 3.4 Fatigue S-N curve for steel sheetpile specimens 37

Chapter 4:

Fig. 4.1	Ranges of suitability for wave theories as suggested by Le Mehaute	47
Fig. 4.2	Typical variation of total pressure (static + dynamic) along the elevation of the breakwater - Stoke's wave theory - wave peak	50
Fig. 4.3	Typical variation of total pressure (static + dynamic) along the elevation of the breakwater - Stoke's wave theory - wave trough	51
Fig. 4.4	Typical variation of total pressure (static + dynamic) along the elevation of the breakwater - Cnoidal wave theory - wave peak	53
Fig. 4.5	Typical variation of total pressure (static + dynamic) along the elevation of the breakwater - Cnoidal wave theory - wave trough	54
Fig. 4.6	Idealization of the side of the breakwater for force evaluation indicating the nodes and pressure points	56
Fig. 4.7	Typical applied pressure variation along the elevation of breakwater - Stokes theory - wave peak	57

Fig. 4.8 Typical applied pressure variation along the elevation of breakwater - Stokes wave theory - wave trough 58

Fig. 4.9 Typical applied pressure variation along the elevation of breakwater - Cnoidal wave theory - wave peak 59

Fig. 4.10 Typical applied pressure variation along the elevation of breakwater - Cnoidal wave theory - wave trough 60

Fig. 4.11 Typical nodal force variation along the elevation of the breakwater - Stokes wave theory - wave peak 61

Fig. 4.12 Typical nodal force variation along the elevation of the breakwater - Stokes wave theory - wave trough 62

Fig. 4.13 Typical nodal force variation along the elevation of the breakwater - Cnoidal wave theory - wave peak 63

Fig. 4.14 Typical nodal force variation along the elevation of the breakwater - Cnoidal wave theory - wave trough 64

Chapter 5:

Fig. 5.1 Typical variation of hoop forces in cell wall vs elevation (wave peak) 69

Fig. 5.2 Typical variation of hoop forces in cell wall vs elevation (wave trough) 70

Fig. 5.3 Typical predicted trend as per SAS analysis 72

Fig. 5.4 Comparison between predicted and measured hoop force variation (Data recorded on Jan. 12th) 78

Fig. 5.5 Comparison between predicted and measured hoop force variation (Data recorded on Feb. 2nd) 79

Fig. 5.6 Comparison between predicted and measured hoop force variation (Data recorded on Feb. 13th) 80

Fig. 5.7 Comparison between predicted and measured hoop force variation (Data recorded on Feb. 24th) 81

Fig. 5.8a Recorded hoop force ranges vs predicted trend at location 17 (Strain Gauges 5,6, and 7) for a wave height of 10.20' 83

Fig. 5.8b Recorded hoop force ranges vs predicted trend at location 17 (Strain Gauges 8,9, and 10) for a wave height of 10.20' 84

Fig. 5.8c Recorded hoop force ranges vs predicted trend at location 10 (Strain Gauge 12) for a wave height of 10.20' 85

Fig. 5.8d Recorded hoop force ranges vs predicted trend at location 13 (Strain Gauge 13) for a wave height of 10.20' 86

Fig. 5.9a Recorded hoop force ranges vs predicted trend at location 17 (Strain Gauges 5,6, and 7) for a wave height of 6.00' 87

Fig. 5.9b Recorded hoop force ranges vs predicted trend at location 17 (Strain Gauges 8,9, and 10) for a wave height of 6.00' 88

Fig. 5.9c Recorded hoop force ranges vs predicted trend at location 10 (Strain Gauge 12) for a wave height of 6.00' 89

Fig. 5.9d Recorded hoop force ranges vs predicted trend at location 13 (Strain Gauge 13) for a wave height of 6.00' 90

Fig. 5.10a Recorded hoop force ranges vs predicted trend at location 17 (Strain Gauges 5,6, and 7) for a wave height of 12.00' 91

Fig. 5.10b Recorded hoop force ranges vs predicted trend at location 17 (Strain Gauges 8,9, and 10) for a wave height of 12.00' 92

Fig. 5.10c Recorded hoop force ranges vs predicted trend at location 10 (Strain Gauge 12) for a wave height of 12.00' 93

Fig. 5.10d Recorded hoop force ranges vs predicted trend at location 13 (Strain Gauge 13) for a wave height of 12.00' 94

Fig. 5.11a Recorded hoop force ranges vs predicted trend at location 17 (Strain Gauges 5,6, and 7) for a wave height of 13.90' 95

Fig. 5.11b Recorded hoop force ranges vs predicted trend at location 17 (Strain Gauges 8,9, and 10) for a wave height of 13.90' 96

Fig. 5.11c Recorded hoop force ranges vs predicted trend at location 10 (Strain Gauge 12) for a wave height of 13.90' 97

Fig. 5.11d Recorded hoop force ranges vs predicted trend at location 13 (Strain Gauge 13) for a wave height of 13.90' 98

Chapter 6:

Fig. 6.1 Typical variation of hoop-force ranges along breakwater elevation 103

Fig. 6.2 Finite element idealization of lake-side and harbor-side hoop forces 107

Fig. 6.2a Fatigue curves with different exponents 109

Fig. 6.3 Estimate of damage along the breakwater elevation (Lake-side) 111

Fig. 6.4 Estimate of damage along the breakwater elevation (Harbor -side) 112

Fig. 6.5 Variation of damage estimate with direction at location 15 (Lake-side) 113

Fig. 6.6 Variation of damage estimate with direction at location 15 (Harbor-side) 114

Appendix A:

Fig. A.1 Tack-welded strain gauge after installation 127

Fig. A.2 Strain gauges covered with epoxy putty 127

Fig. A.3 Welder preparing to weld protective angle barriers 128

Fig. A.4 Angle barriers welded to Strain Gauges 2 and 4 128

Fig. A.5 The CR-7 data acquisition system in connected state 130

Fig. A.6 Substation in the coast guard station indicating the different components; the Hayes telephone modem, R.F. modem, UHF radio, and the power source 130

Fig. A.7 Antenna at the coast guard station, a link in the communication network 132

Fig. A.8 Antenna at the field station 132

Fig. A.9 Schematic diagram for Phase I instrumentation and data acquisition system 135

Fig. A.10 Location of strain gauges on the breakwater 135

Fig. A.11 Installed flexure gauge tack-welded to the sheetpile structure 137

Fig. A.12 Protective PVC cover for the hoop strain gauge 137

Fig. A.13 Protective steel angle cover over the hoop strain gauge 138

Fig. A.14 The CR-10 data logger in the connected state 138

Fig. A.15 Installed microcomputer at the coast guard station for recording the data 140

Fig. A.16 Installed communications antenna at the coast guard station 141

Fig. A.17 Typical variation of recorded pressure and strain values 146

Fig. A.18 Wind speed indicator diagram 150

Appendix B:

Fig. B.1 Test setup with bulb shaped end grips 169

Fig. B.2 Failure of transition specimen at grips indicating interlock opening 170

Fig. B.3 The MTS 880 control unit 170

Fig. B.4 Graphical variation of pattern of deformation 173

Fig. B.5 Figure indicating the dished target specimen 175

Fig. B.6 Free body diagram of steel sheetpile sample under axial loads 175

Appendix C:

Fig. C.1 Relationship between κ^2 and $T(g/d)^{1/2}$ (from 7) 191

Fig. C.2 Relationship between κ^2 and L^2H/d^3 (from 7) 191

Fig. C.3 Relationship between θ and $Cn_2(q)$ (from 6) 193

Fig. C.4 Typical S-N curve relating stress range to number of cycles to failure 193

Fig. C.5 Rayleigh distribution of wave heights in a sea state 193

Appendix D:

Fig. D.1 Variation of hoop-force ranges with elevation and identified critical failure zones 218

Fig. D.2 Variation of hoop-force ranges with elevation and identified critical failure zones 219

Fig. D.3 Variation of hoop-force ranges with elevation and identified critical failure zones 220

Fig. D.4 Variation of hoop-force ranges with elevation and identified critical failure zones 221

Fig. D.5 Variation of hoop-force ranges with elevation and identified critical failure zones 222

Fig. D.6 Variation of hoop-force ranges with elevation and identified critical failure zones 223

Fig. D.7 Variation of hoop-force ranges with elevation and identified critical failure zones 224

Fig. D.8 Variation of hoop-force ranges with elevation and identified critical failure zones 225

Fig. D.9 Variation of hoop-force ranges with elevation and identified critical failure zones 226

Fig. D.10 Variation of hoop-force ranges with elevation and identified critical failure zones 227

Fig. D.11 Variation of hoop-force ranges with elevation and identified critical failure zones 228

Fig. D.12 Variation of hoop-force ranges with elevation and identified critical failure zones 229

Fig. D.13 Variation of hoop-force ranges with elevation and identified critical failure zones 230

Appendix E:

Fig. E.1 Computation flow chart for regression analysis 234

Fig. E.2 Computation flow chart for evaluation of pressures 234

List of Tables

	PAGE
Table 3.1 Results of fatigue tests	35
Table 4.1 Bivariate histogram for ENE direction	42
Table 4.2 Summary of statistical analysis of historical wave data	43
Table 5.1 Typical post-processed ANSYS results	
Table 5.2 Time, date, maximum wave height in the record and corresponding wind and wave directions	76
Table 5.3 Recorded hoop-force ranges	76
Table 5.4 Recorded hoop-force ranges	77
Table A.1 Time, date, max. wave height in the record and corresponding wind and wave directions	152
Table A.2 Recorded hoop-force ranges	153
Table A.3 Recorded hoop-force ranges	154
Table A.4 Wind and temperature data - March 29th, 1989	155
Table A.5 Mean values of the strains	158
Table A.6 Summary of Test 1 data	163
Table A.7 Summary of Test 2 data	164
Table A.8a Summary of Test 3 data	165
Table A.8b Summary of Test 3 data	166
Table B.1 Interlock opening measurements for	172

target specimen

Table B.2 Interlock separation measurements for target specimen 172

Table C.1 Water surface elevation according to the Cnoidal theory; calculations for a typical wave 178

Table C.2 Bivariate histogram for NE direction 179

Table C.3 Bivariate histogram for E direction 180

Table C.4 Bivariate histogram for ESE direction 181

Table C.5 Bivariate histogram for SE direction 181

Table C.6 Bivariate histogram for SSE direction 182

Table C.7 Bivariate histogram for S direction 182

Table C.8 Bivariate histogram for SSW direction 183

Table C.9 Bivariate histogram for SW direction 183

Table C.10 Bivariate histogram for WSW direction 184

Table C.11 Bivariate histogram for W direction 185

Table C.12 Bivariate histogram for WNW direction 186

Table C.13 Bivariate histogram for NW direction 187

Table C.14 Bivariate histogram for NNW direction 188

Table C.15 Bivariate histogram for N direction 189

Table C.16 Bivariate histogram for NNE direction 190

Table D.1 SAS analysis results at location 2 202

Table D.2 SAS analysis results at location 3 203

Table D.3 SAS analysis results at location 4 204

Table D.4 SAS analysis results at location 5 205

Table D.5 SAS analysis results at location 6 206

Table D.6 SAS analysis results at location 7 207

Table D.7 SAS analysis results at location 8 208

Table D.8 SAS analysis results at location 9 209

Table D.9 SAS analysis results at location 10 210

Table D.10 SAS analysis results at location 11 211

Table D.11 SAS analysis results at location 12 212

Table D.12 SAS analysis results at location 13 213

Table D.13 SAS analysis results at location 14 214

Table D.14 SAS analysis results at location 15 215

Table D.15 SAS analysis results at location 16 216

Table D.16 SAS analysis results at location 17 217

ABSTRACT

The primary objective of this research project was to perform a structural failure analysis of the Calumet Harbor breakwater. Two main tasks performed included determination of likely failure mode of the structure and prediction of the future life of the structure.

The research effort concentrated on four major areas. The first was instrumentation of the structure in two phases, the winters of 1988 and 1989 respectively. The data recorded in Phase I were used to qualitatively analyze the behavior of the structure, while the data used in Phase II were used to validate a finite element model of the structure, the preparation of which was the second major area of effort.

The prediction of wave forces was the third major area of effort, achieved by statistical analysis of hindcast wave data and deterministic evaluation of forces using various wave theories.

Investigation of fatigue as a probable cause of failure constituted the fourth major area of effort. Fatigue tests were performed to generate a S - N curve for the steel sheet pile specimens.

The results for the above areas were used (1) to arrive at the fatigue damage to the structure due to hoop forces at

different elevations and (2) to estimate the future life of the structure by using the equivalent damage method.

On the basis of the study, the following conclusions were made: The failure of the structure was initiated and essentially caused by fatigue. The failure was propagated by critical high hoop force zones on the elevation of the structure. A range of values for the design life of the structure was predicted on the basis of the fatigue data.

1.INTRODUCTION

1.1 Background

Calumet harbor breakwater was built in 1934 to mitigate and contain the damage due to wave action on the Calumet harbor in Lake Michigan, near Chicago, Illinois. The breakwater was built in two sections, Reaches A and B, which formed an attached breakwater built of timber cribs, and Reach C, the detached breakwater built of steel sheetpile cells. The structural failure analysis of the steel sheetpile cellular structure is the objective of this research project. The location of the structure is indicated in Fig. 1.1.

The breakwater consists of 131 stone-filled steel sheetpile cells of diaphragm type with a width of 41 ft at their widest point. The cross walls are 38 ft 3 in. apart. The cross-sectional elevation and plan views of the breakwater are illustrated in Fig. 1.2. Type PSA 23 steel sheetpiles, 46 ft long, are used in the construction. The structure is founded on clay and sand at lake bottom and the cell fill consists of quarry run topped by bedding stones and concrete capping stones. Toe protection is ensured on both the lake side and the harbor side by berm, topped by stone riprap (cap stones).

Significant damage to the structure was recorded during a storm in February 1984. Three cells, numbered 115, 116,

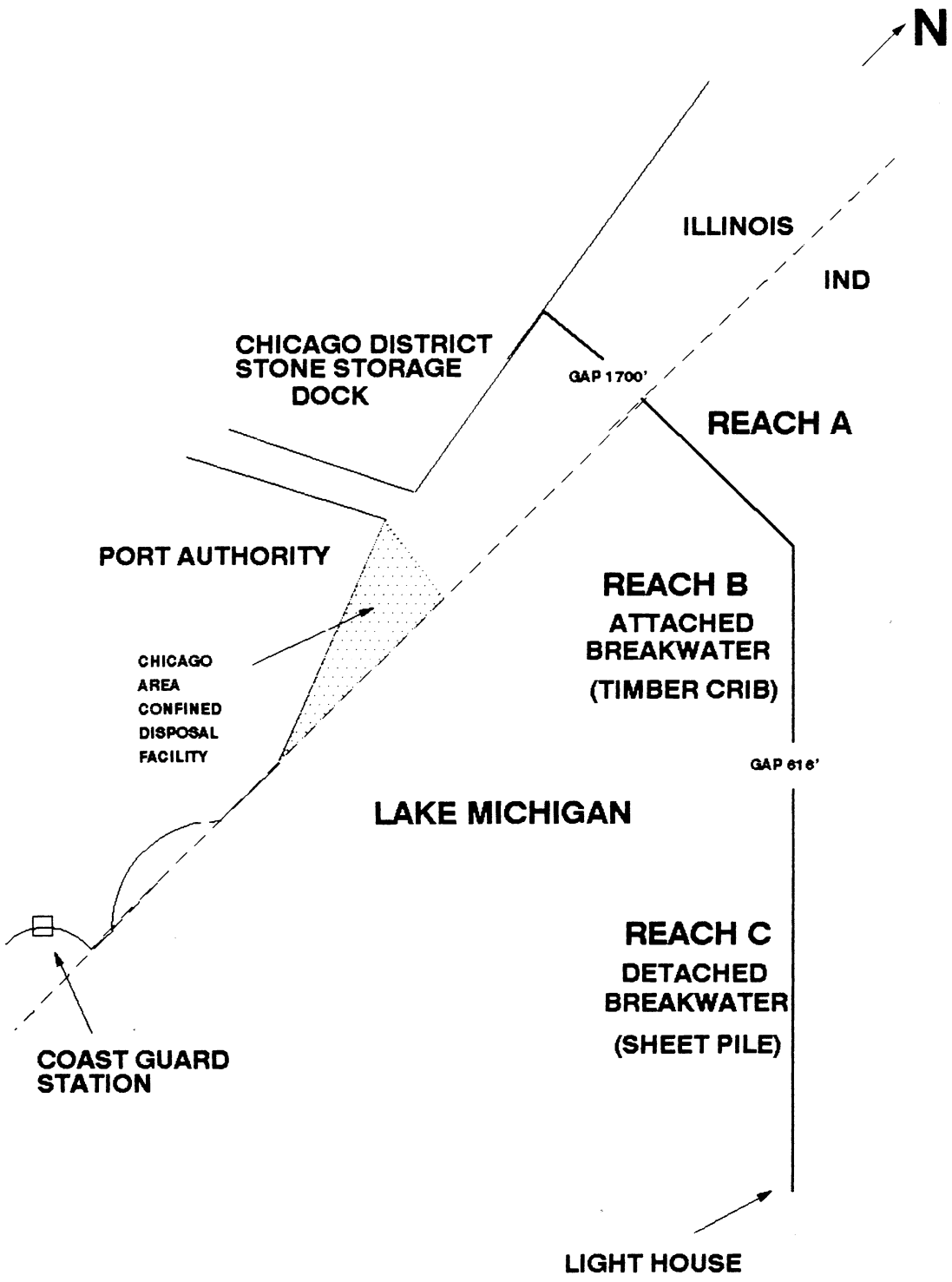

Fig. 1.1 Location of Calumet Harbor breakwater

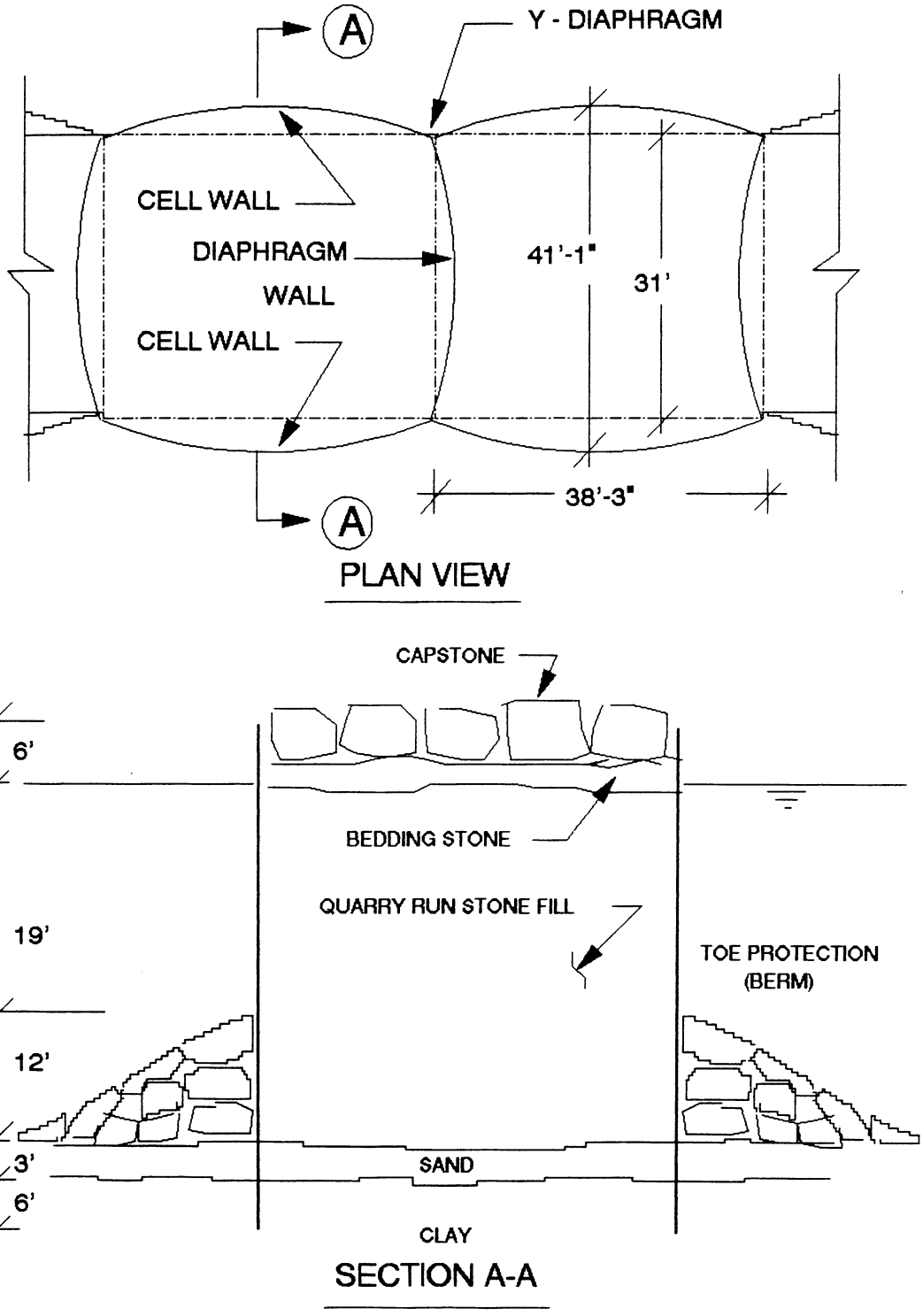

Fig. 1.2 Sectional elevation and plan view of breakwater cells

and 117, located about 600 ft west of the east end of the breakwater, failed (Fig. 1.3, Fig. 1.4 and Fig. 1.5). An inspection in October 1984 by Corps of Engineers personnel revealed split piles at the intersection of two cells and settled capstones as shown in Figs. 1.6 and Fig. 1.7. The split piles were repaired by welding, and protective stone was placed to create a rubble mound in the gap created by the failed sheet piles. The rubble mound is shown in Fig. 1.8.

Other recorded instances of damage to the structure include ship impact damage in 1957 and failure of a cell diaphragm in 1957. Intermittent repairs were made to the structure for the tears that occurred in the cell walls and diaphragm.

The failure of the Reach C was the subject of investigation of two structural analyses as summarized in a reconnaissance report by the Army Corps of Engineers (1). The failure at the top of the cell was attributed generally to fatigue, overstressed interlocks, high bending stresses in the top cantilever portion of the structure, and the like. However, the studies were speculative about the magnitude of the forces acting on the structure and the stresses developed within the structure as well as life estimation of the structure.

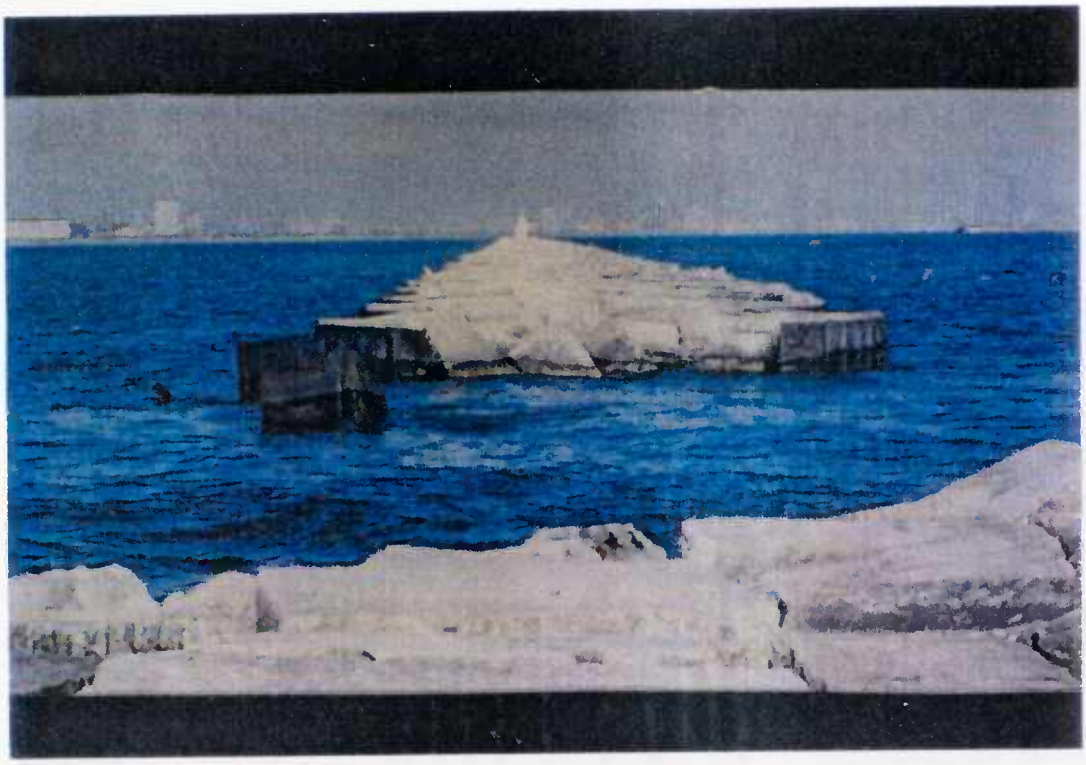

Fig. 1.3. View towards Northwest end of breakwater indicating failed cells

Fig. 1.4. View towards Southeast end of breakwater indicating failed cells

Fig. 1.5. Photograph of the failed cells during a reconnaissance survey

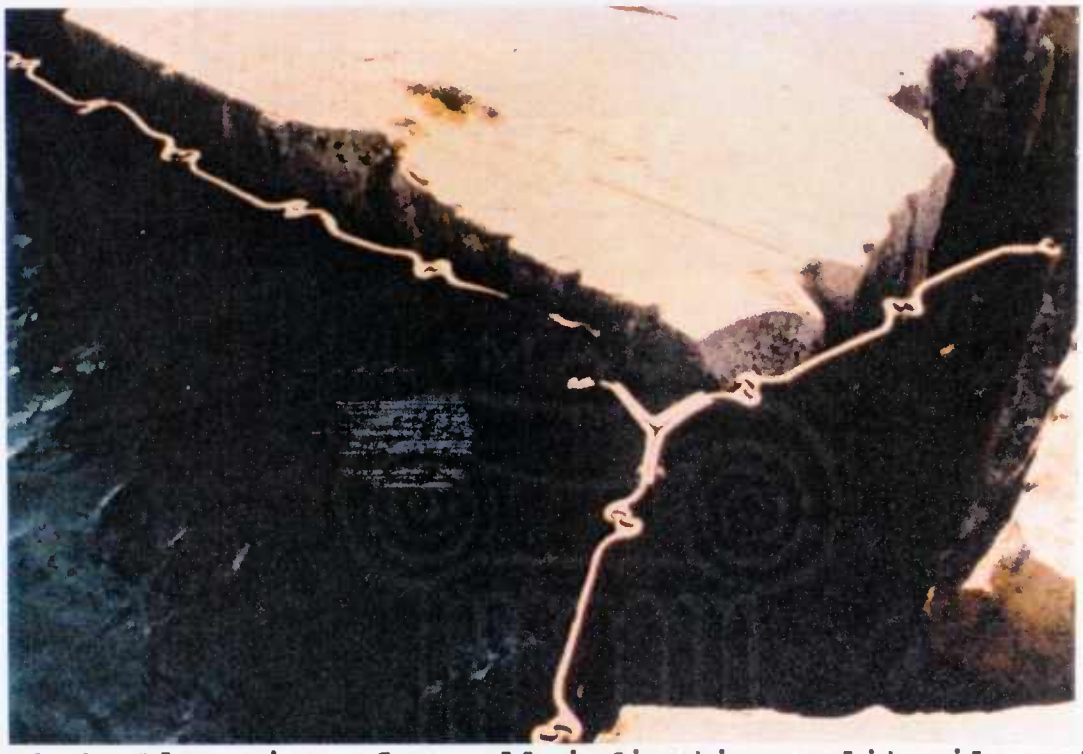

Fig. 1.6. Plan view of a cell indicating split piles at a Y - Intersection

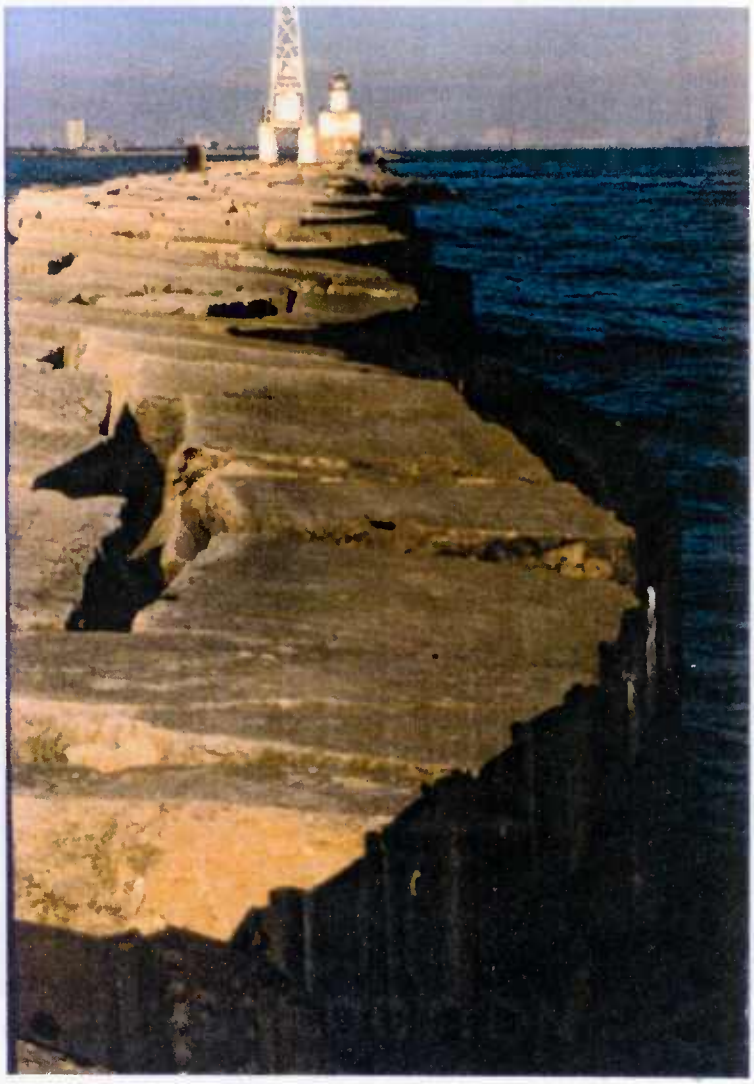

Fig. 1.7. View of the structure towards Southeast end indicating settled capstones

Fig. 1.8. Photograph of rubble mound created at cells 115, 116 and 117

1.2 Objectives and Scope of Work

This research project was sponsored by the Chicago District Army Corps of Engineers as an attempt to understand the behavior of the structure and to review the knowledge about the condition of the structure as the basis of future repair alternatives. The following were the primary objectives of the study:

1. Determine the likely failure mode of the previous failures.
2. Predict future performance of the structure.

In order to assess the potential failure modes of the structure, four major areas of study were identified. Figure 1.9 illustrates the overall solution approach undertaken in these four areas:

1. Laboratory testing
2. Instrumentation scheme
3. Force field estimation
4. Structural analysis

With these four major areas as input to the analysis, a damage evaluation of the structure was performed. The research tasks were carried out in two phases: Phase I ending in September 1989 and Phase II ending in September 1990.

The four major areas of study can be further subdivided into smaller tasks as shown in Fig. 1.10, which indicates

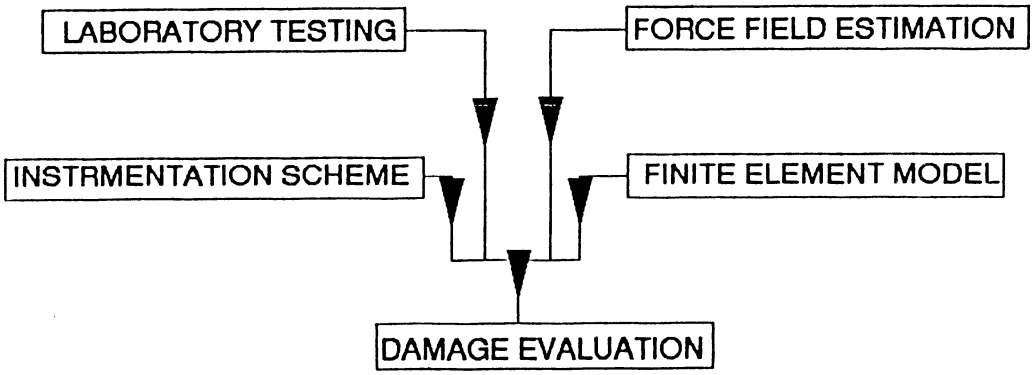

Fig. 1.9. Overall solution approach

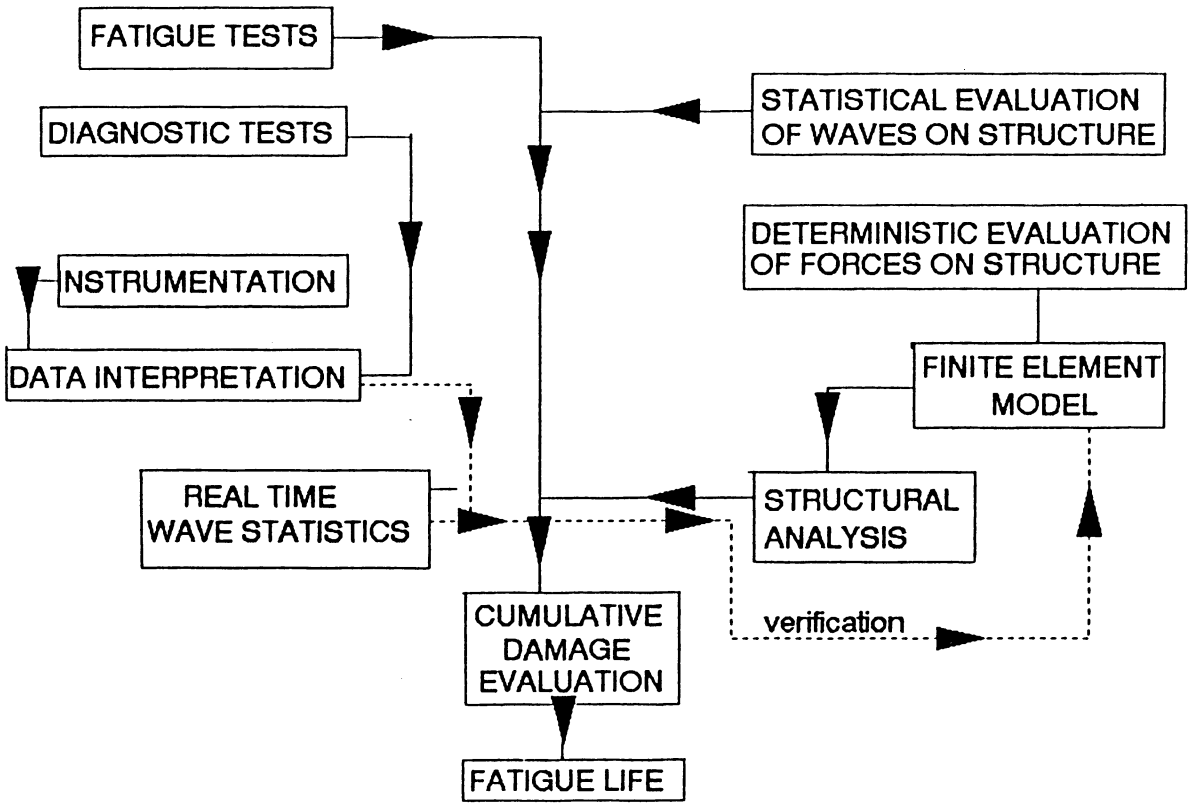

Fig. 1.10 Individual areas of effort in the study

individual areas of effort and their connectivity. The following provides a brief discussion of each of the tasks and their objectives for each individual area of effort.

1.2.1 Instrumentation of the Structure

Instrumentation of the structure was performed during two winter seasons; 1988 and 1989. The instrumentation consisted of strain gauges and a pressure transducer, a data acquisition system to record data, and a remote radio telemetry scheme for data transmission. The results of the instrumentation were to be used as a check of a finite element model developed for the structure which was analyzed by using real time wave statistics.

1.2.2 Fatigue tests and diagnostic tests

One of the main objectives of the project was to determine whether fatigue was a probable cause of failure. Because fatigue data on steel sheetpile specimens were lacking, fatigue tests were performed at the Structures Laboratory at Iowa State University (ISU). Sinusoidal loading was applied to specimens, and the number of cycles to failure was determined. A total of eight fatigue tests were performed, each at different load levels. In addition, diagnostic tests were performed to establish the field characteristics of the strain gauges, calibrate the pressure transducer, and determine the material properties of the steel sheetpiles.

1.2.3 Finite Element Model and Structural Analysis

Classical theories have typically been used in the past for analysis of steel sheetpile cellular structures (3,15). These theories have focused on the failure of the soil medium within the structure. These analyses fail to take into consideration the interaction effects between the soil and the surrounding structure. The need to develop a finite element model for the structure stems from an inability to adequately model the following effects:

1. Soil nonlinearities
2. Irregular dynamic wave pressure profiles
3. Interaction effects between fill material, sheetpiles, and waves.

The two-dimensional finite element model developed in this study was based on the work performed by Clough and Kuppuswamy (4) in developing a vertical slice analysis of Lock and Dam 26. The analysis in this study was performed by using a general-purpose finite element analysis package called ANSYS (5). The package offers a wide selection of elements, provides various nonlinear modeling options and furnishes good graphics output capabilities.

1.2.4 Real Time Wave Statistics

The real-time wave statistics at the site were supplied by the Corps of Engineers for the monitoring period that spanned the winters of 1988-89 and 1989-90. The real time

wave statistics were used to aid in validating the finite element model. The wave statistics were the result of the hindcast of data measured by a wave gauge at the site. The reduction of the hindcast statistics was performed by the Coastal Engineering Research Center (CERC) and presented in the form of the significant wave height and significant period of different sea states at the site.

1.2.5 Statistical Evaluation of Waves on Structure

The statistical evaluation of the waves on the structure contained three primary objectives:

1. Identify and classify individual sea states present at the site during the structure's lifetime.
2. Determine the percentage of occurrence of each sea state in the lifetime of the structure.
3. Determine a relationship between the wave height and period for generating wave pressures for the analysis.

Historical wave data at the Calumet Harbor Breakwater were requested by ISU from the Corps of Engineers. Statistical wave information at the Burns Harbor site in Indiana, which has been used in past studies to represent the wave climate for southern Lake Michigan, was provided and used for the analysis.

1.2.6 Deterministic Evaluation of Forces

Evaluation of the forces on the structure from the wave action was the objective of this part of the research. Wave pressure profiles were generated on the basis of the predicted waves and the relevant wave theory. The applicable wave theories are limited by wave height, wave length and water depth. The generated wave pressures were converted into forces applied at specific nodes on the structure for the analysis.

The results of the finite element analysis were further processed to yield stress ranges at different locations for a range of wave heights. A general-purpose statistical analysis program, the Statistical Analysis System (SAS), was used for polynomial regression of data to relate wave height and stress range.

The damage assessment of the structure was based on the fatigue damage methodology developed initially by Miner (7) and used by Williams and Rinne (8) and Hambly et al. (9) for fatigue evaluation of off-shore structures.

1.3 Literature Survey

The reconnaissance report by the U.S. Army Corps of Engineers (1) provides an overview of the damage sustained by the breakwater. It also lists the initial analyses made to understand the behavior of the failure.

References 2,10,11,12 and 13 provide thorough background on offshore engineering and wave mechanics. References 2 and 11 provide information on offshore engineering; reference 10 lists the engineering applications of the wave theories and provides introduction to the fatigue behavior of the offshore structures. Reference 13 provides an in-depth discussion of the wave mechanics. References 12 and 13 were used specifically in the report to calculate the wave pressures due to Cnoidal waves.

The paper by Williams and Rinne (8) develops simplified equations for making an evaluation of the fatigue failure potential in offshore structures. The general approach involved in failure analysis is outlined, and an example problem is illustrated.

In relation to the assessment of the fatigue damage during the tow of the jacket for Amoco Norway's Valhall Production Platform from Morgan City, Louisiana, to Stord, Norway, Hambly et. al. (9) adopted the equivalent stress range approach. The paper defines the damage criteria and illustrates the analysis involved in maintenance of a fatigue audit during the tow. Arulaih (14) demonstrates the calculations involved in the application of the deterministic analysis approach to evaluate the fatigue damage for an offshore structure.

The design and analysis methods described by Terzaghi (15) for cellular steel sheetpile structures are still widely applied with some modifications. In the Terzhagi method, a cellular cofferdam is first considered as a rigid gravity structure that must be stable against base sliding, overturning, and excessive interlock tension. The internal stability of the structure is also evaluated.

The design manual submitted to the U.S. Army Corps of Engineers by Rossow et. al (3) provides theoretical background for cellular sheetpile structures. Derivations and discussion of several design and analysis procedures mentioned in technical literature are included in this manual.

In relation with replacement of the old Lock and Dam 26 on the Mississippi River, Clough et al. applied finite element methods to the analysis of cellular sheetpile structures (4). Three different two-dimensional finite element models were studied. In all models allowances were made for nonlinear soil response and slippage on the sheet pile-soil interface. Predictions by the models were consistent with the observed trends.

2. FIELD INSTRUMENTATION

2.1 Background

The field instrumentation of the Reach C of the breakwater structure was done in two phases; Phase I of the instrumentation was installed in winter 1988-89 and Phase II during winter 1989-90. Phase I of the instrumentation was discussed in an interim report submitted to the Corps of Engineers (16). A summary of that report is included in Appendix A. In this chapter the Phase II portion of the field operation is discussed along with brief information related to the equipment and installation procedure. Chapter 5 contains a discussion of the correlation between the field data and the results from a finite element model of the structure (See section 5.3).

2.2 Field Instrumentation

The instrumentation system was designed to allow the collection of the data to be controlled at ISU facilities in Ames, Iowa. A schematic diagram of the instrumentation scheme is shown in Fig. 2.1. The instrumentation installed during Phase II consisted of the following four parts:

1. Thirteen strain gauges and a pressure transducer
2. A data acquisition system (DAS) consisting of a CR-7 control module.
3. A communications system consisting of radio frequency, antennae, UHF radios, and phone modems.

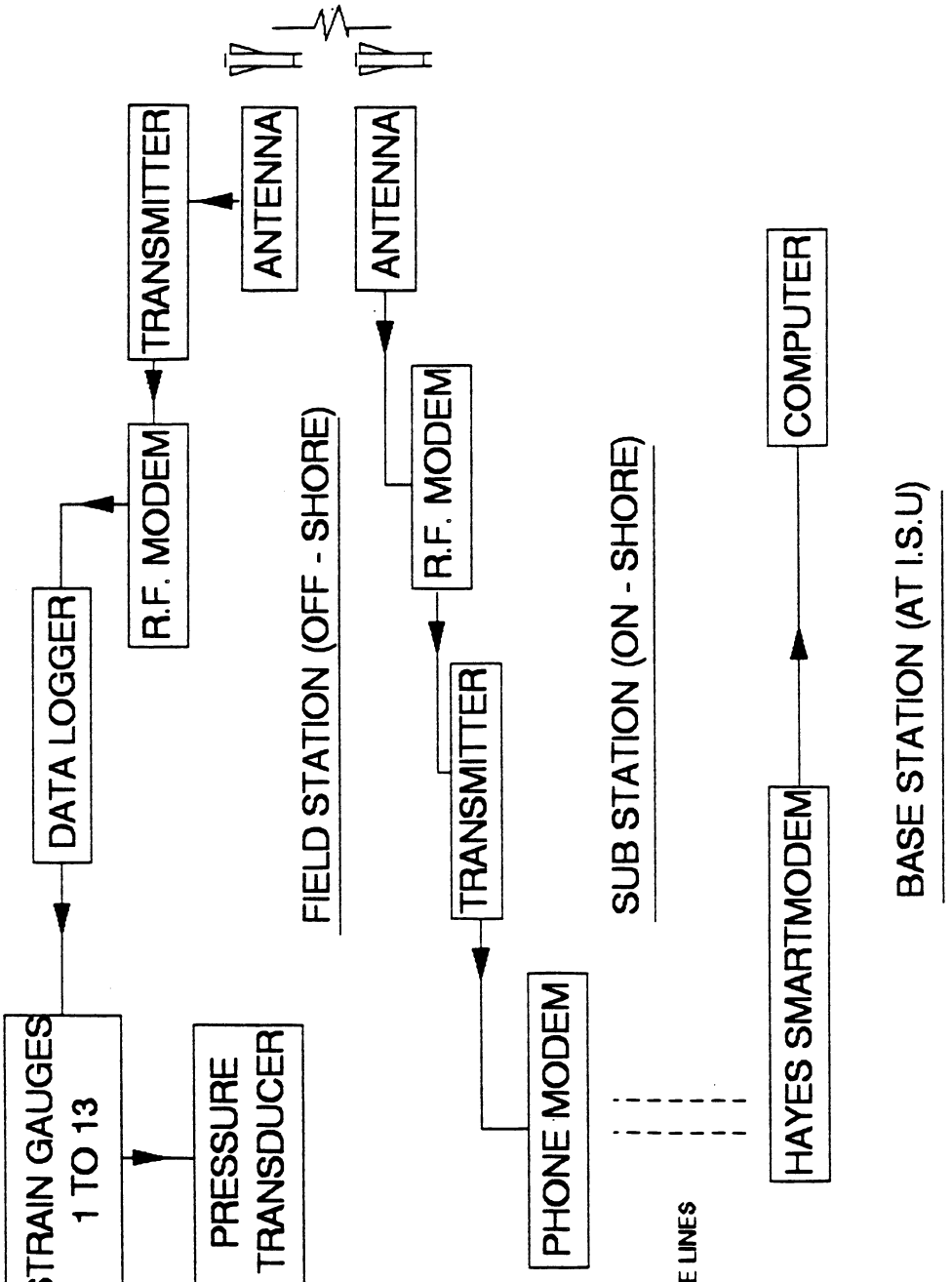

Fig. 2.1 Schematic diagram of instrumentation scheme

4. Microcomputer at ISU to maintain communications protocol, control the data acquisition, and act as a storage module for the collected data.

Figure 2.2. shows the location of the strain gauges on the cells. The strain gauges were installed on two cells immediately to the west of the cell at the eastern end of the breakwater. The location and orientation of the structure was shown in Fig. 1.1. The lighthouse at the eastern end was used to station the system and the communications equipment. This arrangement formed the field station offshore. The Coast Guard Station onshore served as a substation. The control station at ISU is considered the base station.

The Phase II installation operation was performed in two stages. The first stage of operation during the last week of October involved installation of strain gauges and establishment of the field station and communications system. The second stage of operation involved installation of the DAS and establishment of a communications contact between the field station and the base station. Figures 2.3 to Fig. 2.6 indicate the first stage of installation, showing, respectively, the layout of the instrumentation cable network, the diving operation, fixing of the cables to the capstones and the final stages of installation, and inspection on the next day. Figure 2.7 indicates the

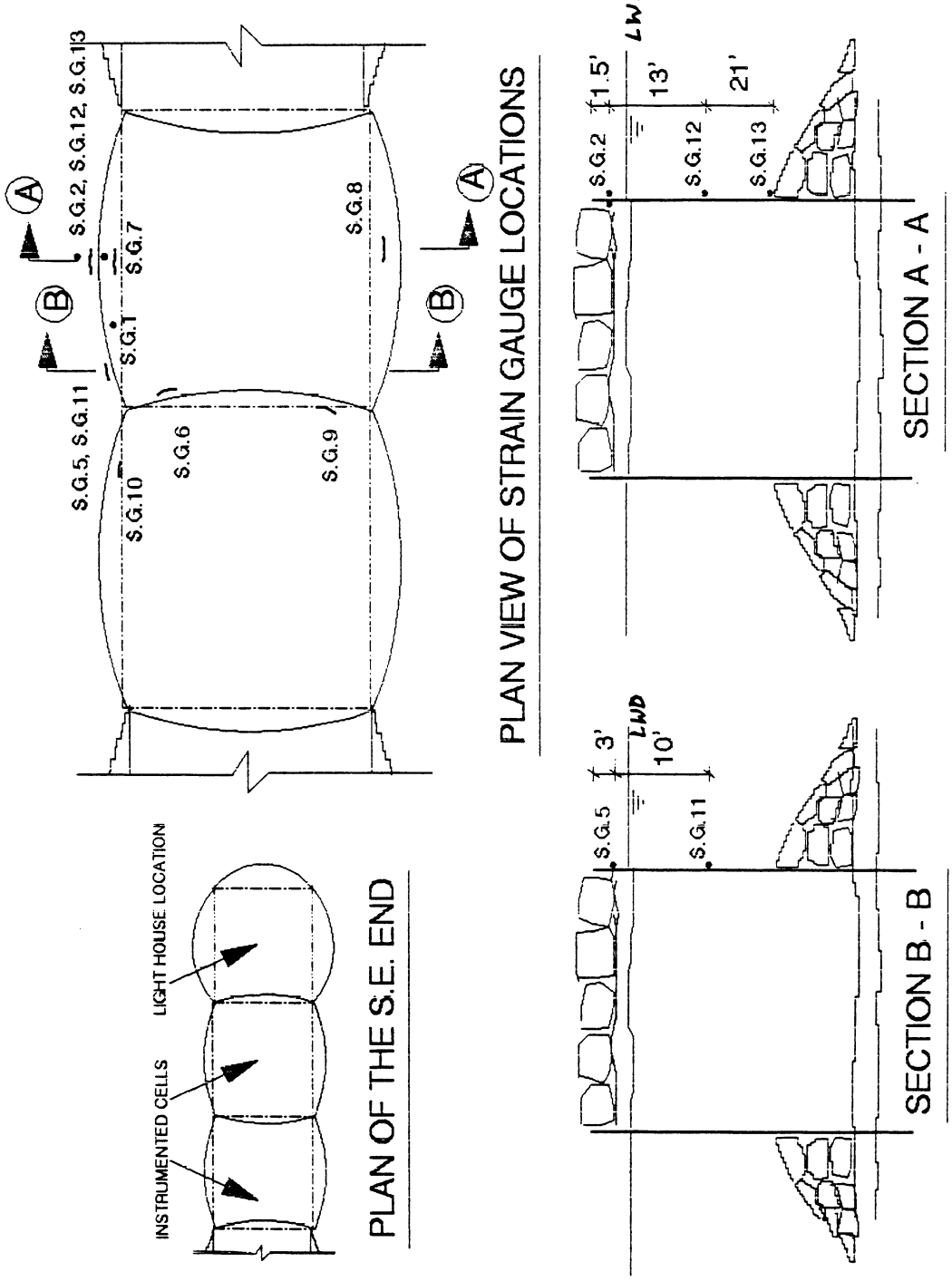

Fig. 2.2 Location of strain gauges on the instrumented cells

Fig. 2.3. Layout of instrumentation Cable network

Fig. 2.4. Underwater Welder surfacing for a tool during Operation

Fig. 2.5 Fixing of cables to capstones

Fig. 2.6 Final stages of the installation operation

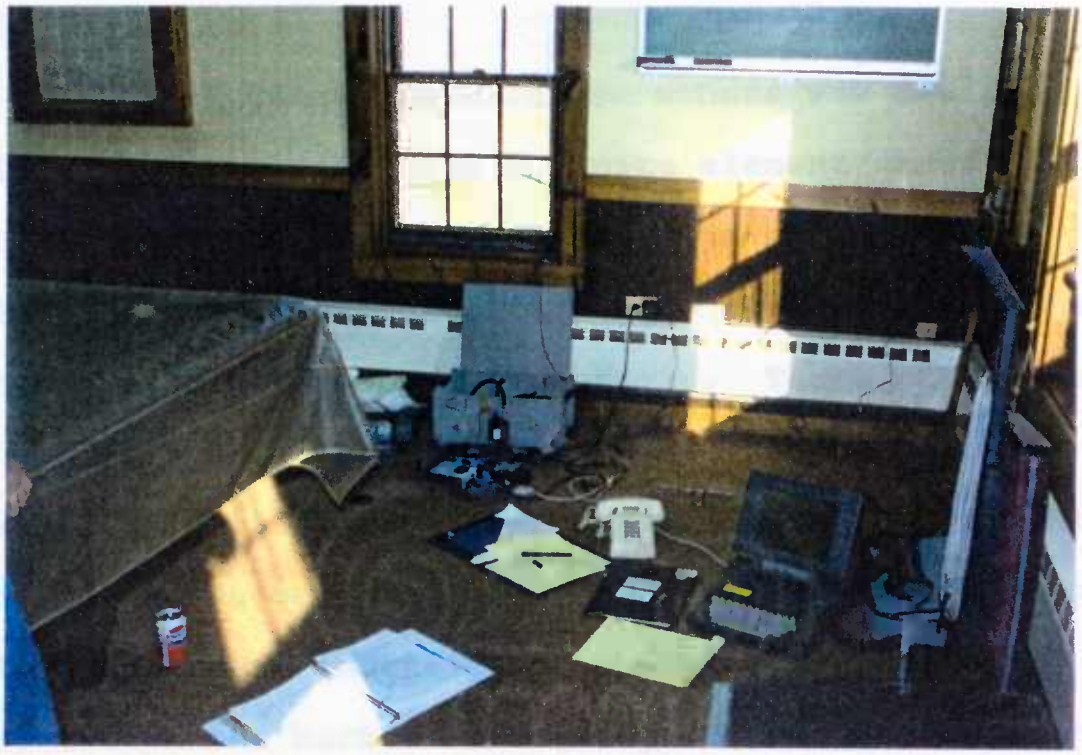

Fig. 2.7. View of the substation during the installation and testing of communications system

establishment of the communications between various stations. This is in the substation at the coast guard station on shore.

The strain gauge installation scheme was designed to obtain data to be used with a finite element structural model of the breakwater structure. The strain gauges consisted of three gauges oriented to measure flexure strain and ten gauges to measure hoop strain. Three of the ten hoop gauges are installed under water (see Fig. 2.2). Two surface hoop strain gauges were installed on the diaphragm of the cells (Gauge 6 and Gauge 9). Three surface hoop strain gauges were installed on the central portion of the cells, two on the harbor side (Gauge 2 and Gauge 7), and one on the lake side (Gauge 8). Two hoop strain gauges were located near the diaphragm of the cells (Gauge 6 and Gauge 9). Of the three underwater strain gauges, one was installed near the diaphragm (Gauge 11) and two were installed at different elevations at the central portion of the cell toward the lake side (Gauges 12 and 13).

Data were collected from December 1989 to early March 1990. A communication transmission breakdown during the last two weeks of January (January 16th to January 30th), traced to a power outage in the system, was repaired. In addition, Strain Gauges 2 and 11 and the pressure transducer ceased operation after the last week of December. The prime

indicator to prompt data collection was to be the presence of the strong winds in the vicinity and corresponding significant wave activity; the data collection procedure was to be initiated by weather reports obtained from the National Weather Service at Chicago, the Coast Guard personnel at Calumet Harbor station and commercial weather reports. However, during the monitoring period, there were no major storms and data were collected on a regular basis.

The data collected by the installed data acquisition system consisted of the pressure values in feet of water and the strains in microstrains. The total data collection time in any one attempt was restricted by memory to about 6.5 mins. This recording period is called a data segment. The data were collected at intervals of 0.3 sec in a data collection segment. Part of the data collected on January 12th is shown in Fig. 2.8. This typical variation was part of a larger data segment. Twenty-four data segments were recorded during the data acquisition period.

Real-time wave data were collected by a wave gauge installed in Lake Michigan near the breakwater Reach C by the Army Corps of Engineers, Chicago District. Fig. 2.9 shows the wave gauge being installed at site. These data were reduced at the Coastal Engineering Research Center at Vicksburg (CERC) and communicated through the Chicago District. The reduced data consisted of the time of

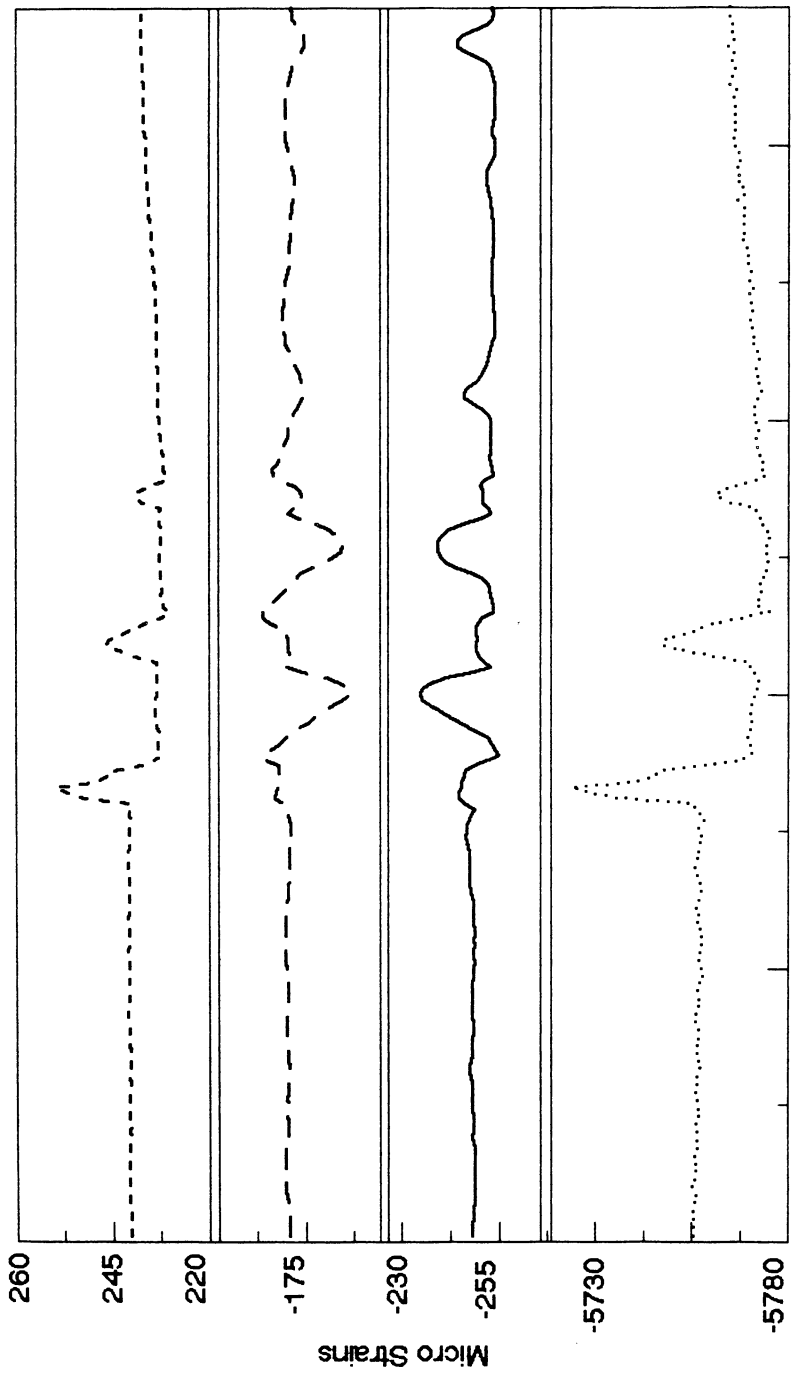

Fig. 2.8a Typical data segment (Strain gauges 1,3,4 and 5)

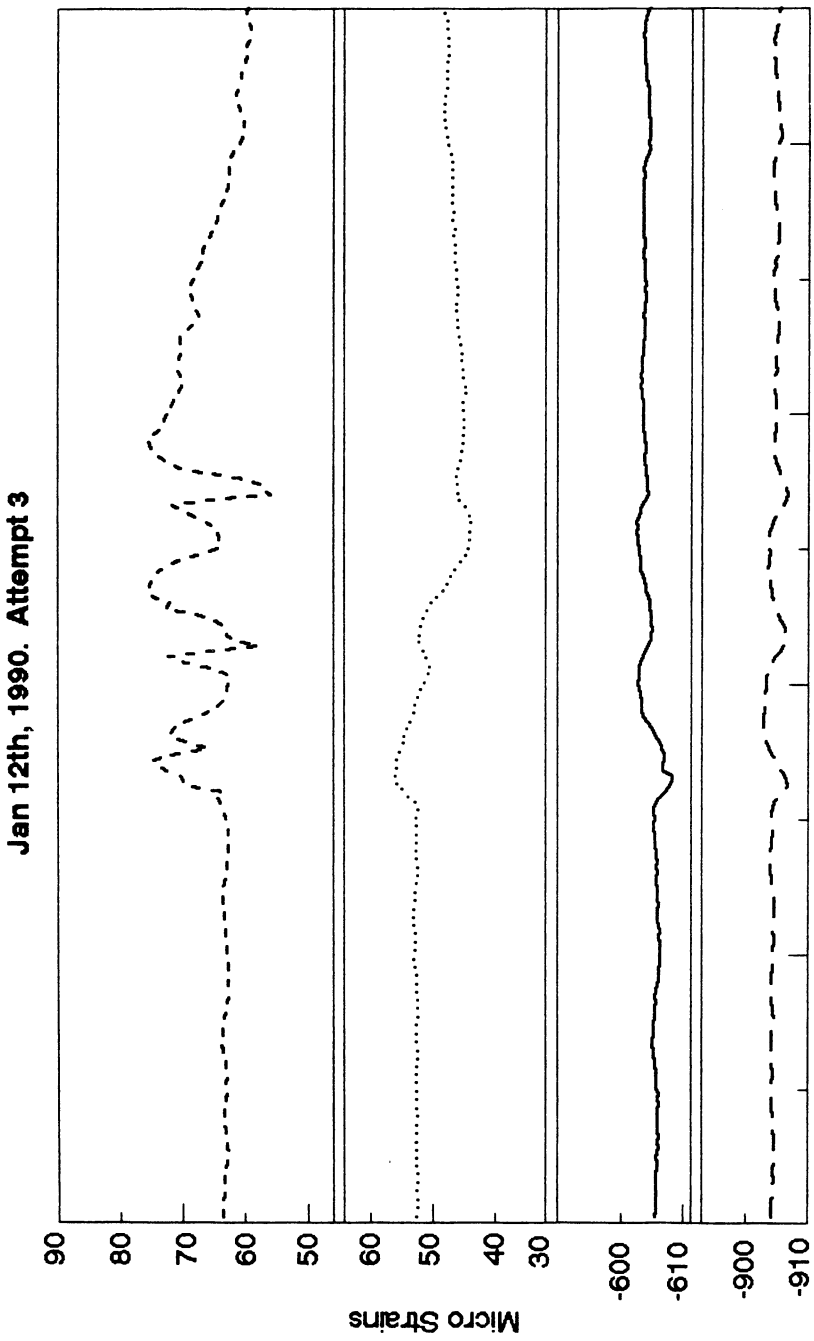

Fig. 2.8b Typical data segment (Strain gauges 6,7,8 and 9)

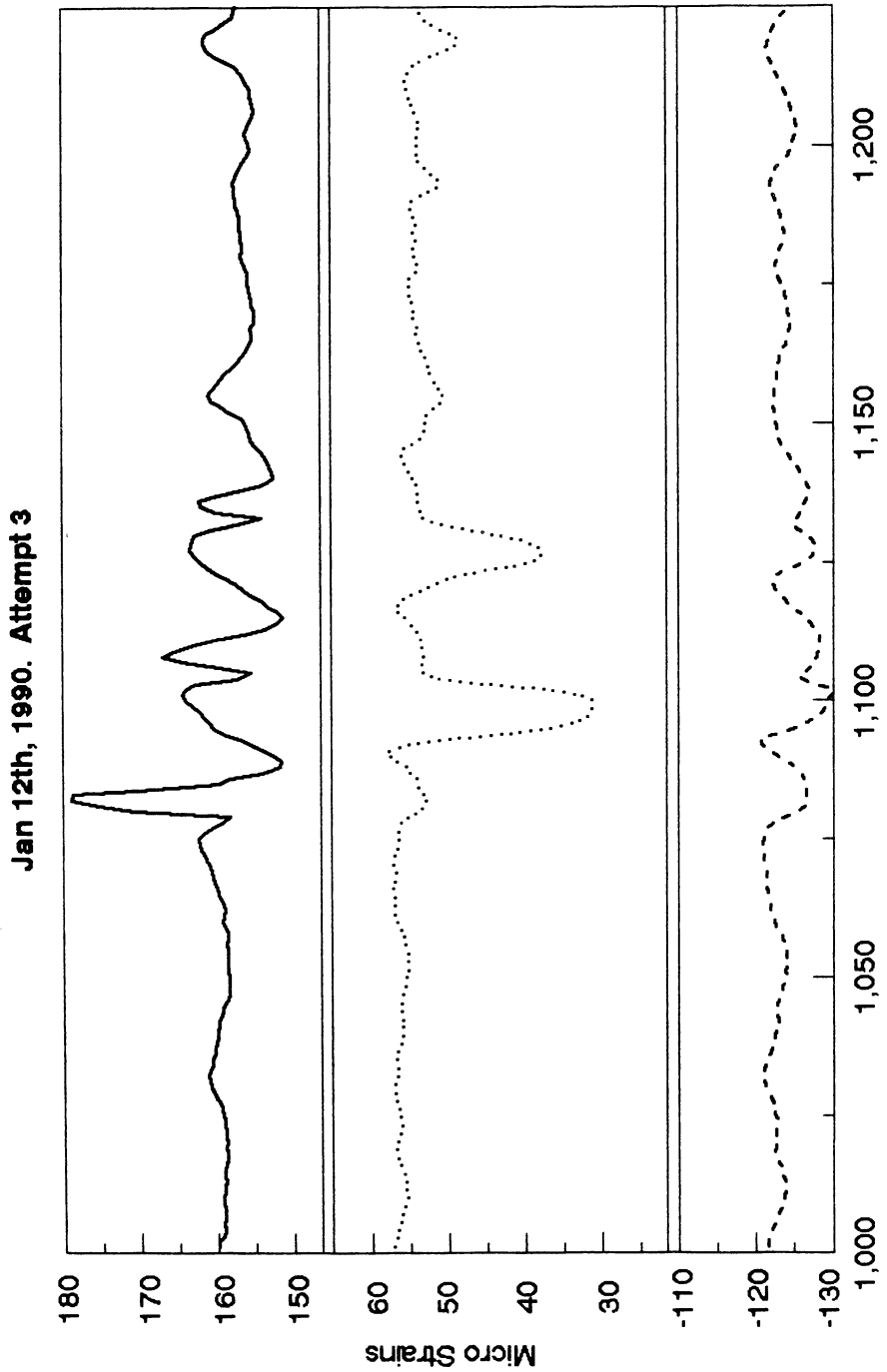

Fig. 2.8c Typical data segment (Strain gauges 10,12 and 13)

Fig. 2.9 Wave gauge being installed at site by the Corps of Engineers personnel

collection and corresponding significant wave height. The data collection time spanned December 1989 to April 1990.

Table A.1 in Appendix A illustrates the dates, recording time, and the maximum wave for the different dates. On the basis of the reduced CERC data, of the 24 recorded segments, only 19 were significant. The other periods for which no reduced data were available probably referred to quiescent lake conditions. The diagnostic tests detailed in Appendix A were used to transform the recorded strain ranges into the hoop-force ranges on the structure. Table A.2 and Table A.3 in Appendix A illustrate the transformed hoop forces.

The data regarding the weather conditions, the wind direction and speed, and other climatological data were obtained from the National Climatic Data Center, Ashville, North Carolina. The data were from the marine coastal weather log maintained at the Calumet Harbor. The recorded data were analyzed with respect to the analytical data. The analysis and results are presented in Chapter 6.

3. FATIGUE TESTS

3.1 Introduction

The type PSA23 steel sheet piles used in the construction of the Calumet Harbor detached Breakwater, Reach C, were tested in the laboratory. The primary objective of the testing program was to determine the behavior of the sheetpile interlocks in fatigue and to develop a fatigue hoop-force range vs. no. of cycles-to-failure curve (S-N curve).

Earlier static load tests of steel sheetpile specimens by others (1,16) had shown that failure occurs because of opening of the interlocks. The minimum ultimate interlock strength as documented by the U.S. Steel Sheetpiling Handbook was 12,000 lb/in. (16). The recommended design value for this pile type is 3000 lb/in.

3.2 Test Procedure

The testing was performed by orienting the sheet pile specimens as shown in Fig. 3.1. The testing was performed with three specimens constituting the test setup: the middle or target specimen, and the other two transition specimens. This setup was considered to simulate the in situ conditions as closely as possible on the target specimen.

The loading on the specimen was sinusoidal, with a frequency of 1 Hz. The specimens were subjected to cyclic loading at maximum force ranges ranging from 2750 lb/in.

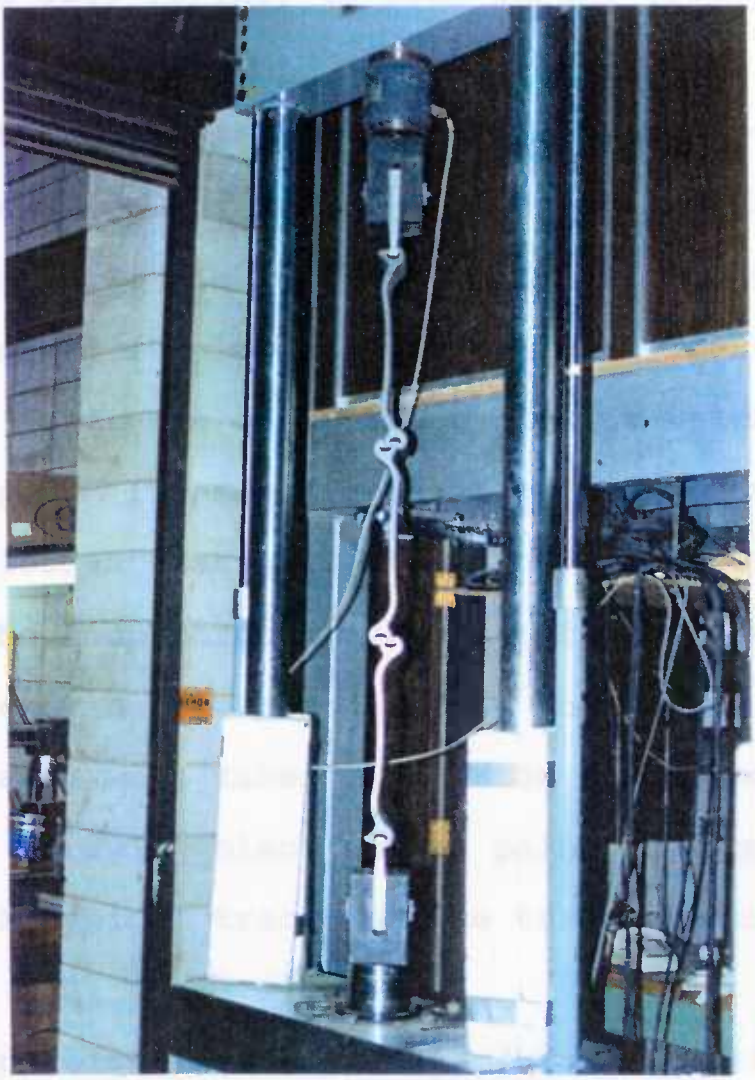

Fig. 3.1 Test set up indicating the MTS loading frame. Load input is by hydraulic load cells at either end of the system

(500 lb/in. to 3250 lb/in.) to 5900 lb/in. (500 lb/in. to 6400 lb/in.).

The quantities measured during the testing were interlock separation and interlock opening. Both are defined in Fig. 3.2. In addition to these measurements, traces of deformed samples were taken. All measurements were taken at intervals of 15,000 cycles at which time the test was stopped. Interlock separation was measured with the specimen loaded statically at a load representing the maximum for the hoop-force range. Interlock opening was measured by removing the samples from the test setup. At this time, traces were taken of all the three samples in the test setup by spraying black enamel paint on a graph paper background. A typical trace for the target specimen is shown in Fig. 3.3.

A total of eight tests were performed; the test results are summarized in Table 3.1. The fatigue curve is shown in Fig. 3.4 as a log-log plot of hoop-force range vs. the no. of cycles to failure. In all the tests, the interlock separation and interlock opening were insignificant. Appendix B contains details of the information from Test No. 6.

3.3 Discussion of Results

Failure occurred consistently in the target specimen (i.e., the central pile in the test setup). The mode of

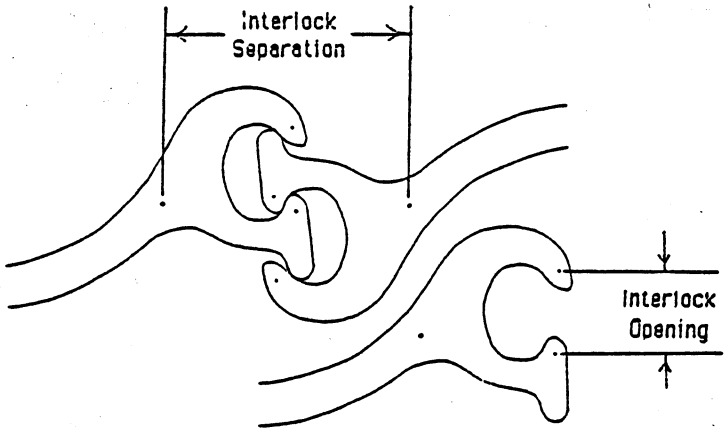

Fig. 3.2 Quantities measured during testing

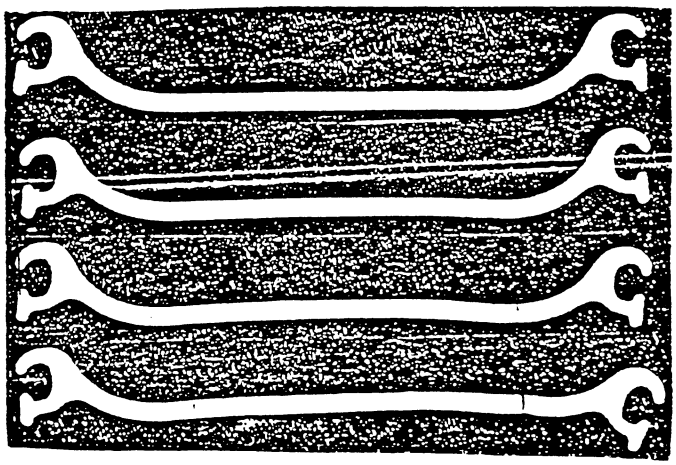

Fig. 3.3 Trace of the target specimen during testi

Table 3.1: Results of fatigue tests

Test #	Max. intlk. load (lb)	Min. intlk. load (lb)	Max. intlk. load/in (lb/in.)	Min. intlk. load/in (lb/in.)	Fatigue loading range (lb/in.)	Number of cycles to failure, N
1	28800	2250[a]	6400	500	5900	21700
2	29500	2500	5900	500	5400	28620
3	27250	2500	5450	500	4950	32150
4	24750	2500	4950	500	4450	34200
5	22250	2500	4450	500	3950	43340
6	19750	2500	3950	500	3450	56160
7	16200	2250[a]	3600	500	3100	67480
8	16250	2500	3250	500	2750	500000

[a]Denotes 4.5 in wide test specimens

failure for the steel sheet pile specimen in all the tests was due to the formation of a crack at a point near the top of the specimen. Tracings as shown in Fig. 3.3 illustrate the typical failure mode and progression to failure. As shown, the deformation of the sample increases until a crack initiates in the specimen near the arch of the web and progresses to failure. Failure was assumed to occur when the specimen cracked completely through. Once the crack begins, failure progresses relatively quickly. The location of the crack for all the specimens was in the same region on the arch at a distance of approximately 4.75 in. to 5.75 in. from the center line of the web.

The crack location seems to be logical when one considers the mechanics of load resistance by the pile subjected to the cyclic loads. Calculations are provided in Appendix B to support the existence of high stresses in the pile at crack location. Bending moment occurs in the sheet pile specimen because of the arched web shape and the hoop force acting through the interlocks. The net moment is proportional to the distance between the web and the line through the interlocks.

An examination of the fatigue curve as summarized in Fig. 3.4 indicates that only seven tests were considered for its development. The Test No. 8 was stopped because of time

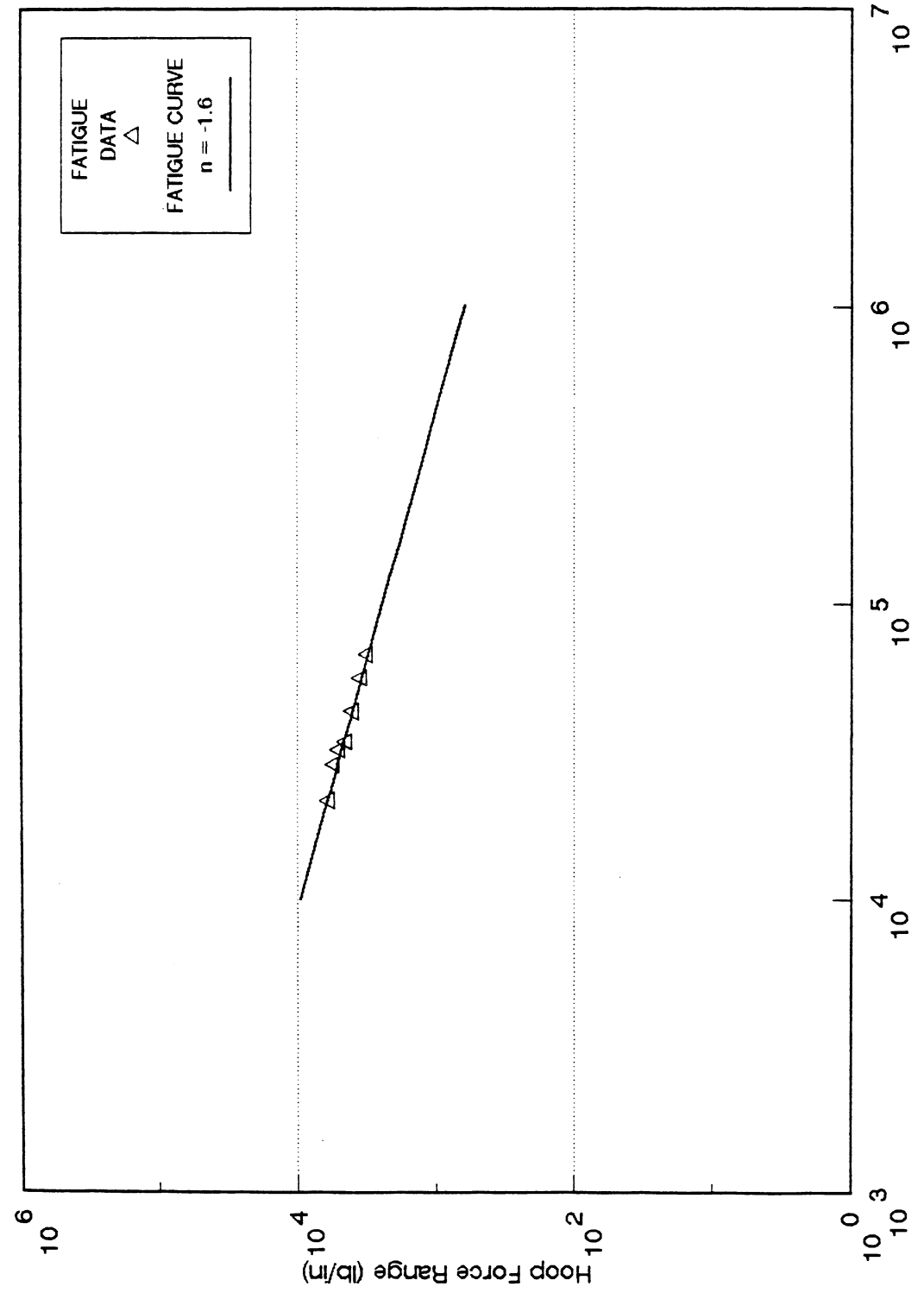

Fig. 3.4 Fatigue S-N curve for steel sheetpile specimens

constraints at 500,000 cycles, which was assumed to be the endurance limit for the sheet pile test specimens.

Though the test sample size was small and the spread of the load ranges was narrow, two important conclusions regarding the fatigue behavior of the sheet pile specimens were found:

1. The failure pattern due to cyclic loading does not involve opening and failure of interlocks; it is caused by crack initiation in the region of high interlock force.
2. This observed failure mode occurs at loads that are much less than the previously observed static failure load and in some cases even less than the recommended design loads.

4. EVALUATION OF FORCES ON THE STRUCTURE

4.1 Introduction

Wave statistics in the form of hindcast wave data were used to predict a suitable or representative design loading history on the structure. Because the waves are random in nature, statistical relationships are typically used to understand their behavior. For a detailed discussion of the topic of wave statistics, the reader is urged to refer to references 2 and 10.

4.2 Burns Harbor Data

In the absence of recorded wave data for the specific location of the breakwater in Lake Michigan, the wave climate at Burns Harbor, Indiana, from hindcast data from a study by Cole and Hilfiker (17), is used to predict the design loading history. The SMB method, formulated by Sverdrup and Munk and modified by Brettschneider, was used to hindcast the wave parameters in the study. The data were reduced from weather charts covering the years 1965, 1966, and 1967. The data are in the form of monthly statistics reported in a bivariate histogram with the significant wave height as ordinate and the period as abscissa. Each observation relating to a specific wave height and period is a multiple of six hours because the weather chart observations are usually taken in multiples of six hours. The data were classified on the basis of 16 different

directions, each direction covering a range of 22.5° of the compass.

Burns Harbor data were used for the analysis performed in the Reach C study. The main tasks of the analysis included:

1. Compilation of monthly statistics into bivariate histograms on a directionwise basis for the whole three-year observation period.
2. Determination of relationships between the wave height and period for the data in the form of bivariate histograms.

As part of the first task, the wave percentage of occurrence for different directions can be evaluated by considering that the observations, temporal in nature, span the whole hindcast period of three years. The statistical data are in the form of certain and uncertain data with regard to the wave heights. The certain data are classified into observable and calm data, each pertaining to the data generated during observable wave activity and quiescent wave conditions respectively. The uncertain data, which occur for 3.65% of the total recorded time, are distributed among the directionwise data and calm data in the respective ratios of occurrence. Finally, the observable wave data are distributed directionwise among the 16 directions. As part of Task 1 above, bivariate wave histograms were generated for each direction. A typical histogram is illustrated in

Table 4.1. The other histograms are listed in Appendix C. Each bin in the bivariate histogram refers to the number of hours in hindcast data that are represented by a significant wave height (H_s) with an associated significant period (T_s).

The results of the first task are summarized in tabular form as shown in the Table 4.2. The parameters used in Table 4.2 are briefly explained as follows: the sea conditions at a specific site can be defined by different sea states. Each sea state is a unit of time for which the sea condition is assumed to be represented statistically by a significant wave and a significant period. The statistical analysis was performed for each direction. The directions SW, SSW, WSW, NNW, WNW, and NW are predominant with respect to the percentage of occurrence. Note that the total percentage of occurrence of different directions does not sum to 100%. This is because calm data (recorded when the sea is in a quiescent condition) accounted for 51.2% of the data. Also note that the theoretical maximum wave height at the site was limited by the depth of the lake bed below the still water level. Any wave height exceeding 29.7 ft would be assumed to become unstable and break.

The relationship between the maximum wave height and the associated period for a particular direction was established by means of regression analysis. The analysis was performed in two steps as follows:

Table 4.1: Bivariate histogram for ENE direction

Wave height (ft)	Wave Period (Sec) 2 to 3	3 to 4	4 to 5	5 to 6	6 to 7	7 to 8	8 to 9	9 to 10
1.0 to 2.0	6[a]							
2.0 to 3.0	30	108	12	6				
3.0 to 4.0		18	108	30				
4.0 to 5.0			48	60				
5.0 to 6.0				78	6			
6.0 to 7.0				66	42	6		
7.0 to 8.0					30	12		
8.0 to 9.0					6	12		
9.0 to 10.0						12		
10.0 to 11.0						6		
11.0 to 12.0							6	
12.0 to 13.0							12	
13.0 to 14.0								
14.0 to 15.0								
15.0 to 16.0								6
16.0 to 17.0								
17.0 to 18.0								6

[a]Numbers in bins refer to the no. of hours of hindcast data

Table 5.2: Summary of statisitical analysis of historical wave data

Direction of waves	Highest significant wave (ft)	Maximum wave (ft)	% of occurrence	No. of sea states
NE	28 - 29	29.7[a]	2.84	22
ENE	17 - 18	29.7	3.05	26
E	7 - 8	13.3	1.70	10
ESE	3 - 4	5.3	0.43	5
SE	3 - 4	5.3	0.91	7
SSE	3 - 4	5.3	0.99	5
S	4 - 5	8.0	1.65	5
SSW	4 - 5	8.0	4.04	8
SW	5 - 6	9.8	7.00	11
WSW	4 - 5	8.0	5.30	7
S	9 - 10	17.0	2.84	10
WNW	7 - 8	13.3	3.90	11
NW	8 - 9	15.0	3.83	14
NNW	12 - 13	22.0	3.88	22
N	19 - 20	29.7	3.17	28
NNE	12 - 13	22.0	3.22	26

[a]Denotes the maximum possible wave height at site

1. Generation of a regression equation on the basis of a weighted regression analysis by treating the significant wave height, H_s, and the significant period, T_s, as the variables and considering the number of observations at each bin as weight. The regression equation is of the form

$$\omega_s = A.e^{-B.Hs}$$

_____Eqn. 4.1

where,

ω_s = frequency of the waves = $2\Pi/T_s$

H_s = wave height

A,B = constants

2. Transformation of the parameters ω_s and T_s to maximum wave height H_{max} and associated period T_p can be done by considering the following relationships between H_s and H_{max} and T_s and T_p.

$$H_{max} = 1.77\ H_s$$ _____Eqn. 4.1a

$$T_p = 1.408\ T_z$$ _____Eqn. 4.1b

The resulting transformed equation as shown below was used to generate various peak waves and associated periods on the structure for structural analysis.

$$\omega_p = C.e^{-D.Hmax}$$

____Eqn. 4.2

The constants C and D vary for different directions. This format allows application of a method for generating waves of specific wave height and associated period for analysis.

4.3 Evaluation of the Force Field on the Structure

Forces that act on rigid vertical walls such as the side of the breakwater comprise static and dynamic pressure components of the waves. Depending on the depth at the toe of the structure from the still water level, d, and the wave height, H, the waves are either nonbreaking, standing, or breaking waves. If the water is sufficiently deep at the toe ($d > 1.3H$), a standing wave system will be set up on the breakwater with fluctuating pressures. For shallower water depths ($d < 1.3H$), the waves will break on the structure (reference 11, p. 163).

Considering the breakwater structure at Reach C, three kinds of waves have been considered for analysis; non-breaking waves, breaking waves, and standing waves. The method of determining the forces on the structure consisted of

1. Consideration of a specific wave height and associated period pair (Eqn. 4.2)
2. Application of the valid wave theory to generate the wave pressures on the structure
3. Conversion of the wave pressures into nodal forces

Only the components of the waves that act perpendicular to the structure were used in the analysis. Other effects

that might modify the wave pattern on the structure, such as wave refraction and diffraction, were not considered.

4.4 Determination of Wave Pressures

Different methods exist for the evaluation of pressures on rigid vertical walls. Most of the formulae for evaluation of pressures on vertical walls for design conditions are empirical in nature, and they consider the maximum values of likely pressures on the structure. Because the time-dependent varying forces are of concern in this research, classical theories of waves were considered for generation of pressures through the depth of the structure. The pressures were generated for the peak and trough conditions of each wave applied on the structure and were transformed into the nodal forces to be applied on the structure.

The degree of complexity involved in calculation and the accuracy of the solution for wave motion changes in the case of the higher order theories. The primary problem that arises in usage of various theories is to determine which theory is pertinent to a given situation. Le Mehaute's graph, which (18) describes different domains of validity for different wave theories, was used as the basis for selection of the appropriate wave theory in the analysis. The graph is indicated as Fig. 4.1.

The theories used for computation of pressures and forces on the structure were Stokes' second-order theory,

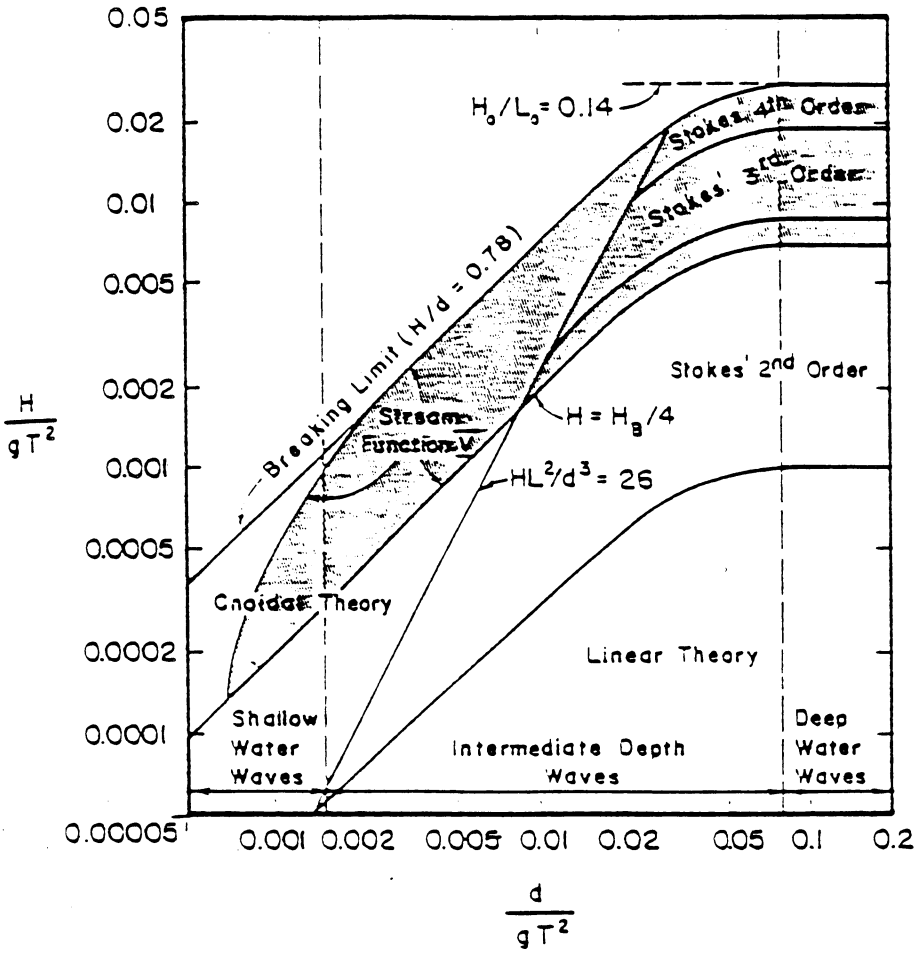

Fig. 4.1 Ranges of suitability for wave theories suggested by Le Mehaute

standing wave theory, and Cnoidal theory. Only brief explanations of these theories are outlined in this report. For further details and derivations, the reader is urged to consult references 10 and 12.

Second-Order Stokes Theory:

Surface profile:

$$\eta = \frac{H}{2}\cos(kx-\omega t) + \frac{H^2}{8}\left(\frac{\pi}{\lambda}\right)\frac{\cosh kd}{\sinh^3 kd}\left[2+\cosh(2kd)\right]\cos\left[2(kx-\omega t)\right]$$

____Eqn. 4.3

Dynamic pressure distribution:

$$p = \frac{H}{2}(\rho g)\cosh\left[k(2+d)\right]\cos(kx-\omega t) + \frac{3}{4}H^2\left(\frac{\rho g\pi}{\lambda}\right)\left[\frac{1}{\sinh 2kd}\right]$$

$$+\left[\frac{\cosh 2k(z+d)}{\sinh^2 kd} - \frac{1}{3}\right]\cos\left[2(kx-\omega t)\right]$$

____Eqn. 4.4

Correction to the first-order static pressure distribution:

$$\frac{1}{4}\rho g\pi\left(\frac{H^2}{\lambda}\right)\frac{1}{\sinh 2kd}\left\{\cosh\left[2k(z+d)\right]-1\right\}$$

____Eqn. 4.5

The pressure distributions at wave troughs and peaks were calculated for 32 waves by using the methods described above. The values of the calculated pressures and the pressure profiles for a wave height of 8.0 feet with an associated period of 7.38 sec from the NNE direction are illustrated in Figs. 4.2 and 4.3. The associated period was developed from the wave histogram for the NNE direction according to the methodology developed earlier.

Cnoidal Theory:

The pressure calculation below any cnoidal wave at any elevation **y** above the lake bed depends on local fluid velocity; it is complex. However, it can be approximated by the expression

$$p=\rho g(Y_s-Y)$$

____Eqn. 4.6

with the pressure distribution varying hydrostatically from zero at the surface to $\rho g Y_s$ at the bottom. The problem now reduces to the determination of the water surface elevation, which can be accomplished by using the curves specified in the Shore Protection Manual (13) published by the Corps of Engineers.

The pressure distributions at wave troughs and the wave peaks are calculated for 18 waves by using the method described above. The values of the calculated pressures and the pressure profiles for a wave height 24.0 feet with an

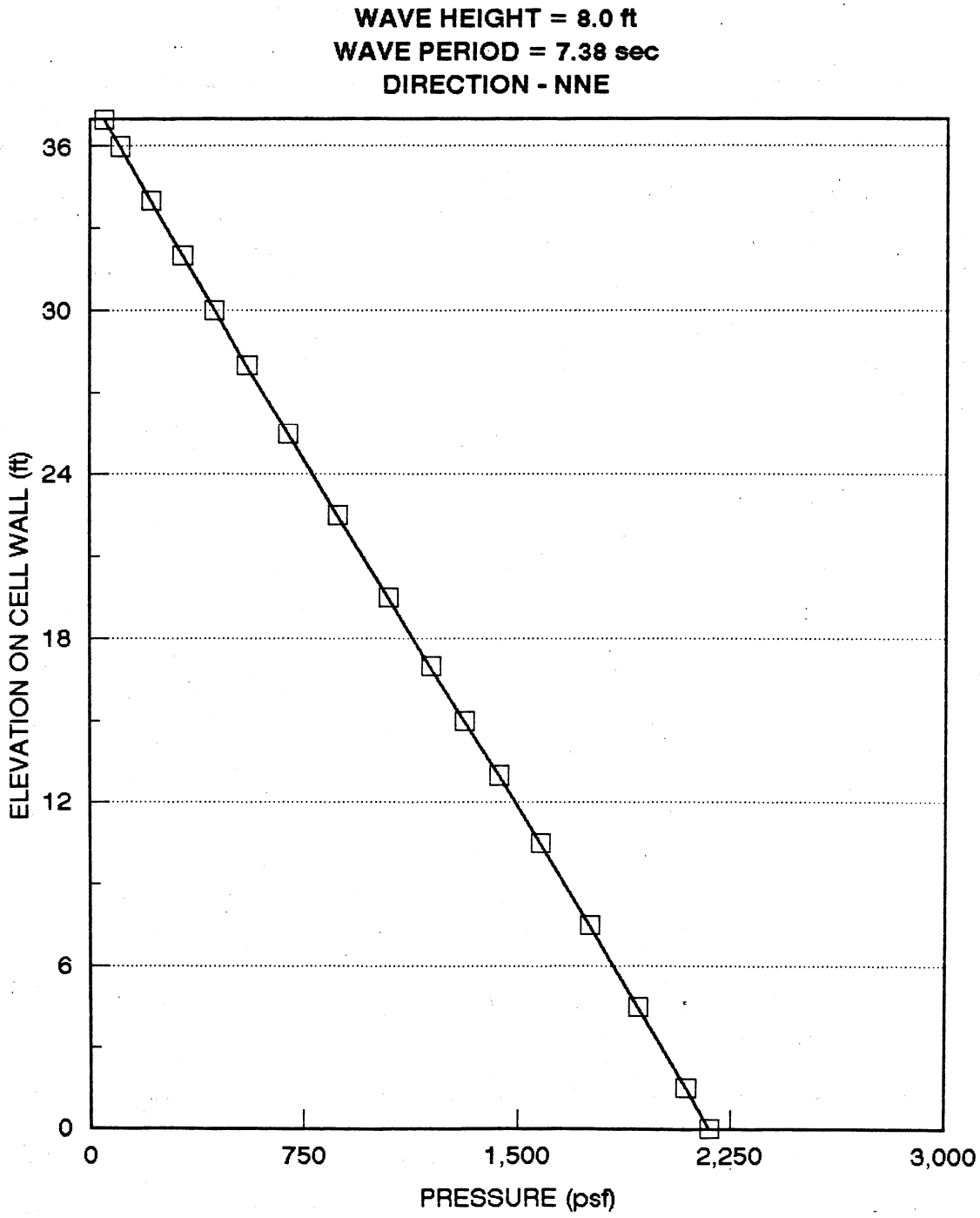

Fig. 4.2 Typical variation of total pressure (static+dynamic) along the elevation of the breakwater - Stoke's wave theory - wave peak

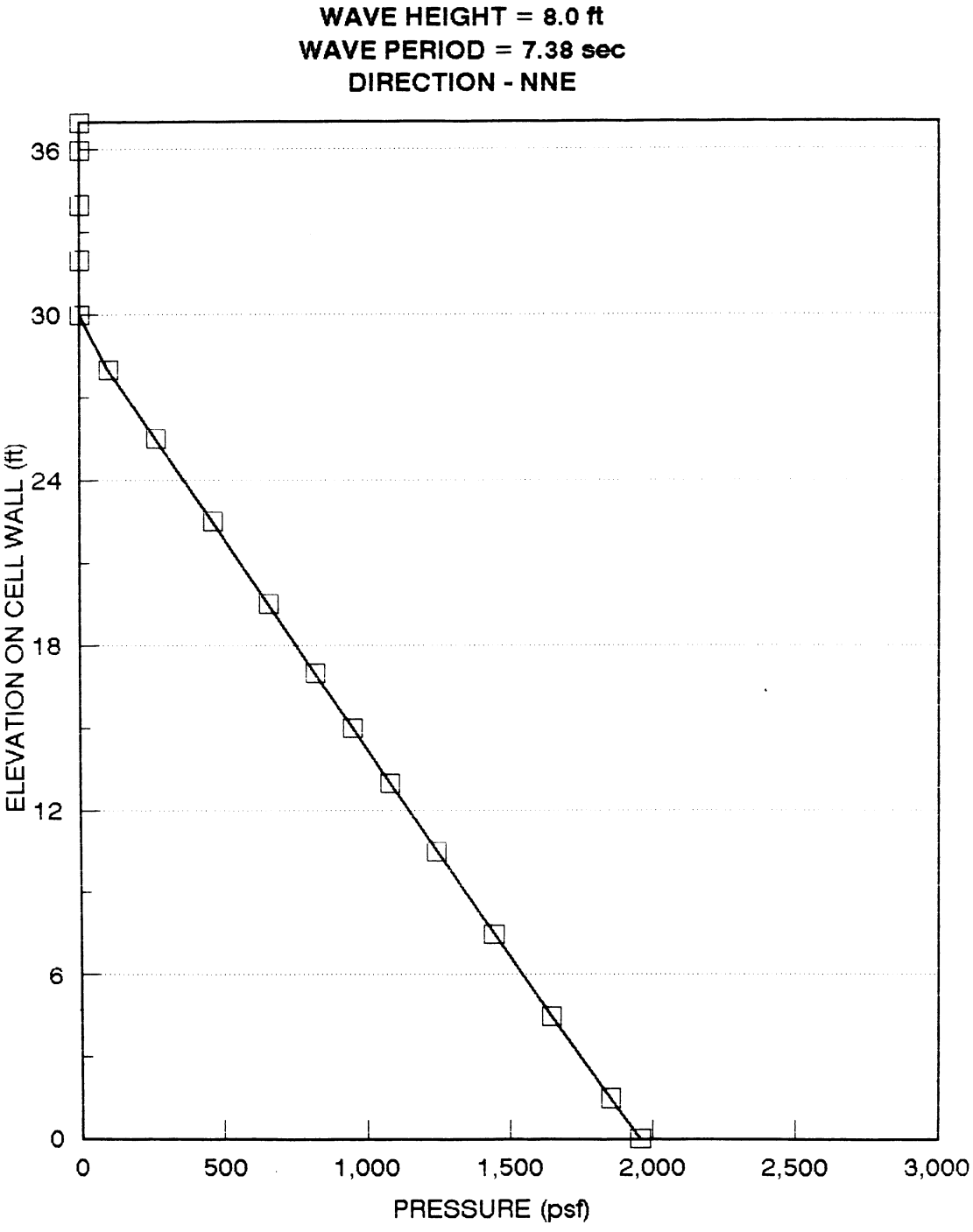

Fig. 4.3 Typical variation of total pressure (static+dynamic) along the elevation of the breakwater - Stoke's wave theory - wave trough

associated period of 19.80 sec from the NE direction are illustrated in Figures 4.4 and 4.5. The total calculation for the Cnoidal wave is attached in Appendix C.

Standing wave theory:

The equation for the surface profile is

$$\eta = H \cos(\omega t) \cos(kx \sin \alpha)$$

____Eqn. 4.7

Dynamic pressure variation is

$$p = \rho g H \, [Cosh\, k(z+d) \,/\, Cosh\, kd] \; Cos(kx \sin \alpha) \; Cos(\omega t)$$

____Eqn. 4.8

where α is the angle between the normal to the wave train and the breakwater.

The pressure distributions for the wave peaks and wave troughs are calculated for 28 waves.

4.5 Determination of Forces on the Breakwater

Using the general methodology described for determination of the pressures due to the waves incident on the structure, the pressures and forces on the outer face of the breakwater due to individual waves were calculated. The idealization of the breakwater side is shown in Fig. 4.6. Forces due to the wave pressures were determined at the various finite element nodes. The pressures are calculated at different elevations, termed pressure points. The

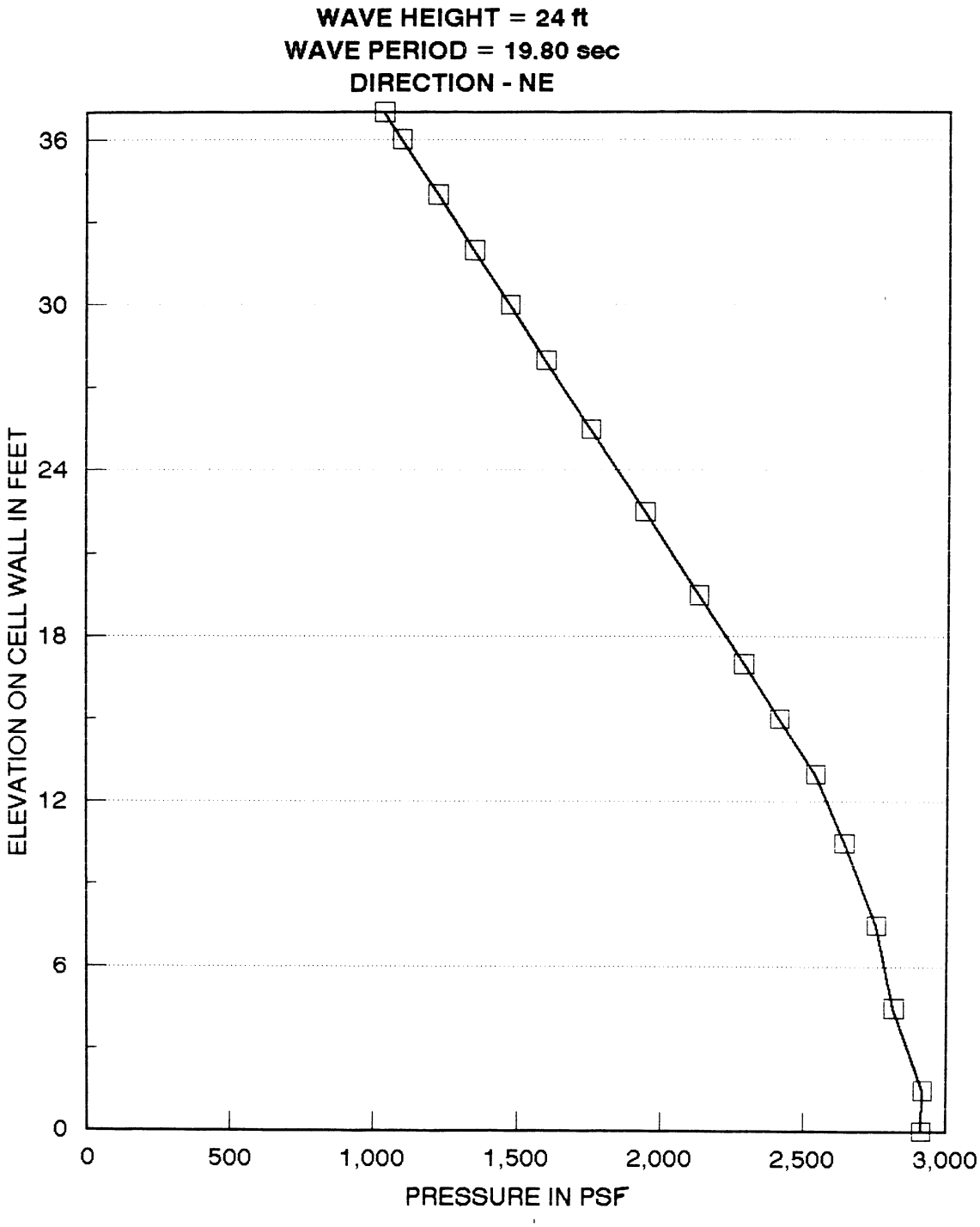

Fig. 4.4 Typical variation of total pressure (static+dynamic) along the elevation of the breakwater - Cnoidal wave theory - wave peak

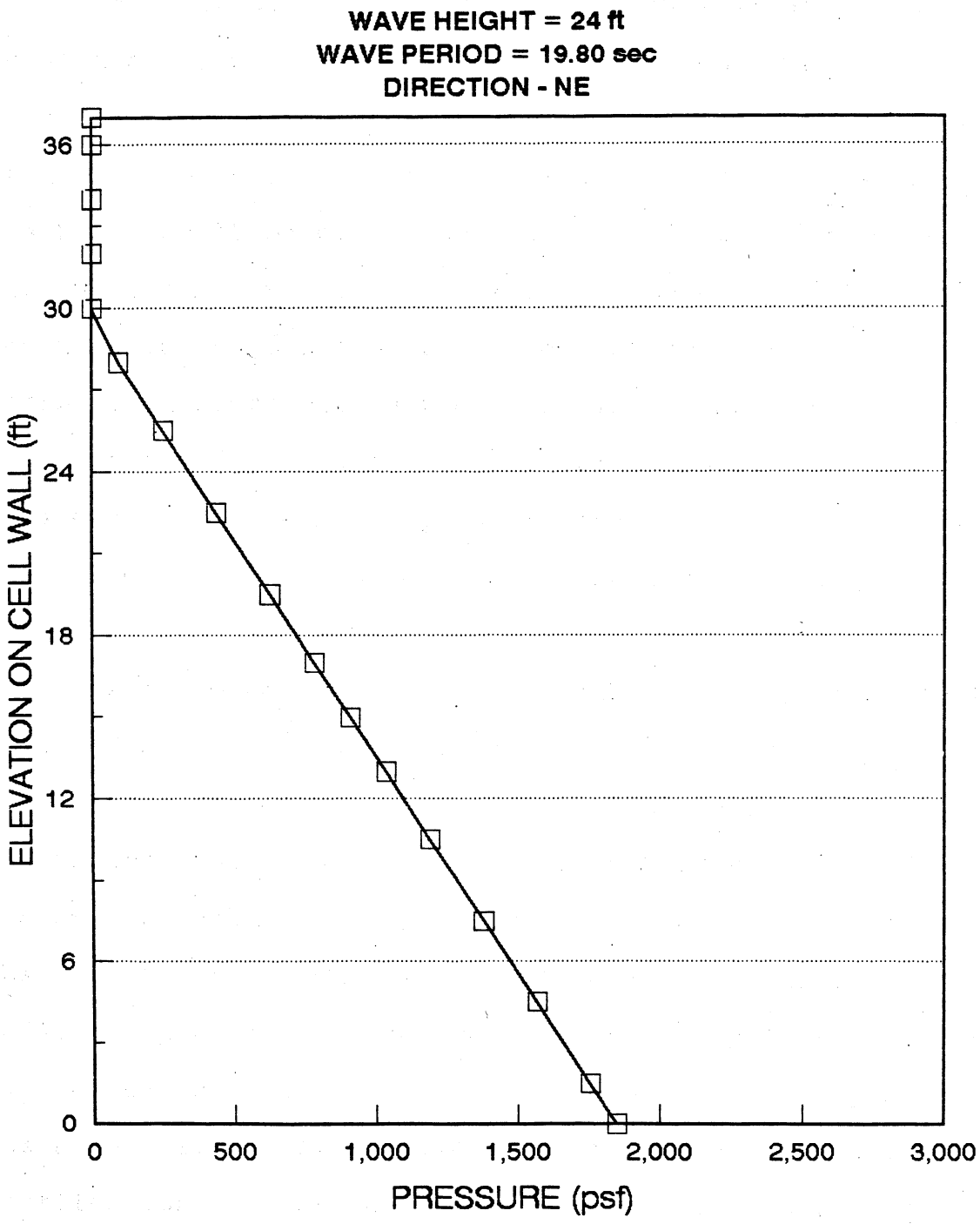

Fig. 4.5 Typical variation of total pressure (static+dynamic) along the elevation of the breakwater - Cnoidal wave theory - wave trough

pressure points and nodes are indicated in Fig. 4.6.

The interior soil mass of the breakwater is assumed to be at a saturated condition. The inside water pressure, which is time independent, varies hydrostatically from zero at the top of the pile stones. The net pressure is the algebraic addition of the opposing inside water pressure and the outside pressure. The difference consists primarily of the dynamic component of the wave, which has a net harborward pressure when the crest is at the breakwater and a net lakeward pressure when the trough is at the breakwater. The applied pressure profiles for each of the waves indicated earlier are shown in Figs. 4.7, Fig. 4.8, Fig. 4.9, and Fig. 4.10.

The two-dimensional finite element model represents the unit width between two vertical slices through the elevation. Each node on the vertical elevation of the model has a contributory area. The contributory area is defined the area bounded by the pressure points on either side of the node times the unit width. To calculate the force at a node, the pressures calculated at pressure points on either side of the node are multiplied by the contributory area for the node. Figs. 4.11 to 4.14 indicate the nodal force profiles for each of the cases indicated earlier. The force distribution (shape of the profile) varies from the applied pressure distributions because of the differences in contributory area. The calculated forces were transformed

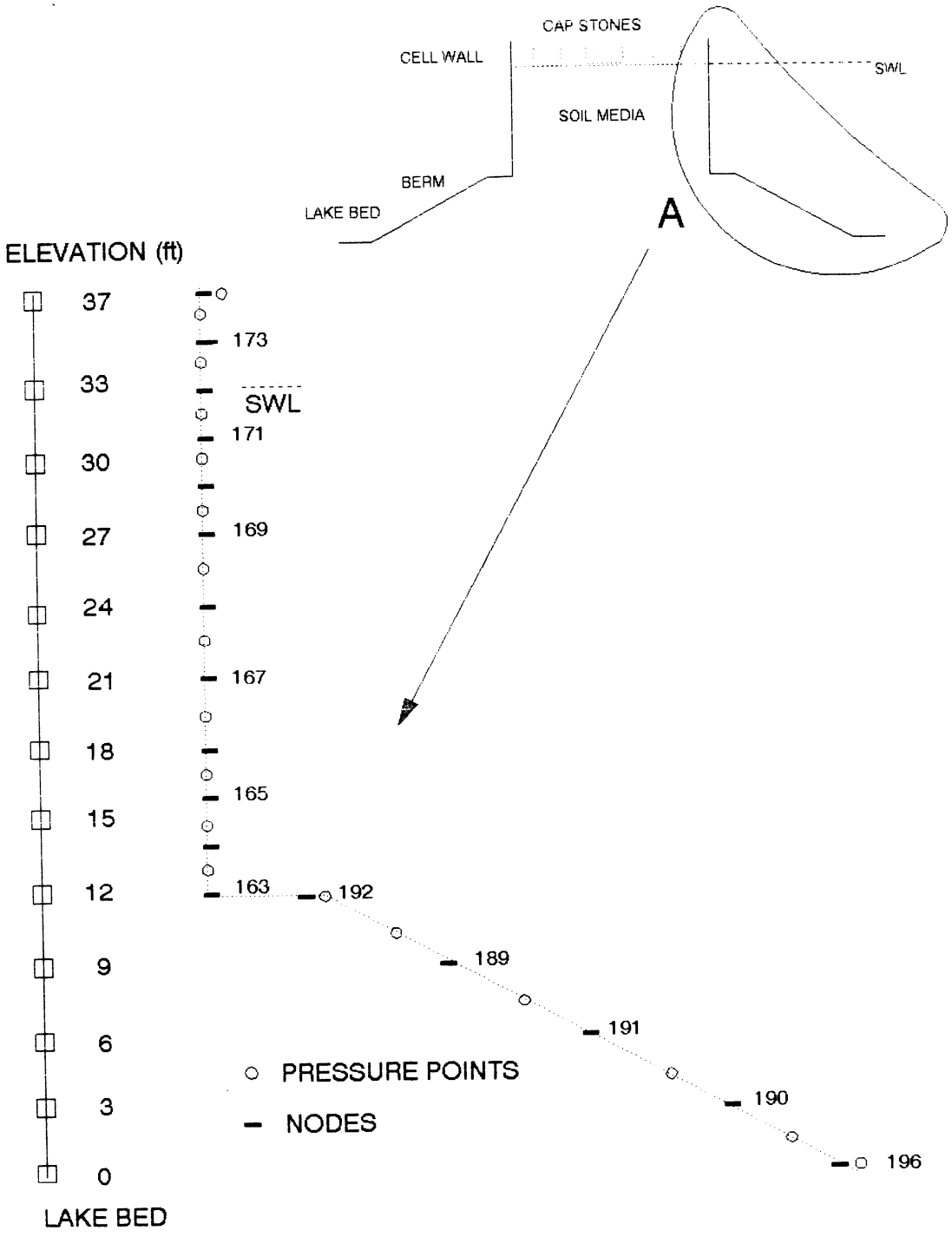

Fig. 4.6 Idealization of the side of the breakwater for force evaluation indicating the nodes and pressure points

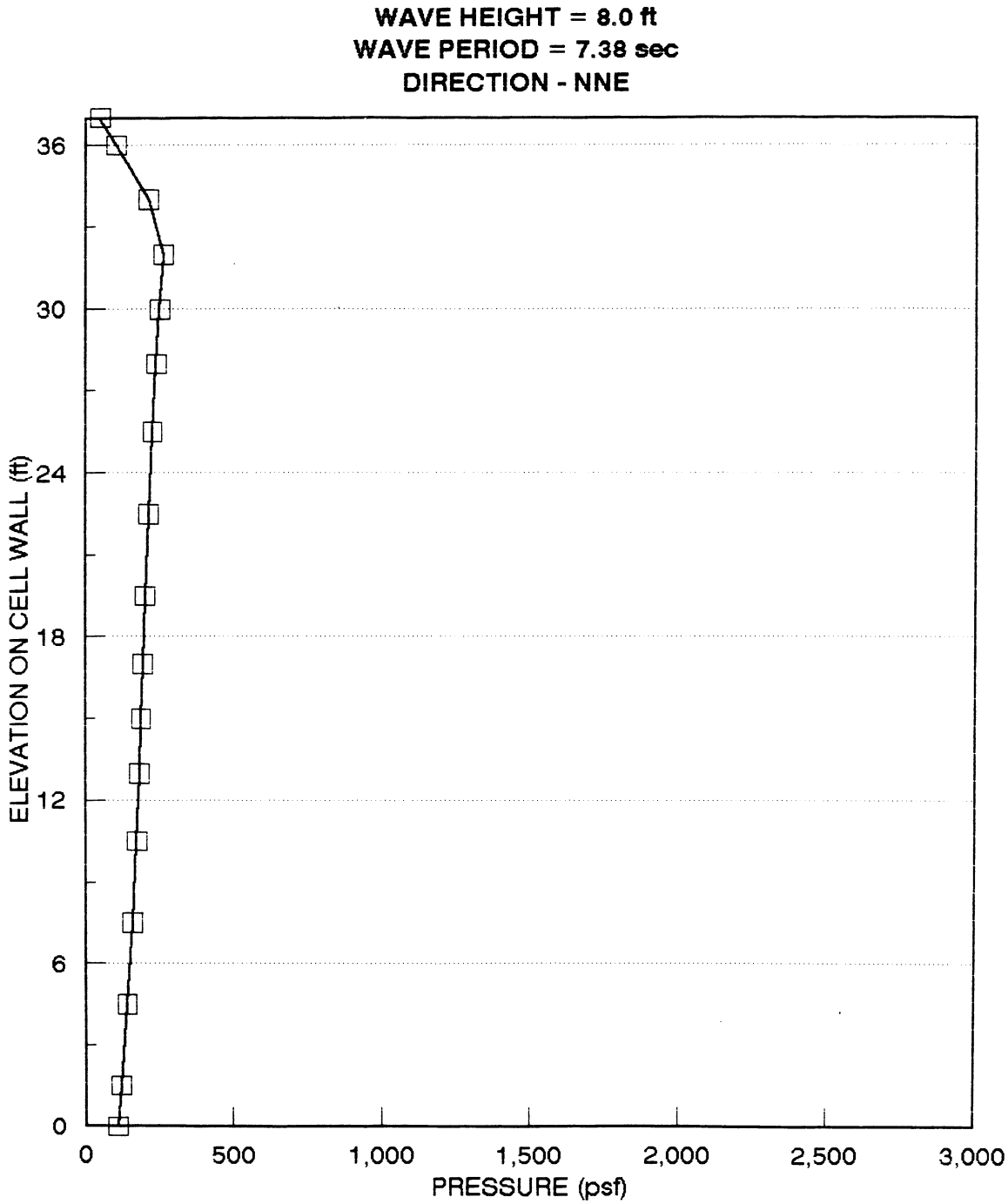

Fig. 4.7 Typical applied pressure variation along the elevation of breakwater - Stoke's theory - wave peak

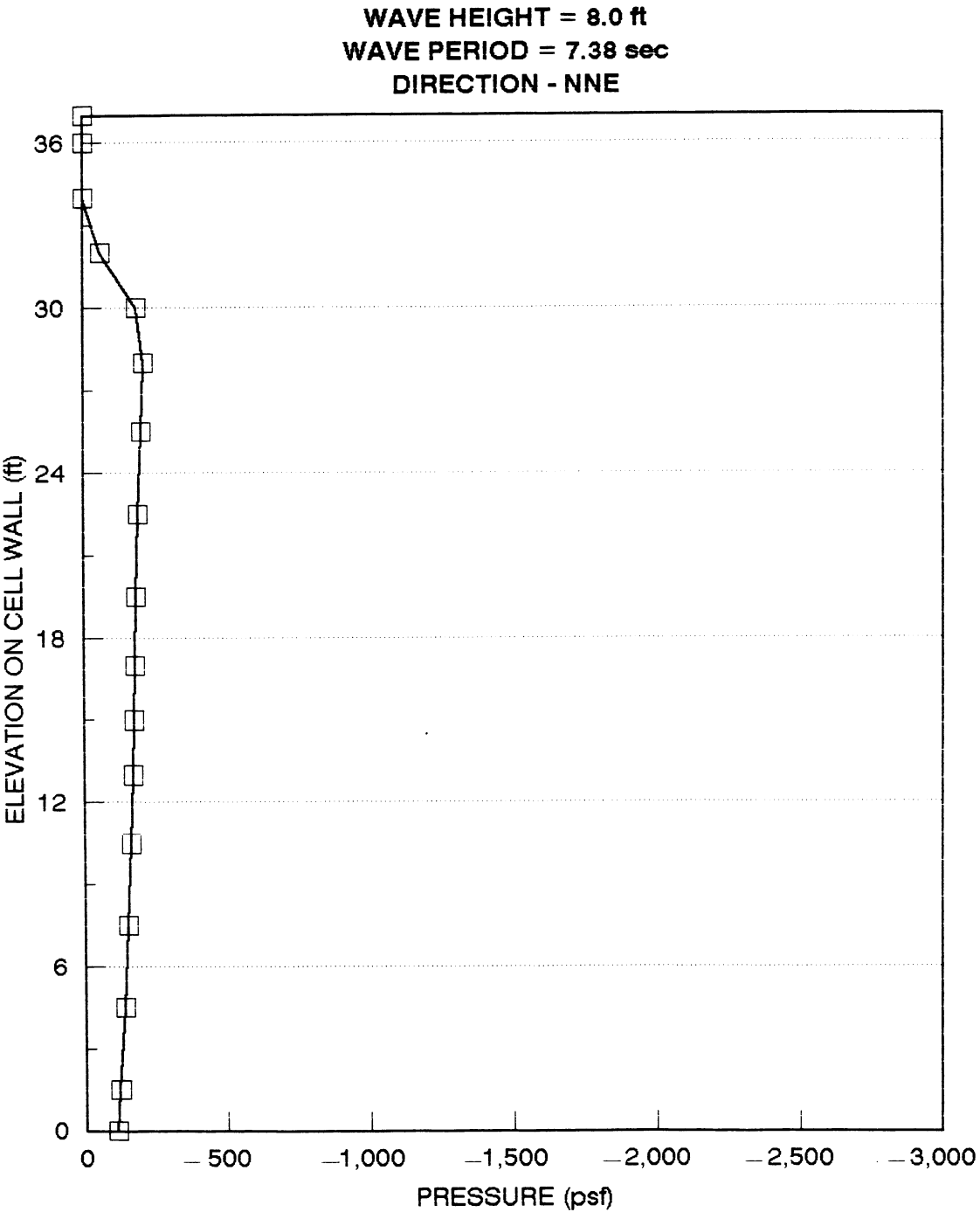

Fig. 4.8 Typical applied pressure variation along the elevation of breakwater - Stoke's wave theory - wave trough

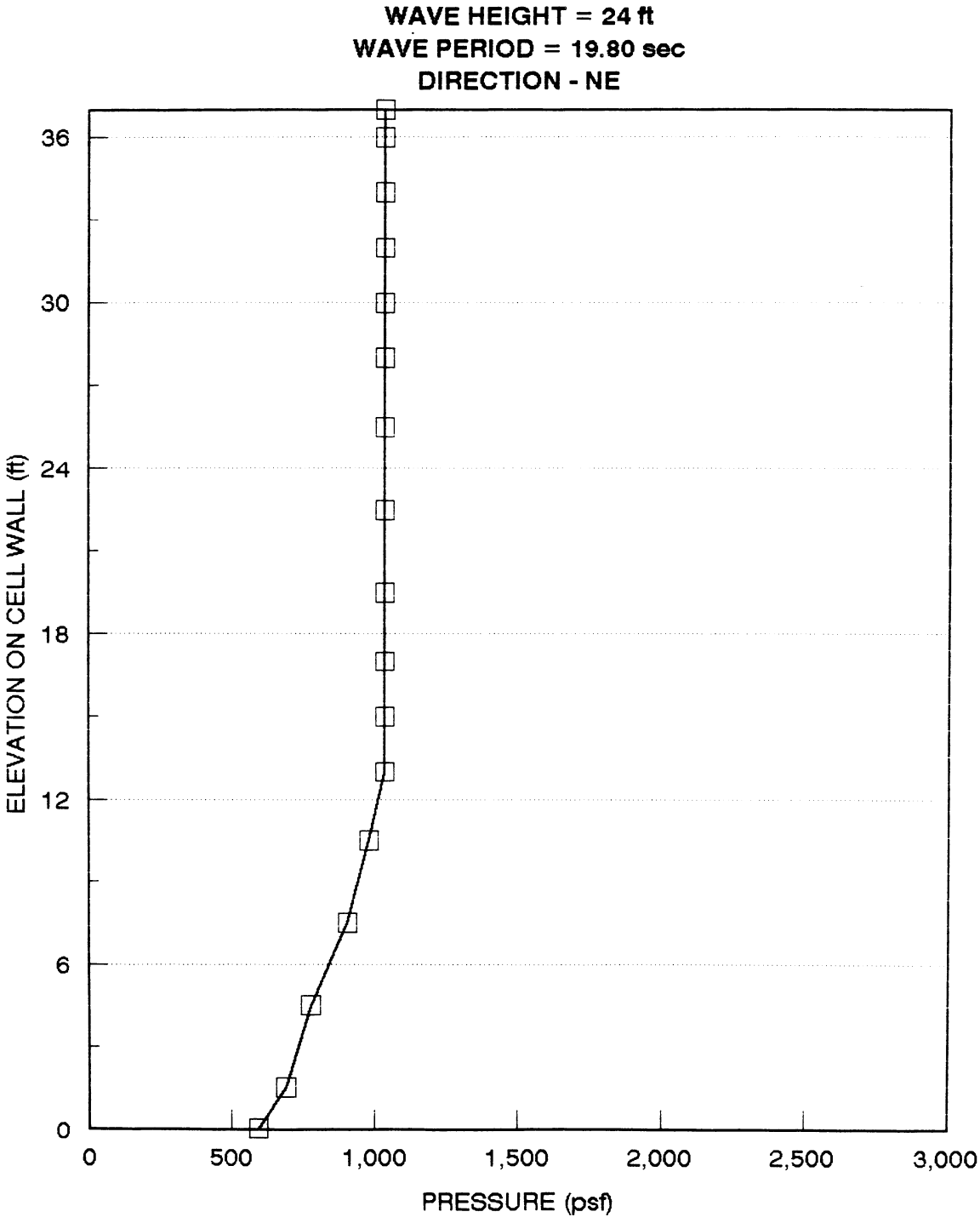

Fig. 4.9 Typical applied pressure variation along the elevation of breakwater - Cnoidal wave theory - wave peak

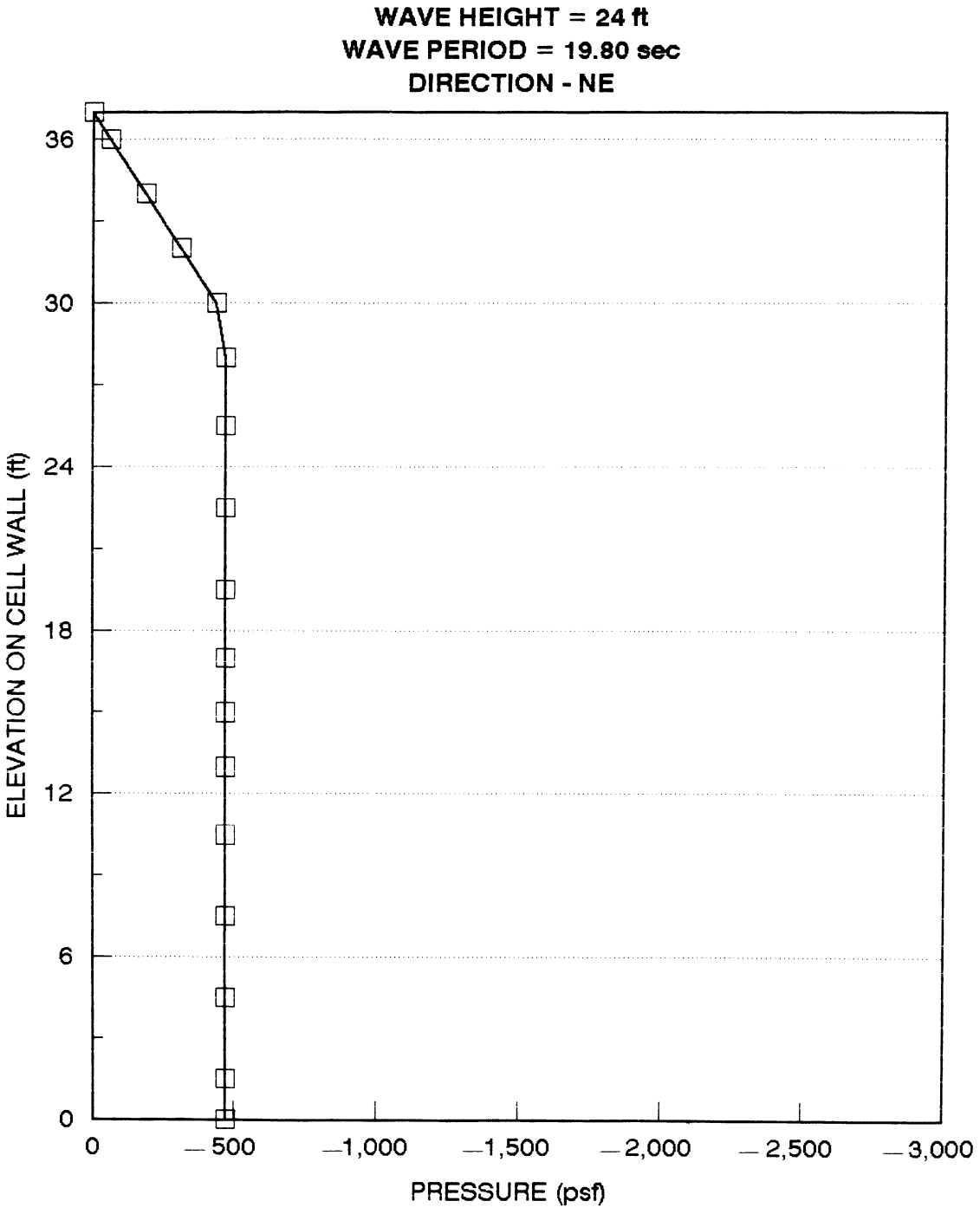

Fig. 4.10 Typical applied pressure variation along the elevation of breakwater - Cnoidal wave theory - wave trough

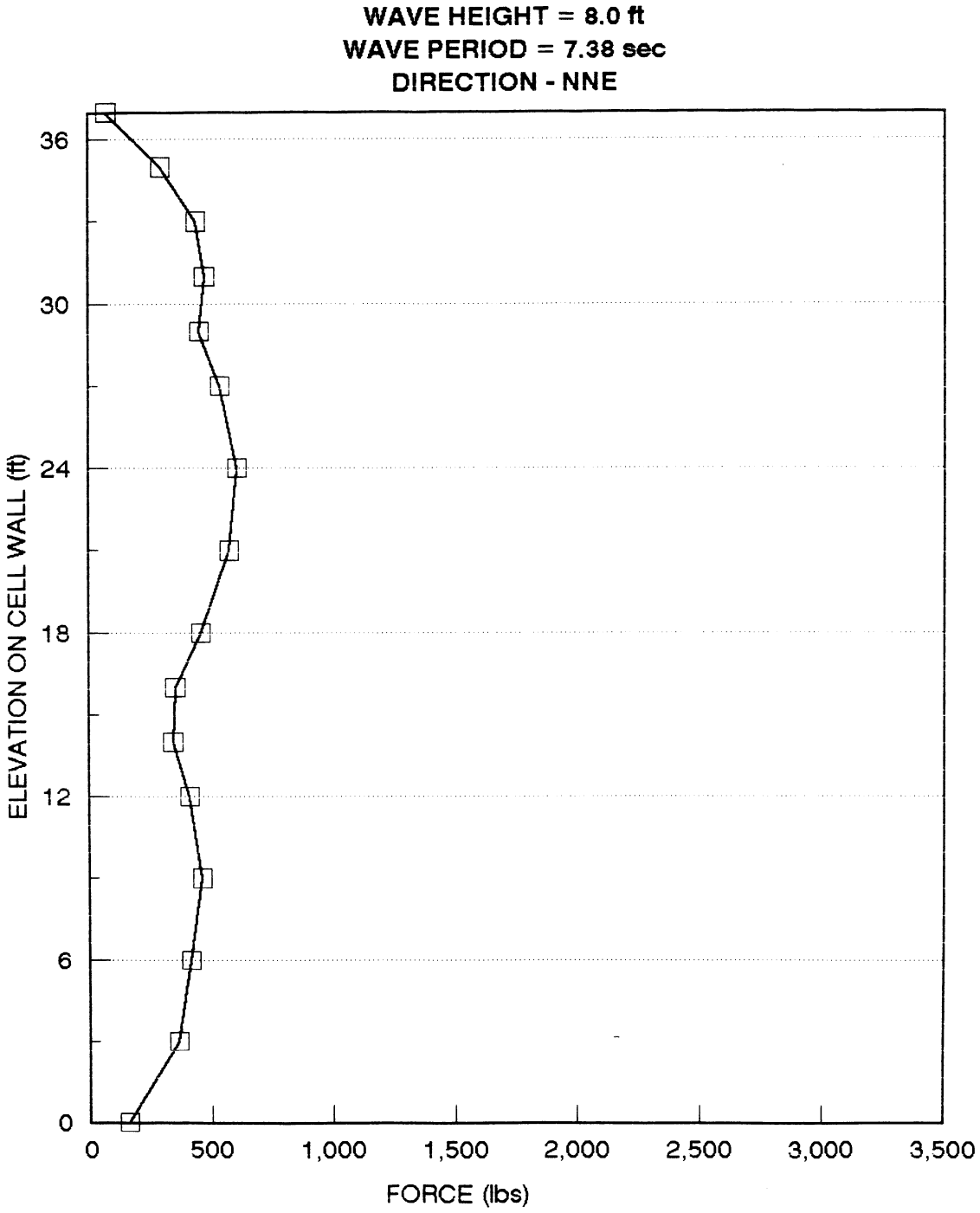

Fig. 4.11 Typical nodal force variation along the elevation of the breakwater - Stoke's wave theory - wave peak

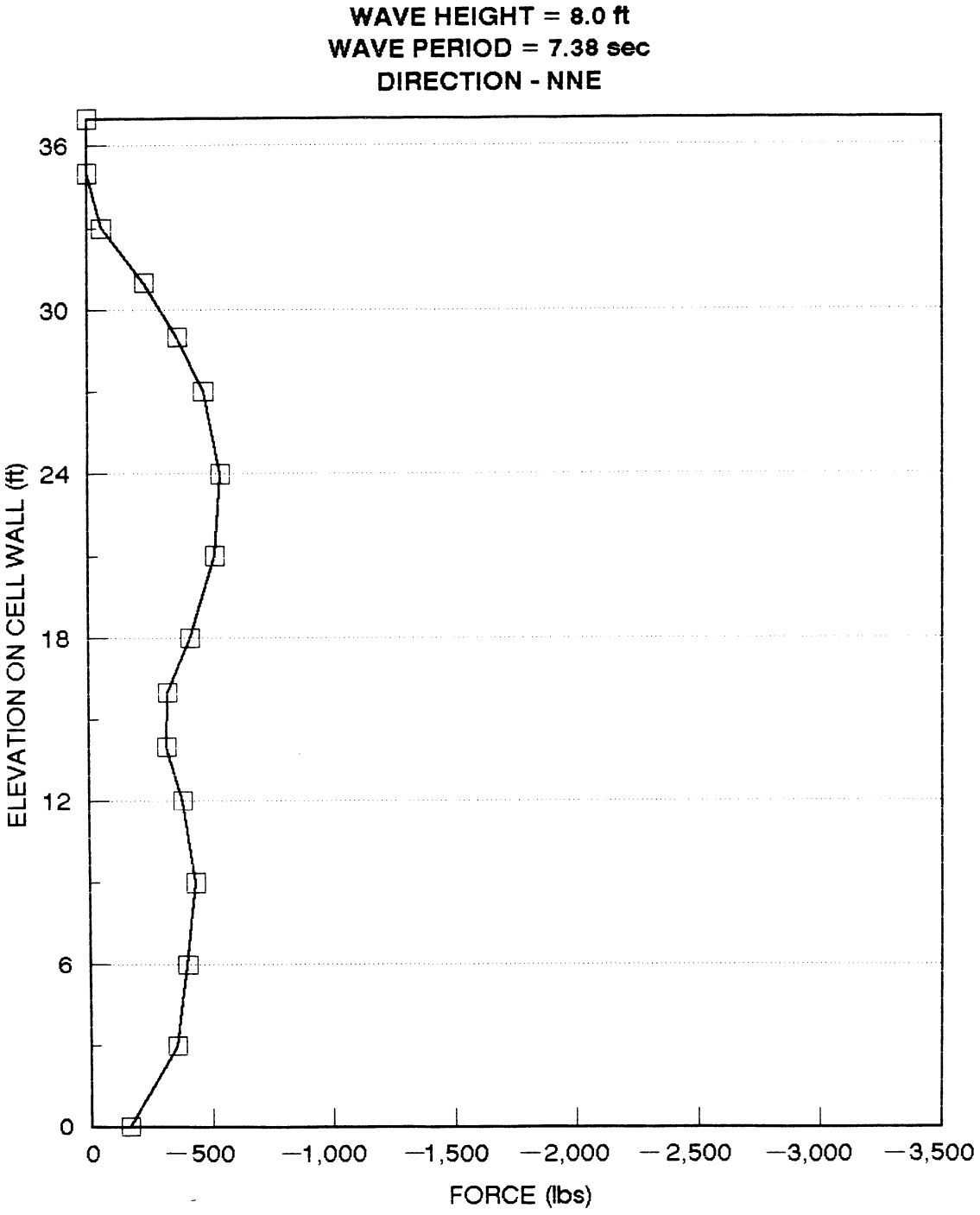

Fig. 4.12 Typical nodal force variation along the elevation of the breakwater - Stoke's wave theory - wave trough

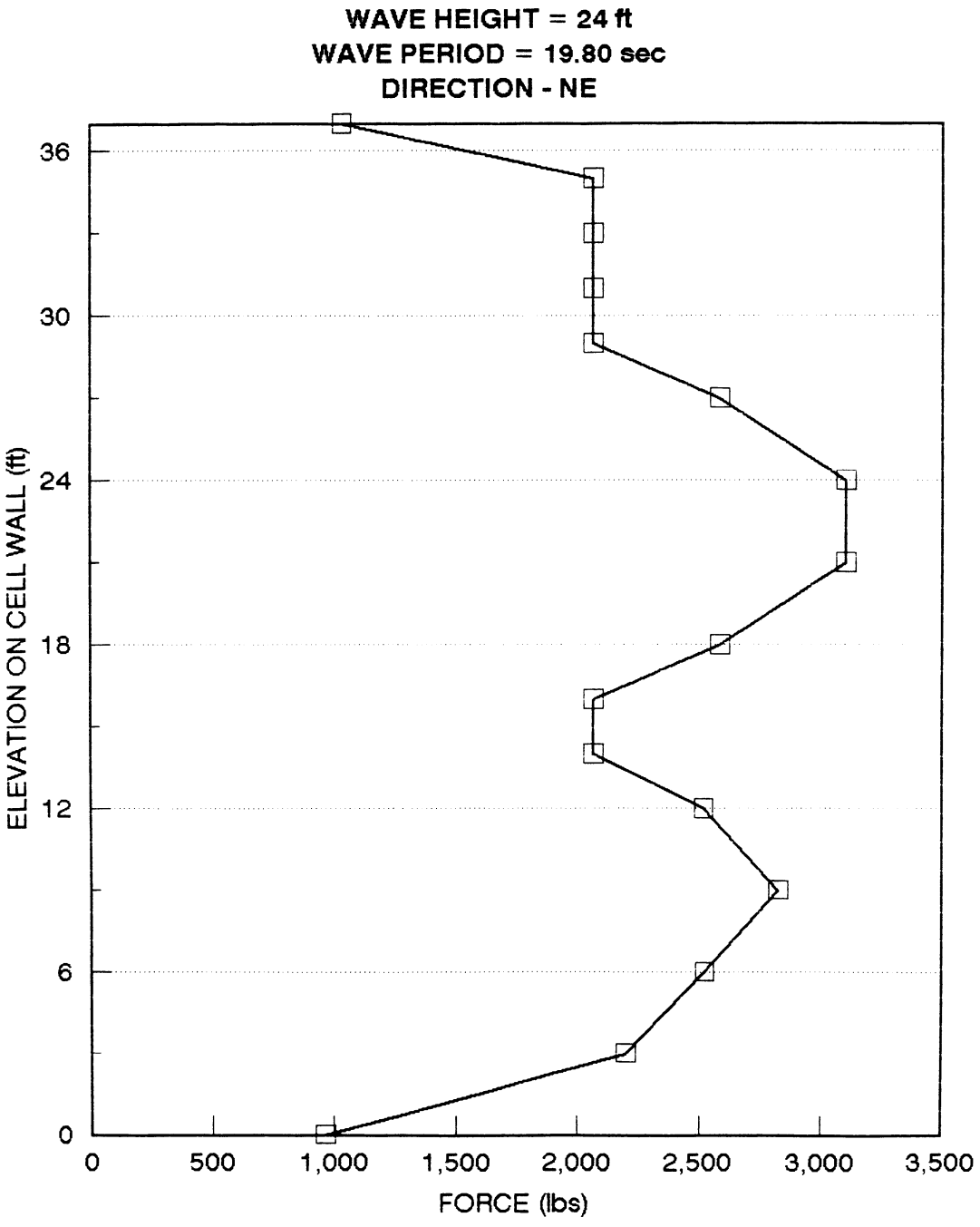

Fig. 4.13 Typical nodal force variation along the elevation of the breakwater - Cnoidal wave theory - wave peak

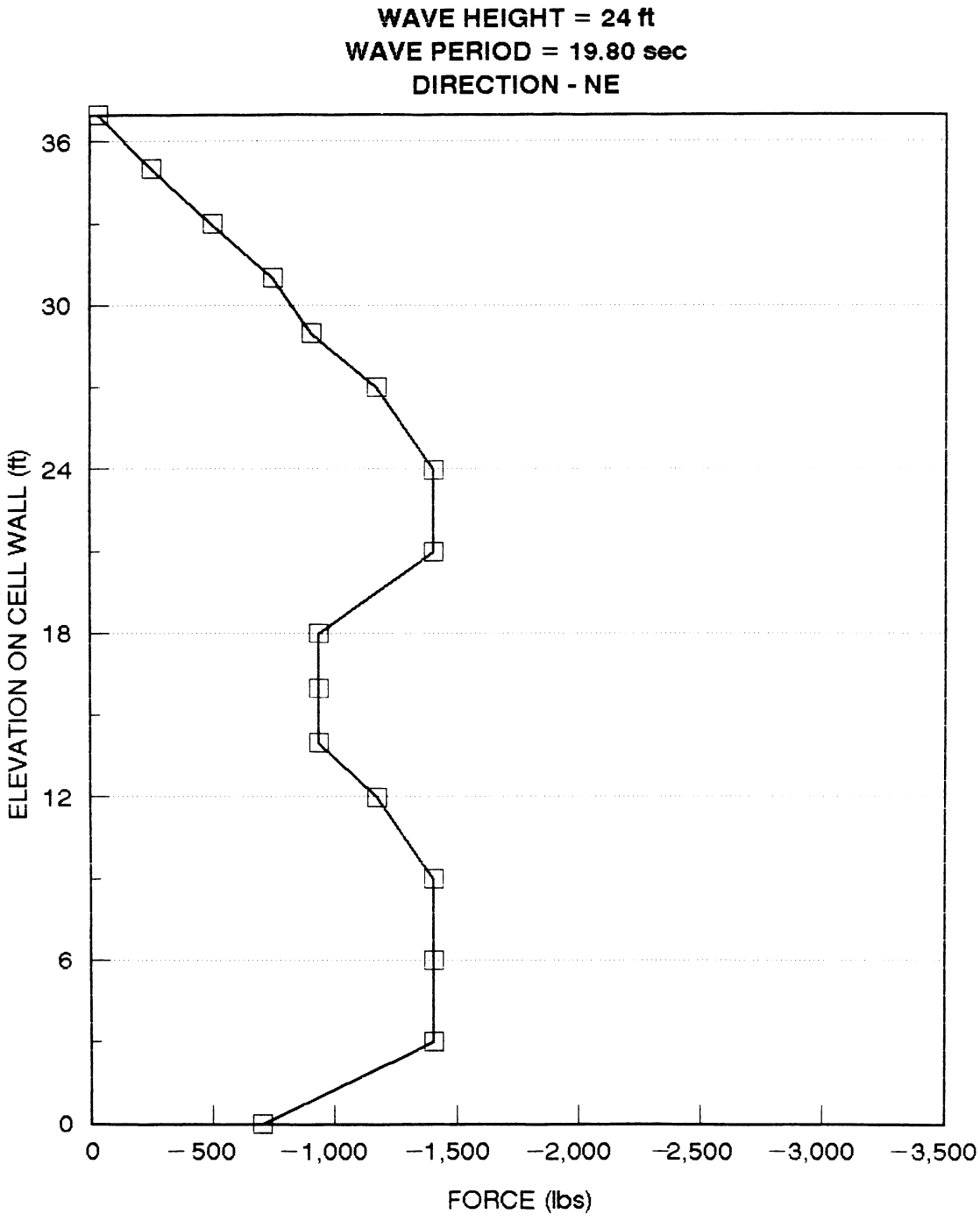

Fig. 4.14 Typical nodal force variation along the elevation of the breakwater - Cnoidal wave theory - wave trough

into the ANSYS input mode for application on the model.

All the calculations were performed by using computer programs developed for each of the various theories. The computer programs were developed on the VAX mainframe. The computation and data analysis were also performed on the VAX. Descriptions of the programs are provided in Appendix E.

5. DATA ANALYSIS AND COMPARISON OF FIELD DATA

5.1 Data Analysis

The objective of the work in this chapter was to:

1. Establish a relationship between the wave height and the stress range in the structure for each wave direction.
2. Compare the measured field data with the finite element results.

The evaluation of the structural damage based upon the analysis results of this chapter is presented in Chapter 7. The Equivalent Stress Range Method was used to determine the damage due to long-term accumulation of fatigue. This analysis approach was used by Williams and Rinne (8) and Hambly et.al (9) for analysis of offshore structures. The approach uses the Miner's Rule (7) for accumulation of damage. The Equivalent Stress Range Method is discussed in detail in Appendix C. The main constituent parts of the method are as follows:

1. Determination of the relationship between the stress ranges and the wave heights for different locations on the vertical profile of the structure.
2. Determination of the number of the waves expected in a sea state.
3. Establishment of an equivalent stress range for a sea state assuming a Rayleigh distribution of

stresses and using the S - N curve.

5.2 Processing of the Data

The nodal force files created by the deterministic evaluation of forces on the structure were entered in the finite element model. The ANSYS runs are processed as follows:

1. The ANSYS results were obtained for the wave peak and wave trough conditions for each wave. These were transformed into spring forces. The spring-force ranges were the differences between peak and trough results.
2. The spring-force ranges are transformed into hoop-force ranges on the structure. Table 5.1, Fig. 5.1, and Fig. 5.2 indicate the post-processed ANSYS results for a wave of wave height 16 ft and incident on the structure from the NE direction. Figures 5.1 and 5.2 indicate the hoop forces (lb/in.) tabulated at various elevations along the height of the structure for the peak and trough wave loading respectively. As an observation, Table 5.1 indicates the percentage of exceedance of 3000 lb/in. of interlock, representing the accepted design value for type PSA23 sheet piles.
3. The data files were grouped on a direction wise basis and manipulated so that files were generated

Table 5.1: Typical Post-processed ANSYS Results

WAVE HEIGHT = 16 FT
WAVE DIRECTION - NE

LOCATION NO	ELEVATION (FT)	HOOP FORCE PEAK (LB/IN)	HOOP FORCE TROUGH (LB/IN)	FATIGUE FORCE (LB/IN)	OVERSTRESS WRT 3000 (LB/IN)
1	-9	0	0	0	0
2	-6	1,711	1,897	186	0
3	-3	2,623	3,122	499	4
4	0	2,804	3,634	830	21
5	3	2,852	3,650	798	22
6	6	2,822	3,213	391	7
7	9	2,623	2,318	304	0
8	12	1,791	1,912	121	0
9	14	1,240	2,508	1,268	0
10	16	1,015	3,018	2,003	0
11	18	919	3,029	2,110	0
12	21	597	1,901	1,304	0
13	24	736	2,133	1,397	0
14	27	745	2,743	1,998	0
15	29	741	2,535	1,794	0
16	31	1,327	1,915	588	0
17	33	627	1,655	1,028	0

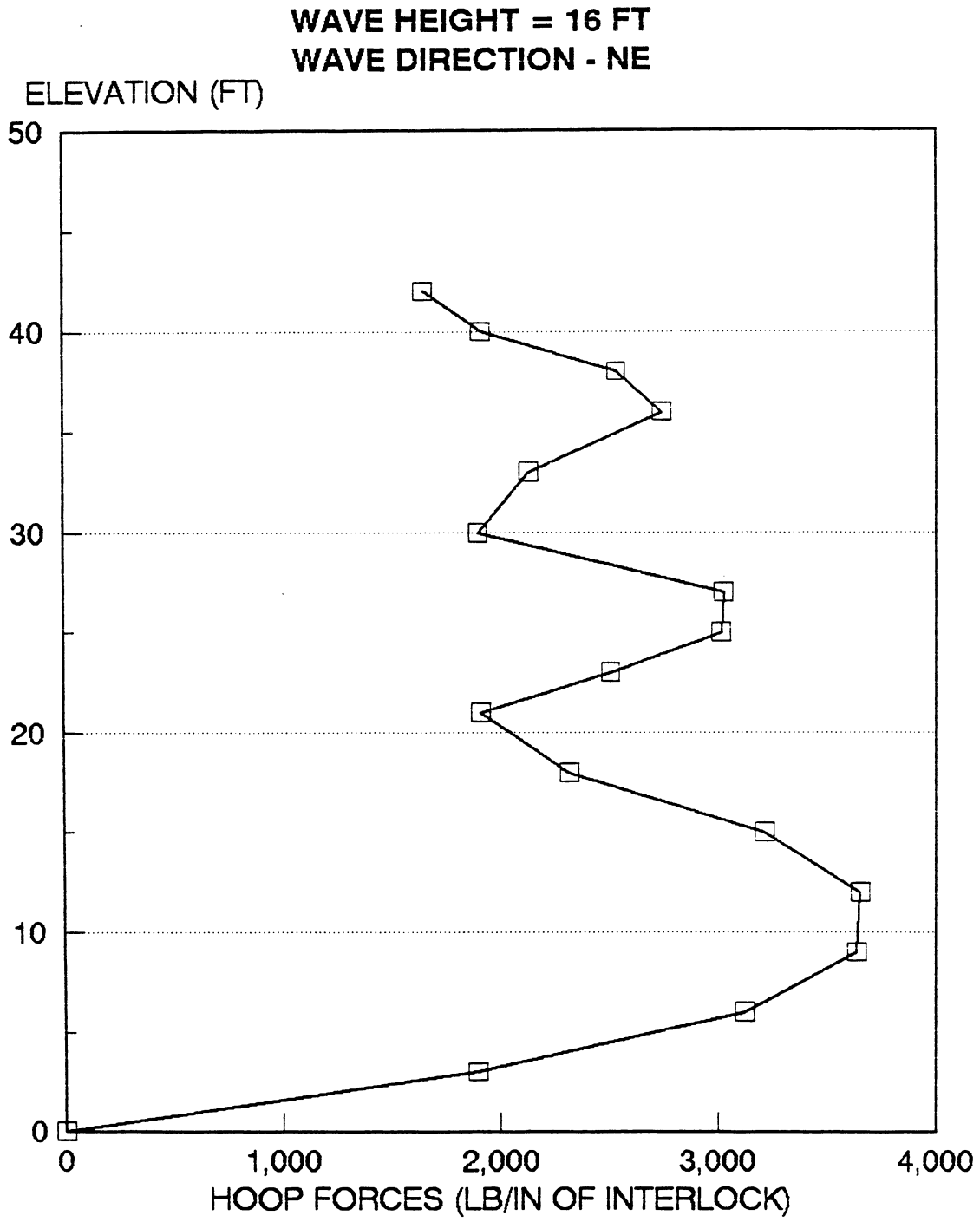

Fig. 5.1 Typical variation of hoop forces in cell wall Vs elevation (wave peak)

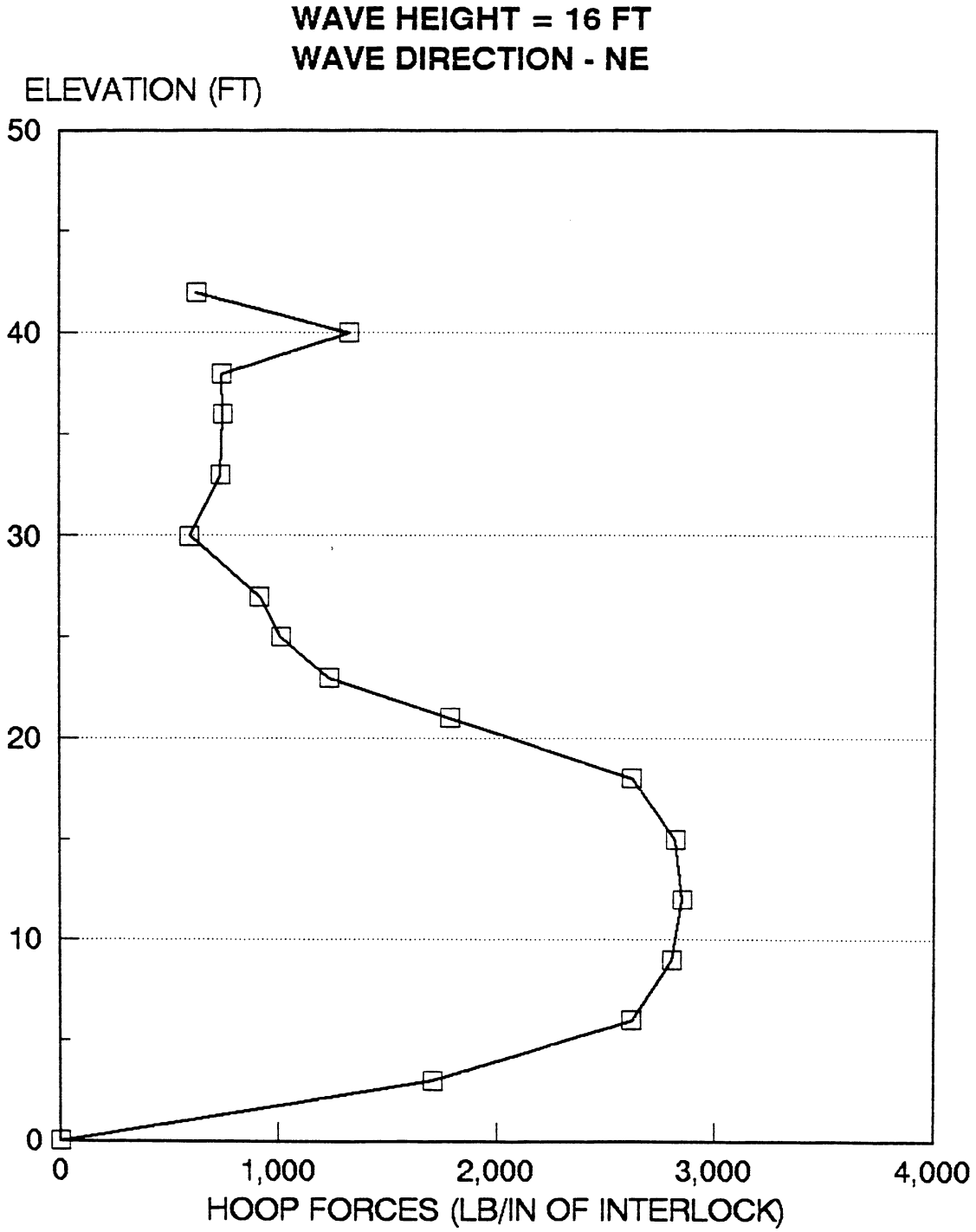

Fig. 5.2 Typical variation of hoop forces in cell wall Vs elevation (wave trough)

for each location on the breakwater elevation. Hence, 17 files were created for each direction

4. A general purpose statistical program, SAS, was used to generate a third-order regression curve relating the wave height and hoop-force range for each of the files created in Step 3. The generated third-order curves illustrate the predicted trend of the analysis results. A total of 286 regression curves were generated. A typical predicted trend from SAS is shown in Fig. 5.3. The regression equation from the analysis is of the form:

$$S_r = A_1 H + A_2 H^2 + A_3 H^3$$

____Eqn (5.1)

where

S_r = hoop-force range

H = wave height

A_1, A_2, A_3 = coefficients of regression

The particular curve illustrated in Fig. 5.3 is generated for location 9 for the waves from the NNW direction. The coefficients for all the curves are listed in Appendix D.

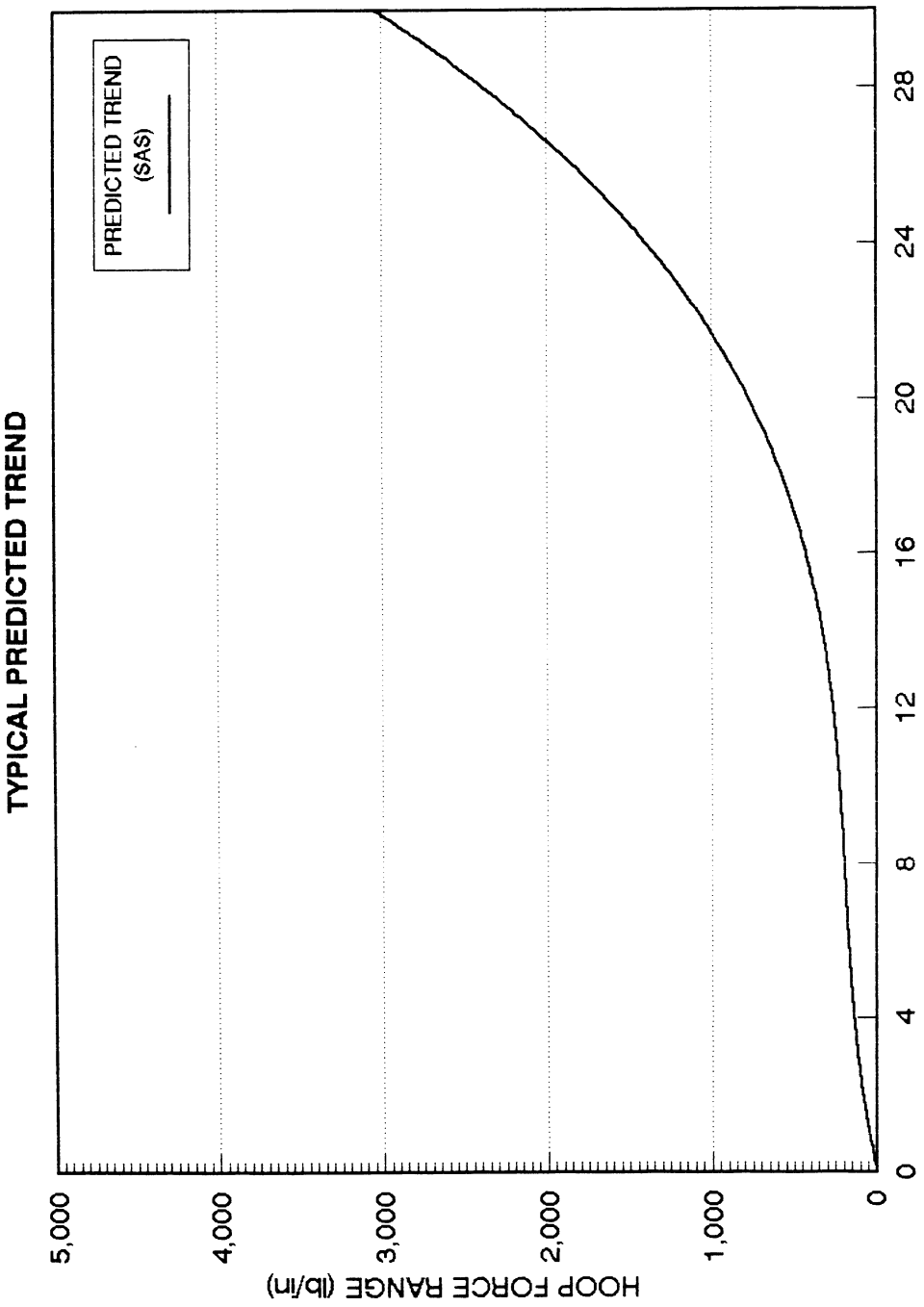

Fig. 5.3 Typical predicted trend SAS analysis

5.3 Correlation of the Finite Element Data with Field Data

Two separate correlations of the measured field data and the data predicted by the finite element model (FEM) are presented. They are:

1. Comparison of field data with FEM data at different elevations for a fixed wave height.
2. Comparison of field data with the FEM results at different wave heights for a fixed location on the elevation.

The field instrumentation can be associated with the finite element model as follows (Figs. 2.1, 2.2, and 4.6). Strain Gauge 12 (21 ft below the water level) corresponds to location 10 (Node 165). Strain Gauges 11 and 13 (13 ft below water) correspond to location 13 (Node 168). All the other hoop strain gauges correspond to location 17 (Node 172).

For the purpose of correlation, the real-time wave statistics as recorded by the installed wave gauge and transformed by CERC are used. The data recorded by the wave gauge are transformed in the form of significant wave (H_s). In order to determine the maximum wave incident on the structure at the time of data recording, the following relationship is used:

$$H_{max} = 1.77H_s \qquad \text{Eqn. 5.2}$$

The ranges of the recorded strains are a result of this

maximum wave being incident on the structure. In addition to the CERC data, data obtained from the National Climatic Data Center was used to obtain information about the existing climatological conditions at the time of the record.

The hoop-force ranges are determined from the strains that are recorded on different days by using the data acquisition system. The strain ranges are transformed into hoop-force ranges with the aid of the diagnostic tests as listed in Appendix A. The transformed hoop force ranges are also indicated in Appendix A.

The intention of field study by ISU was to record as many waves as possible from the significant directions predicted by the statistical data analysis, which was presented in Chapter 5. However, the recorded field data were primarily from the NNW direction. The maximum wave height recorded during the data collection period was 13.90 ft.

In order to correlate the finite element data with the field data, four cases were selected. The data for analysis were recorded on Jan 12th, Feb 2nd, Feb 13th, and Feb 24th. The data for the four cases are presented in Tables 5.2 through 5.4. Table 5.2 indicates the time of wave record, maximum wave height, wind direction as recorded on the marine log, and the wave direction as per real-time wave

statistics. Table 5.3 indicates the experimental hoop-force ranges that are used to determine the hoop-force range variation along the breakwater elevation. Table 5.4 indicates the recorded hoop-force ranges for the other strain gauges. The maximum wave height indicated in the tables is the result of the transformation process made on the CERC data as described earlier. The recorded CERC data used corresponds to the time at which the strains are recorded. Tables A.1, A.2 and A.3 contain the recorded data other than the illustrated cases.

Figures 5.4 through 5.7 indicate the variation of the hoop forces along the vertical profile of the structure for the five cases selected. The analytical and the experimental force variations for all other cases are similar to those shown in Figs. 5.4 through 5.7. The predicted values in Fig. 5.5 are considerably above the experimental values. As indicated earlier, Table 5.2 compares the marine log data with the CERC data. From the table for Feb. 2nd, the marine log data reads NW, while the CERC data is closer to NNW. If the waves are predominant in the NW direction, the hoop forces show considerably less variation than those predicted on basis of NNW direction. Also, as discussed in Section 5.4 all waves below 4 ft height are assumed to be standing waves. This almost doubles the predicted force values because of reflection of

Table 5.2: Time, date, max. wave height in the record and corresponding wind and wave directions

Date	Time of record	Maximum wave height H_{max} (ft)	Wind dir. marine log	Wave dir. real-time statistics
Jan 12th	5:00 hrs	10.20	NW	WNW
Feb 2nd	13:59 hrs	6.00	NE	NNW
Feb 13th	20:49 hrs	12.00	NE	NNW
Feb 24th	14:27 hrs	13.90	NW	NNW

Table 5.3: Recorded hoop-force ranges

Date	H_{max} (ft)	S.G. 12 (lb/in.)	S.G. 13 (lb/in.)	S.G.7 (lb/in.)
Jan 12th	10.20	135.28	327.52	71.84
Feb 2nd	6.0	46.70	50.92	20.84
Feb 13th	12.0	63.34	41.48	2.67
Feb 24th	13.90	167.42	667.70	122.91

Table 5.4: Recorded hoop-force ranges

Date	H_{max} (ft)	S.G.5 (lb/in.)	S.G.6 (lb/in.)	S.G.8 (lb/in.)	S.G.9 (lb/in.)	S.G.10 (lb/in.)
Jan 12th	10.20	124.92	24.00	34.97	18.53	73.54
Feb 2nd	6.0	28.85	36.00	10.05	40.00	45.82
Feb 13th	12.0	3.27	4.30	3.64	3.00	3.57
Feb 24th	13.90	123.24	48.16	47.83	22.36	106.65

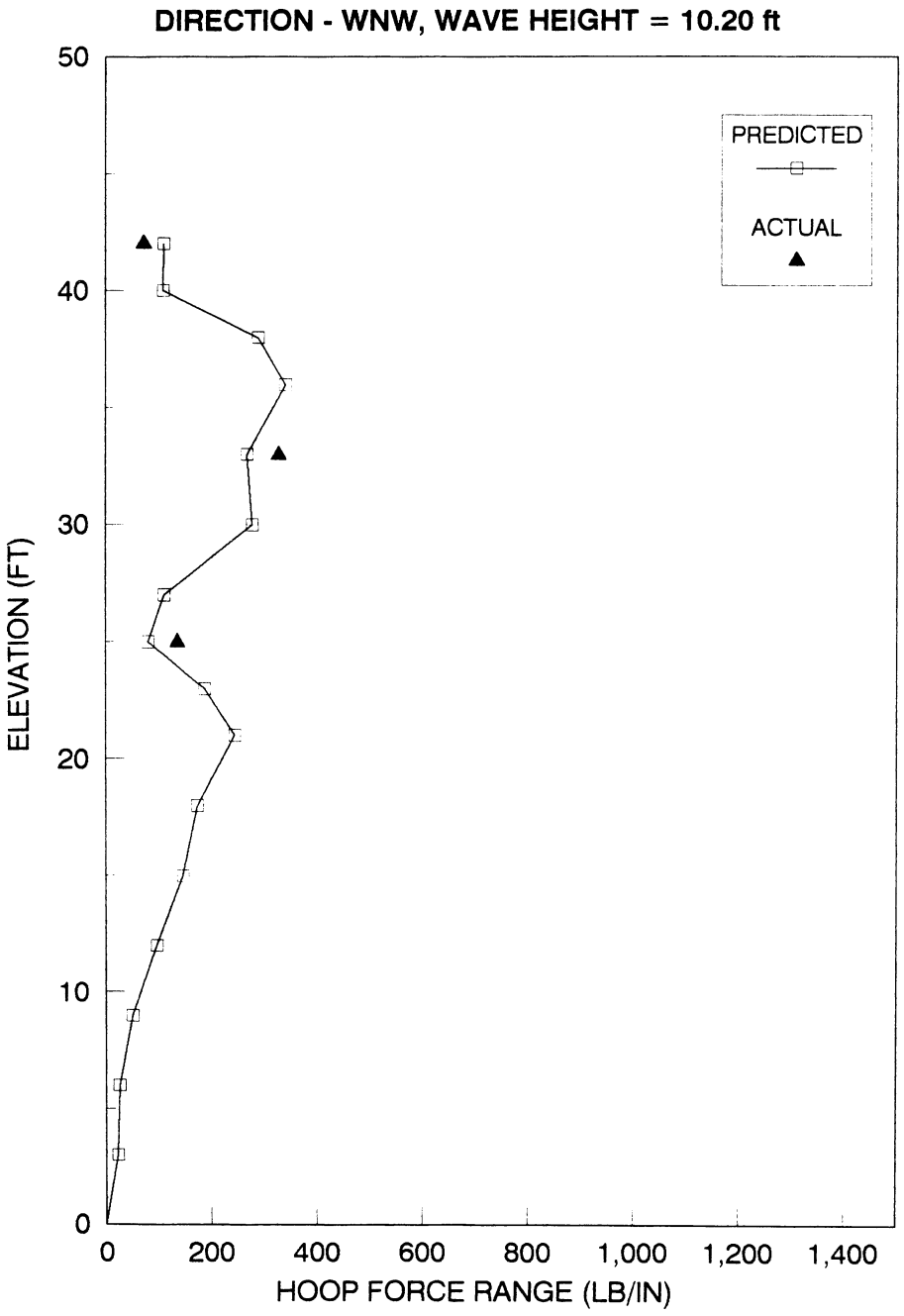

Fig. 5.4 Comparison between predicted and measure hoop force variation (Data recorded on Jan. 12th)

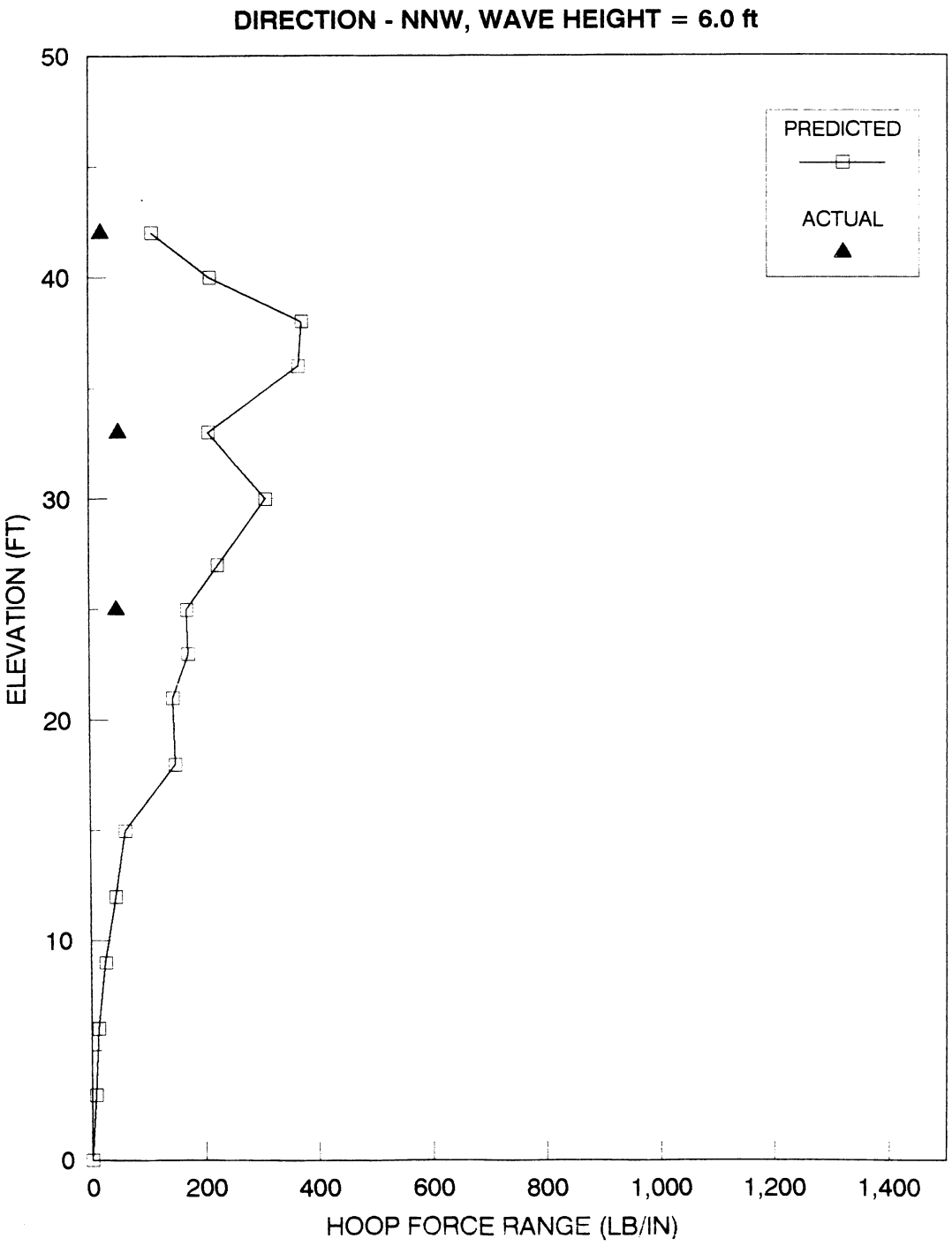

Fig. 5.5 Comparison between predicted and measured hoop force variation (Data recorded on Feb. 2nd)

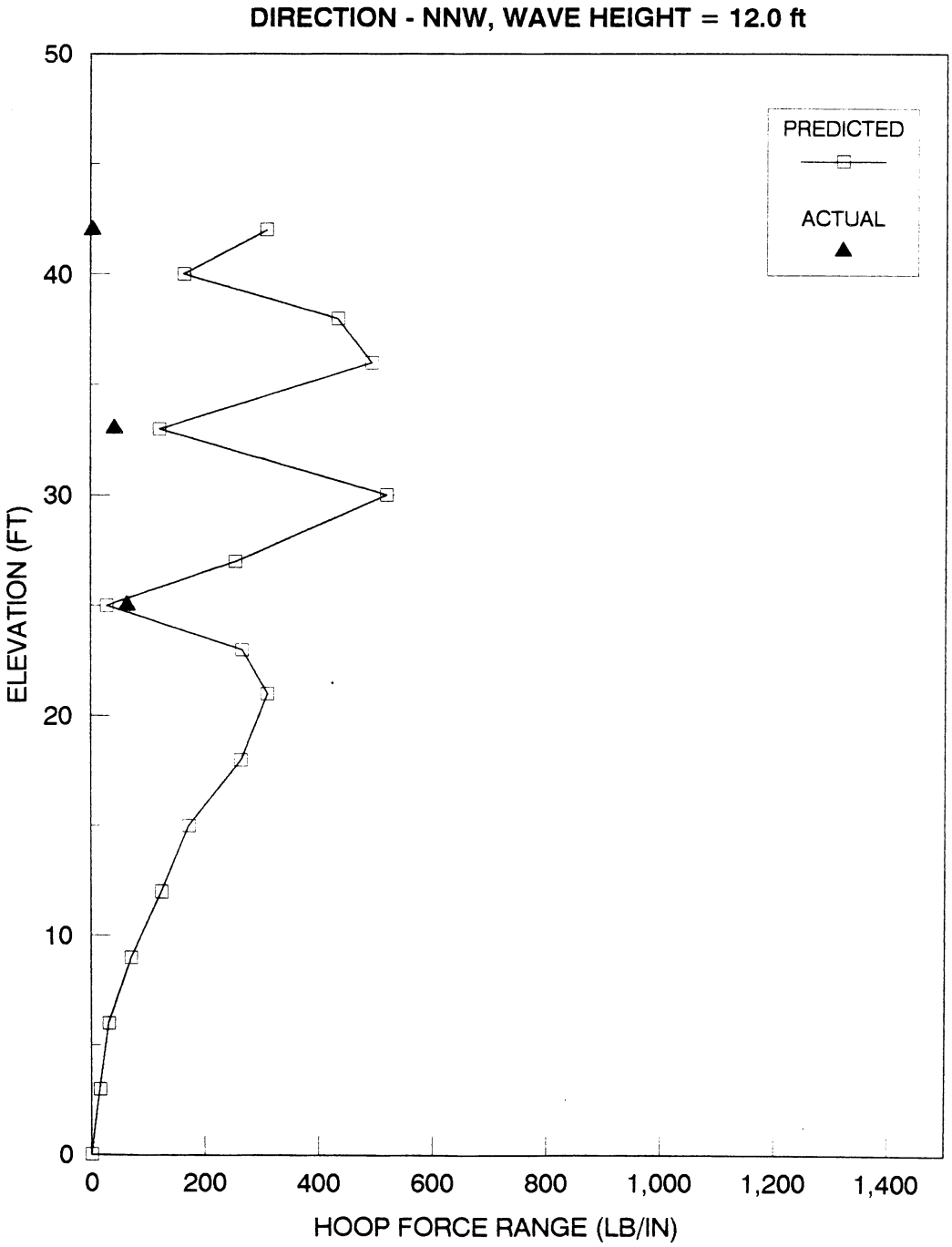

Fig. 5.6 Comparison between predicted and measured hoop force variation (Data recorded on Feb. 13th)

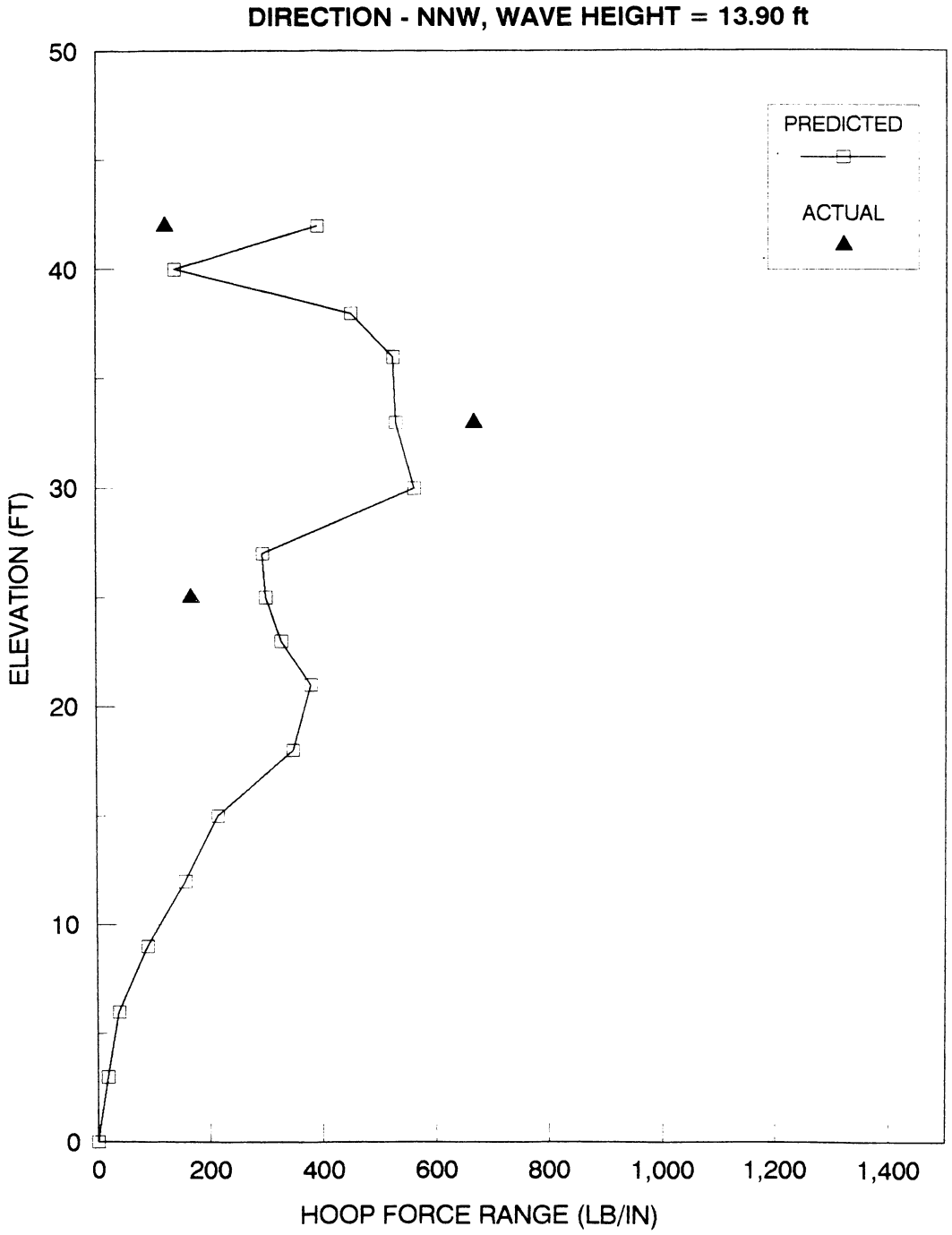

Fig. 5.7 Comparison between predicted and measured hoop force variation (Data recorded on Feb. 24th)

the standing waves from the breakwater wall. The actual waves at the structure may not be standing waves. On the other hand, the standing wave assumption is supported by Fig. 5.5. The wave height of 6.0 ft is close to 4 ft, and some wave components of that particular sea state are standing waves. This is supported by a significant wave height of 3.40 ft as recorded by the CERC wave gauge.

Figures 5.8.a to Fig. 5.11d compare the recorded hoop forces at specific locations with the predicted values for different wave heights. The solid curve in these figures is the developed relationship between the hoop-force ranges and the wave height from the SAS package.

From the figures it is evident that the predicted trend does not always show an increase in hoop-force range with increasing wave height but follows a curvilinear path. The Figures D.1, D.2 and D.3 which indicate waves from the north, will be considered for this possible reason: reduction in the hoop-force range occurs as the wave height increases from 16 ft to 20 ft at the locations 12, 13 and 16. A similar change is also observed considering the wave height increase from 20 ft to 24 ft. However, the reduction in the hoop-force range is local, and the average hoop force range increases with increasing wave heights. As the wave heights increase above four feet, a large decrease in the predicted trend occurs because of the standing waves

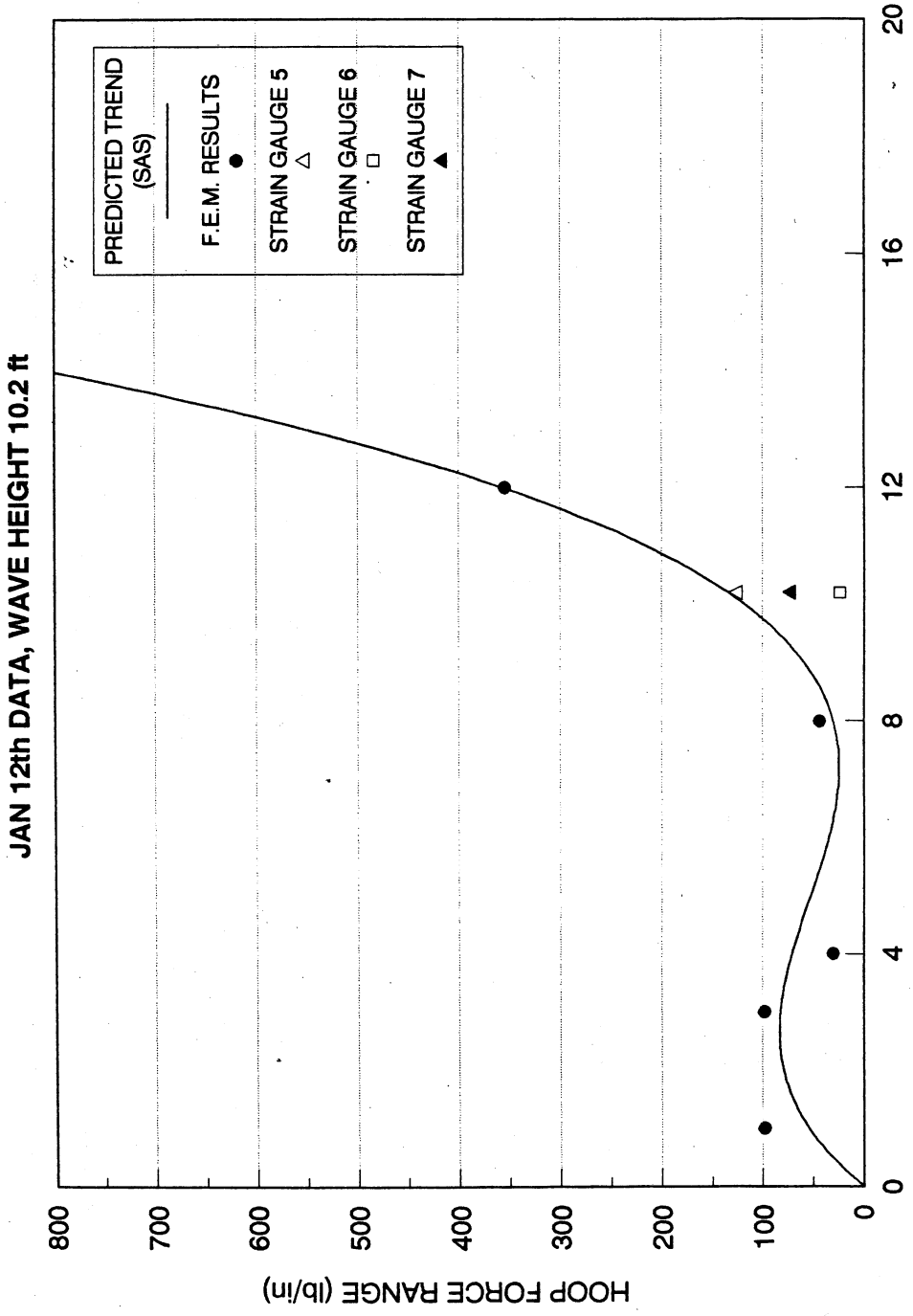

Fig. 5.8a Recorded hoop force ranges vs predicted trend at location 17 (Strain Gauges

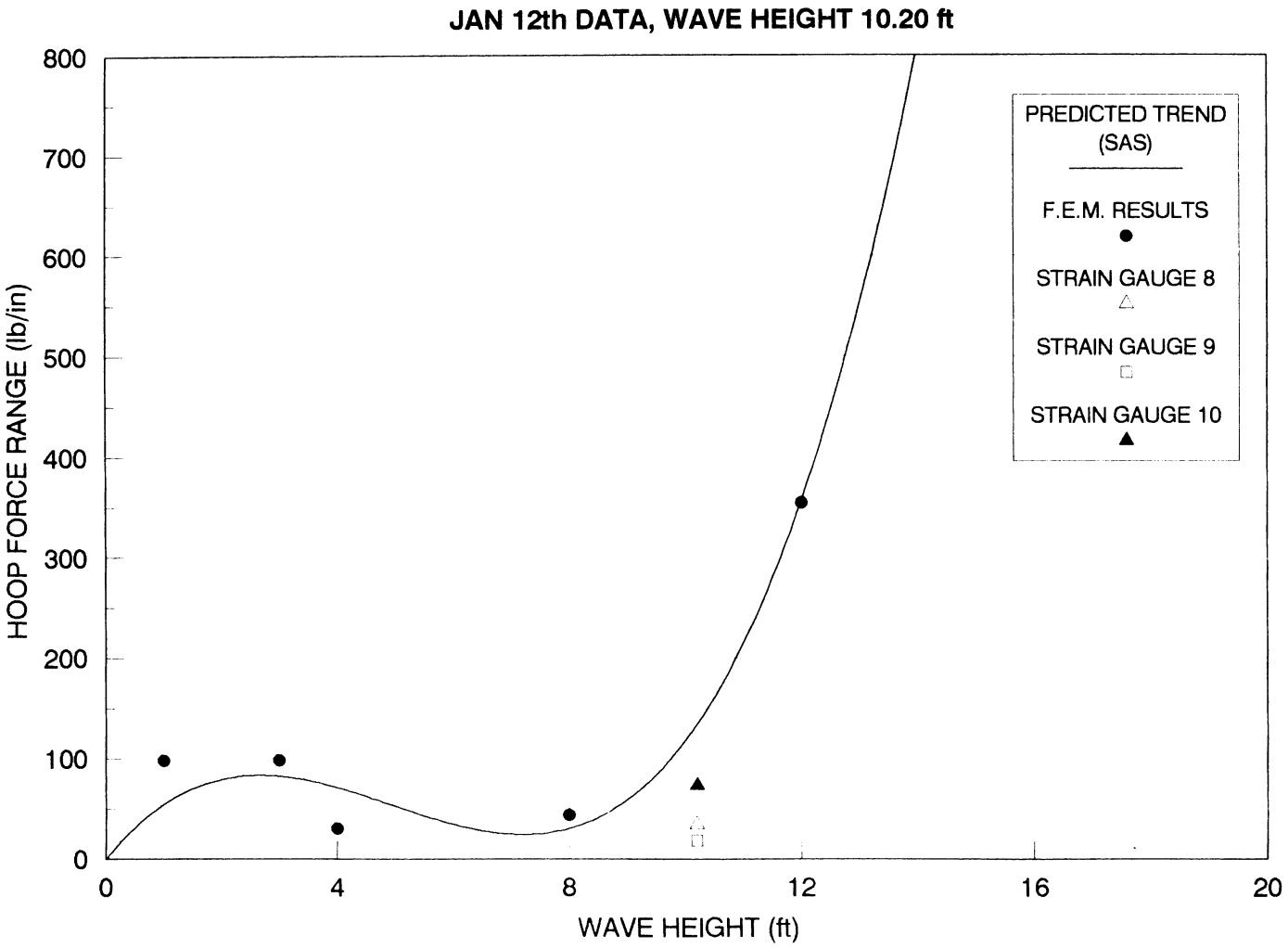

Fig. 5.8b Recorded hoop force ranges vs predicted trend at location 17 (Strain Gauges 8,9, and 10) for a wave height of 10.20'

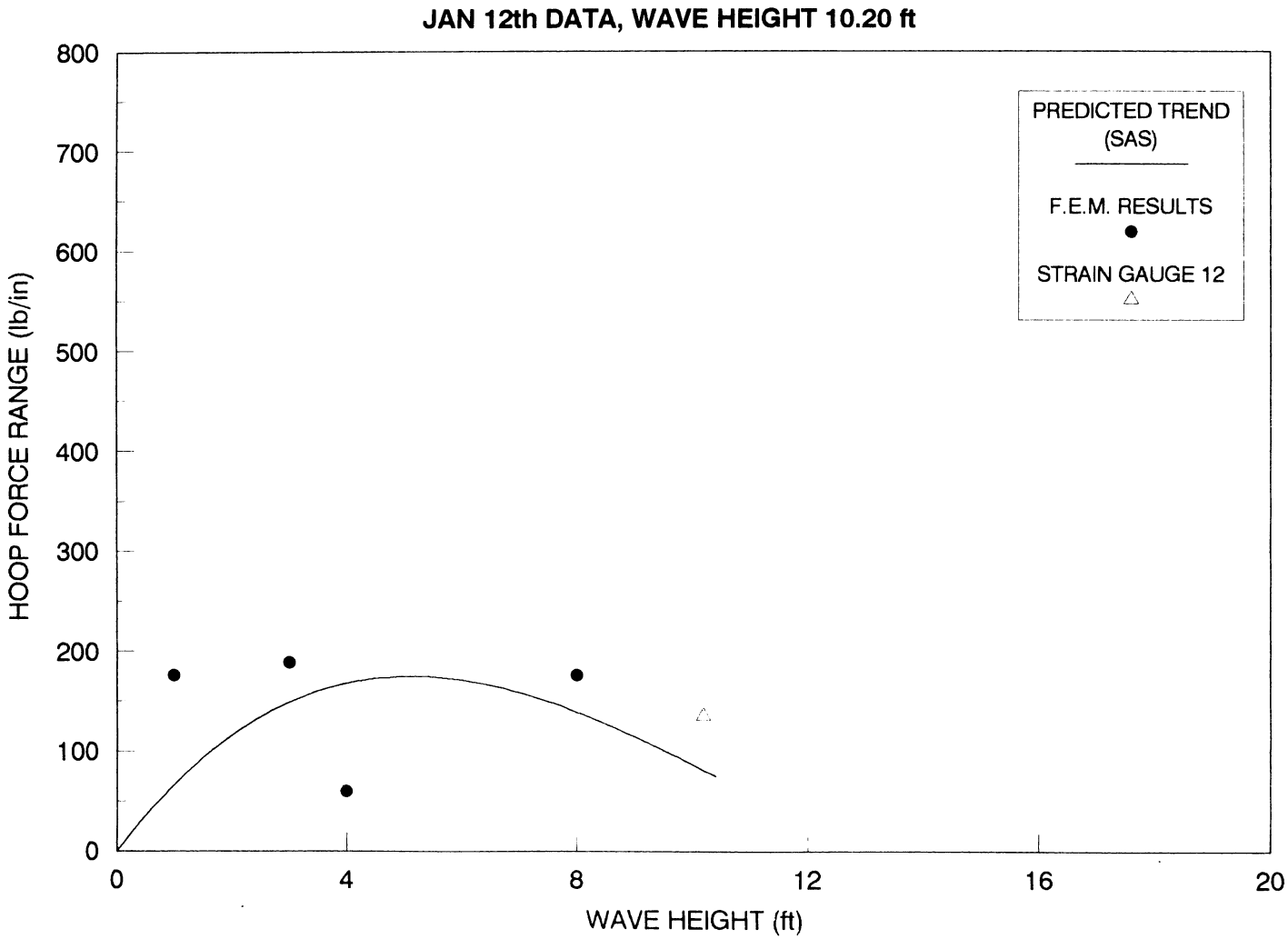

Fig. 5.8c Recorded hoop force ranges vs predicted trend at location 10 (Strain Gauge 12) for a wave height of 10.20'

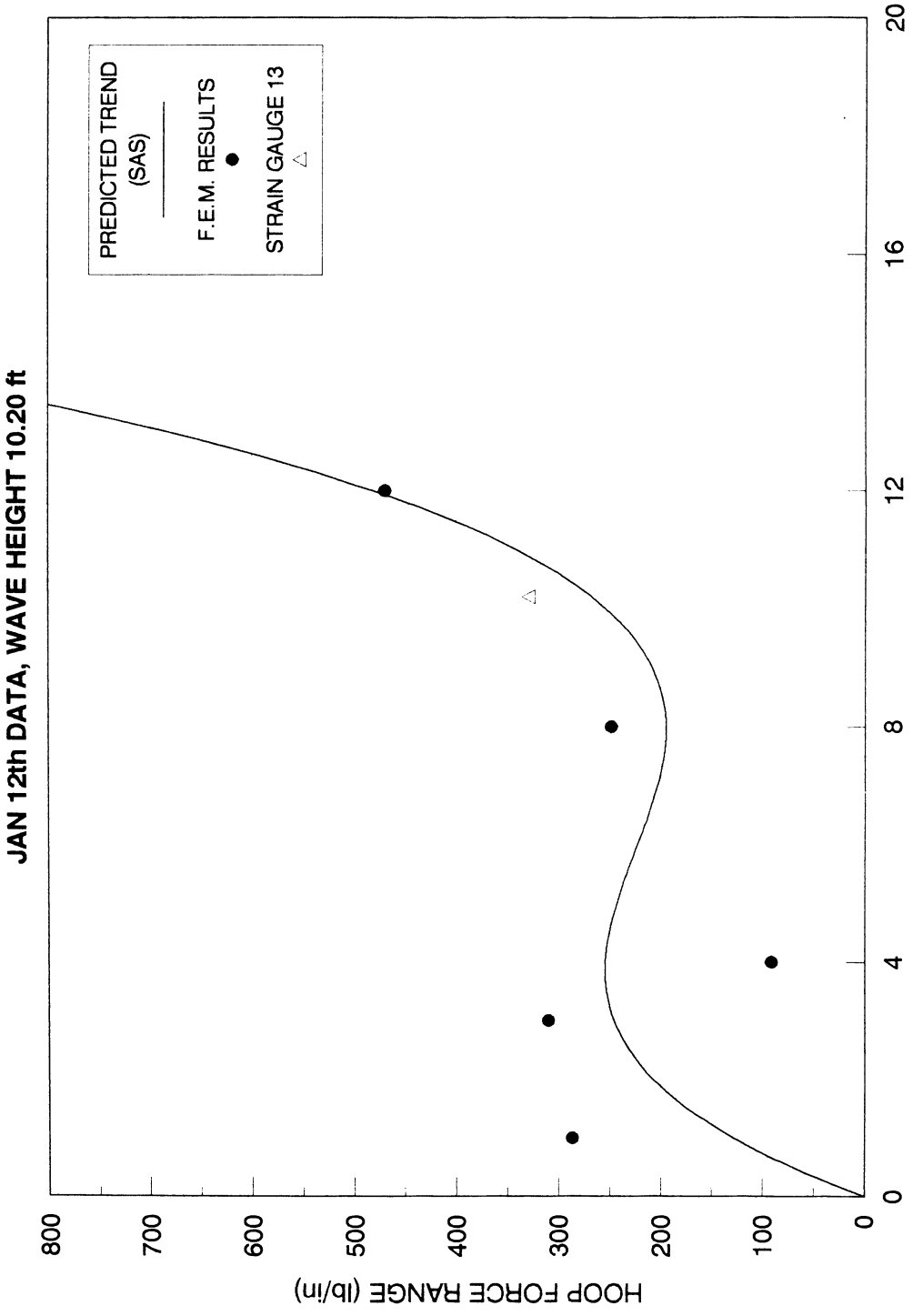

Fig. 5.8d Recorded hoop force ranges vs predicted trend at location 13 (Strain Gauge 13) for a wave height of 10.20'

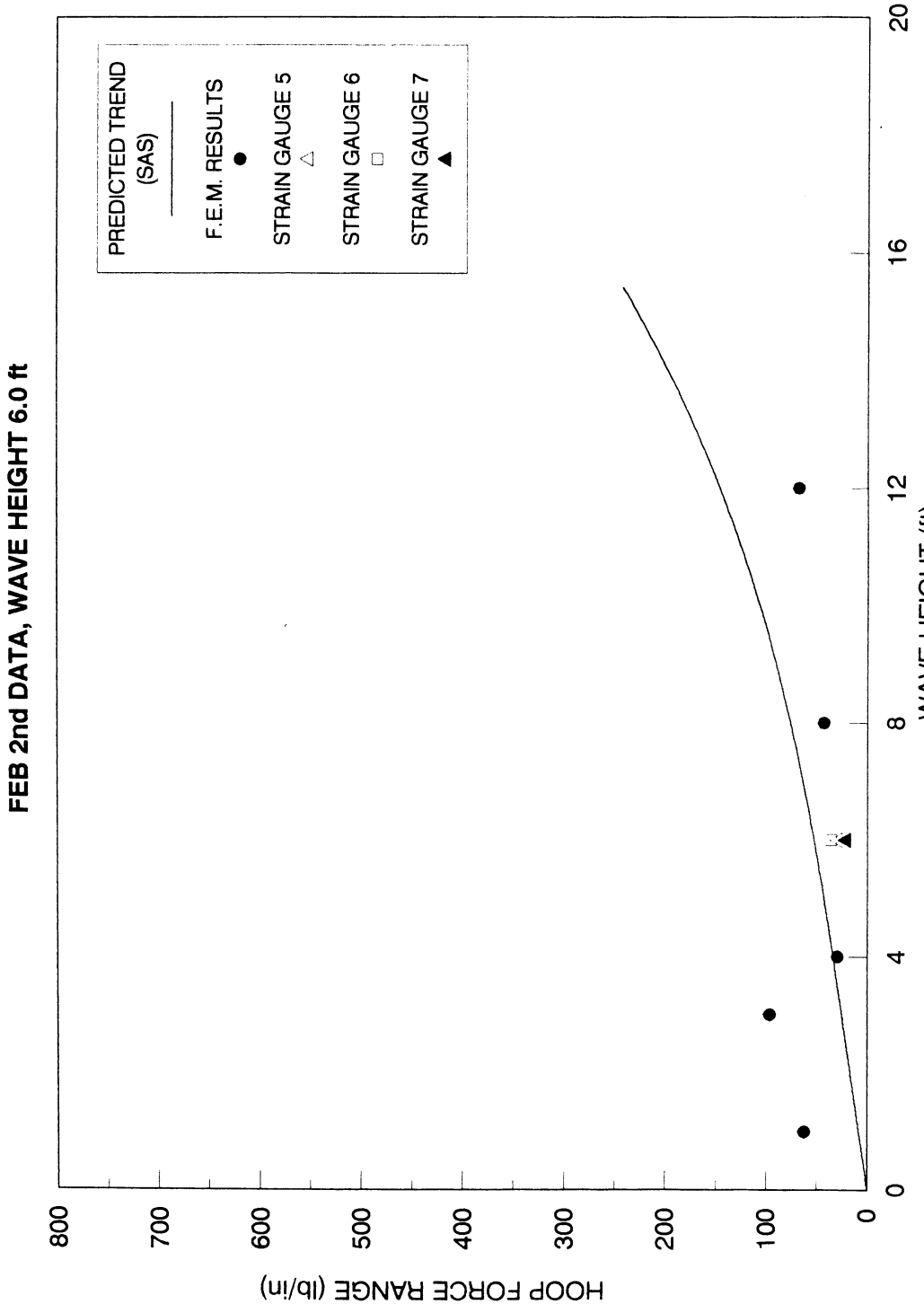

Fig. 5.9a Recorded hoop force ranges vs predicted trend at location 17 (Strain Gauges 5,6, and 7) for a wave height of 6.00'

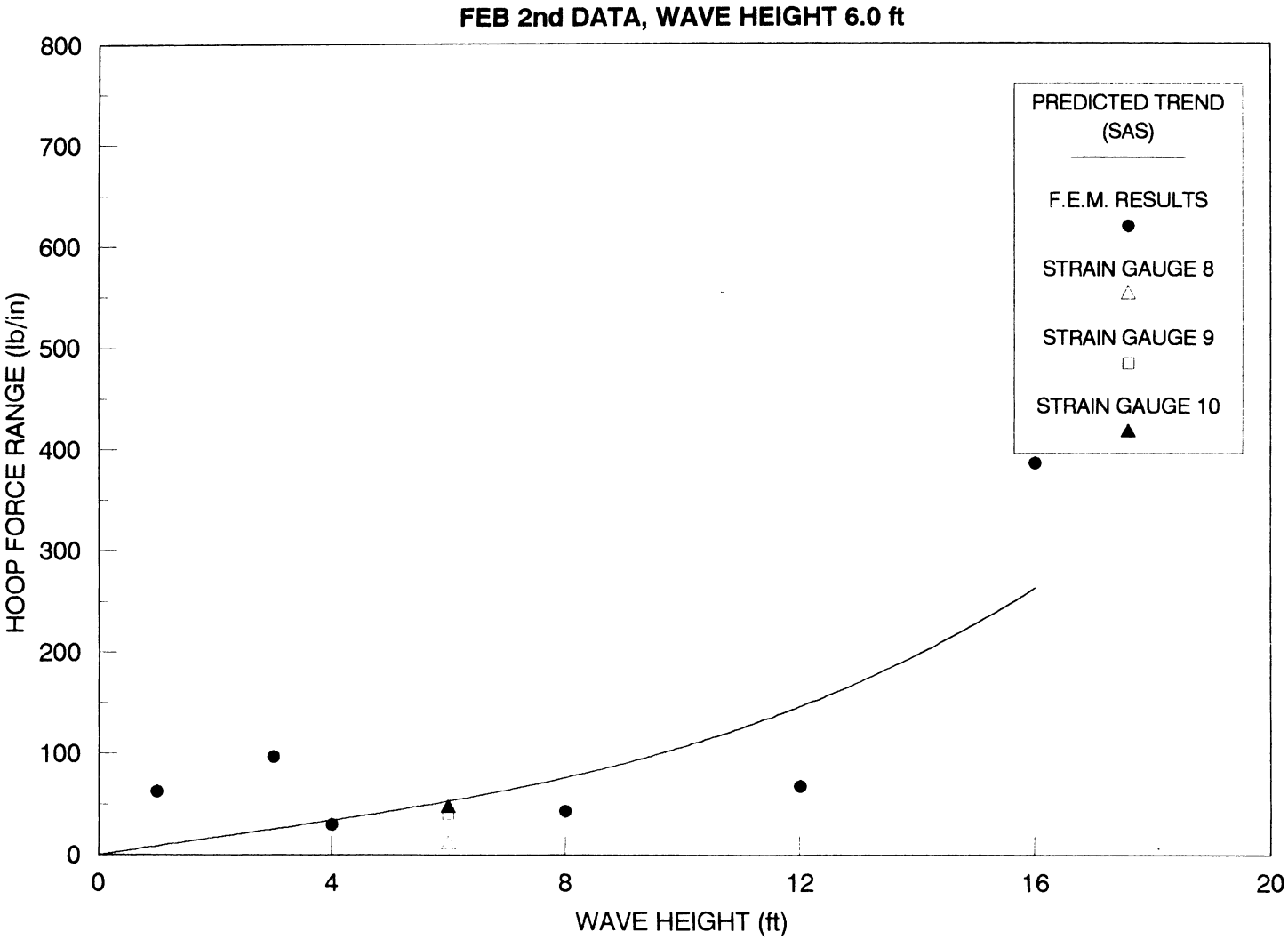

Fig. 5.9b Recorded hoop force ranges vs predicted trend at location 17 (Strain Gauges 8,9, and 10) for a wave height of 6.00'

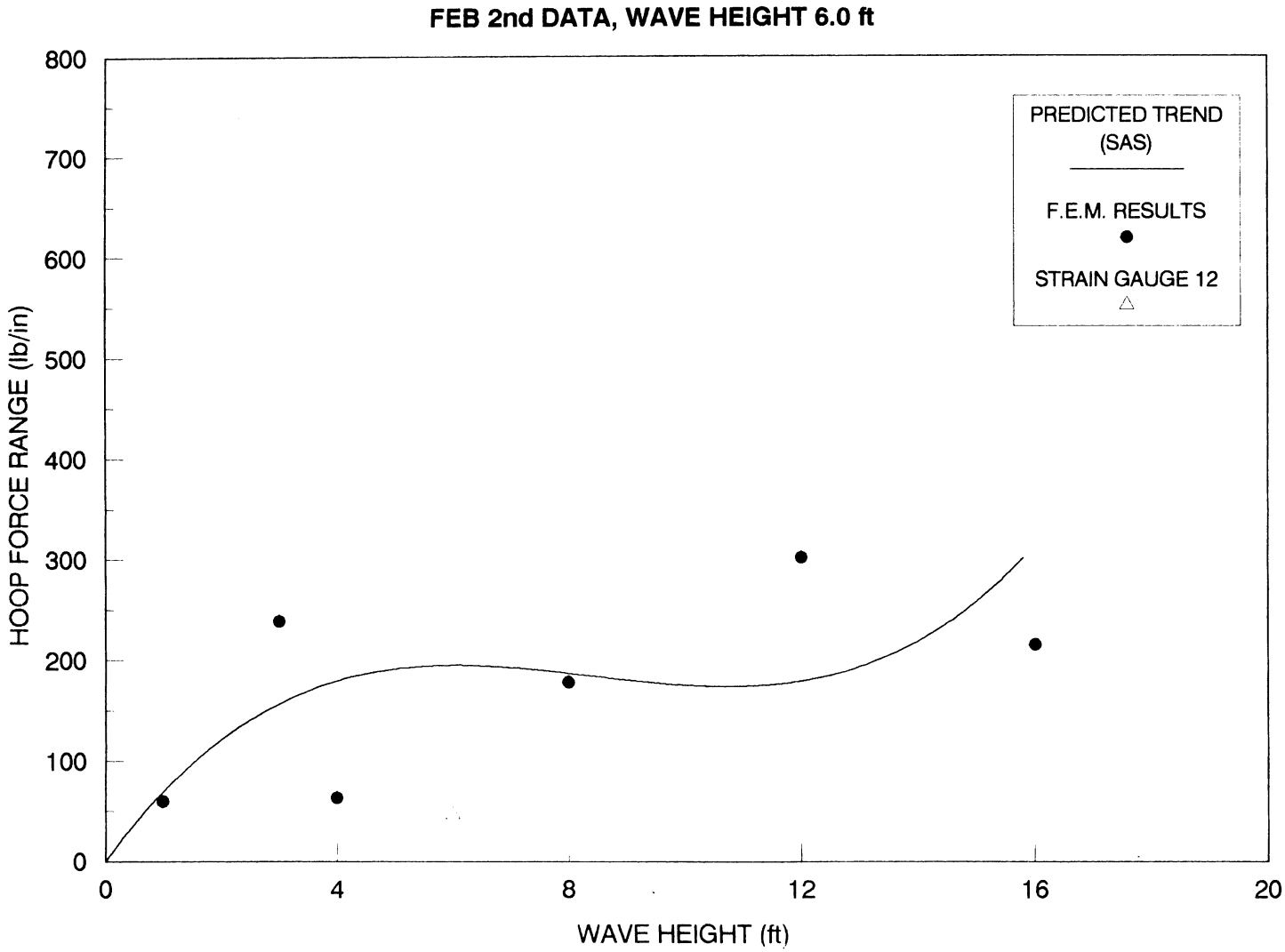

Fig. 5.9c Recorded hoop force ranges vs predicted trend at location 10 (Strain Gauge 12) for a wave height of 6.00'

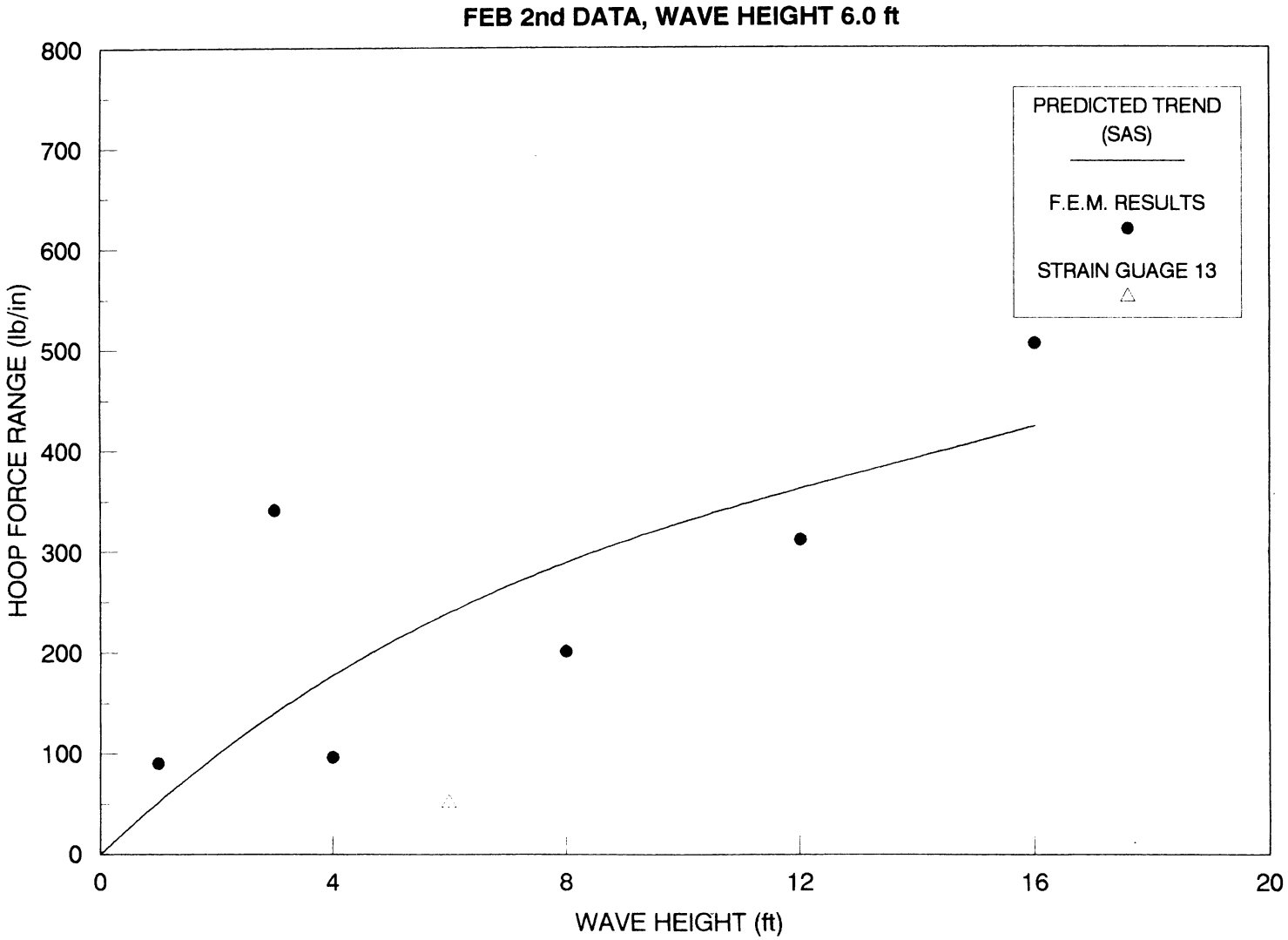

Fig. 5.9d Recorded hoop force ranges vs predicted trend at location 13 (Strain Gauge 13) for a wave height of 6.00'

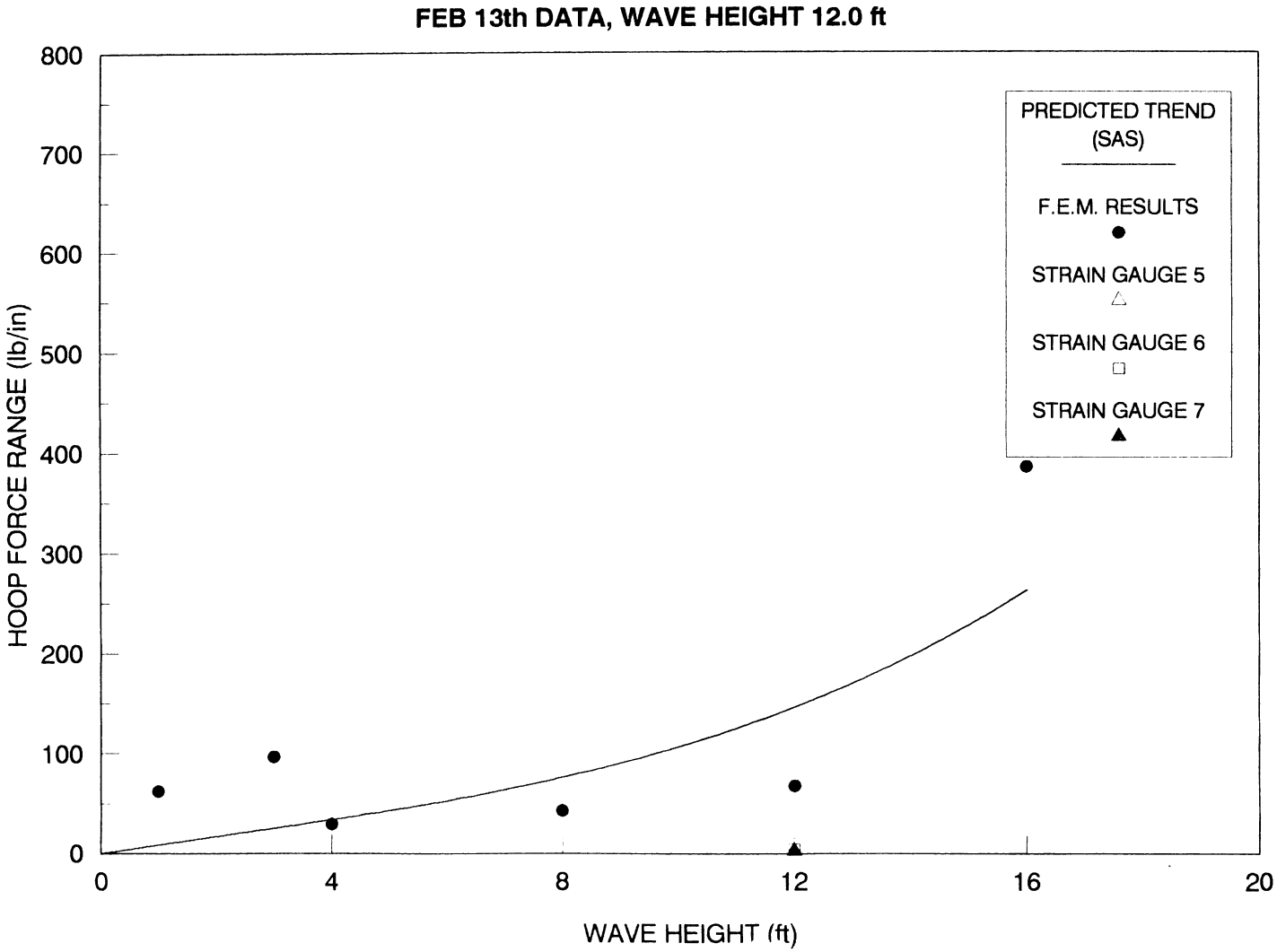

Fig. 5.10a Recorded hoop force ranges vs predicted trend at location 17 (Strain Gauges 5,6, and 7) for a wave height of 12.00'

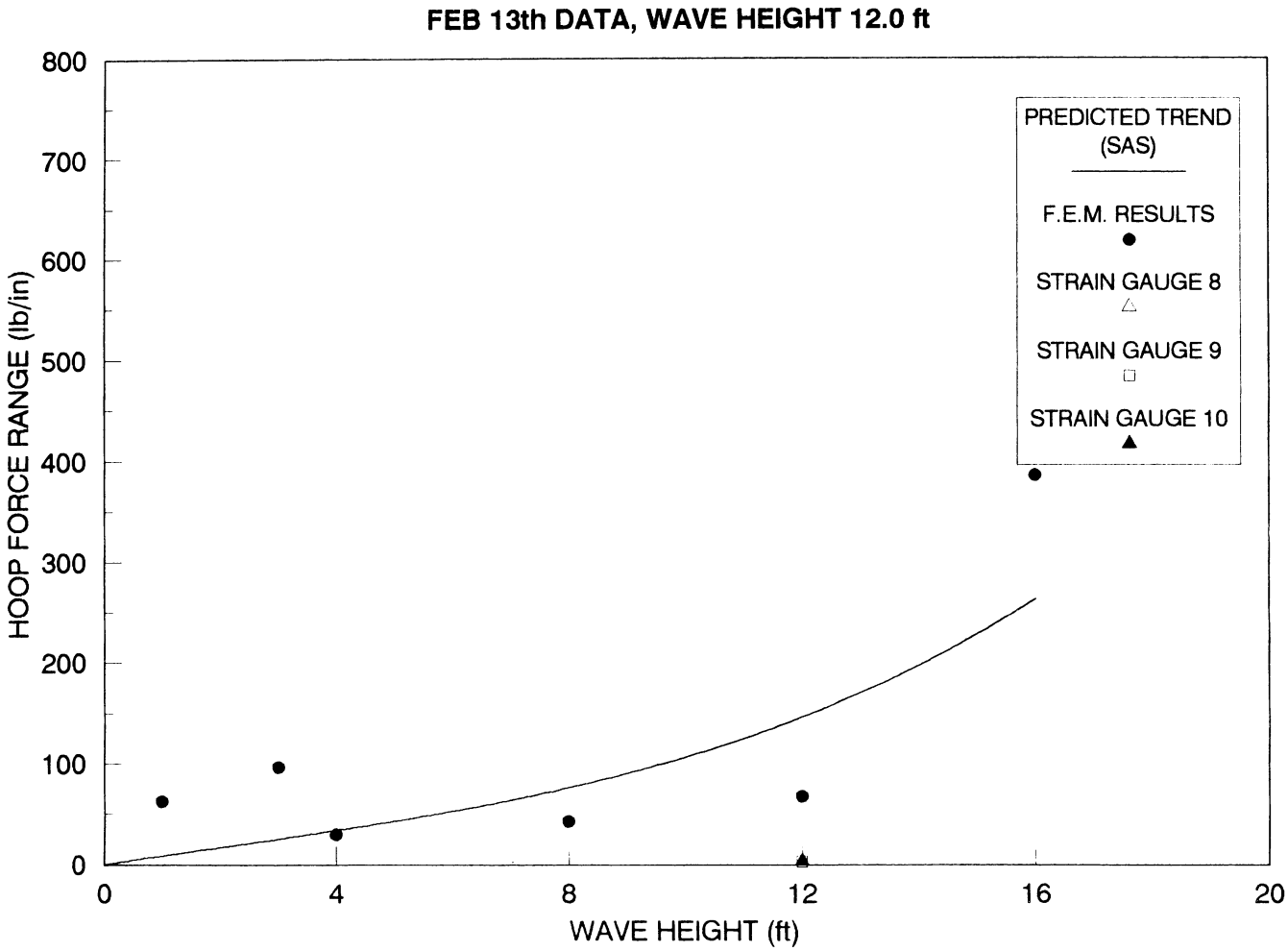

Fig. 5.10b Recorded hoop force ranges vs predicted trend at location 17 (Strain Gauges 8,9, and 10) for a wave height of 12.00'

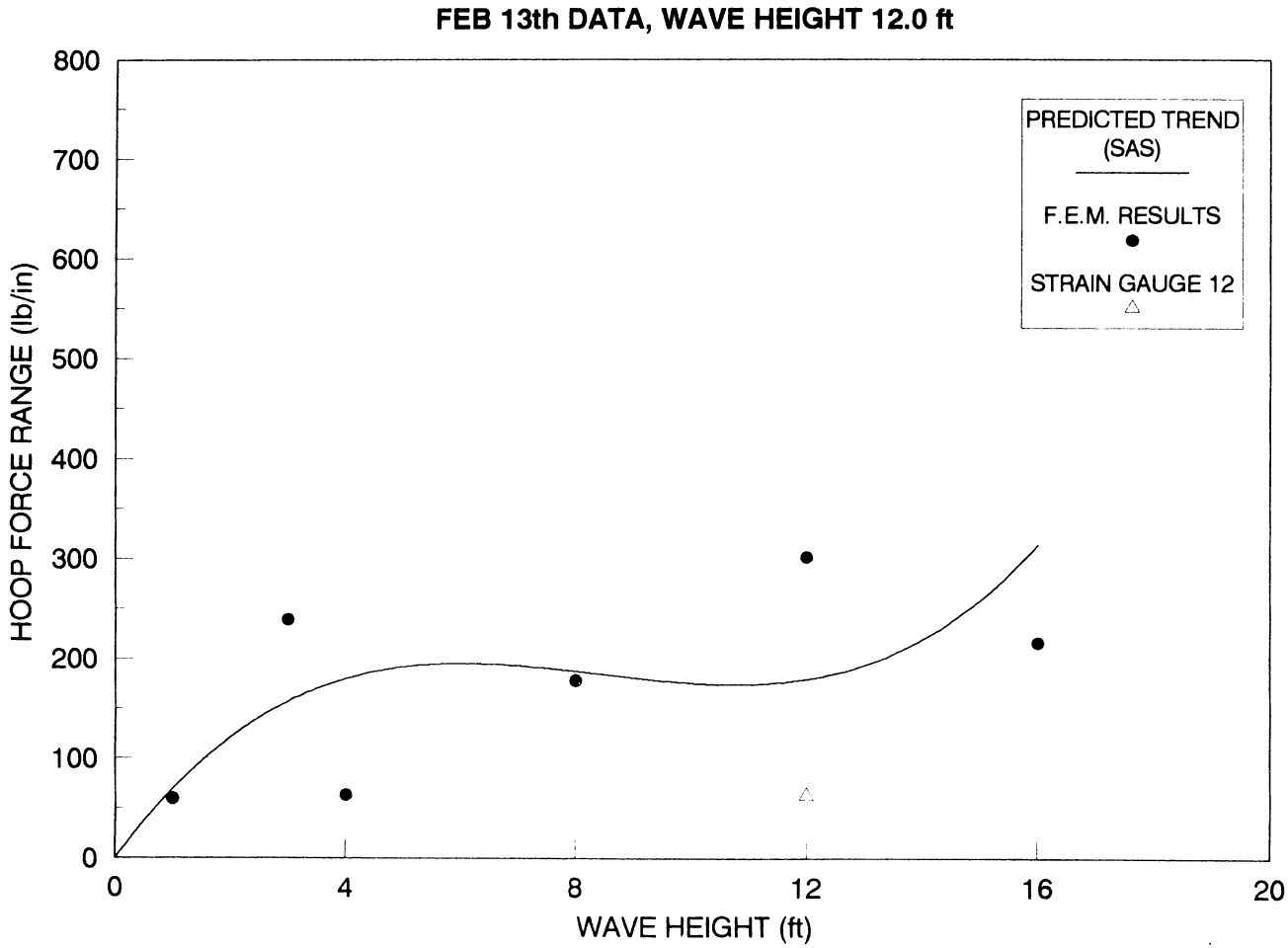

Fig. 5.10c Recorded hoop force ranges vs predicted trend at location 10 (Strain Gauge 12) for a wave height of 12.00'

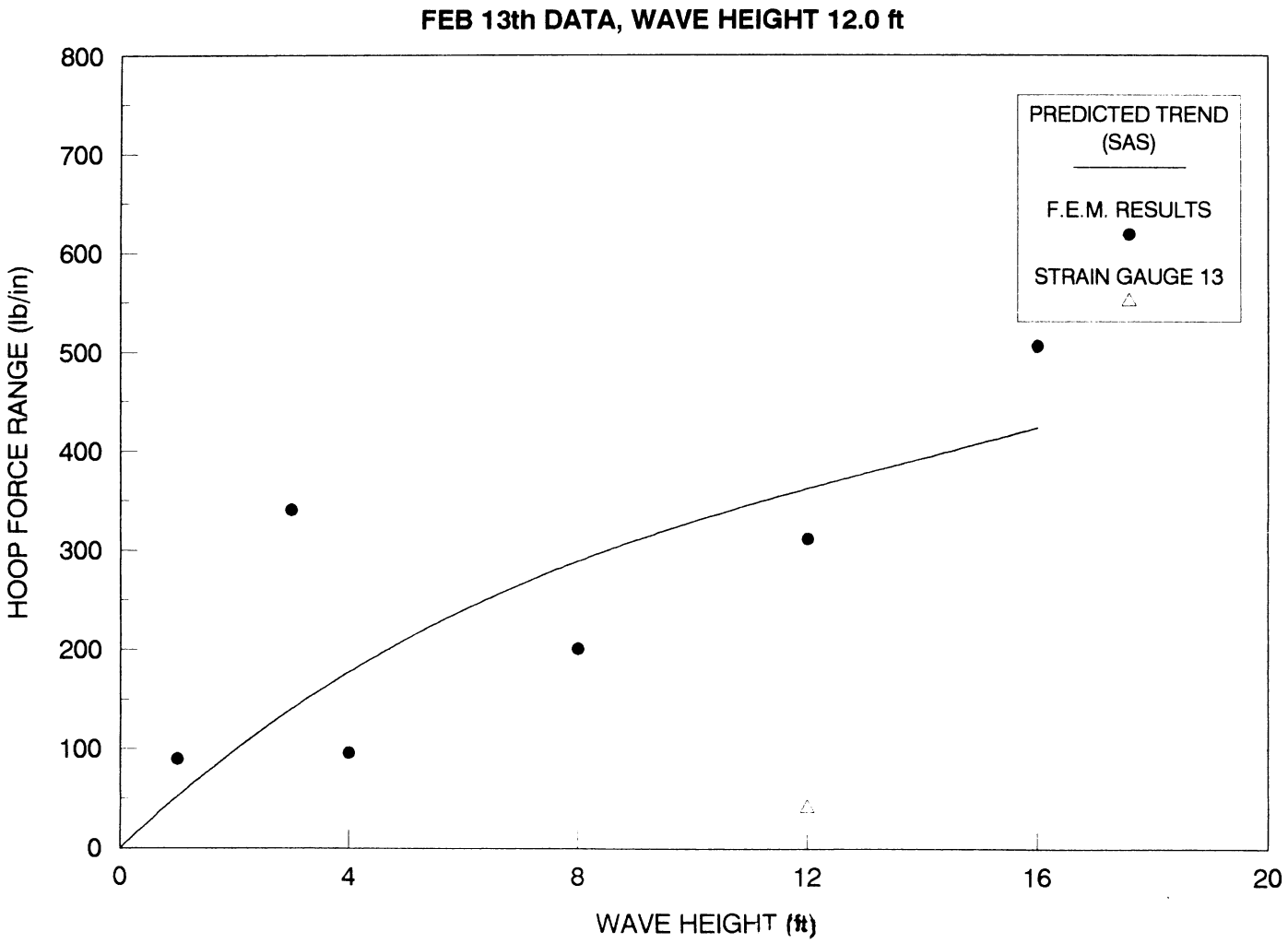

Fig. 5.10d Recorded hoop force ranges vs predicted trend at location 13 (Strain Gauge 13) for a wave height of 12.00'

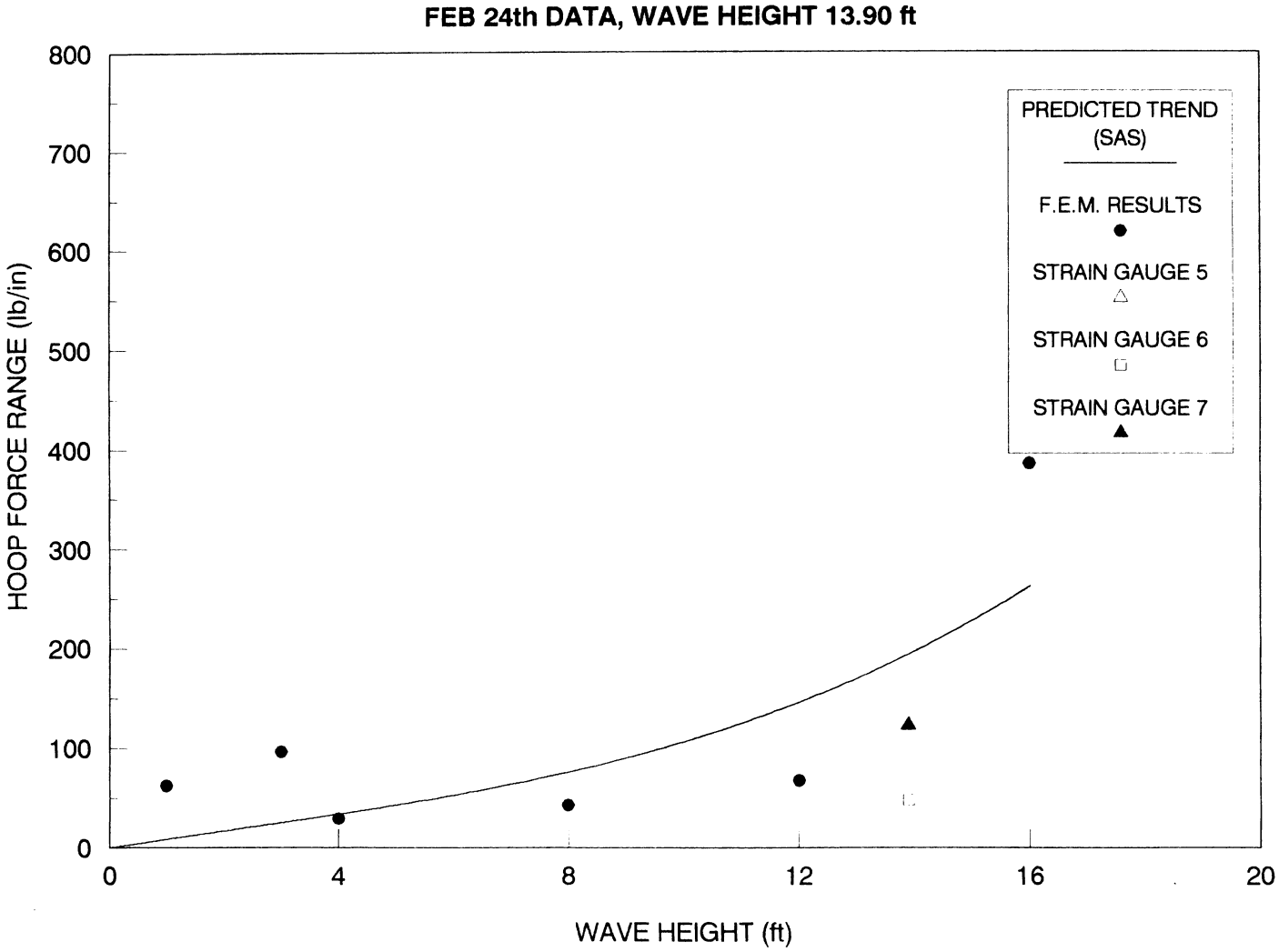

Fig. 5.11a Recorded hoop force ranges vs predicted trend at location 17 (Strain Gauges 5,6, and 7) for a wave height of 13.90'

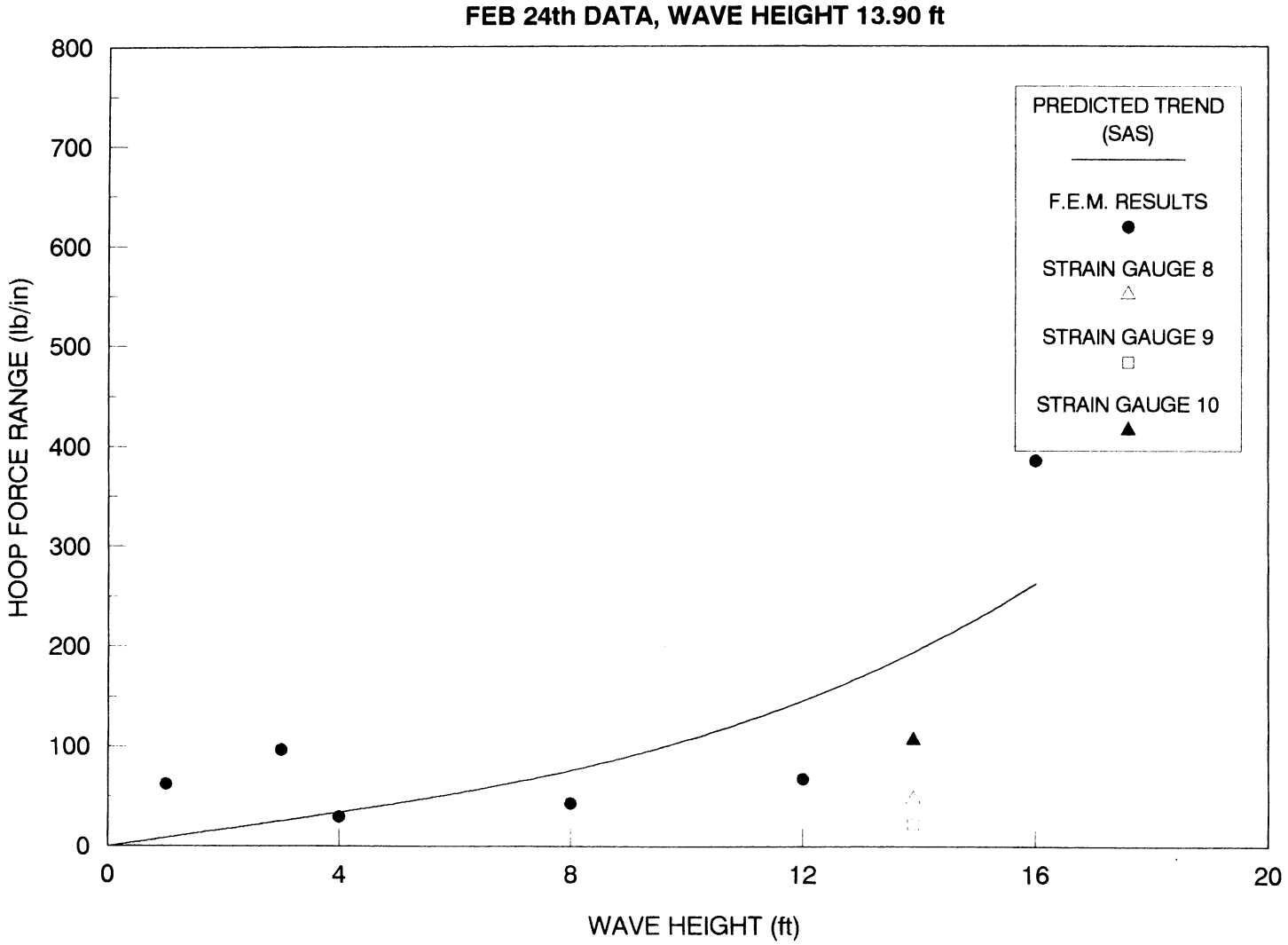

Fig. 5.11b Recorded hoop force ranges vs predicted trend at location 17 (Strain Gauges 8,9, and 10) for a wave height of 13.90'

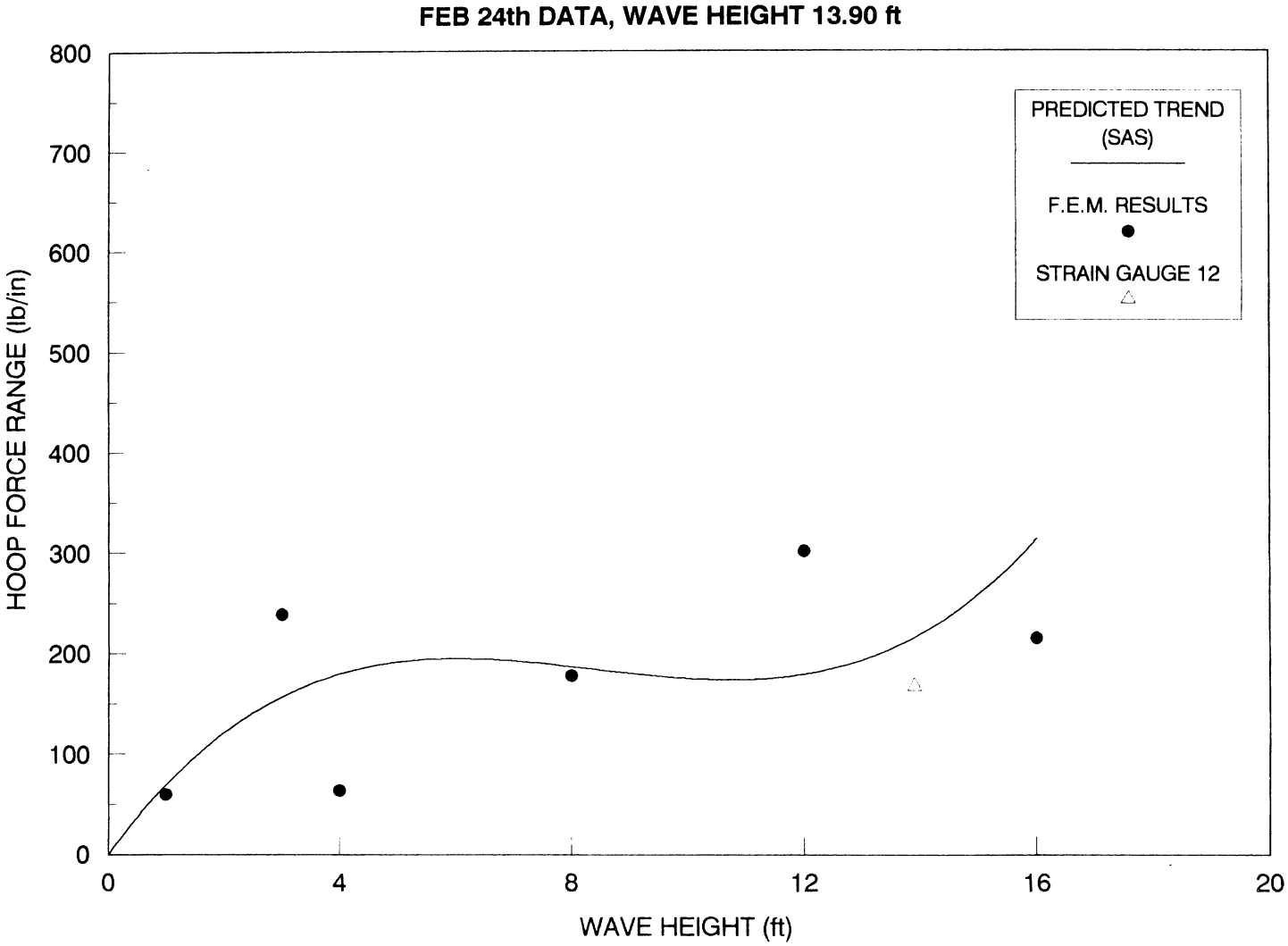

Fig. 5.11c Recorded hoop force ranges vs predicted trend at location 10 (Strain Gauge 12) for a wave height of 13.90'

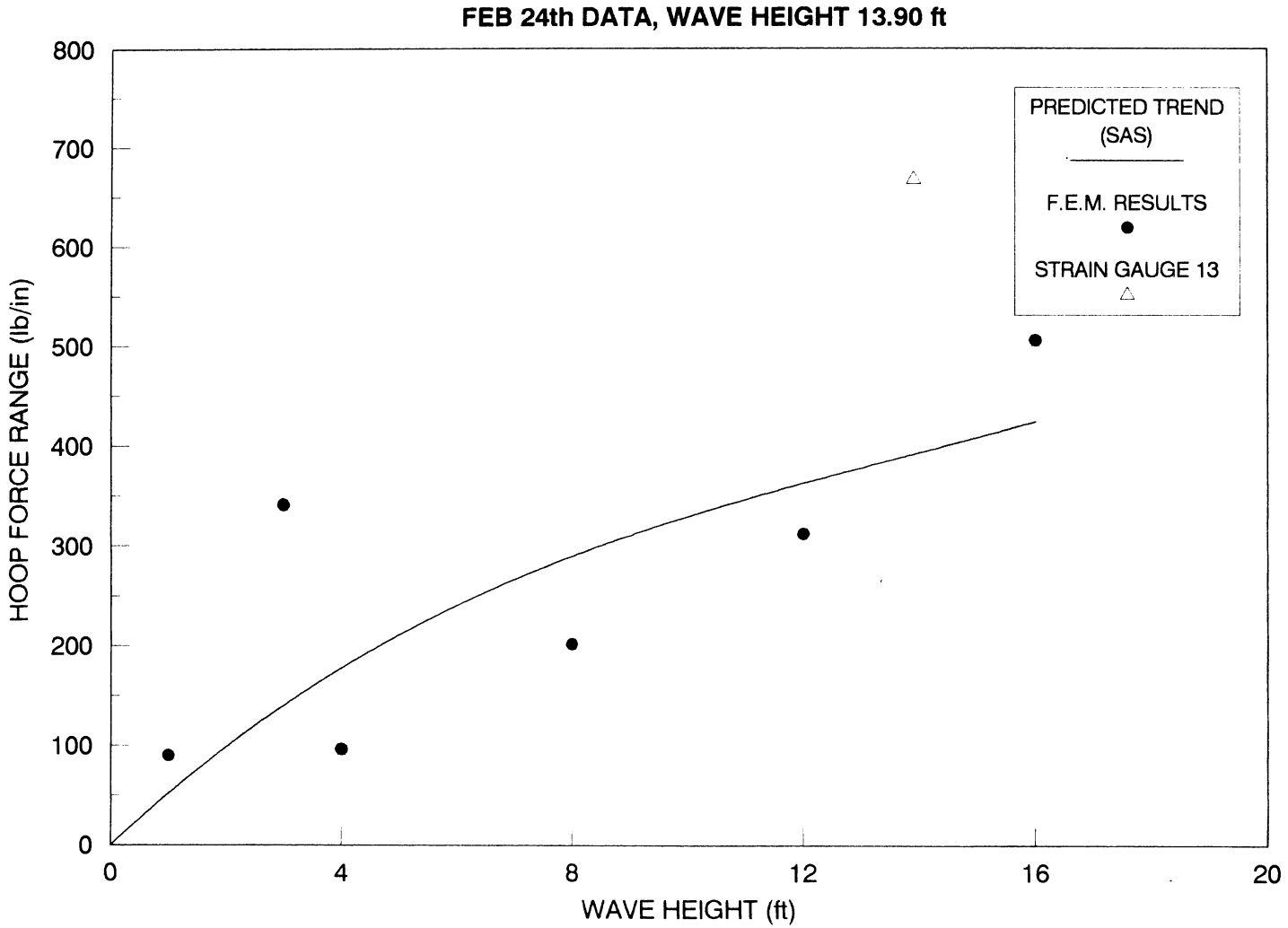

Fig. 5.11d Recorded hoop force ranges vs predicted trend at location 13 (Strain Gauge 13) for a wave height of 13.90'

assumption explained earlier.

Considering the individual response of individual strain gauges, a few comments can be made with regard to general behavior. The variations of strain at the top are in the same range for Strain Gauges 7, 5, 6, and 10. Strain Gauges 8 and 9, which are on the harbor side, show comparatively smaller changes.

The typical behavior of the strain gauges can be discerned by considering Figs. 5.11a through 5.11d, which indicate the data recorded on Feb. 24th, 1990. Strain Gauges 7 and 5 show the maximum variation in strains, followed by Strain Gauge 10. Strain Gauges 7,5, and 10 are located on the cell wall. The strain value recorded by Strain Gauge 6 is lesser because Strain Gauge 6 is mounted on the diaphragm. Strain Gauges 8 and 9 show the least recorded values, which is expected since they are on the harbor side.

The flexural Strain Gauges 3 and 4 are generally observed to measure larger strain values than Strain Gauge 1, nearer to the diaphragm. This can be expected because the sheet pile on which Strain Gauge 1 is mounted is partially supported on either side by the rock face. The presence of the diaphragm also stiffens the response of Strain Gauge 1.

The variations between the recorded data and the

predicted data can be attributed to various reasons both local and global in magnitude. The global reasons that might account for some strain variation include:

1. Wave height and period relationship:

The results of the structural analysis are due to the forces calculated from the statistical waves based on hindcast data. These forces due to the waves are based on a deterministic relationship between the wave heights and wave periods. The wave that causes the actual recorded strains may not follow the predicted relationship.

2. Climatic conditions:

Climatic conditions affect the response of the instrumentation. Also the effect of ice on the structure would modify the structural response to the wave forces. The presence of ice in the lake would cause the waves to be quiescent.

3. Strain gauge installation:

The installed strain gauges, especially those underwater are assumed to act in the same way as tested laboratory specimens. The method of installation might vary.

4. Structural modeling:

As the structure was modeled, the berm, the toe protection, riprap, and the like were considered as shown in

the reconnaissance report. The site conditions, such a non-uniform pile depths, however, might vary from the assumed model.

6. FAILURE ANALYSIS AND FATIGUE EVALUATION

6.1 Introduction

The results of the finite element analyses are presented in this chapter in a format that represents the probable failure modes of the structure. The damage accumulation and the life of the structure are estimated, and a sensitivity analysis is provided in order to explain the effects of various parameters involved in the analysis. The limitations of the study are illustrated, and the rehabilitation measures are considered.

6.2 Potential Failure Modes of the Structure

The potential failure modes of the structure can be discussed by considering the variation of the hoop-force range at various elevations on the breakwater, caused by the successive applications of a peak and a trough wave, as shown Fig. 6.1. The location of the maximum variation is typical for all different cases tested; however, the magnitudes varied for each case. The hoop-force range is critical at a number of locations on the breakwater elevation: in Fig. 6.1, they are locations 10, 11 and locations 14, 15. Figures D.1 to D.13 are representative of the hoop-force range variation for other waves and are attached as Appendix D. In these two zones, large hoop-force ranges have the capability to cause a failure because of fatigue from recurrent loading.

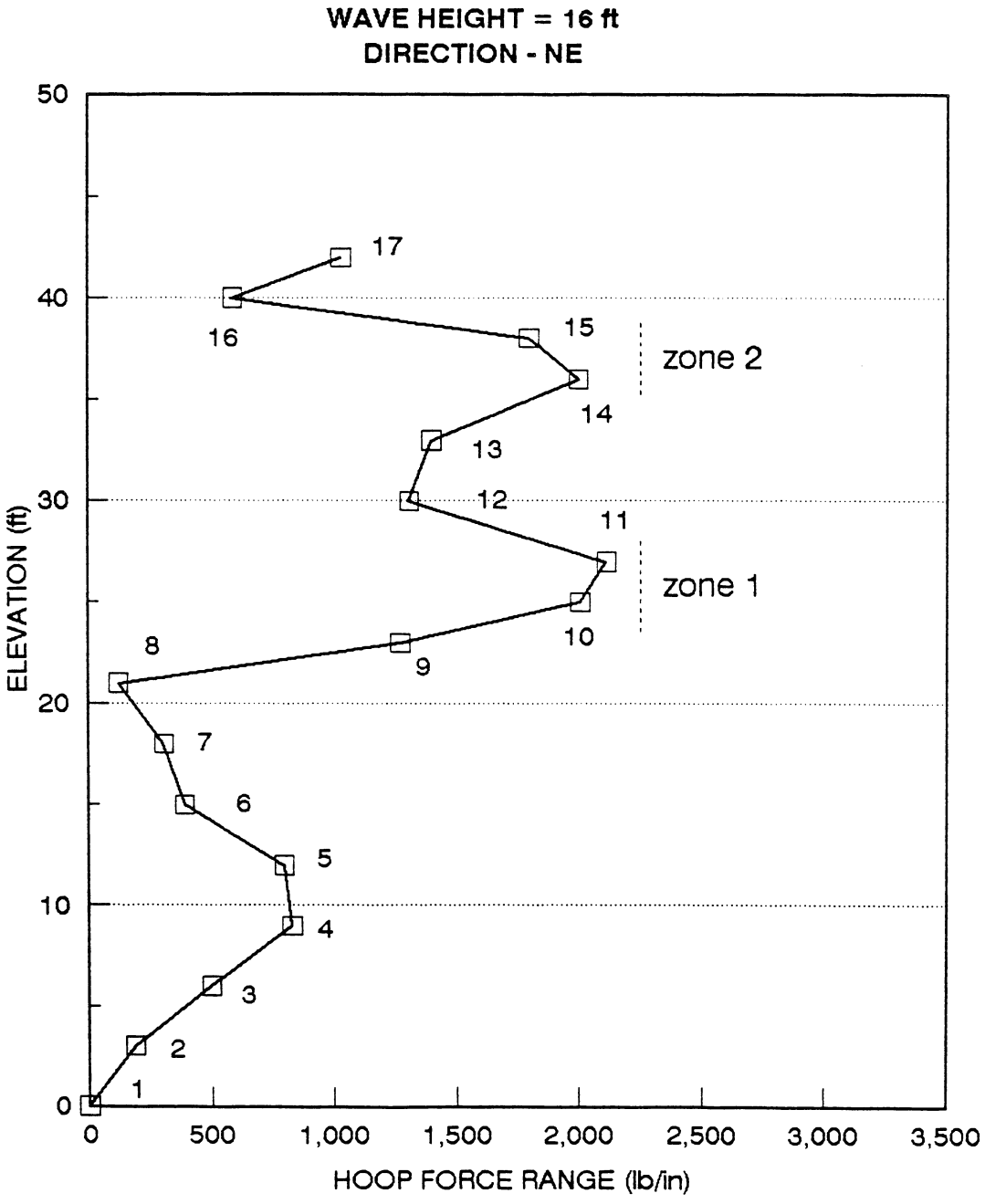

Fig. 6.1 Variation of hoop-force ranges with elevation and identified critical failure zones

If these conditions develop, the pattern of failure would be a crack initiation, crack propagation, and the structural failure. Considering Fig. 6.1, the initiation of a fatigue crack at location 11 could cause significant overstresses at adjacent locations as load is transferred. Thus, location 10 would become a critical region and could cause an opening wide enough to cause spilling of the fill material as the crack progresses. Another possible mode of failure might begin at the top, even though force ranges as shown at location 17 are not as large as at the other locations. However, an initial flaw or crack due to extraneous reasons such as pile driving or corrosion could enhance the potential for crack growth, causing failure at the top location that would progress downward as load is transferred. Another factor that would aid in the crack propagation will be the cantilever action of the cell wall at top.

6.3 Fatigue Life Evaluation

The process of estimating the fatigue life of the structure is to determine initially the damage at discrete locations on the structure. The most critical location on the structure is defined as that susceptible to maximum damage. The fatigue damage evaluation was achieved by using computer programs created at ISU. The details of the computer programs are listed in Appendix E. The algorithm

for evaluating the damage, called the equivalent damage method, is shown in Appendix C. The Equivalent Stress Range method indicated in Appendix C is based on Miner's Rule (7), which attempts to quantify the damage evaluated on the structure as a ratio of the number of cycles in service to the theoretical number of cycles to failure. This ratio is called the damage fraction. Failure is assumed to occur when the calculated damage fraction equals or exceeds unity. As a ramification of Miner's rule, the fatigue life can be estimated. Considering a time period of **T** for the loading on the structure, which causes a calculated damage fraction **D** at a location, the fatigue life of the structure is defined to be **T/D**. The fatigue life for an existing structure can be divided into two parts, the period for which the structure has been in service and the future life until failure. The components of the algorithm for evaluating the damage at a location are as follows:

1. Determination of a significant hoop-force range for the sea state from the wave height and hoop-force range relationship.
2. Conversion of the significant hoop-force range into equivalent hoop-force range.
3. Determination of the number of cycles to failure for the equivalent hoop-force range from the fatigue curve.

4. Determination of the damage value for the sea state as the ratio of the total number of waves calculated from the probability of occurrence of the sea state and the number of cycles to failure for the equivalent hoop force range.
5. Determination of the damage for a direction as the total of the damage evaluated in constituent sea states.
6. Determination of the total damage at the location (as the aggregate of all directionwise damages).

For the analysis, a distinction was made between the lakeside accumulation and the harborside accumulation of damage. A limitation of the two-dimensional finite element model is the assumption that the hoop forces evaluated on the structure are equal on the lake side and harbor side regardless of the direction of the wave loading. This assumption is illustrated in Fig. 6.2; however, this simplifying assumption is not true because a lakeside wave would cause smaller hoop-forces on the harbor side than on the lake side (Fig. 6.13). The finite element analysis will be assumed to give reliable results on the side of wave incidence, that is, on the lakeside if the waves are from the lakeside. The hoop-forces on the opposite side are neglected. The lakeside damage was evaluated considering

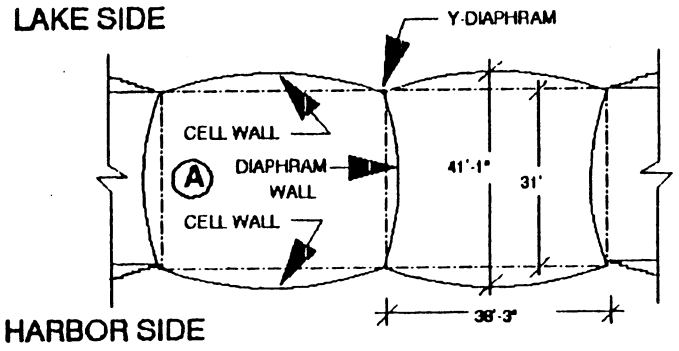

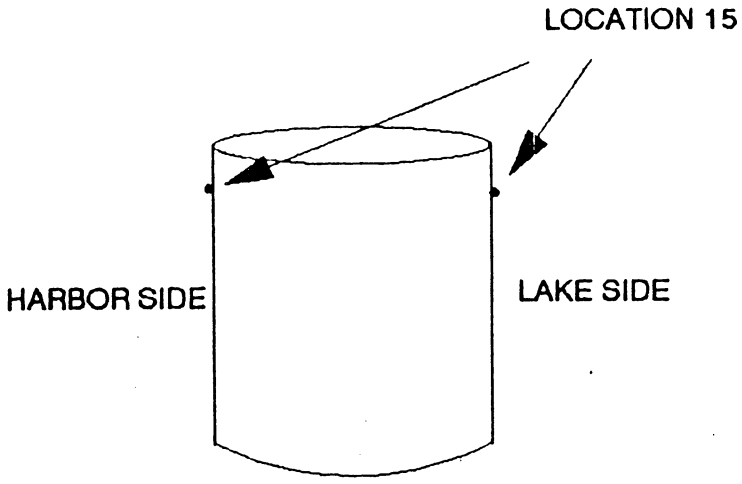

Fig. 6.2 Finite element idealization of lake-side a side hoop forces

the directions NNW, N, NNE, NE, ENE, E, and ESE. The harborside damage was evaluated considering the directions SSE, S, SSW, SW, WSW, W, and WNW.

The calculated fatigue life is very sensitive to the fatigue data. The fatigue curve for this study (Fig. 3.4) was based on a relatively small number of tests (8 in total). In addition, Test 8, representing the smallest fatigue range of 2750 lb/in., was tested to 500,000 cycles without failure before the test was stopped.

Fatigue tests in literature are usually presented in the form of an exponential relationship between the stress range and number of cycles to failure as

$$N = A.\ S_r^{-n}$$

----- Eqn. 6.1

Where,

N = Number of cycles to failure

A = Intercept on the stress range axis

η = Exponent of the fatigue curve

A straight-line fit of the seven fatigue tests gives an exponent, η, of 1.68. Results from the fatigue tests on typical structural details by others (19) show the exponsnt to be around 3. Figure 6.2a shows the fatigue curves with exponents of 1.68 and 3 with the data from the fatigue tests. Based on these fatigue curves, the life estimate,

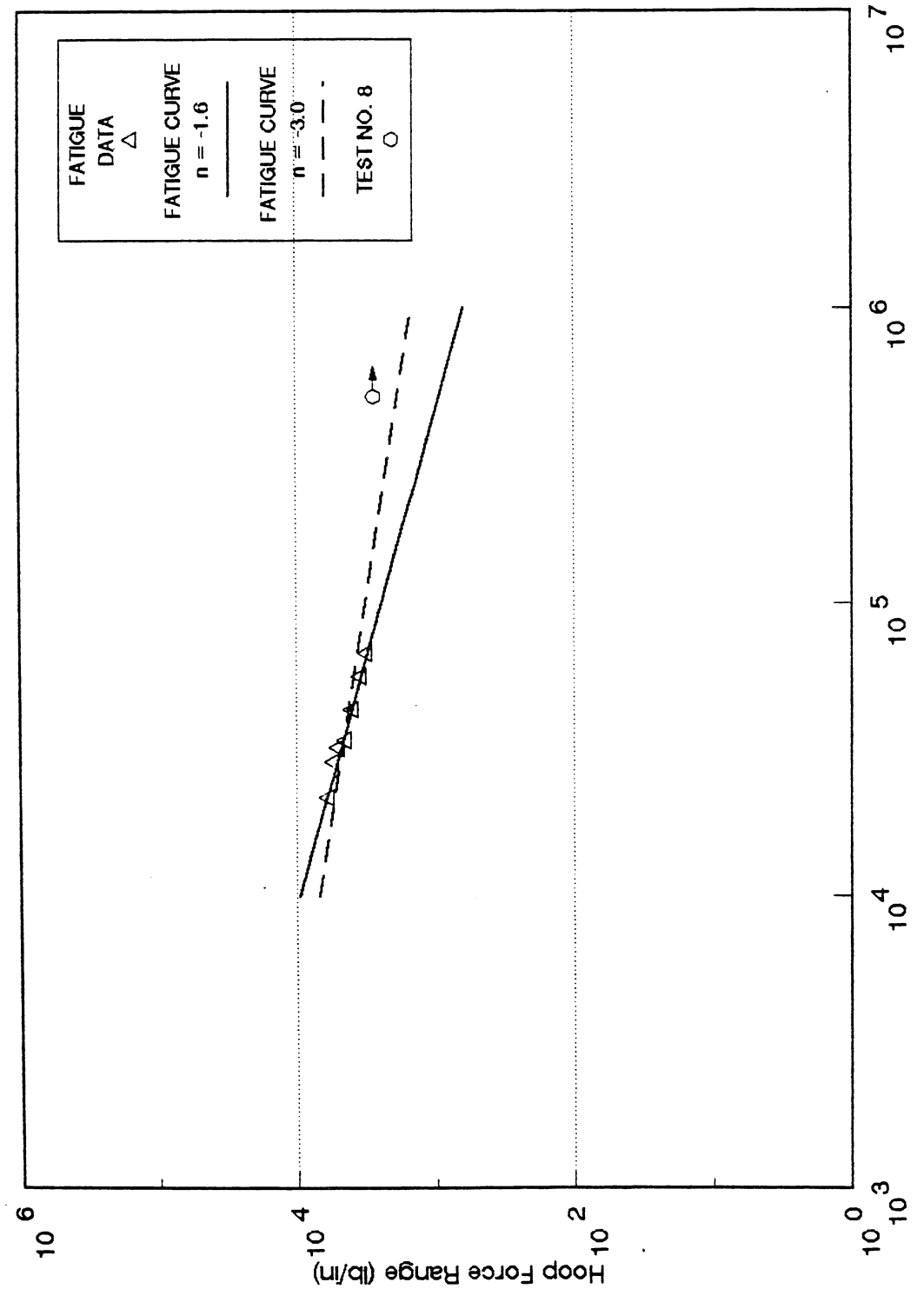

Fig. 6.2a Fatigue curves with different exponents

considering the lakeside data to be more representative, varies from 3.3 years to 49.5 years. The life estimates were calculated at the most critical location on the breakwater, location 15.

In order to gain a perspective on the life estimates, another format for the damage is considered. Figures 6.3 and 6.4 show the damage estimate as a function of the location along the vertical profile of the structure. These data are based on the fatigue curve with an exponent of 1.68. Based on damage estimates, the most susceptible on the breakwater are locations 14 and 15. Figures 6.5 and 6.6 illustrate the damage for the various wave directions on the lake and harbor side, respectively.

From the wave data shown in Table 5.1, the directions that have a greater probability of occurrence are SW, WSW, and SSW. The sea states with larger wave heights can be identified as NNE, NE, ENE, and N. The predominant directions of damage accumulation are SW, WSW, WNW, and NNE. Damage accumulation for a particular sea state is a combination of the number of waves and the equivalent force ranges. The damage accumulation for a direction is the result of the aggregate damage for constituent sea states. No simple correlation can be made between the probability of occurrence of a wave direction and the evaluated damage.

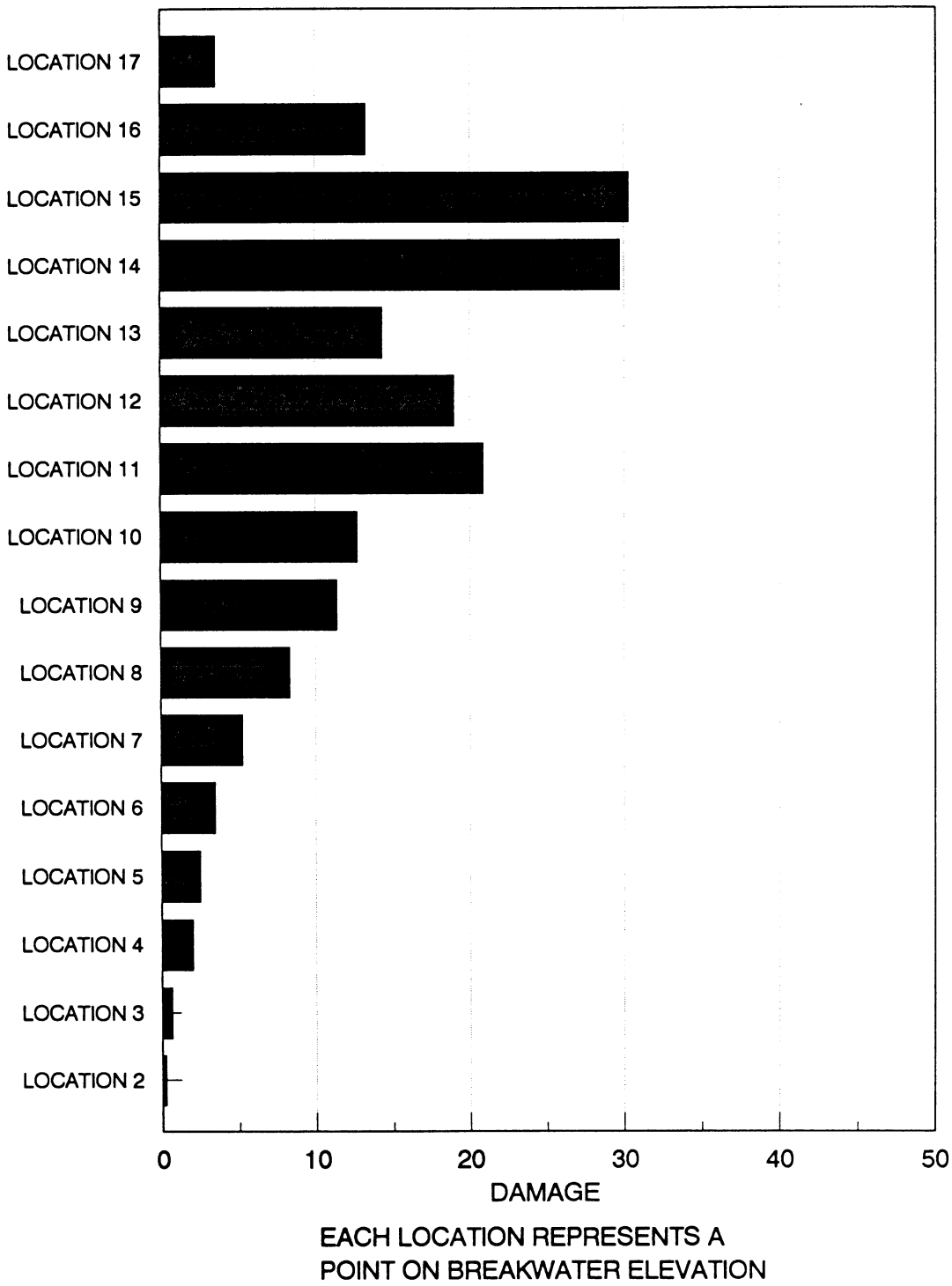

Fig. 6.3 Estimate of damage along the breakwater elevatio (Lake-side)

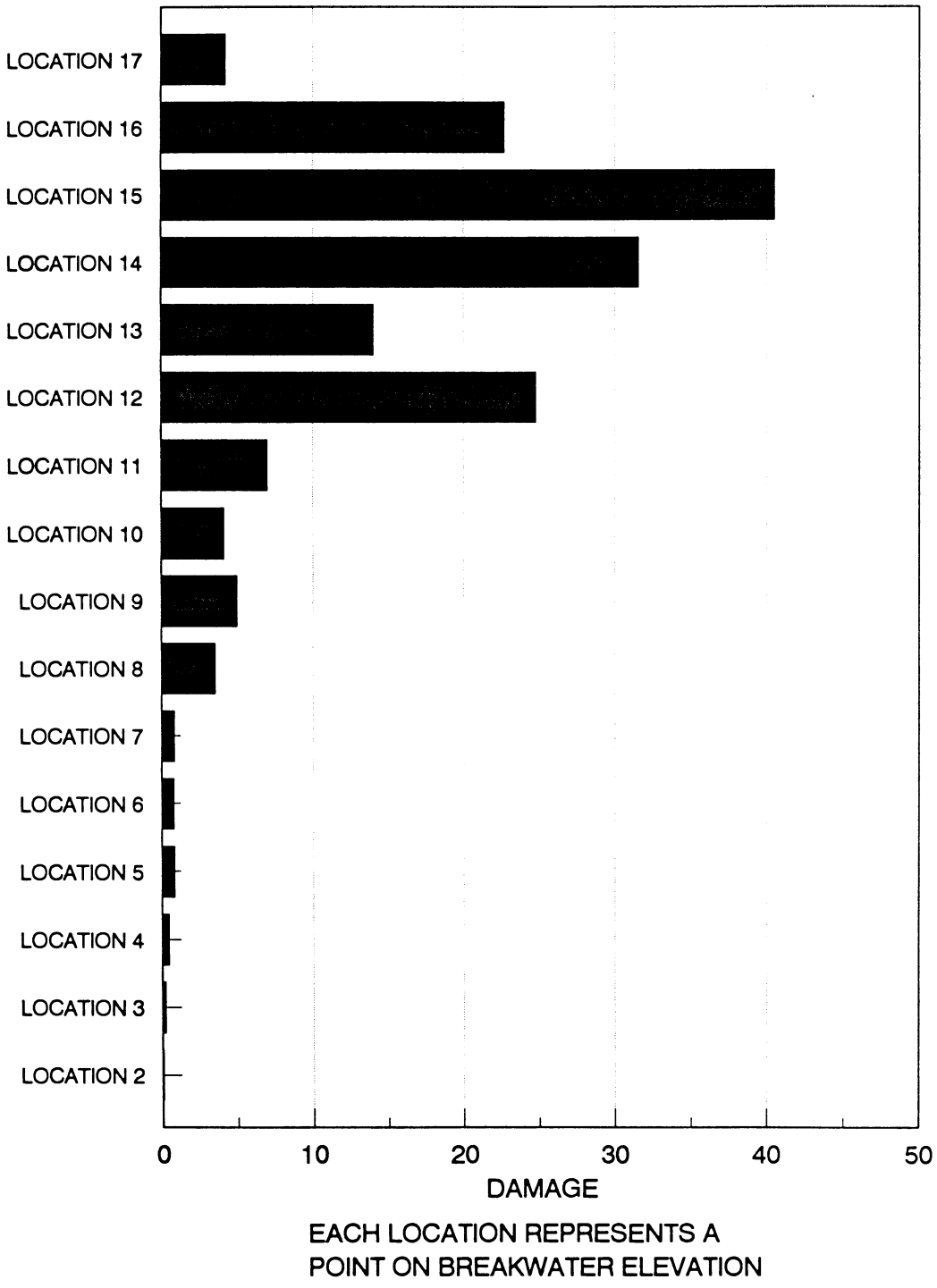

Fig. 6.4 Estimate of damage along the breakwater elevatio (Harbor-side)

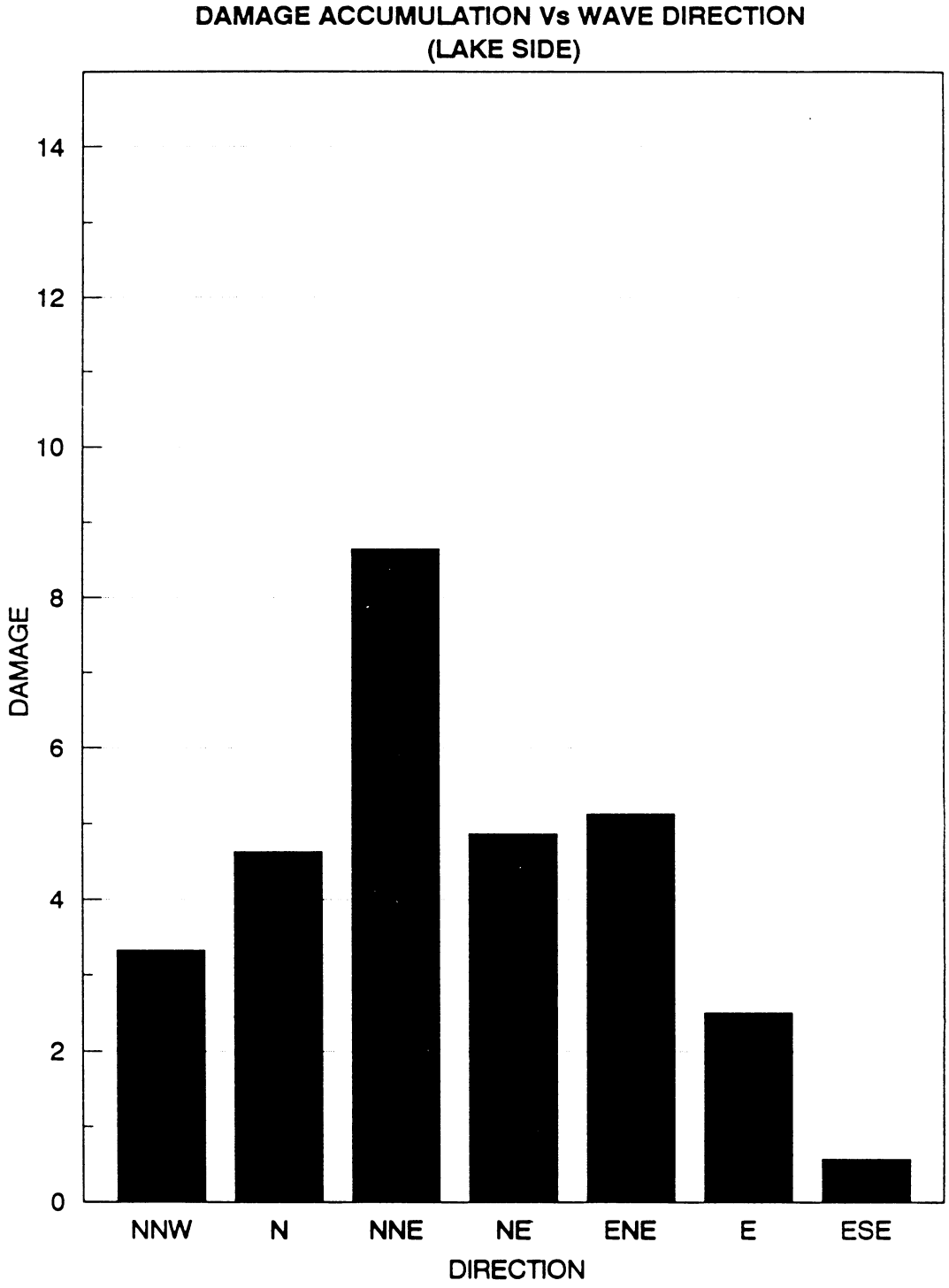

Fig. 6.5 Variation of damage estimate with direction at location 15 (Lake-side)

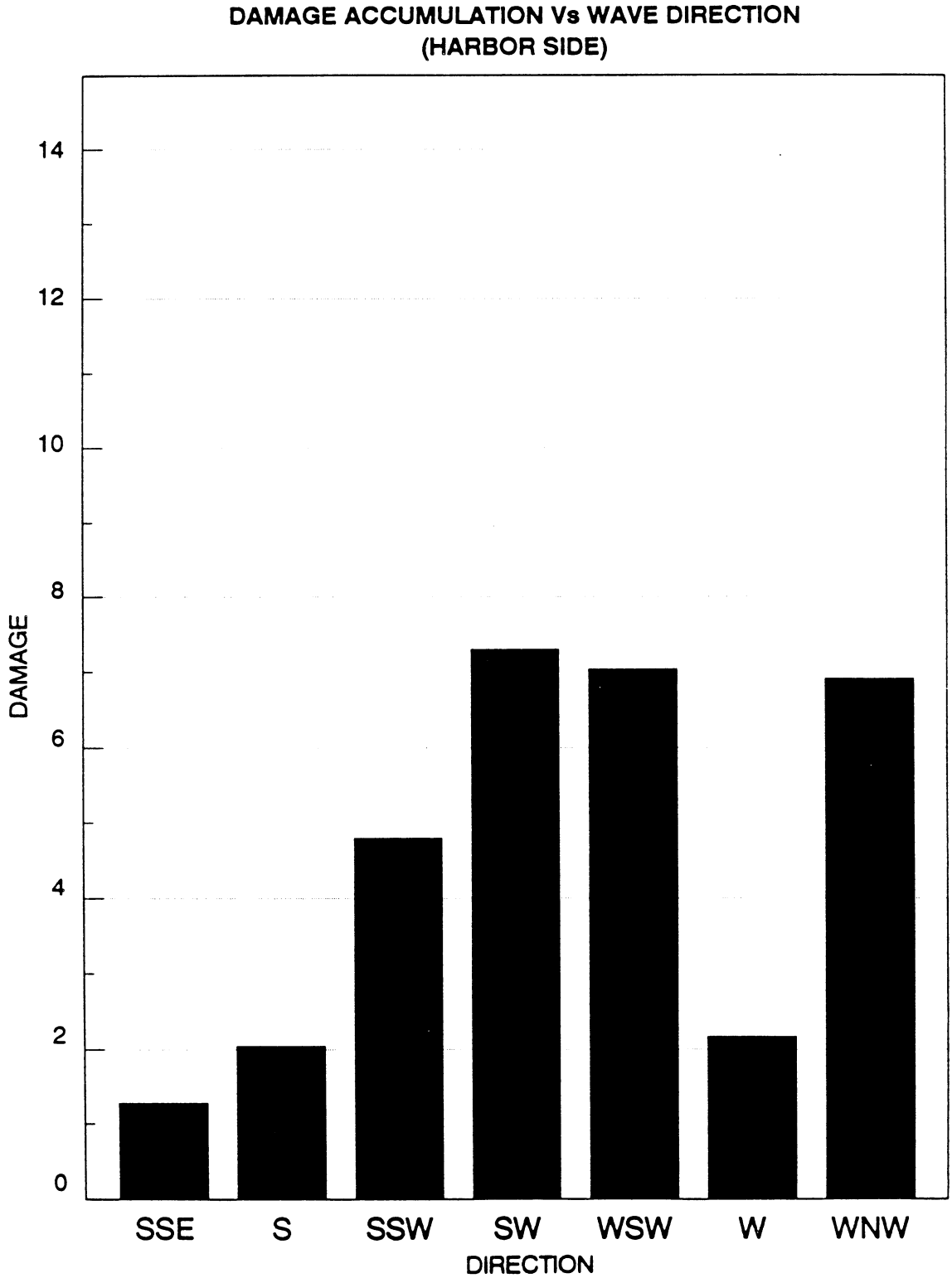

Fig. 6.6 Variation of damage estimate with direction at location 15 (Harbor-side)

6.4 Limitations in Analysis

The previous analysis suggests that the remaining structure life is dependent on and sensitive to a number of variables. The following discussion provides an assessment of the limitations on the analysis for each of the four major areas of the study.

6.4.1 Force Field Estimation

1. Burns Harbor data was considered representative of the wave climate at the Calumet Harbor.
2. The effects of wave diffraction on the wave force prediction were considered insignificant.
3. A weighted regression analysis of the bivariate histograms was used to arrive at the relationship between the wave height and the associated period in a specific direction.

6.4.2 Finite Element Model

1. The material properties for the soil media are considered to be representative of the site conditions.
2. A two-dimensional model was considered to represent the three-dimensional soil/structure interaction. The three dimensional behavior was represented by linear springs.

6.4.3 Fatigue Tests

1. A relatively small sample size was considered for determining the fatigue curve.
2. The effect of internal forces due to the saturated fill was not considered.

6.4.4 Damage Evaluation

1. Cumulative damage evaluation is dependent on the loading sequence. Representation of the varied loading within a sea state with single sinusoidal loading is conservative.
2. Consideration of the linear damage rule for evaluation of fatigue life is conservative.

6.5 Rehabilitation Alternatives

The previous discussion of damage evaluation indicates that the structure is in imminent danger of failing. An exact prediction of when an actual failure event may occur is difficult because the return period for the most severe loading on the structure is unknown. The most probable prediction is that the failure can be expected during the next severe storm. In order to rehabilitate the structure, two alternatives may be considered. One is to convert the whole structure into a rubble mound. The other alternative is repair the structure as it deteriorates. The drawback with the second alternative is that the extent of the next failure is unknown.

7. SUMMARY, CONCLUSIONS AND RECOMMENDATIONS

7.1 Summary

The intent of this research project was to investigate the structural failure of the Calumet Harbor Breakwater. Likely failure mode of previous and future failures are predicted. To accomplish these objectives, four major areas of effort were identified and investigated.

The structure was instrumented during two winters, 1988 - 89 and 1989 - 90. During both attempts, the structure was monitored by strain gauges and a pressure transducer. The data were collected by data acquisition systems. Communication systems were installed to initiate the data monitoring process and communicate the recorded data on shore. A computer was used to control all the systems and collect the recorded data. The data in the 1988 - 89 operations were used to obtain a qualitative analyis of the behavior of the structure. The data collected in 1989 - 90 operations were used to validate the finite element model.

A two-dimensional vertical slice model of the breakwater structure with the assumption of plane strain conditions was prepared. The Drucker - Prager plastic material model was used for the fill and foundation materials. The model was used to determine the stresses in sheet piles under the wave loads. Comparison of the finite element analysis with the classical methods of analysis

shows that the finite element model gives lower maximum pressure and total relative pressure over the classical computational methods. Peak and trough conditions of different waves were analyzed for a total of 156 cases.

The wave forces on the structure were evaluated through two subtasks: statistical analysis of waves and deterministic evaluation of the forces. The hindcast data at the Burns Harbor site was assumed to represent the wave climate at the site. The statistical analysis yielded bivariate histograms of wave height versus wave period for different directions and probabilities of occurrence. A relationship between wave height and wave period was achieved by weighted regression analysis of the data in a bivariate histogram, for each of the directions separated by 22.5°. These relationships were used to generate wave heights and corresponding periods for use in deterministic evaluation of forces. The forces applied at nodes of the finite element model were evaluated by the classical theories such as Stokes' theory, cnoidal theory, and standing wave theory to generate the wave pressures.

Eight fatigue tests were performed at ISU to determine a fatigue curve for steel sheetpile specimens. In addition to the fatigue tests, diagnostic tests were conducted to help understand and interpret behavior of the strain gauges in the instrumentation phase.

The finite element results were post-processed to yield the hoop-force ranges between the peak and trough parts of different waves. Third-order curves were fit through the post-processed data to relate wave heights and hoop force ranges. A total of 238 such curves were generated.

The evaluation of damage and design life of the structure was made using the approach developed by Williams and Rinne (8) and Hambly et.al (9). This approach, called the equivalent damage approach, makes use of Miner's rule. The post-processed data were analyzed further to evaluate the critical failure zones on the structure.

7.2 Conclusions

Based on this study, the following may be concluded:

1. The failure of sheetpile specimens from repeated loadings occurred at stress ranges between 3100 lb/in. and 5900 lb/in., which are considerably below the static strength of 10,000 lb/in. reported by others.
2. The mode of failure is the formation of fatigue crack in the sheet pile on the arch at a distance of 4.75 in. to 5.75 in. from the center line of the web and not at the interlock.
3. Three different zones for potential crack growth can be identified. The first two zones are locations 9,10, and 11 and locations 14 and 15,

which are 28 ft to 32 ft from the bed of the breakwater. In addition, crack growth at the top of the cell wall caused by extraneous effects such as pile driving, hoop forces, and the cantilever effect could have a significant influence on the failure.

4. The damage evaluation and service life prediction of the structure are difficult to quantify exactly, because they are dependent on many factors. However, assuming the linear damage rule of Miner (7) and that the exponent of a steel sheetpile fatigue curve is similar to that of structural steel details, which is around 3, the design life of the structure may be predicted at 49 years.
5. A probability cannot be attributed to the occurrence of the next failure. Two alternatives are suggested for rehabilitation of the structure. The first alternative is to convert the entire structure into a rubble mound structure. The other method is to convert the structure into a rubble mound incrementally as it deteriorates.

7.3 Recommendations for Further study

Several areas need further investigation related to this study, including

1. Additional monitoring of the structure, including remote video data to improve correlation between loading and response of the structure. The effect of ice loads should be considered for analysis; the video data will be useful for this process. The data acquired during a large storm event will be useful for validating the finite element model.
2. Better hindcast data for the wave climate at the Calumet harbor, for gaining a better understanding of the behavior of the structure.
3. Extreme loading of the structure due to other reasons such as temperature, for a better understanding of the long-term effects.
4. A larger number of fatigue tests to predict a more representative fatigue curve for steel sheetpile specimens.
5. A three-dimensional finite element model that would allow the behavior of the structure to be better understood.
6. An investigation into the post failure analysis to determine the failure mechanisms after the initial failure. In addition, an investigation into crack propagation from location to location by using further refinement in the model and additional elements, to simulate the crack initiation and

propagation environment, will be useful. The analysis of failed samples at site would aid in determining the mode of failure of the structure.

8. REFERENCES

1. U.S. Army Corps of Engineers, Chicago District. Reconnaisance Report, Major Rehabilitation, Calumet Harbor Breakwater, Illinois. Chicago: U.S. Army Corps of Engineers, 1986.
2. J. Gaythwaite. The Marine Environment and Structural Design. New York: Van Nostrand Reinhold Co., 1981.
3. M. Rossow, E. Demsky and R. Mosher. Theoretical Manual for Design Cellular Sheet Pile Structures. Washington D.C.: U.S. Army Corps of Engineers, 1987
4. G.W. Clough and T. Kuppuswamy. "Finite Element Analysis of Lock and Dam 26 Coffer Dam." Journal of Geotechnical Engineering, Vol III, No. 4, April, 1985.
5. G.J. DeSalvo and J.A. Swanson. ANSYS Engineering Analysis System - User Manuals I and II, Theoretical Manual and Examples Manual. Houston, Pa., Swanson Analysis Systems Inc., 1985.
6. Statistical Analysis System - Introductory Manual, Users Manual and Applications Manual. Cary, N.C., S.A.S. Institute, 1984.
7. M.A. Miner. "Cumulative Damage in Fatigue." Journal of Applied Mechanics. 12, A 159 - A 164, 1945.

8. A.K. Williams and J.E. Rinne. "Fatigue Analysis of Steel Offshore Structures." Proceedings of the Institution of Civil Engineers, London. 60 (1), 149 - 152, 1976.

9. E.C. Hambly. et al. "Fatigue Considerations For Ocean Towage." Proceedings of the Offshore Technology Conference. Paper OTC - 4163, 1981.

10. J.F. Wilson, Editor. Dynamics of Offshore Structures. New York: John Wiley & Sons., 1984

11. R.M. Sorenson. Basic Coastal Engineering. New York: John Wiley & Sons., 1978

12. T. Sarpakaya and M. Isaacson. Mechanics of Wave Forces On Offshore Structures. New York: Van Nostrand Reinhold Co., 1981.

13. U.S. Army Corps of Engineers, Waterways Experiment Station, Vicksburg. Shore Protection Manual, Volumes I and II. Washington D.C.: U.S. Army Corps of Engineers, 1984

14. P. Aruliah. "Fatigue Durability Under Wave Action." Proceedings of the Institution of Civil Engineers, London. 60, 635 - 654, 1976.

15. K. Terzaghi. "Stability and Stiffness of Cellular Coffer Dams." A.S.C.E. transactions, Paper No. 2253. September, 1944.

16. Steel Sheet Piling Hand Book. Chicago: U.S. Steel, 1979

17. Cole and Hilfiker. Wave Statistics for Lake Michigan, Huron and Superior. Detroit: U.S. Army Corps of Engineers, Detroit District, 1970.

18. B. Le Mehaute. An Introduction to Hydrodynamics and Water Waves. New York: Springer - Verlag, 1976.

19. J.W. Fisher. Fatigue and Fracture in Steel Bridges, Case Studies. New York: John Wiley & Sons, 1984.

20. T.J. Wipf, L.F. Greimann, R.K. Challa, D.L. Wood. "Status of Experimental Phase of Calumet Harbor Breakwater Study." C.C.E. Dept., I.S.U., 1989 (unpublished)

21. U.S. Army Corps of Engineers, Chicago District. General Design Memorandum and Environmental Assessment - Major Rehabilitation. Chicago: U.S. Army Corps of Engineers, 1988.

Acknowledgements

The study presented in this report was sponsored by the Corps of Engineers, Chicago District, Chicago through the Construction Engineering Research Laboratory (CERL), Urbana.

I wish to record my deep appreciation to Dr. Terry J. Wipf for his supervision, guidance, encouragement and support throughout the research and in writing of thesis. I wish to express my appreciation to Dr. Lowell Greimann for his guidance in research and for serving as my co-major professor. I would like to express my appreciation towards my colleague and friend Mr. Sadik Bakir for his contribution to the project. I am appreciative of the help I received from Mr. Douglas Wood, Structural Lab Supervisor during instrumentation and laboratory testing phases of the project. I wish to thank the undergraduate student Mr. Jonathan Lutz who contributed significantly in the Laboratory work and on site.

I would like to thank Dr. Frederick Graham for serving on my committee. I would like to thank Dr. Anthony Kao of CERL and Mr. Jim Przewoznik of the Corps of Engineers for their help during the course of the project. There were a lot of individuals whose help I solicited during the progress of my research especially Mr. Ken Gibbons of Campbell Scientific Inc. and personnel of the Calumet Harbor Coast guard station at Chicago. I am appreciative of their help. I am thankful to my parents, family and friends for their guidance and support throughout my career. Finally, I would like express my gratitude to the almighty.

APPENDIX A.

A.1 Field Instrumentation - Phase II Operations

The schematic diagram for installation of instrumentation is indicated in Fig. 2.1. The following describes the major components of the monitoring system.

A.1.1 Strain Gauges:

The 13 strain gauges installed at the site were full-bridge weldable strain gauges, which were chosen over the conventional quarterbridge configuration because of reduced cable length errors and better noise characteristics. In addition, these strain gauges exhibit excellent behavior in harsh environments. When used in Phase I operations, they were found to have good service life. Figures A.1 to A.4 exhibit the sequence of installation. Figures A.1 and A.2 indicate the gauges after they have been tack welded to the prepared surface of the pile sections. Figure A.2 indicates the first of the three protective covers applied to the gauges. The epoxy coating acts as a moisture barrier to eliminate possible corrosion damage to the tack weld. A second barrier is provided by a steel angle section placed directly over the epoxy covered gauge. Figure A.4 indicates the welding of the angle. The strain gauges, which are installed underwater, were first tackwelded to a plate 3 in. wide by 5 in. in depth. An angle section 5 in. by 5 in. is welded to the plate so that it acts as a barrier to the

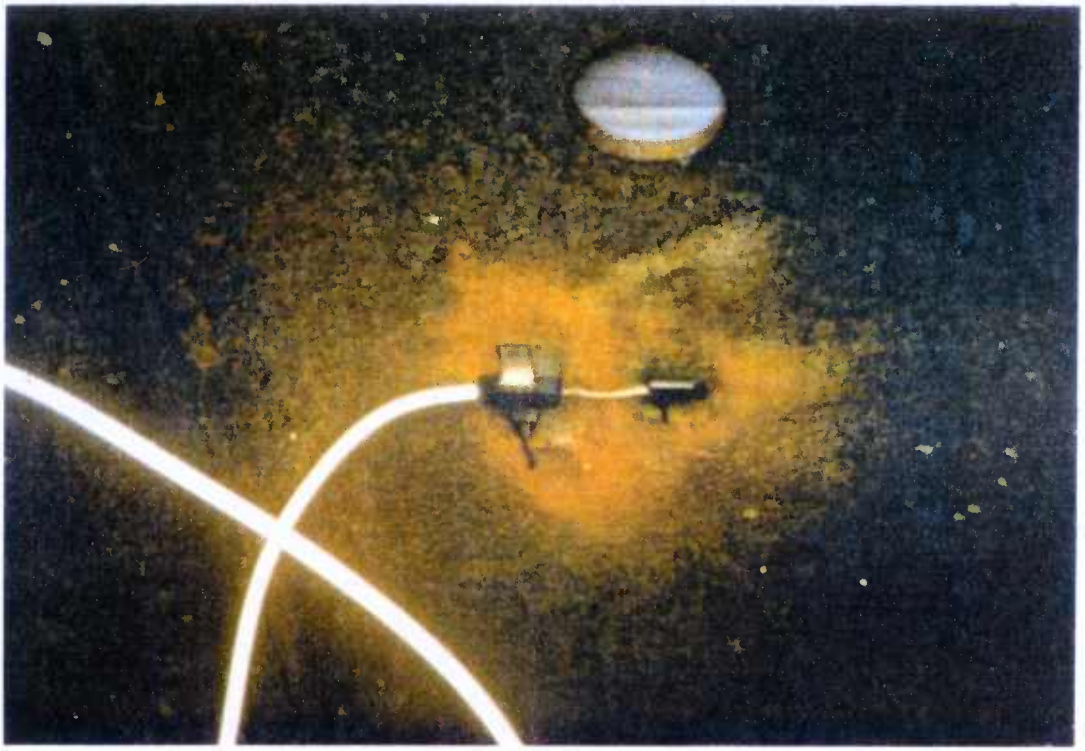

Fig. A.1. Tack welded strain gauge after installation

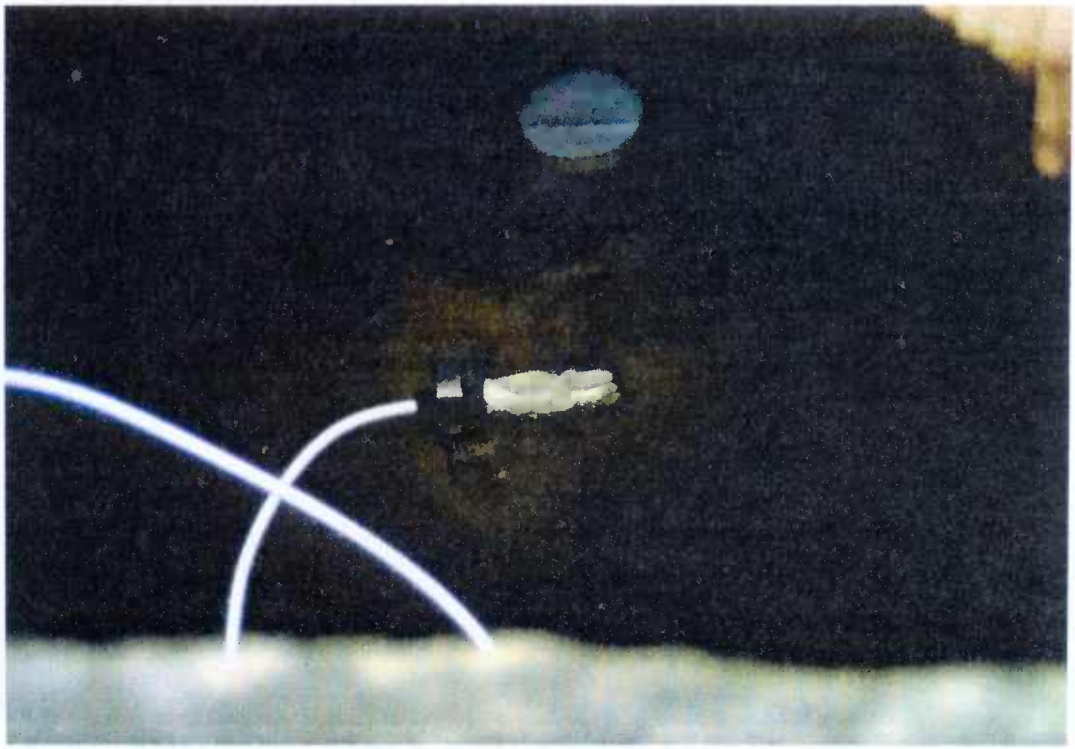

Fig. A.2. Strain gauges covered with epoxy putty

Fig. A.3. Welder preparing to weld protective angle barriers

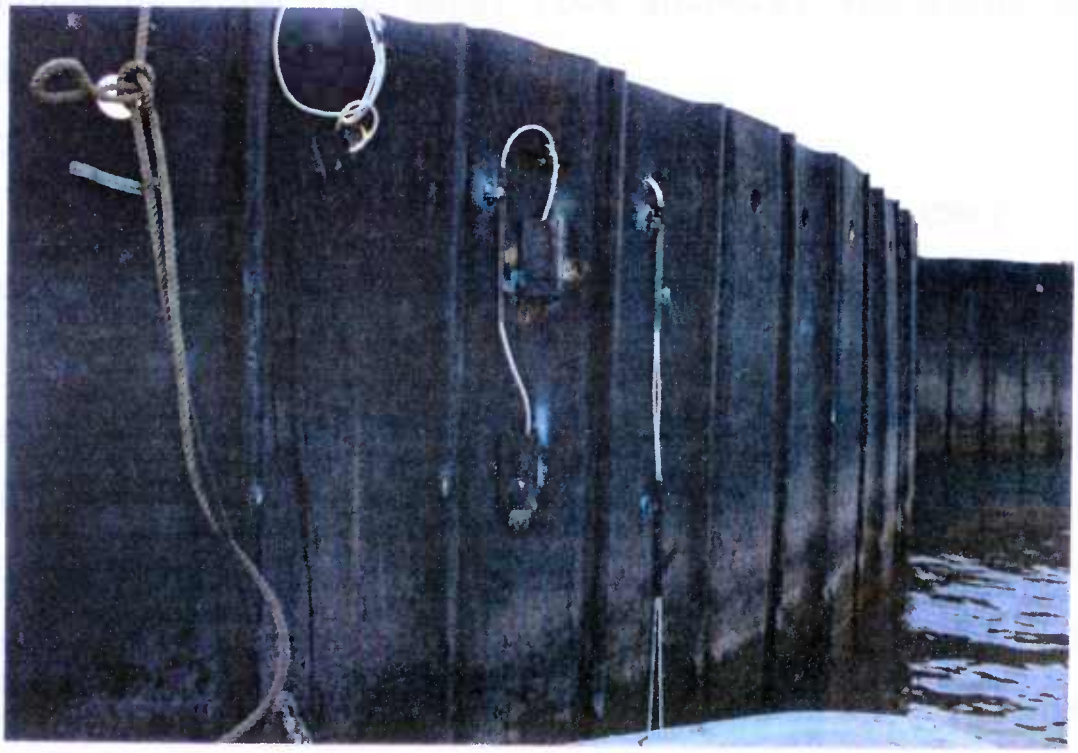

Fig. A.4. Angle barriers welded to strain gauges 2 and 4

strain gauges. This whole assembly is welded underwater to the pile section.

A.1.2 Pressure Transducer:

The pressure transducer used is a Druck PDCR-830 type with a pressure range of 10 psi and a supply voltage of 10 volts. The transducer measures the head of water as the wave contacts the monitored sheetpile cell. The capillary tubing from the pressure transducer was kept in a dry condition by isolating the end in a bottle of dendrite.

The sheathed cables with protective armor in the network from the strain gauges and the pressure transducer were each 125 ft. long. These were clamped to the concrete capstones by plastic clamps, rock anchors, and structural steel angles.

A.1.3 Data Acquisition System:

The data acquisition system consists of a CR-7 measurement and control module or a data logger. The CR-7 data acquisition system is a programmable data logger/controller installed in a small rugged box and is shown, in connected condition, in Fig. A.5. The data sampling rate was 0.30 sec; the sampling was done across 14 channels. The data logger is controlled by means of the base station micro-computer. It is generally quiescent until activated to start the data acquisition. The datalogger, acting on the instructions of a program in its

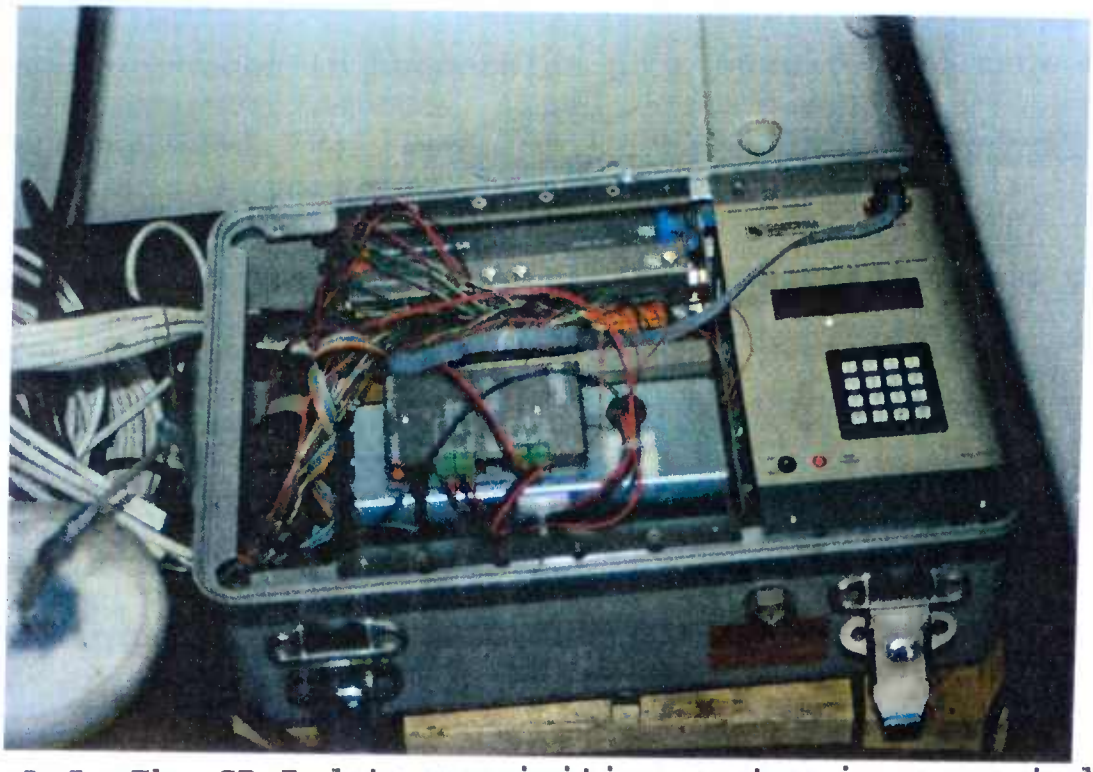

Fig. A.5. The CR-7 data acquisition system in connected state

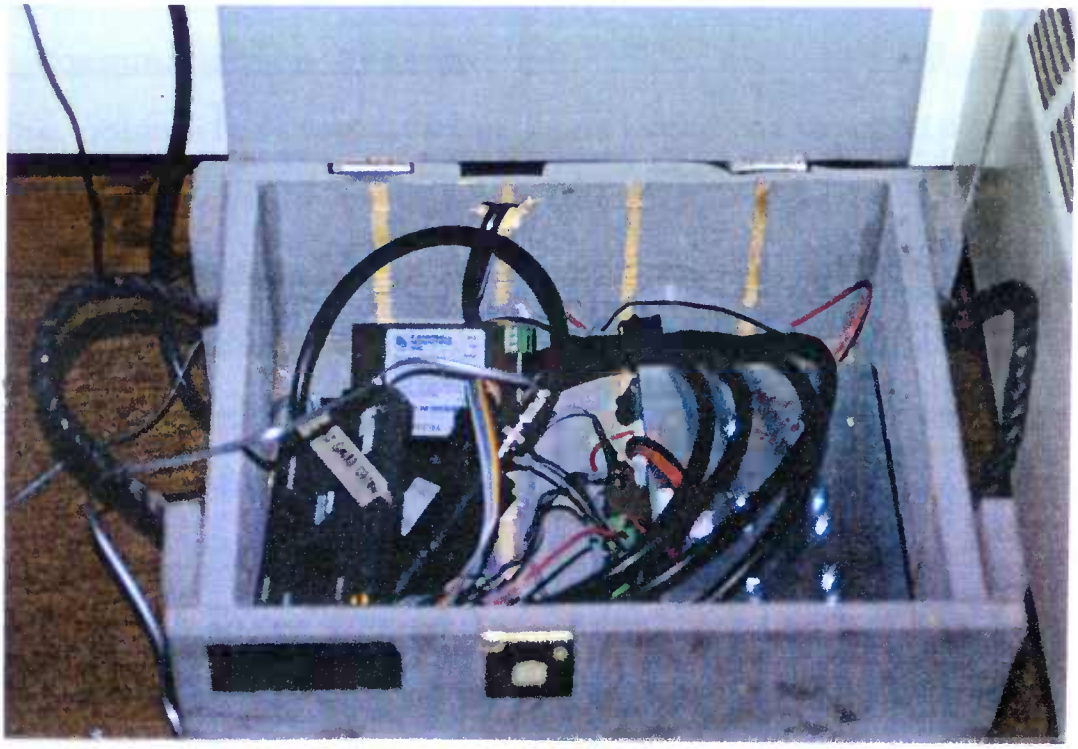

Fig. A.6 Substation in the coast guard station indicating the different components; the Hayes telephone modem, R.F. modem, UHF radio and the power source

internal memory, excites the strain gauges and then the pressure transducer in succession at a specific voltage and records the output voltage. The recorded output voltage is transformed into microstrains and feet of water using intermediate processing instructions. The strains and the pressures are stored for retrieval. The program also records the Julian day, real time at the start of the record, and elapsed time at sampling points starting at zero for the initial condition. The power supply to the data logger is primarily by the 110 v supply available at the lighthouse structure. This supply also float-charges lead acid batteries in the CR-7 that provide the power to the datalogger in case of a power failure.

A.1.4 Communication System:

The communication system consisted of a radio frequency (R.F.) network and a telephone network. The R.F. network of Motorola UHF radios with R.F. modems is interconnected by antennae and the telephone network by means of Hayes-compatible modems at the substation and the base station, which are connected in turn by the long-distance telephone lines. The radio frequency that is used for communications purposes is owned by ISU for the data logging period. Figures A.6, A.7 and A.8 show the different components. The communication protocol is controlled by means of the software installed in the computer at the base station.

Fig. A.7. Antenna at the Coast gaurd station, a link in the communication network

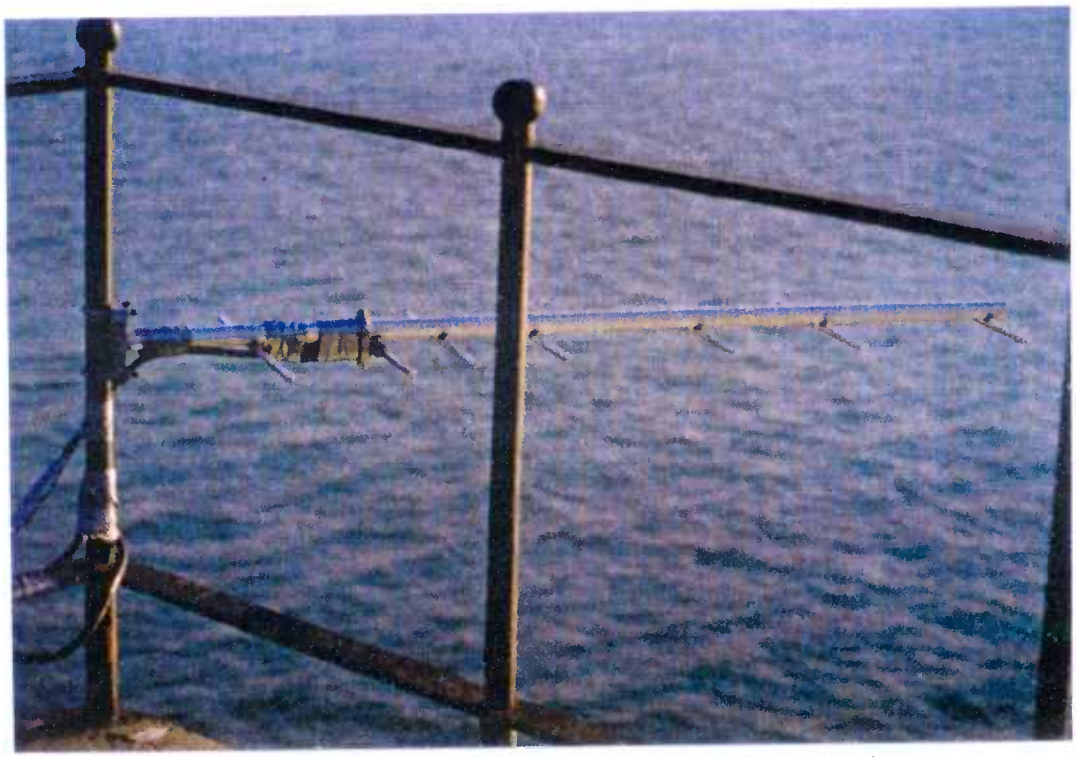

Fig. A.8. Antenna at the field station

A.1.5 Microcomputer:

The computer installed at the base station is an IBM compatible Zenith personal desktop computer. The computer is used to activate, program, control and retrieve the data from the data logger by means of the communications network.

Appendix. A.2 Recorded Data of Phase II Operations

The analysis of the data for different dates recorded during the Phase II operations is as shown in Chapter 6. The examples of recorded data for the examples illustrated along with the results, which were used to illustrate the different conclusions of the analysis, are shown in Tables 6.3 through 6.4. This section of Appendix A summarizes the results for the other cases. The maximum wave height indicated in the tables is the result of the transformation process described in Chapter 6, and the time at which it is computed from the CERC data corresponds to the time at which the strains are recorded.

A.3 Field Instrumentation - Phase I Operations

This part of Appendix A consists of the summary of a progress report sent to the sponsors in April 1989. The results of Phase I instrumentation and their analysis are included in Appendix A.3.

A.3.1 Preliminary Survey and Instrumentation:

The preliminary survey and inspection of Reach C of the Calumet Harbor breakwater structure were performed on October 11, 1988. The survey team inspected the facility to examine the modes of failure in the different cells of the structure. Locations were selected for placement of the instrumentation and a strategy selected for connection of instrumentation. The data acquisition system at the site, the method of data retrieval, and the microcomputer for recording the data were also designed. Figure A.9 shows a schematic of the instrumentation and data acquisition system at the substation (south end of breakwater) and the base station (Coast Guard Station at Calumet Harbor).

A.3.2 Instrumentation:

The instrumentation installed at the substation consisted of:

1. 5 strain gauges
2. 1 pressure transducer

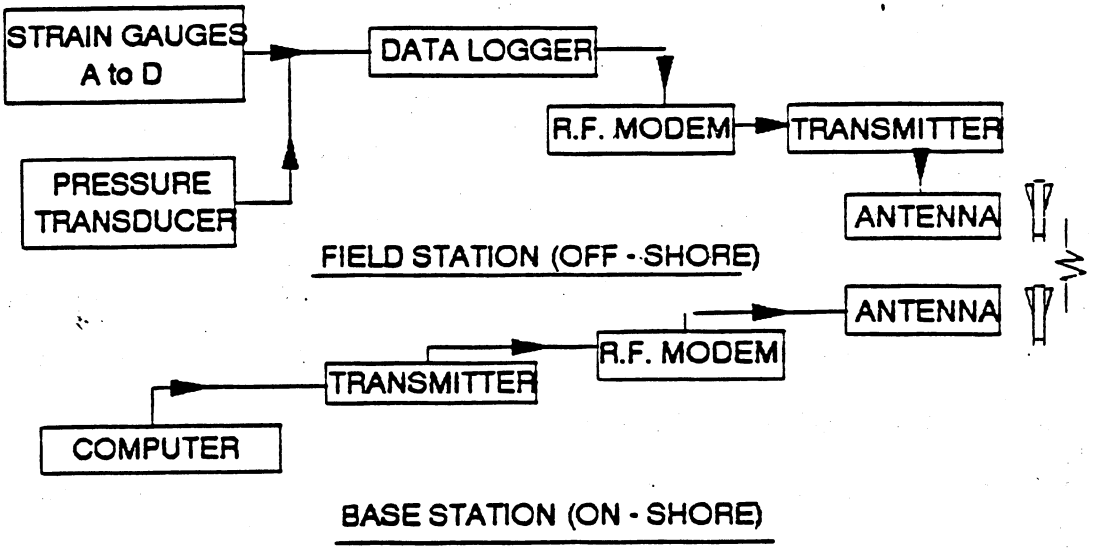

Fig. A.9 Schematic diagram for Phase I instrumentation and data acquisition system

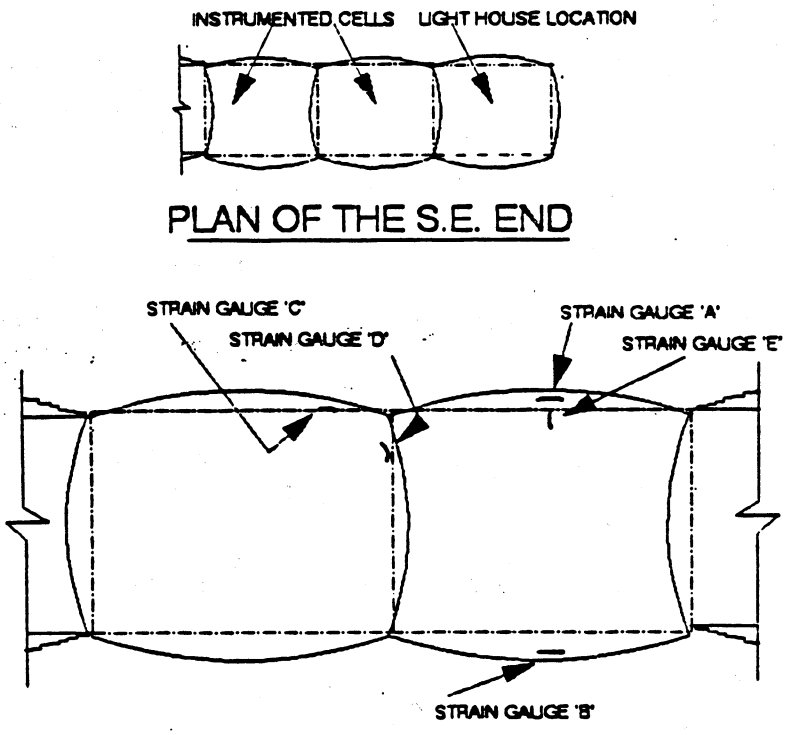

Fig. A.10 Location of strain gauges on the breakwater

3. A data acquisition system consisting of a programmable micrologger with a radio frequency link to a microcomputer located at the base station.

The instrumentation installed in the Phase I operation is similar to that used in Phase II operations. Because the strain gauges, pressure transducer, and communications system used were similar to Phase II, Appendix A.1 may be referred to for details regarding installation and operation of that equipment. Figure A.10 shows the location of the strain gauges on the breakwater. Figures A.11, A.12, and A.13 show the different stages in installation of the strain gauges used in monitoring the structure. The design of the data acquisition system was different from Phase I with respect to the micrologger used and operation of the system.

The CR-10 is a programmable data logger/controller installed in a small rugged box (see Fig. A.14). The data logger, as instructed by a program stored in its internal memory, excites the strain gauges and pressure transducer in succession at a specific voltage and records the output voltage. The recorded output voltage is transformed to microstrains and feet of water (for the pressure transducer) using the intermediate processing instructions. The recorded values of the strains and the pressures are stored in final storage of the data logger for eventual retrieval. In addition, the program records the Julian day, real time

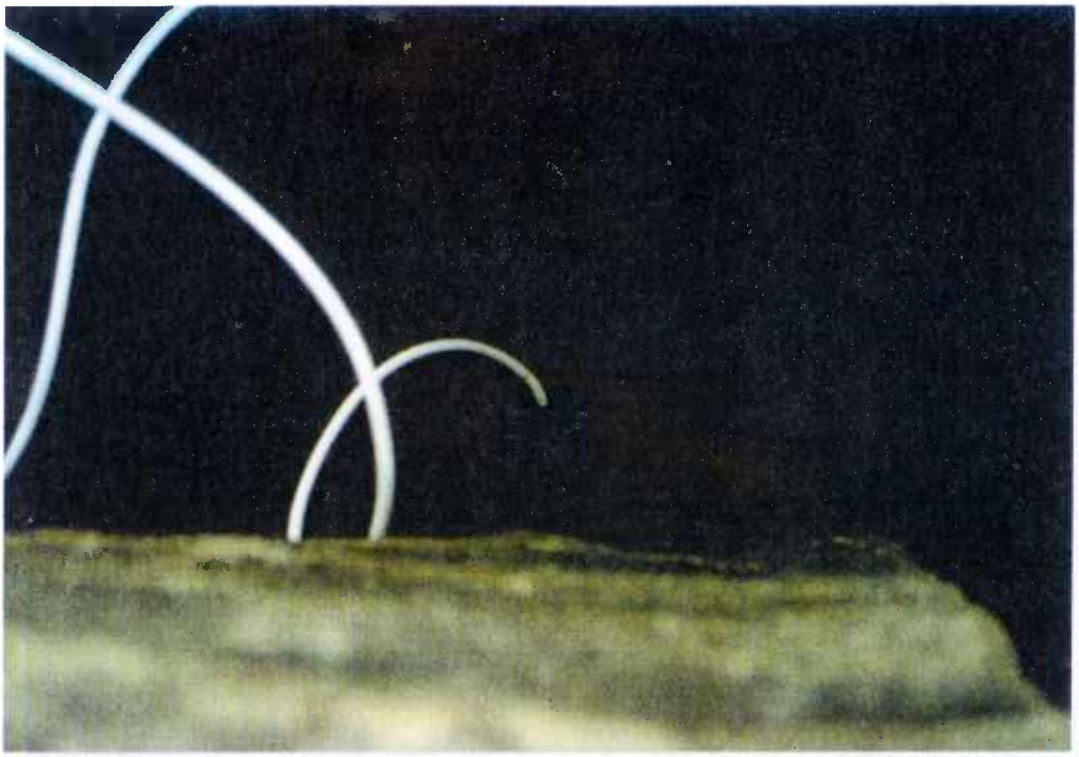

Fig. A.11. Installed flexure gauge tackwelded to the sheet pile structure

Fig. A.12. Protective PVC cover for the hoop strain gauge

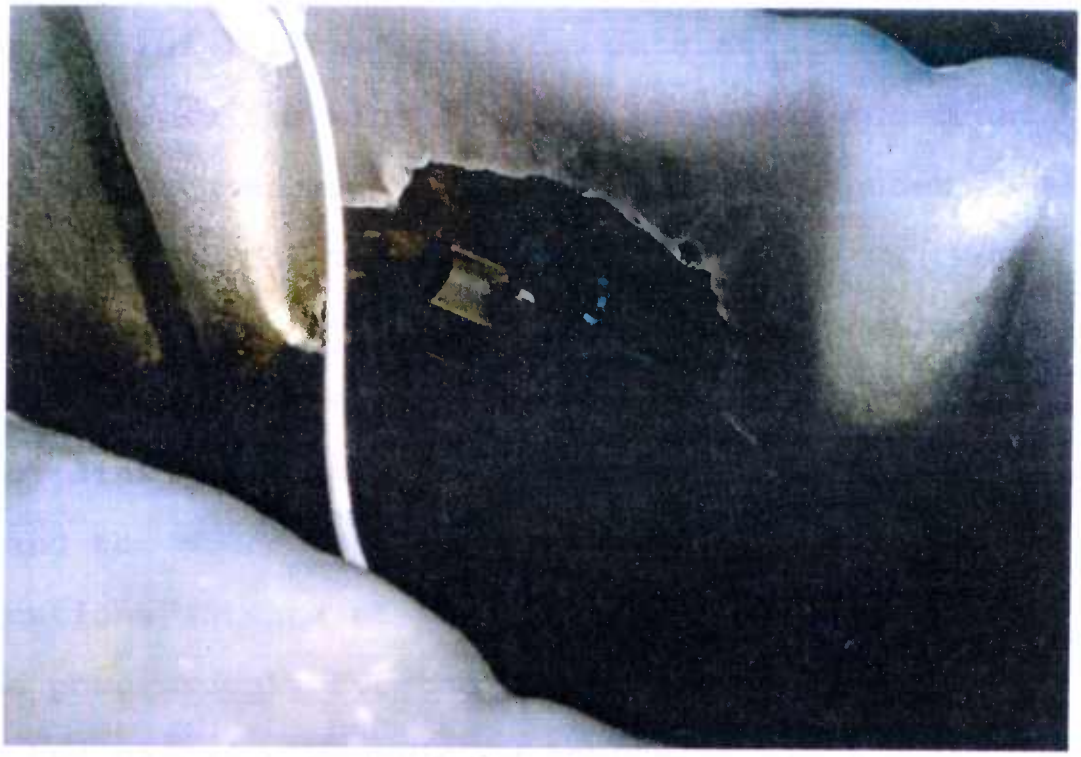

Fig. A.13. Protective steel angle cover over the hoop strain gauge

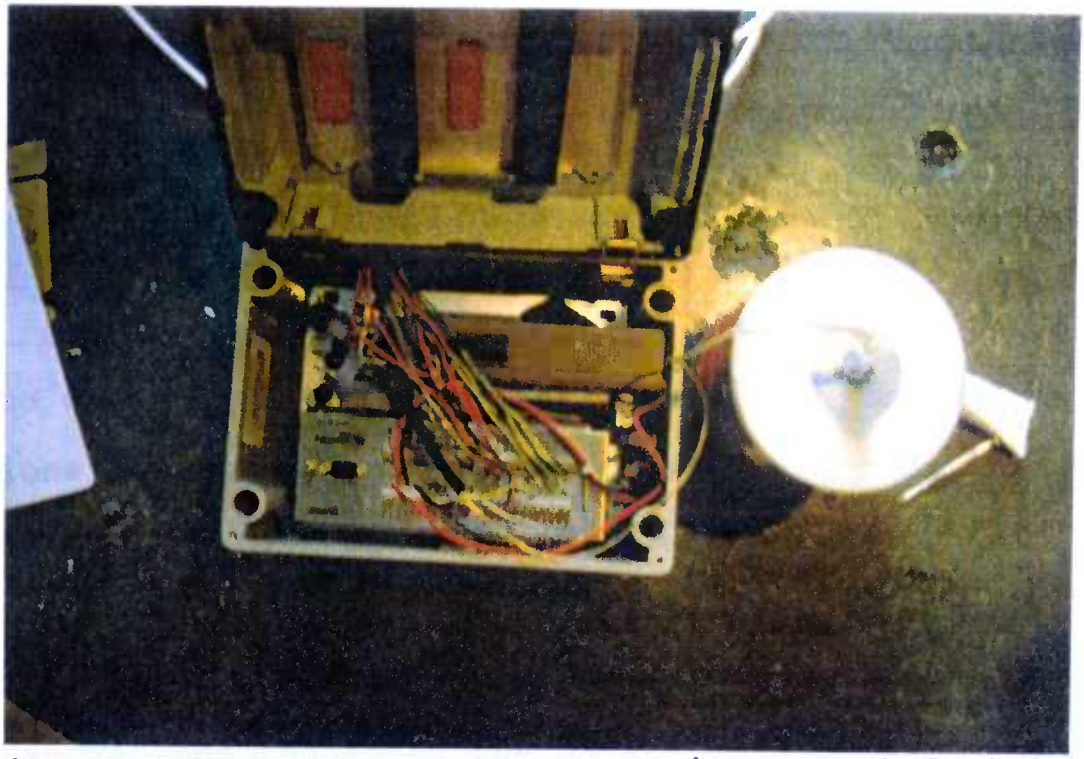

Fig. A.14. The CR-10 data logger in connected state

at the start of the record and real elapsed time starting at zero for the initial reading. The data acquisition system was controlled by the microcomputer housed in the Coast Guard Station at Calumet Harbor. The microcomputer is shown in Fig A.15. The Coast Guard personnel at the Calumet Harbor Coast Guard Station initiated the data collection activities by operating the microcomputer. A radio frequency link maintains the communication between the data logger and the microcomputer. Figure A.16 shows the communications antenna at the Coast Guard Station.

The power supply for the data logger is provided through two paths. The primary source is 110 V.A.C. power supply in the light house. In addition to powering the data logger, the supply also float-charges lead acid batteries in the CR-10. In case of power failure, the charged lead acid battery will provide power to the data logger.

A.4 Recorded Data of Phase I Operations

A.4.1 Introduction:

The experimental results for Phase I monitoring operations during winter and spring 1989 were submitted to the sponsors in the form of an interim report (20). In the report the data analysis, along with selected graphs illustrating the structural response, were provided, along with observations regarding the data. This part of the report summarizes the important conclusions regarding the

Fig. A.15. Installed microcomputer at the Coast guard station for recording the data

Fig. A.16 Installed communications antenna at the coast guard station

experimental data that are indicated in that report.

Section A.3 of this appendix documents the design of the data acquisition system and placement of gauges. Figure A.10 shows the location of Strain Gauges A, B, C, D, and E. The pressure transducer was placed near gauges A and E on the lake side of the cell.

The placement of the system began at the end of November 1988. The complete system contained numerous components and required multiple steps to complete successful installation.

The following summarizes the installation and validation process for the data acquisition system (DAS):

- End of November 1988 - system installation began
    - Transducers
    - Datalogger
    - Communications system at breakwater and base station
- Middle December 1988 - programmed system
    - Begin recording the data
- First of January 1989 - recorded data received by ISU for processing
    - data out of range for programming limits
- Third week of January 1989 - program limits corrected
    - Begin recording data February 2
- Middle of February to middle of March 1989 - various communication problems encountered

  - Problems corrected
- Middle of March 1989 to third week of April 1989 - data recorded on several days
- Third week of April 1989 - data acquisition system removed from field

The Calumet Harbor Coast Guard Station personnel and facilities near the breakwater were part of the communication system. They were instructed to communicate with the datalogger on the breakwater any time they observed waves approximately equal to or greater than 4 ft. After the system became operational again in March, storms causing waves of this magnitude seemed unlikely with the advancing spring season. Personnel were then instructed to communicate at any convenient times. As a result, data were taken during relatively minor wave activity.

A nondirectional wave gauge was placed in the Breakwater, Reach C, vicinity from Nov. 29, 1988, to Feb. 28, 1989, by the U.S. Army Engineers Coastal Engineering Research Center (CERC). The gauge provided records of the wave height and period of the free field waves. It was intended to provide wave data in the breakwater region to correlate with strain data measured at the structure. In addition, it would provide information that could be related to historical wave data for the region. As illustrated by the DAS installation summary above, strain and pressure

transducer data were obtained during January 1989, a period that corresponds with the CERC wave gauge data. These periods were January 13 at 15.30 hr, January 24 at 15.41 hr, and January 25 at 8.23 hr. However, problems with the program limits for the data logger made those data unusable.

The criteria by which the experiment was designed is emphasized as follows. A number of failure modes had been discussed by others (21) after review of previous Breakwater, Reach C failures. Swatek (21) concluded that inward and outward flexing of the piles (cantilever effect) above the cell fill was the primary cause of failure. This flexing caused flexural tearing to occur near or at a diaphragm, initiating at an existing crack. Although Swatek discussed interlock failure at the point of likely maximum interlock stress (at a lower elevation), his calculations discounted this bursting failure. Tearing near the diaphragm had occurred prior to the cell failures in 1984 and had been repaired in a number of locations.

Based on this information, ISU designed locations for measurements of pile strains. Given the time of the year (winter advancing), it was not feasible to locate gauges below water near theoretical locations of maximum interlock stress. The only feasible locations were near the top of the cell. To validate (or discount) the Swatek failure hypothesis, gauges were placed in two adjacent cells to

measure hoop strain effects at midcell (Gauge A and B), near a Y diaphragm connection (Gauge C), and on a diaphragm (Gauge D). In addition, a gauge was located near midcell to measure possible cantilever action (Gauge E).

A.4.2 Experimental Results:

Five strain gauges installed on the system (Fig. A.10) monitored the strains with respect to time. In addition, the pressure transducer provided a time history record. Four of the strain gauges measured strain in a hoop direction; the fifth measured flexural strain in a vertical direction. The pressure transducer was used to prove a "timing mark" for the time history records and monitor the time-varying head of water at site. A general overview of the recorded data is provided in Fig. A.17. A broken ordinate scale is used to allow the strain gauges and the pressure transducer to be plotted on the same graph. Two different ordinate scales are used; the pressure transducer records the data in terms of feet of water and the strain gauges in terms of microstrains. The abscissa represents 250 data points at 0.375 sec time increments representing 90 sec of real-time data. The strain values are referenced to the initial readings from Dec. 30, 1988, when the system was installed. The subsequent data can be considered relative to existing strains on this date. Gauges A-C register positive values and represent the net tensile changes since

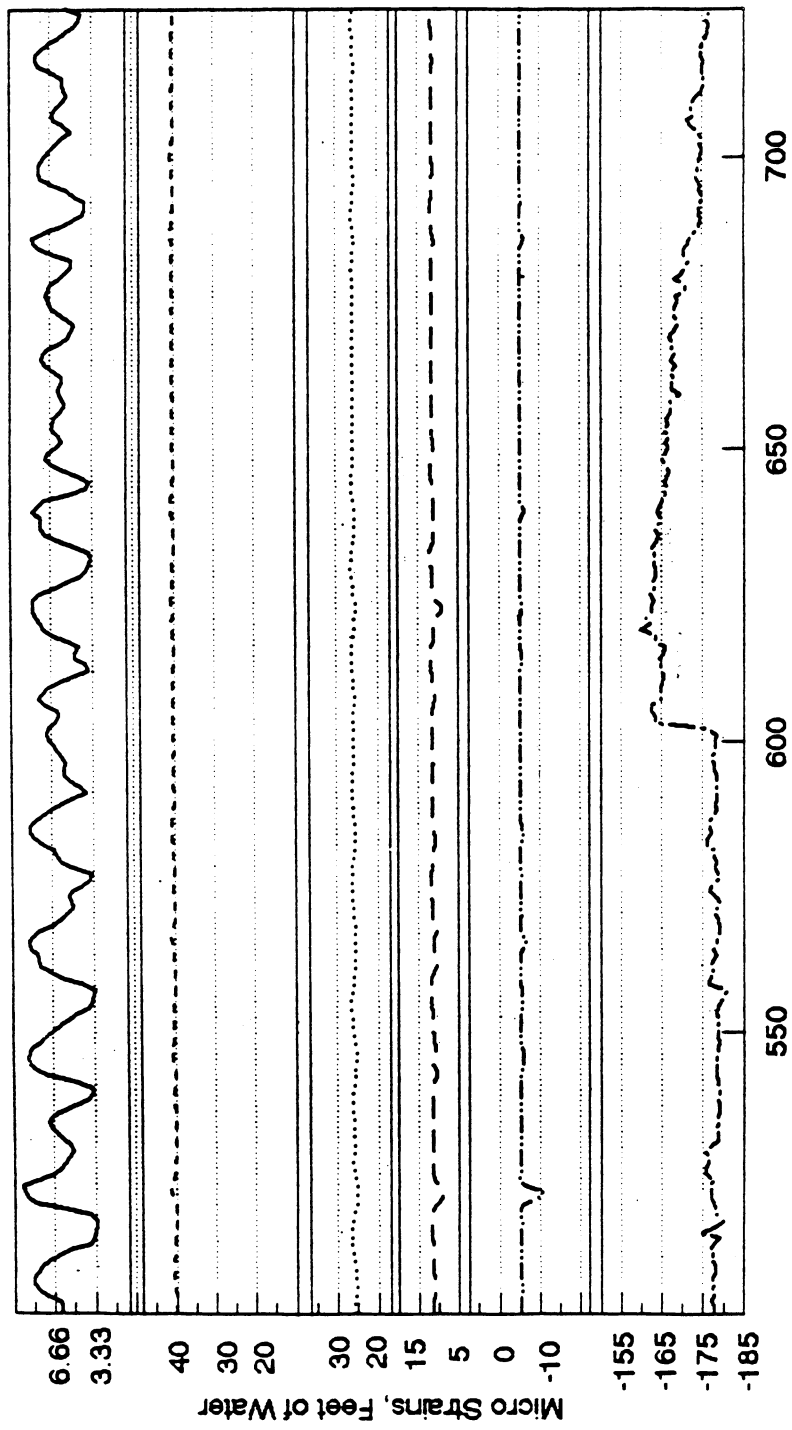

Fig. A.17 Typical variation of recorded pressure and strain values

December. Gauge D and E register negative values, suggesting net compressive changes since initialization.

A number of qualitative comparisons may be made from these plots. While output from the pressure gauge is not to be interpreted as an accurate measure of wave height, it does indicate the time of occurrence of the peaks and troughs of the waves. The frequency of occurrence may also be observed. It is interesting to compare the general response of each strain gauge (A-E) as the peaks and troughs of the wave readings occur. The records illustrated in Fig. A.17 are somewhat representative of the records obtained during the monitoring period, though the peak magnitudes in some cases may be larger. Strain gauge E records, however, are not necessarily as representative as the record shown in Fig. A.17. As shown, there is an obvious correlation between peaks and troughs in pressure gauge data and the strain data (at least for Gauges A-D).

Gauges A, B, C, and D are isolated for discussion as a group since they all refer to the measurement of strain in the circumferential (hoop) direction of the cell. In addition, the general response indicated by these gauges is similar throughout the monitoring period. Although there are some noticeable peaks in the strain data, the magnitudes are not great. However, the stability of the strain gauge readings over time and coincidence of strain and wave peaks

should also be noted. This observation gave considerable confidence that the instrumentation was stable and functioning properly and that the strain gauges are sensitive to the structural response.

Strain gauge E, which monitors the flexural response of the pile near midcell (cantilever action), behaved differently than Gauges A - D. Some periods indicated minimal strain activity, whereas other periods were more active and the output was much more random than the hoop gauge output. It was perhaps more indicative of wave - structure interaction.

The information that may be observed from the study of individual strain history records for different dates can be summarized as follows. The total length of each daily record as acquired by the data acquisition system spanned a period of approximately 10 1/2 min. Each record was subsequently reduced in the format of seven separate plots of 250 data points, or approximately 1 1/2 min.

Although direct correlation between wind records and wave activity for analysis was beyond the scope of this study, wind data were obtained and summarized. They provided qualitative information to assist interpretation of this preliminary data. A diagram illustrating the wind direction and speed is shown in Fig. A.18. The data were obtained from information from the weather log of the

Calumet Harbor Coast guard station, which was obtained from the National Climatic Data Center of the National Oceanic and Atmospheric Administration (NOAA), Asheville, North Carolina. The diagram indicates the general direction and speed of the wind during the recording events and approximately four hours prior. The diagram also quantifies the wind data in different zones for evaluation. The experimental observations have been divided into (1) fluctuating structural response and (2) mean structural response.

The fluctuating records (characterized by the changes in the daily record) provide information about the wave/structure interaction and subsequent structural response. The mean response referred to changes in output from one date to the next. Evaluation of mean data must consider a number of factors, including temperature, mean water level, and the like, which are not of primary interest in this study. However, in order to interpret the data accurately, these factors were considered. The data will be presented in a format based on the zone of predominant winds that acted on that date.

A.4.2.1 Assessment of Fluctuating Response:

The fluctuating response was primarily assessed by considering the different zones of incidence for the waves. The analysis is summarized as follows.

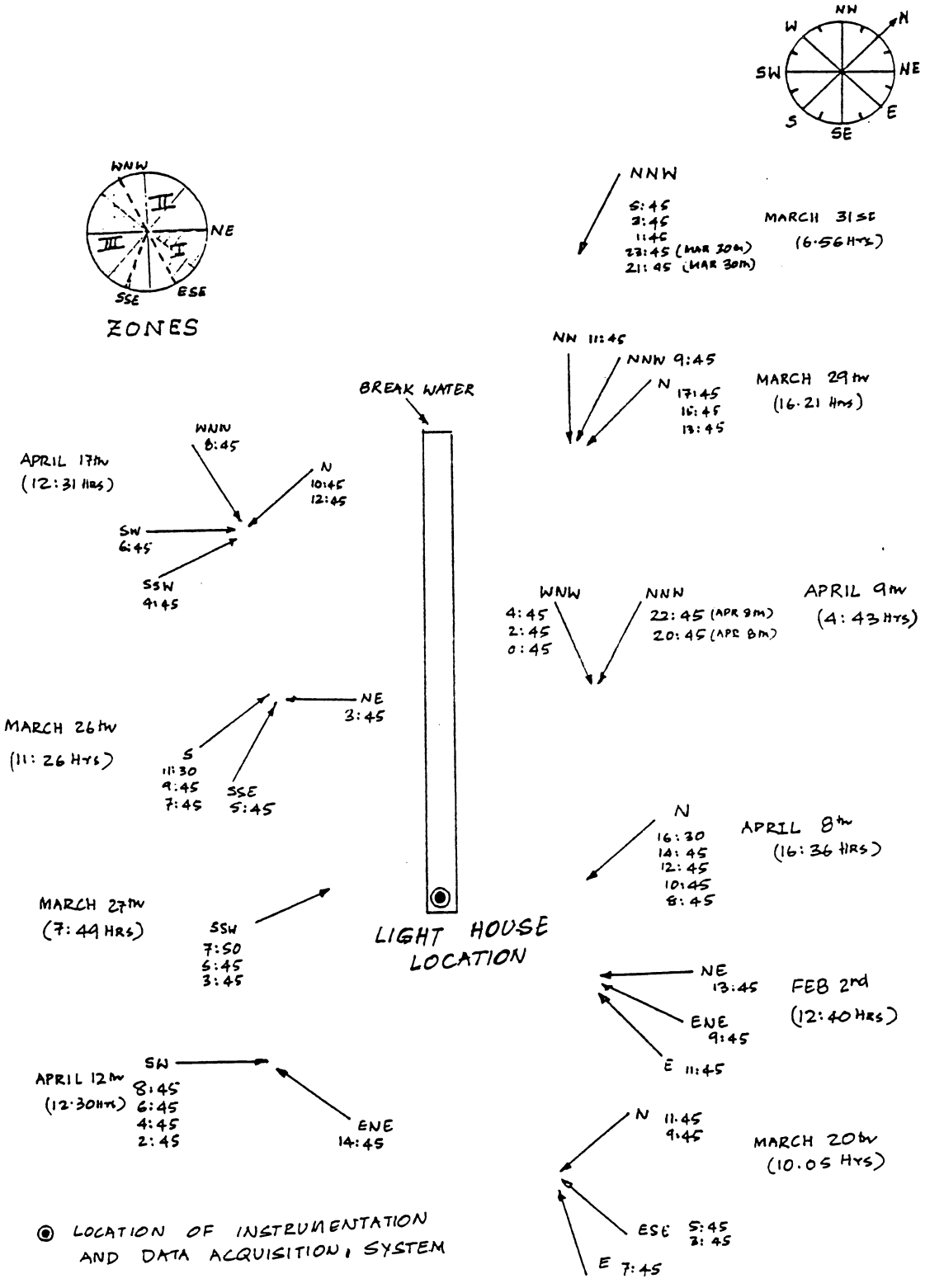

Fig. A.18 Wind speed indicator diagram

1. The ebb and the increase of the lake level had a net effect on the overall recorded strain readings, causing an overall tensile or compressive change in the observed values.
2. The presence of ice cover over the lake surface had an effect on the recorded strain data.
3. Some variations in the recorded strain data can be attributed to the local flexural effects in individual sheet piles.
4. The inward and outward flexing of the sheet piles causes a temporary locking up of the joints due to friction for short durations of 18 to 20 sec in the recorded data. This causes a net shift in the measured overall strain records.

The data analysis for the data recorded on the March 29th, 1989, are shown as follows. The wind direction recorded at the time of recording of the data was predominantly in Zone II. The strain records are shown in Fig. A.17. Data were recorded from 16.21 hours to 16.32 hrs. A representative summary of wind and temperature data for March 29th are shown in Table A.4.

The pressure transducer record indicates that the time-varying pressure head ranged between approximately 1 and 5 ft. The range of strain gauge output for Gauge E is from 168 to 180 microstrains. The record is characterized by

Table A.1: Time, date, max. wave height in the record and corresponding wind and wave Directions

Date	Time of record	Maximum wave height H_{max} (ft)	Wind dir. marine log	Wave dir. real time statistics
Dec 3rd	20:46 hrs	4.01	SW	NNW
Dec 10th	22:30 hrs	6.41	N	NW
Dec 12th	21:07 hrs	3.13	NW	NW
Dec 21st	13:51 hrs	3.01	NW	NW
Jan 12th	11:46 hrs	9.40	NW	WNW
Jan 12th	14:57 hrs	9.40	NW	NNW
Feb 4th	14:35 hrs	3.03	NE	NNW
Feb 24th	11:17 hrs	13.90	NW	NW
Mar 5th	16:47 hrs	6.21	NE	N

Table A.2: Recorded hoop-force ranges

Date	H_{max} (ft)	S.G. 12 (lb/in.)	S.G. 13 (lb/in.)	S.G.7 (lb/in.)
Dec 3rd	4.01	164.32	165.31	5.38
Dec 10th	6.41	373.97	299.20	141.32
Dec 12th	3.13	23.92	35.40	1.70
Dec 21st	3.03	39.74	50.05	6.18
Jan 12th	9.40	62.47	78.00	11.76
Jan 12th	9.40	121.47	332.61	68.47
Feb 4th	3.03	24.96	50.92	3.74
Feb 24th	13.90	130.91	382.54	135.54
Mar 5th	6.21	44.71	60.24	6.68

Table A.3: Recorded hoop-force ranges

Date	H_{max} (ft)	S.G.5 (lb/in.)	S.G.6 (lb/in.)	S.G.8 (lb/in.)	S.G.9 (lb/in.)	S.G.10 (lb/in.)
Dec 3rd	4.01	6.11	51.41	41.12	52.68	12.53
Dec 10th	6.41	71.94	74.35	55.88	161.94	32.13
Dec 12th	3.13	3.96	11.83	3.07	3.31	3.11
Dec 21st	3.03	7.48	5.33	7.78	5.08	3.94
Jan 12th	9.40	31.39	8.64	12.02	7.22	27.19
Jan 12th	9.40	95.98	25.24	40.25	17.03	93.92
Feb 4th	3.03	3.40	6.02	5.88	3.44	7.01
Feb 24th	13.90	73.14	39.13	51.70	18.92	72.65
Mar 5th	6.21	10.19	24.08	3.91	9.46	23.45

Table A.4: Wind and Temperature data - March 29, 1989

Time (hrs)	Wind Dir	Wind Speed (Knots)	Sea State Height (ft)	Air temp. (°F)	Sky Conditions
17:45	N	14	1	33	CYS
15:45	N	17	1	33	CYS
13:45	N	16	1	33	CYL
11:45	NW	13	1	35	CY
9:45	NNW	19	1	30	CY

Time of Strain Record 16:21 hrs

continuous peaks and troughs throughout. Because of randomness of the gauge output, it is difficult to associate a wave gauge peak or trough reading with a corresponding local peak or trough on the gauge. A definite cause and effect relationship exists between them. The orientation of gauge E describes flexing inward and outward of the cell wall from a cantilevering effect. It can be expected that an inward pressure (associated with a peak wave reading) is associated with a compressive strain in the pile (a trough on strain Gauge E). The output for Gauges A - D demonstrates that distinct peaks and troughs occur at similar times and in the same relative sense. Again, even though the relative changes in magnitude are not considered to be significant, a definite cause and effect exists that is associated with peaks in the pressure gauge data. By considering data point 525 as a typical example, a peak pressure reading corresponds to peak strains in Gauges A-D. Gauge A recorded an increase in tension, Gauge B a decrease in tension, Gauge C a decrease in tension, and Gauge D an increase in compression. These changes occur apparently because of an inward flexing of the cell walls due to wave action. The general inward flexing of the cell walls would result in an increase in compressive strain at the diaphragm (at Gauges C and D). Similarly, there should be a compressive change at midcell (Gauge A). However, it is

feasible that the inward pressure acting at midcell could cause a local inward flexing of the individual pile section, thus causing a tensile change. The corresponding effect on the harbor side of the cell (at Gauge B) is not clear, but it is interesting to note that the response of Gauge B is not as pronounced.

A.4.2.2 Assessment of Mean Response:

A summary of the mean values for strain and pressure gauge readings is provided in Table A.5. The fluctuating structural response (waves/structure interaction) is of primary interest in this study. The overall behavior of the structure can be understood in a better manner by reviewing the data. The following quanlitative observations are intended to suggest only part of the explanation for differences in recorded mean values for strain between the monitoring dates.

The effect of temperature differentials on the structure over time is not known but could account for some of the differences in measured mean values for the different dates. As the structure expands near the top relative to the submerged portion, a net increase in the compressive hoop strains would occur near the top. As a result, one would expect a flexing outward (cantilevering away from the cell) as the top of the cell expands. A gauge oriented like Gauge E would therefore register a net tensile change in

Table A.5: Mean values of the strains

Date	Gauge A (Micro-strains)	Gauge B (Micro-strains)	Gauge C (Micro-strains)	Gauge D (Micro-strains)	Gauge E (Micro-strains)	Pressure Gauge (ft)	Range for Pr. gauge (ft)
Mar. 20	31.6	23.9	11.8	-1.9	-28.3	2.91	2.84 - 2.96
Feb. 2	19.3	21.8	7.8	-3.5	-44.1	3.06	0.63 - 5.70
Mar. 29	40.4	26.1	11.6	-5.4	-173.8	2.91	0.00 - 6.08
Apr. 8	56.5	30.1	17.9	-	-426.4	3.27	1.57 - 4.52
Apr. 17	64.4	43.2	27.3	_	-46.2	3.67	1.26 - 4.92
Mar. 31	45.8	26.6	11.9	-22.5	-138.1	2.94	0.00 - 6.23
Apr. 9	57.6	25.4	15.7	-	-237.1	2.94	0.15 - 5.45
Mar. 26	37.9	41.1	11.4	-0.79	-34.7	2.62	2.48 - 2.78
Mar. 27	37.0	33.0	10.6	-1.70	-28.7	2.64	2.50 - 2.80
Apr. 12	59.1	52.2	25.5	-	-62.9	2.87	2.09 - 3.35
Apr. 1	46.5	31.8	9.7	-	-69.3	2.57	1.37 - 3.79

strain. Of course, a number of local temperature differential effects must also be considered in attempting to evaluate these effects.

Another possible external effect that may affect the mean strain reading from date to date is related to the pressure distribution, which is directly related to the lake level. In general, a higher lake level could cause a net increase of the pressure on the outside of the cell and (assuming no corresponding increase of lake level on the inside of the cell) would cause a greater inward flexing of the cell. This would have the effect of causing a net change in compression on Strain Gauge E (or a larger negative value). Strain Gauge A could be thought to measure a net change in tension due to same pressure change.

A.4.3 Summary:

The failure mode hypothesized by Swatek (21) regarding cantilever action of the piles above the cell fill suggests that failure was initiated by splits in top of the diaphragm wall or the face of the cell on the lake side. In addition to the cantilever effect as a possible source of failure, fatigue, overstressed interlocks and stress concentrations in the stepped - down diaphragm walls had been mentioned. The experimental program was intended to address these possible failure modes. Because of the late starting date (Nov. 1988), strain gauges could not be located beneath the

lake surface to investigate the cantilever action primarily, as well as the possible development of large stresses near and on the diaphragm wall. The maximum wave loadings that occurred during the monitoring period could, at best, be described as minor events relative to the magnitude of storms generated in the lake region. However, information regarding the structural response was gained and the data appeared to be useful in better understanding the overall cell behavior subjected to minor wave action. In addition, it does appear from the data that the primary mechanism required to validate Swatek's failure hypothesis has been observed.

A.4.4 Solution Approach:

The analysis presented above culminated one task of the study begun in November 1988. At that time, the study was undertaken at the request of and with the support of the U.S. Army Corps Chicago District. The perceived solution approach by ISU was believed to be consistent with that of the District. The data obtained until then has borne out of the fact that the problem was complex but solvable. The understanding gleaned from Phase I operations was used in the design of the Phase II monitoring system. In addition, the analysis contributed to consideration of Swatek's (21) hypothesis as a possible cause of failure.

A.5 Diagnostic Tests

A.5.1 Introduction:

In addition to the fatigue tests performed in the lab, certain diagnostic tests have been done to aid the interpretation of the data gathered as part of the field instrumentation effort. The real-time data recorded can be analyzed in two ways. The first method is to use the strength of materials approach to determine the stresses from the strains and transform the stresses into forces. This cannot be easily done for the complex stress distribution, as in this case. The second method uses the laboratory tests to simulate the field behavior. Basically four different tests were performed. The four tests are done as follows:

1. Determination of the existing hoop force condition by the strain gauge on the inside of the test specimen.
2. Determination of the hoop force condition by the strain gauge on the outside of the test specimen.
3. Determination of the hoop force condition by the strain gauge on the plate mounted on the outside of the test specimen.
4. Determination of the material constants of the sheet pile specimens.

Tests 1 and 2 are done simultaneously as summarized in Tables A.6 and A.7 respectively. The results of the Test 3 is summarized in Table A.8.

A.5.2 Equipment:

1. Three- and five-in. wide type PSA 23 Steel sheetpile specimens for Tests 1, 2, and 3. Test coupon cut out of the PSA 23 sheet pile for Test 4.
2. MTS loading frame with load cell for Tests 1, 2, and 3. MTS control unit 880 for Tests 1, 2, and 3.
3. Strain indicator for Tests 1, 2, and 3.
4. Hitec full-bridge weldable strain gauges (similar to ones used in on-site instrumentation). Quarter-bridge weldable strain gauges.

A.5.3 Procedure:

The quarter-bridge weldable strain gauges are mounted on the test specimen. The specimen is loaded by special end- grips fashioned for fatigue testing. The test is controlled by the 880 control unit with load control. The strain values are read at different points in the test. A total of two tests are performed. A regression analysis is done on the results to relate strain reading to hoop force.

Test 3 is performed in two stages. A test specimen 5 in. wide is used in the test. In the first stage a 3 in. x 5 in. plate is welded on the outside of the specimen. The

Table A.6: Summary of test 1 data. Tests performed on PSA23 sheetpile sample 5 in. wide

Trial 1		Trial 2	
Load (lb)	Measured mean strain (Micro - strains)	Load (lb)	Measured mean strain (Micro - strains)
0	0	0	0
3020	282	3030	286
4010	391	4050	392
5020	496	5000	490
6010	596	6040	598
6990	699	7000	697
8010	800	8020	796
9000	896	9000	891
9840	982	10030	994

Table A.7: Summary of test 2 data. Tests performed on PSA23 sheetpile sample 5 in. wide.

Trial 1		Trial 2	
Load (lb)	Measured mean strain (Micro - strains)	Load (lb)	Measured mean strain (Micro - strains)
0	0	0	0
3020	-216	3030	-218
4010	-298	4050	-301
5020	-379	5000	-378
6010	-459	6040	-464
6990	-539	7000	-538
8010	-617	8020	-618
9000	-689	9000	-688
9840	-759	10030	-770

Table A.8a: Summary of test 3 Data. tests performed on PSA23 sheet pile sample 5 in. wide with 6 in. angle welded on top

Total load (lb)	Load/in. (lb/in.)	Trial 1 Average strain (μ - strains)	Trial 2 Average strain (μ - strains)	Trial 3 Average strain (μ - strains)	Mean value (μ - strains)
0	0	33.5	68.5	1	34.3
1000	200	99	127	66	97.33
2000	400	148.5	178	113.5	146.67
3000	600	194.5	226	165	195.17
4000	800	239	267	204.5	236.80
5000	1000	280.5	307	245.5	277.67
6000	1200	322.5	345	307	315.83
7000	1400	363.5	383	316.5	354.33
8000	1600	405.5	422	354.5	394
9000	1800	447.5	455	387	429.8
10000	2000	484	492	428	468

Table A.8b: Summary of test 3 data. Tests performed on PSA23 sheet pile sample 5 in. wide with 6 in. angle welded on top.

Total load (lb)	Load/in. (lb/in.)	Trial 1 Average strain (μ - strains)	Trial 2 Average strain (μ - strains)	Trial 3 Average strain (μ - strains)	Mean value (μ - strains)
0	0	-18.5	-36.5	-28.5	-27.67
1000	200	-46	-61	-56.5	-56.5
2000	400	-69	-82.5	-77	-77
3000	600	-86.5	-102	-98	-98
4000	800	-104	-118	-114.5	-114.5
5000	1000	-122	-133	-1227.5	-127.5
6000	1200	-137	-148	-142.5	-142.5
7000	1400	-153	-161	-155.5	-156.5
8000	1600	-168.5	-173	-168.5	-170
9000	1800	-181.5	-185	-179.5	-182
10000	2000	-192	-196	-191	-193

Hitec strain gauge is mounted on the plate and a quarter-bridge strain gauge is mounted on the inside surface of the specimen. The specimen is tested in the same procedure as in the paragraph above. A total of 3 tests are performed. An angle 5 in. x 5 in. is welded on the plate; similarly to the underwater strain gauge installation on the breakwater. Again, a total of 3 tests are performed on the sample. These tests measure the stiffening of the sheetpile specimen by the plate and the angle. A regression analysis is done and the results are used in computation of wave forces on breakwater. Test 4 is performed on the 0.5 in. square test coupon. The coupon is held in the universal testing machine and the load is increased gradually. The coupon is tested until failure.

From the results of the tests, three specific regions of linear behavior can be identified. The initial behavior can be attributed to the redistribution of the loads due to factors like the tightening of the jaws of the testing machine. The average Young's modulus for the sample was found to be 29.00 E 06 PSI.

APPENDIX B.

B.1 Fatigue Tests - Equipment

The following equipment was used in the fatigue tests:

1. MTS loading frame with actuator and load cell.
2. MTS series 880 control unit.
3. PSA 23 steel sheetpile specimens (5" wide samples).
4. End-grips for the tests.

The PSA 23 steel sheetpile specimens were obtained from the Chicago district of the Corps of Engineers in unstrained condition. A set of three specimens was used for each test with the middle specimen forming the test sample and the two end specimens acting as transition specimens to mitigate the end effects. The testing setup is as shown in Figures 3.1 and B.1. The objective of this arrangement was to simulate, as closely as possible, the insitu behavior of the test specimens under actual loading conditions. Two different types of grips were used. Bulb-shaped grips as shown in Fig. B.1 were used initially. It was felt that these grips were inefficient in modeling the actual behavior because they were found to stiffen the transition specimens and reduce the inherent flexibility present in the interlocks. Their failure is shown in Fig. B.2. The bulb-shaped grips were then replaced by grips fabricated by removing the interlock portions of a 5-in.-wide specimen and using them as grips for testing after further reinforcement with steel

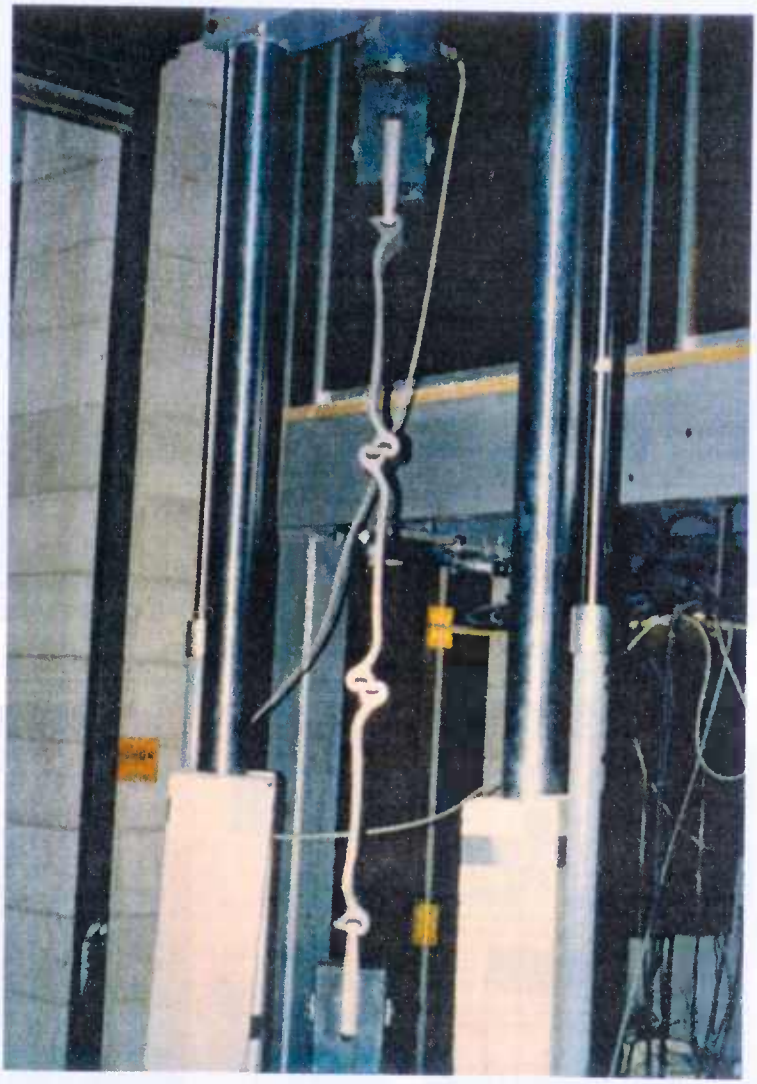

Fig. B.1. Test setup with bulb shaped end grips

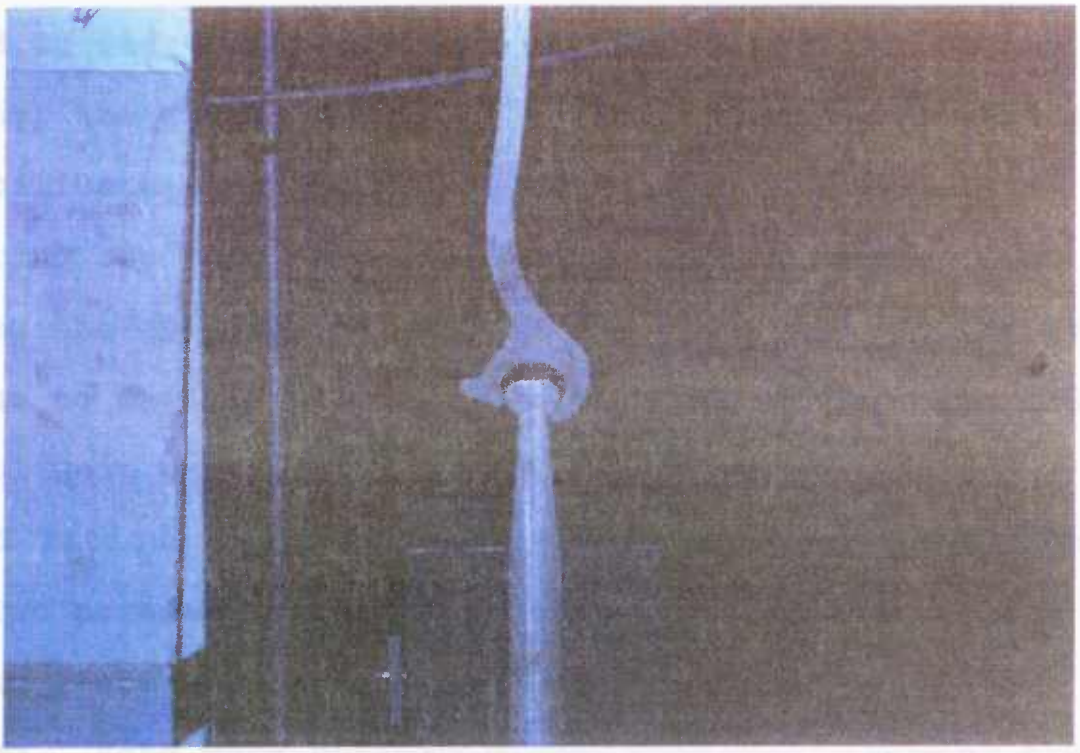

Fig. B.2. Failure of transition specimen at grips indicating interlock opening

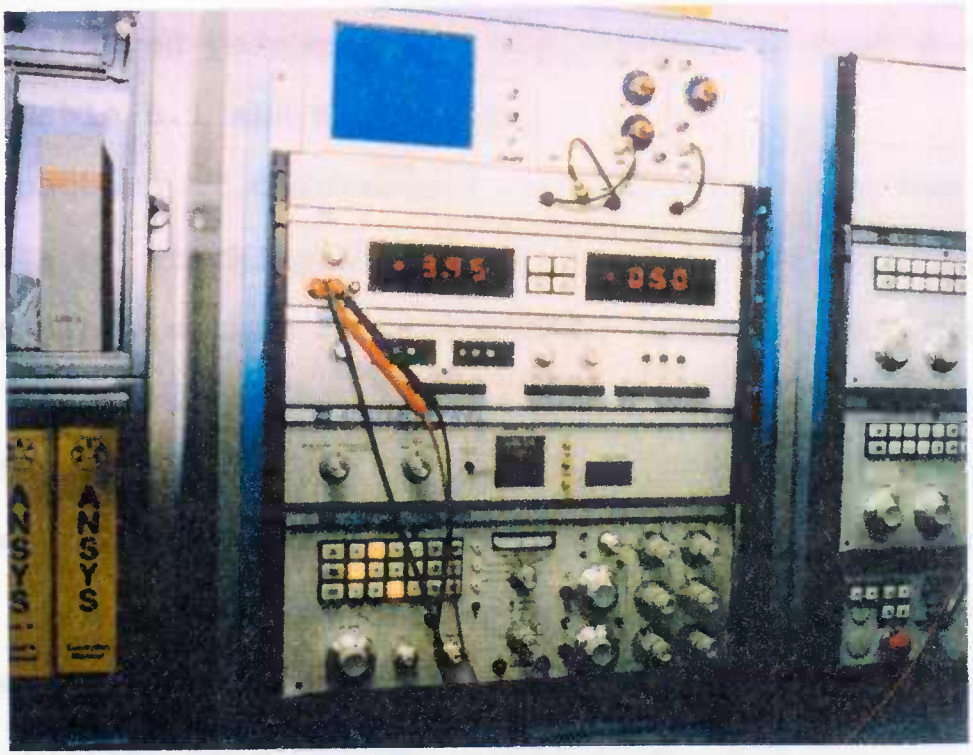

Fig. B.3. The MTS 880 Control unit

plates. The specimen was cut and the interlock portions welded to reduce the moment on the grips. Prior to the testing, the sample sheets were smoothed by using sand paper to facilitate easy tracing. The testing was done by orienting the sheetpile specimens as shown in Fig. B.1. Loading the specimen was sinusoidal, with the loading from minimum to maximum being achieved in one cycle. The MTS control unit was set for a cyclic loading of 1 Hz.

B.2 Fatigue Tests - Discussion of Measured Parameters

Two parameters measured during the progress of the fatigue tests were interlock separation and interlock opening. Both were defined as per Fig. 3.2. During the testing, it was found that there was negligible change in both the measured parameters. The results of Test 6 are shown in Table B.1 and Table B.2.

The pattern of deformation is determined for two of the eight tests by tracking of the MTS stroke reading. The MTS stroke reading is then transformed to displacement from the original length in inches. This gives a pattern of total deformation of the sample in progressive stages. Figure B.4 summarizes the stroke reading and the displacement values for Test 7 in a graphical form. The deformation pattern can be divided into three zones as indicated in the figure. They are initial deformation, transition, and failure. Initial deformation is deformation due to settling of the

Table B.1: Interlock opening measurements for target specimen

Cycles	Top (in.)		Bottom (in.)	
	Left	Right	Left	Right
0	0	0	0	0
10000	- 0.007	0.003	0.001	0.002
20000	0.001[a]	0.005	0.002	0
30000	- 0.005	0.002	0.003	0.002
40000	- 0.006	0.003	0.002	0.001
50000	- 0.006	0.004	- 0.002	- 0.001

[a]+ denotes elongation

Table B.2: Interlock separation measurements for target specimen

Cycles	Top (in.)		Bottom (in.)	
	Left	Right	Left	Right
0	0	0	0	0
10000	0.001[a]	0	0.002	0.001
20000	0.007	0	0.001	0.013
30000	0.004	0.002	- 0.003	0.011
40000	0.005	0.004	- 0.003	0.015
50000	0.004	0.001	- 0.004	0.013

[a]+ denotes elongation

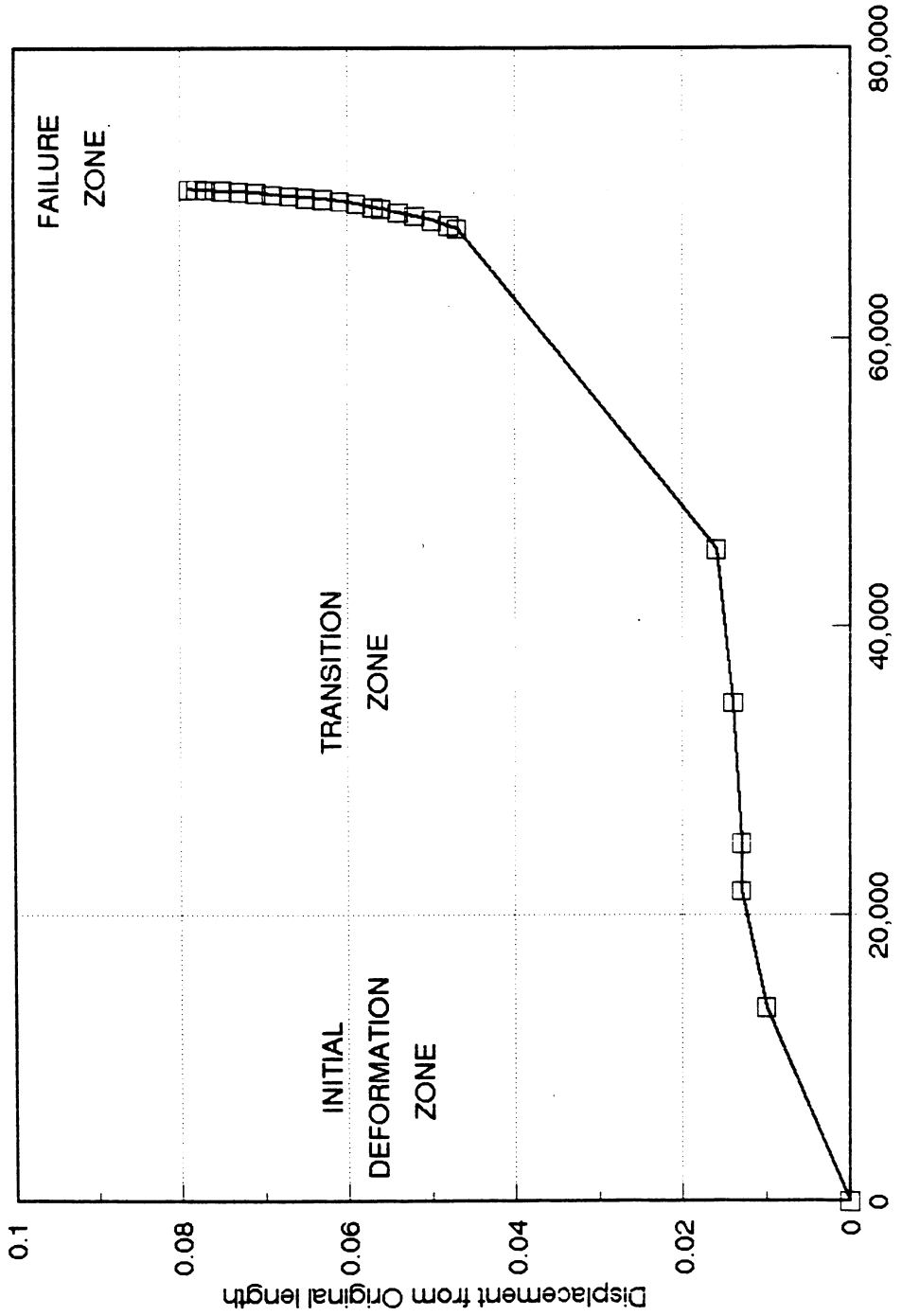

Fig. B.4 Graphical variation of pattern of deformation

grips, the presence of mill scale, and other initial effects. During the transition zone, the specimen deforms with noticeable dishing. This is indicated by Fig. B.5, which was a photograph taken during an interruption in the testing program in Test 3. The dished shape of the target specimen is clearly seen in the figure. The final zone is termed the failure zone. This zone is characterized by rapid deformation and failure.

B.3 Fatigue Tests - Discussion of the Failure Mechanism

The failure of the steel sheetpile specimen is due to setting up large cyclic bending moments. The calculations using the free body diagram in Fig. B.6 are as shown below: Considering Fig. B.6,

$$\sigma_{tmax} = \frac{P}{A} + \frac{My}{I}$$

_____Eqn. B.1

where

P = axial load on the specimen

M = bending moment setup

A = area of cross section

Y = distance to the extreme fiber from neutral axis

I = moment of inertia of cross section

Fig. B.5. Figure indicating the dished target specimen

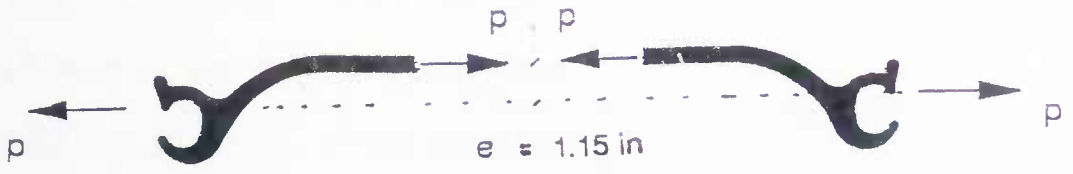

Fig. B.6. Free body diagram of steel sheet pile sample under axial loads

which on simplification means

$$\sigma_{tmax} = P\left(\frac{1}{bt} + \frac{6e}{b^2}\right)$$

_____Eqn. B.3

where,

t = thickness of the specimen

b = width of the specimen

e = eccentricity of the load

Considering the thickness of the specimen as 0.5 in., and the maximum stress in the specimen to be the yield stress, the sheetpile specimen begins to yield in tension at a load of only 1350 lb/in. It is also important to note that e, the eccentricity of the load, reduces with the deformation of the specimen.

APPENDIX C

C.1 Bivariate Histograms

Tables C.1 to C.16 indicate the bivariate histograms resulting from the statistical analysis of the Burns Harbor data shown in Chapter 4. These bivariate histograms are subjected to weighted regression analysis to derive the relationships between wave height and wave periods.

C.2 Typical Calculations Using the Cnoidal Wave Theory

The following are the calculations for a typical Cnoidal wave. The calculations follow the calculation method outlined in the Shore Protection Manual of the U. S. Army Corps of Engineers (13). The calculation is for a Cnoidal wave from the NE direction of wave height 24 feet and wave period 19.8125 sec.

Wave height, H = 24 ft

Wave period, T = 19.8125 sec

The depth from the S.W.L to the bed, d = 33 ft

The ratio, H/d = 24/33 = 0.7273

The value, $T(g/d)^{1/2}$ = 19.5709

From Fig. C.1 (Fig. 2-11 of 13):

$\kappa^2 = 1 - 10^{-6.25} = 0.9999994$

From Fig. C.2 (Fig. 2-12 of 13):

Since κ^2 is close to 1.0, assuming that the wave length calculated from the Airy's Theory is the same as the

Table C.1: Water Surface elevation according to the Cnoidal theory; calculations for a typical wave

X - value	x = 0	x = 7	x = 13	x = 19	x = 25	x = 28
t = 0	53.52	52.65	51.45	49.41	48.03	46.49
t = 9.91	29.52	29.52	29.52	29.52	29.52	29.52

Table C.2: Bivariate histogram for NE direction

Wave Period (Sec)

Wave Height (ft)	< 2	2 to 3	3 to 4	4 to 5	5 to 6	6 to 7	7 to 8	8 to 9	9 to 10	> 10
1.0 to 2.0		24	102							
2.0 to 3.0			60	42	24					
3.0 to 4.0				42	66					
4.0 to 5.0					48	66				
5.0 to 6.0					18	36				
6.0 to 7.0					6	54				
7.0 to 8.0						12	30			
8.0 to 9.0							24			
9.0 to 10.0							6	6		
10.0 to 11.0										
11.0 to 12.0								6		
12.0 to 13.0										
15.0 to 16.0									6	
16.0 to 17.0										
17.0 to 18.0									6	
25.0 to 26.0										6
28.0 to 29.0							6			

Table C.3: Bivariate histogram for E direction

Wave Period (Sec)

Wave Height (ft)	< 2	2 to 3	3 to 4	4 to 5	5 to 6	6 to 7	7 to 8	8 to 9	9 to 10	> 10
0.5 to 1.0		6								
1.0 to 2.0		6	132							
2.0 to 3.0			36	54						
3.0 to 4.0				66						
4.0 to 5.0				18	72					
5.0 to 6.0					18					
6.0 to 7.0										
7.0 to 8.0						6				
8.0 to 9.0										

Table C.4: Bivariate histogram for ESE direction

Wave Height (ft)	Wave Period (Sec) < 2	2 to 3	3 to 4	4 to 5	5 to 6	6 to 7	7 to 8	8 to 9	9 to 10	> 10
0.5 to 1.0										
1.0 to 2.0		12	42							
2.0 to 3.0			24	18						
3.0 to 4.0				6						
4.0 to 5.0										

Table C.5: Bivariate histogram for SE direction

Wave Height (ft)	Wave Period (Sec) < 2	2 to 3	3 to 4	4 to 5	5 to 6	6 to 7	7 to 8	8 to 9	9 to 10	> 10
0.5 to 1.0		24	6							
1.0 to 2.0		102	48							
2.0 to 3.0			18							
3.0 to 4.0			6	6						
4.0 to 5.0										

Table C.6: Bivariate histogram for SSE direction

Wave Height (ft)	Wave Period (Sec) < 2	2 to 3	3 to 4	4 to 5	5 to 6	6 to 7	7 to 8	8 to 9	9 to 10	> 10
0.5 to 1.0		84								
1.0 to 2.0		96	30							
2.0 to 3.0			24							
3.0 to 4.0				6						
4.0 to 5.0										

Table C.7: Bivariate histogram for S direction

Wave Height (ft)	Wave Period (Sec) < 2	2 to 3	3 to 4	4 to 5	5 to 6	6 to 7	7 to 8	8 to 9	9 to 10	> 10
0.5 to 1.0		144								
1.0 to 2.0		168	24							
2.0 to 3.0			60							
3.0 to 4.0										
4.0 to 5.0				6						

Table C.8: Bivariate histogram for SSW direction

Wave Period (Sec)

Wave Height (ft)	< 2	2 to 3	3 to 4	4 to 5	5 to 6	6 to 7	7 to 8	8 to 9	9 to 10	> 10
0.5 to 1.0		330	6							
1.0 to 2.0		384	78							
2.0 to 3.0			144							
3.0 to 4.0			24	12						
4.0 to 5.0				6						

Table C.9: Bivariate histogram for SW direction

Wave Period (Sec)

Wave Height (ft)	< 2	2 to 3	3 to 4	4 to 5	5 to 6	6 to 7	7 to 8	8 to 9	9 to 10	> 10
0.5 to 1.0		348	6							
1.0 to 2.0		630	258							
2.0 to 3.0	6	6	354							
3.0 to 4.0			60	18						
4.0 to 5.0				6						
5.0 to 6.0				6						

Table C.10: Bivariate histogram for WSW direction

Wave Period (Sec)

Wave Height (ft)	< 2	2 to 3	3 to 4	4 to 5	5 to 6	6 to 7	7 to 8	8 to 9	9 to 10	> 10
0.5 to 1.0		168								
1.0 to 2.0		354	294							
2.0 to 3.0			342							
3.0 to 4.0			54	42						
4.0 to 5.0				30						

Table C.11: Bivariate histogram for W direction

Wave Height (ft)	Wave Period (Sec) < 2	2 to 3	3 to 4	4 to 5	5 to 6	6 to 7	7 to 8	8 to 9	9 to 10	> 10
0.5 to 1.0		6								
1.0 to 2.0		84	222							
2.0 to 3.0			216	6						
3.0 to 4.0				72						
4.0 to 5.0			6	54						
5.0 to 6.0					18					

Table C.12: Bivariate histogram for WNW direction

Wave Height (ft)	Wave Period (Sec) < 2	2 to 3	3 to 4	4 to 5	5 to 6	6 to 7	7 to 8	8 to 9	9 to 10
0.5 to 1.0									
1.0 to 2.0		30	252						
2.0 to 3.0			324	66					
3.0 to 4.0			6	144					
4.0 to 5.0				90	6				
5.0 to 6.0					18				
6.0 to 7.0					6				
7.0 to 8.0					6				

Table C.13: Bivariate histogram for NW direction

Wave Period (Sec)

Wave Height (ft)	< 2	2 to 3	3 to 4	4 to 5	5 to 6	6 to 7	7 to 8	8 to 9	9 to 10
0.5 to 1.0			6						
1.0 to 2.0		30	240						
2.0 to 3.0			132	114					
3.0 to 4.0				192					
4.0 to 5.0				24	78				
5.0 to 6.0					48	6			
6.0 to 7.0					6	36			
7.0 to 8.0						12			
8.0 to 9.0						6			

Table C.14: Bivariate histogram for NNW direction

Wave Height (ft)	Wave Period (Sec) < 2	2 to 3	3 to 4	4 to 5	5 to 6	6 to 7	7 to 8	8 to 9	9 to 10
0.5 to 1.0									
1.0 to 2.0		24	144						
2.0 to 3.0			72	156					
3.0 to 4.0			6	126	42				
4.0 to 5.0				12	120				
5.0 to 6.0					60	24			
6.0 to 7.0				6	6	30			
7.0 to 8.0						36	6		
8.0 to 9.0						12	18		
9.0 to 10.0							24		
10.0 to 11.0									
11.0 to 12.0							6	6	
12.0 to 13.0								6	

Table C.15: Bivariate histogram for N direction

Wave Period (Sec)

Wave Height (ft)	< 2	2 to 3	3 to 4	4 to 5	5 to 6	6 to 7	7 to 8	8 to 9	9 to 10	> 10
0.5 to 1.0										
1.0 to 2.0		24	90							
2.0 to 3.0	6		36	54	30					
3.0 to 4.0				48	66	6				
4.0 to 5.0				24	96	12				
5.0 to 6.0					12	42				
6.0 to 7.0					6	48				
7.0 to 8.0						24	24			
8.0 to 9.0							30			
9.0 to 10.0							12			
10.0 to 11.0							24			
11.0 to 12.0							12			
12.0 to 13.0								6		
13.0 to 14.0									6	
16.0 to 17.0										6
17.0 to 18.0										6
18.0 to 19.0										6
19.0 to 20.0										12

Table C.16: Bivariate histogram for NNE direction

Wave Height (ft)	Wave Period (Sec) < 2	2 to 3	3 to 4	4 to 5	5 to 6	6 to 7	7 to 8	8 to 9	> 30
0.5 to 1.0		6							
1.0 to 2.0		24	72						
2.0 to 3.0			72	48	60				
3.0 to 4.0				48	84				
4.0 to 5.0				12	60	24			6
5.0 to 6.0					18	54			
6.0 to 7.0					12	48	6		
7.0 to 8.0						18	36		
8.0 to 9.0						12	30		
9.0 to 10.0								6	
10.0 to 11.0								6	
11.0 to 12.0							6	6	
12.0 to 13.0								6	
14.0 to 15.0									

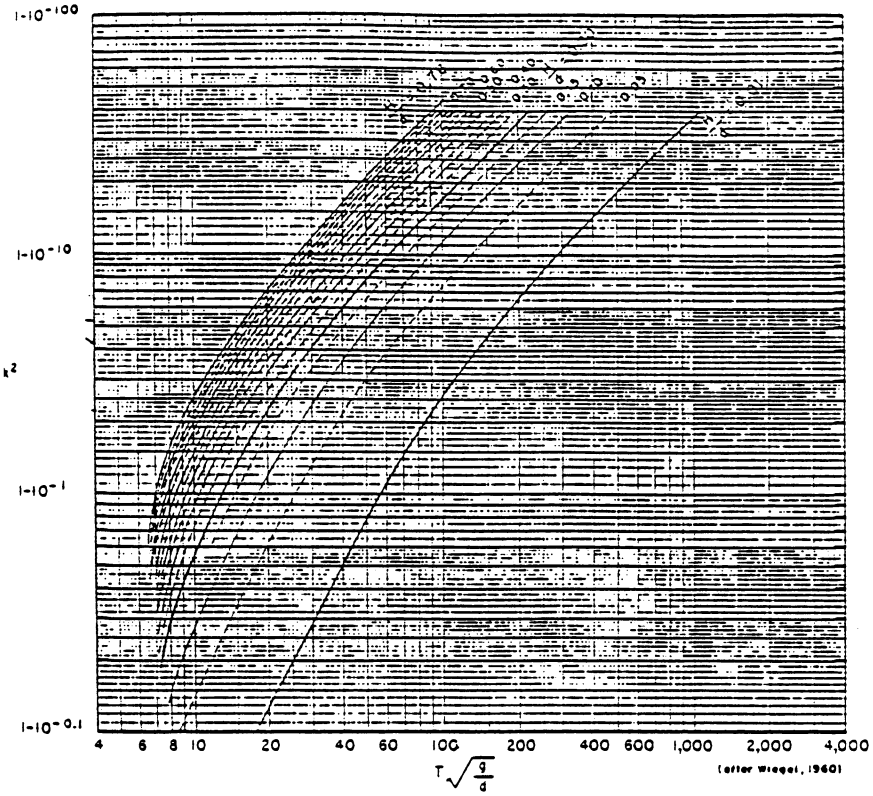

Fig. C.1 Relationship between K^2 and $T(g/d)^{1/2}$ (from 7)

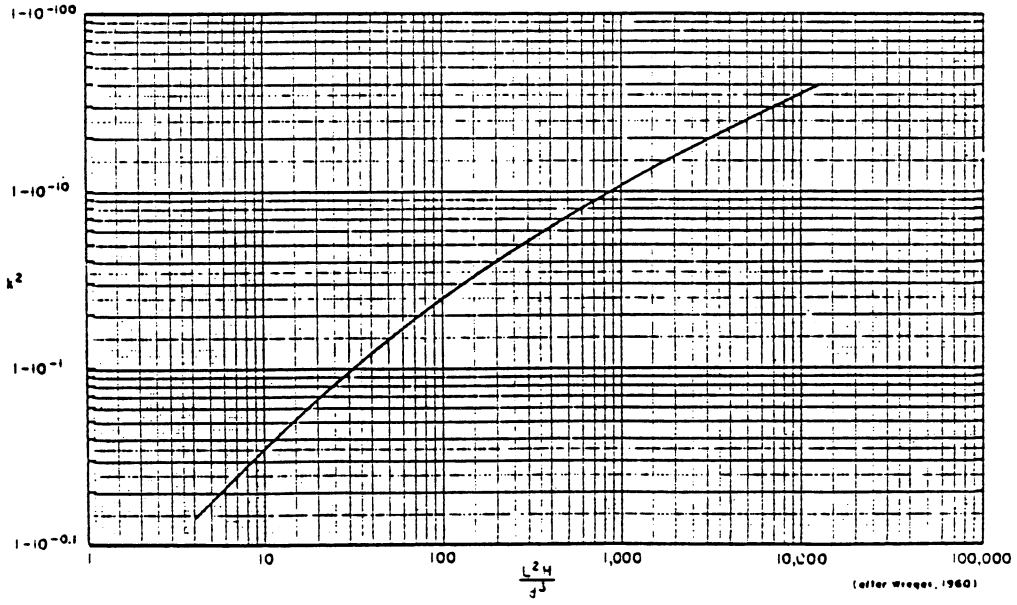

Fig. C.2 Relationship between K^2 and L^2H/d^3 (from 7)

wavelength L for the Cnoidal wave.

Hence L = 632.20

Since, $L^2H/d^3 = 266.91 > 26$; usage of Cnoidal theory is justified. Considering the elevation to the wave peak as Y_c and wave trough as Y_t,

$(Y_c-d)/H = 0.855$

$(Y_t-d)/H + 1 = 0.855$

$Y_c = 53.52$ ft

$Y_t = 29.52$ ft

Using the graph from Fig. C.3 (from 12) which relates θ and $Cn^2(q)$,

$$\theta = Kx - \omega t \qquad \text{----- Eqn. C.1}$$

where

$K = 2\pi/L = 0.009939$

$\omega = 2\pi/T = 0.3171$

and

$$Y_s = Y_t + Cn^2(q) \qquad \text{----- Eqn. C.2}$$

where Y_s is the water surface elevation. The value of the water surface elevation at the t=0 and the t=9.9063 are calculated and are illustrated in Table C.1.

The pressure distribution due to a cnoidal wave is approximated by a hydrostatic distribution from zero at the top to γY_s at the bottom.

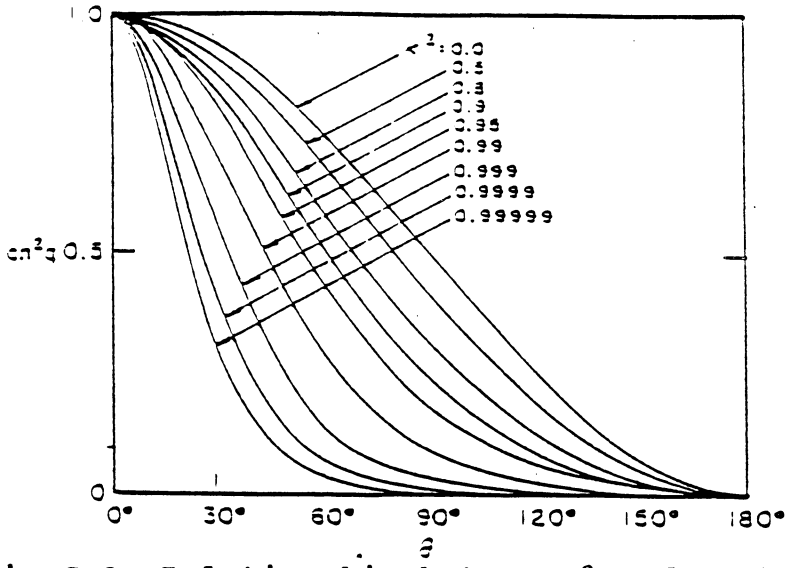

Fig.C.3 Relationship between θ and $Cn_2(q)$ (from 6)

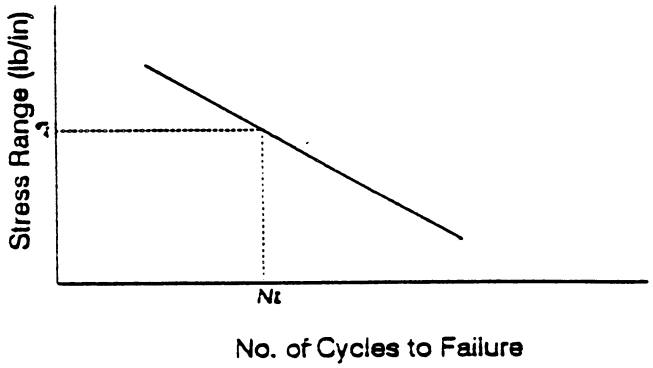

Fig. C.4 Typical S-N curve relating stress range to number of cycles to failure

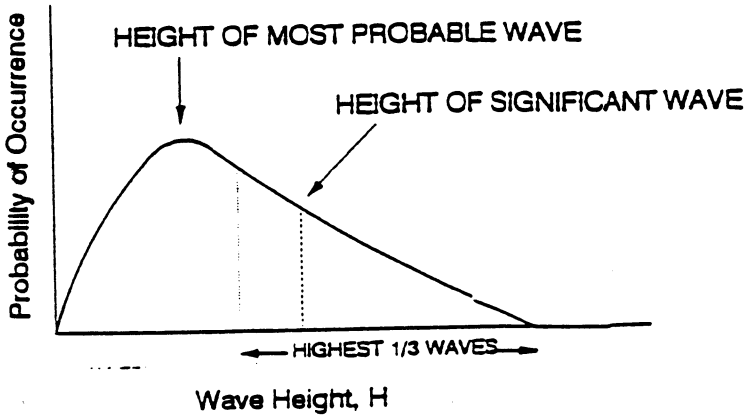

Fig. C.5 Rayleigh distribution of wave heights in a sea state

C.3 Equivalent Stress Analysis Method

The following derivation summarizes the equivalent stress analysis method used for determining the life of the structure. The basis for the method is summarized in the papers of Williams and Rinne (8) and Hambly et.al (9).

Consider the fatigue S-N curve for a structure as shown in Fig. C.4. Considering the curve is a log - log plot, the following relationship can be drawn:

$$\log(\sigma) = \log(\sigma_1) + m_1 LOG(N)$$

----- Eqn. C.3

which can be simplified as

$$\sigma = \sigma_1 (N)^{m_1}$$

----- Eqn. C.4

where

σ = stress range

σ_1 = stress range for 1 cycle (theoretical)

m_1 = slope of the S-N curve

n = number of cycles to failure for a stress range of σ

The equivalent stress range method is based on Miner's

Linear Damage Rule. From Eqn. C.4, if the number of cycles to failure for a stress range σ_i is N_i and if the specimen endures only n_j cycles instead of N_i cycles, the damage endured is

$$D_j = n_j / N_i \qquad \text{----- Eqn. C.5}$$

D_j is known as the damage fraction. According to Miner's Rule, failure is assumed when

$$\Sigma D_j = 1 \qquad \text{----- Eqn. C.6}$$

The distribution of stress ranges in a sea state follows a Rayleigh distribution. From the Rayleigh distribution as shown in Fig. C.5, the probability of occurrence of a stress range σ in a sea state is

$$P(\sigma) = \frac{4\sigma}{\sigma_s^2} e^{-2\frac{\sigma^2}{\sigma_s^2}}$$

----- Eqn. C.7

where σ_s is the stress range for the significant wave in that sea state. Considering the total number of the waves in the sea state as n_i, the number of waves in an interval $d\sigma$ are

$$dn = n_i \frac{4\sigma}{\sigma_s^2} e^{-2\frac{\sigma^2}{\sigma_s^2}} d\sigma$$

----- Eqn. C.8

The incremental damage **dD** in this interval **dn** will be **dn/N.**

Hence,

$$dD = \frac{n_i}{N} \frac{4\sigma}{\sigma_s^2} e^{-2\frac{\sigma^2}{\sigma_s^2}} d\sigma$$

----- Eqn. C.9

From the relationship between **N, σ and σ_1,**

$$dD = \frac{n_i \frac{4\sigma}{\sigma_s^2} e^{-2\frac{\sigma^2}{\sigma_s^2}}}{(\frac{\sigma}{\sigma_1})^{1/m_1}} d\sigma$$

----- Eqn. C.10

Considering all the waves in the sea state, the complete damage in a sea state will be

----- Eqn. C.11

The integration is carried out from **0** to **α.** The solution is

$$D_i = \frac{4n_i(\sigma_1)^{1/m_1}}{\sigma_s^2} \int \frac{\sigma e^{-2\frac{\sigma^2}{\sigma_s^2}}}{\sigma_1^{1/m_1}} d\sigma$$

in the form of a gamma function whose result is

$$D_i = \frac{4n_i(\sigma_1)^{1/m_1}}{\sigma_s^2} \frac{\Gamma\left(\frac{2-1/m_1}{2}\right)}{2\left(\frac{2}{\sigma_s^2}\right)^{(2-1/m_1)}}$$

----- Eqn. C.12

which becomes, on simplification,

$$D_i = \frac{n_i \Gamma(1-1/2m_1)(\sigma_s)^{-1/m_1}}{(\sqrt{2}\sigma_1)^{(-1/m_1)}}$$

----- Eqn. C.13

If a single equivalent stress σ_e is now defined, which causes the same damage as the entire family of the stresses in the sea state,

$$\sigma_e = \sigma_1 (N_e)^{m_1}$$

----- Eqn. C.14

where

σ_e = equivalent stress range and

N_e = number of cycles to failure due to equivalent stress range.

The damage due to σ_e for N_e cycles is

$$D_i = \frac{n_i}{N_e} = \frac{n_i}{\left(\frac{\sigma_e}{\sigma_1}\right)^{1/m_1}}$$

----- Eqn. C.15

From Eqn. C.13 and Eqn. C.15, we have the relationship between the equivalent stress range and the significant stress range for the particular sea state as follows:

$$\frac{\sigma_e}{\sigma_s} = \left[(2)^{1/2m_1}\Gamma(1-1/2m_1)\right]^{-m_1}$$

----- Eqn. C.16

Hence, for a particular fatigue curve, a sea state represented by a significant stress range can be replaced by an equivalent stress range, which relates to the significant stress range by a constant K, as

$$\sigma_e = K * \sigma_s$$

----- Eqn. C.17

The damage due to all sea states can be determined by estimating the damage due to one sea state and adding the damages for all the sea states considering all the directions of analysis.

The damage in one sea state can be represented as follows: For every direction the relationship between the wave height and the stress range at a particular location on the elevation of the breakwater is

$$\sigma = A_1 H + A_2 H^2 + A_3 H^3$$

----- Eqn. C.18

For a significant height of H_{si},

$$\sigma_s = A_1 H_{si} + A_2 H_{si}^2 + A_3 H_{si}^3$$

----- Eqn. C.19

From the significant stress range σ_s, the equivalent stress range σ_e can be determined by using Eqn. C.17. $\mathbf{N_e}$, the no. of cycles to failure due to the equivalent stress range $\boldsymbol{\sigma_e}$ can be determined, from Eqn. C.4. The number of waves in the sea state $\mathbf{N_i}$ can be determined by the

percentage of occurrence of the sea state. Hence the damage in the sea state **i** is

$$D_i = \frac{n_i}{N_e}$$

----- Eqn.C.20

The total damage due to all the sea states is

$$D = \Sigma D_i \qquad \textbf{(17)}$$

----- Eqn. C.21

where **D** is the total damage.

APPENDIX D

D.1 SAS Analysis Results

This appendix lists the coefficients A1, A2, and A3, which are the result of the SAS analysis. The coefficients are generated as a result of fitting a third-order curve to the post processed ANSYS results. The third-order curves relating the wave height with the stress ranges are according to the following equation:

$$S_r = A_1H + A_2H^2 + A_3H^3 \qquad \text{Eqn. D.1}$$

where

S_r = hoop force range

H = wave height

The curve fit is done for 17 locations in 14 directions. The results are presented in Tables D.1 to D.16.

D.2 Hoop Force Range Variations with Elevation

In Section 6.6, the potential zones for a failure mechanism are discussed. Figures D.1 to D.13 illustrate the interior zones at which hoop force ranges can cause failure.

Table D.1: SAS analysis results at location 2

Direction	A_1	A_2	A_3
NE	8.095	-0.038	0.0
ENE	7.91	-0.24	0.0
E	3.38	-1.24	0.13
ESE	10.61	-1.83	0.08
SSE	1.09	-0.49	0.08
S	1.38	-0.75	0.15
SSW	0.15	0.32	0.04
SW	7.04	-1.33	0.08
WSW	1.11	-0.08	0.07
W	4.68	-0.07	0.0
WNW	2.15	0.0	0.0
NNW	0.88	0.03	0.0
N	1.07	0.19	0.0
NNE	8.51	-0.087	0.0

Table D.2: SAS analysis results at location 3

Direction	A_1	A_2	A_3
NE	10.02	0.65	0.0
ENE	3.87	0.69	0.0
E	4.71	-1.42	0.17
ESE	5.44	0.03	0.0
SSE	3.46	-1.10	0.16
S	7.20	0.0	0.0
SSW	8.39	0.0	0.0
SW	6.18	-0.61	0.07
WSW	8.57	0.0	0.0
W	8.80	-0.11	0.0
WNW	9.52	-2.63	0.19
NNW	1.49	0.09	0.0
N	2.08	0.45	0.0
NNE	12.90	0.40	0.0

Table D.3: SAS analysis results at location 4

Direction	A_1	A_2	A_3
NE	13.84	1.38	0.0
ENE	22.02	0.35	0.0
E	13.50	-3.65	0.38
ESE	5.44	0.03	0.0
SSE	7.55	-2.13	0.28
S	1.21	-0.50	0.27
SSW	12.95	0.0	0.0
SW	5.75	-0.19	0.13
WSW	13.25	0.0	0.0
W	15.74	-0.15	0.0
WNW	17.40	-4.49	0.32
NNW	2.39	0.29	0.0
N	2.50	0.85	0.0
NNE	30.55	0.04	0.0

Table D.4: SAS analysis results at location 5

Direction	A_1	A_2	A_3
NE	10.66	0.99	0.06
ENE	13.53	0.37	0.07
E	27.91	-7.08	0.67
ESE	9.17	-0.14	0.0
SSE	12.49	-3.21	0.38
S	4.68	-1.18	0.38
SSW	18.74	0.0	0.0
SW	4.08	0.42	0.23
WSW	19.17	0.0	0.0
W	23.98	-0.12	0.0
WNW	27.41	-6.86	0.50
NNW	4.19	0.51	0.0
N	0.37	1.74	-0.01
NNE	39.65	0.0	0.0

Table D.5: SAS analysis results at location 6

Direction	A_1	A_2	A_3
NE	88.14	-11.30	0.46
ENE	61.93	-7.55	0.36
E	47.44	-10.64	0.92
ESE	7.55	0.37	0.0
SSE	18.32	-4.43	0.49
S	9.89	-2.41	0.55
SSW	0.46	1.44	0.32
SW	1.50	0.64	0.45
WSW	-0.08	1.78	0.29
W	32.80	-0.11	0.0
WNW	40.07	-10.07	0.74
NNW	4.44	1.07	-0.02
N	7.38	1.58	0.01
NNE	6.59	3.54	-0.07

Table D.6: SAS analysis results at location 7

Direction	A_1	A_2	A_3
NE	153.76	-22.42	0.85
ENE	128.08	-20.30	0.85
E	53.08	-9.46	0.71
ESE	9.38	0.38	0.0
SSE	23.21	-5.45	0.59
S	12.14	-1.77	0.43
SSW	4.82	0.76	0.39
SW	1.38	0.97	0.51
WSW	21.93	0.79	0.0
W	49.85	-12.15	0.88
WNW	7.05	1.18	-0.02
NNW	46.63	-5.17	0.26
N	73.69	-12.36	0.58
NNE	116.09	-17.97	0.84

Table D.7: SAS analysis results at location 8

Direction	A_1	A_2	A_3
NE	96.76	-10.76	0.45
ENE	97.58	-11.22	0.51
E	45.33	0.21	-0.18
ESE	18.55	0.29	0.0
SSE	43.18	-9.97	1.01
S	24.86	-2.88	0.56
SSW	19.08	-1.40	0.73
SW	49.80	0.0	0.0
WSW	11.73	1.80	0.46
W	68.83	-11.15	0.65
WNW	77.20	-16.44	1.10
NNW	26.99	-0.81	0.06
N	142.67	-20.79	0.85
NNE	116.09	-17.97	0.84

Table D.8: SAS analysis results at location 9

Direction	A_1	A_2	A_3
NE	100.76	0.0	0.0
ENE	43.04	0.31	0.10
E	33.68	6.70	-0.78
ESE	-12.55	15.77	-1.42
SSE	52.43	-12.12	1.18
S	31.08	-3.29	0.56
SSW	27.53	-2.63	0.79
SW	55.80	0.0	0.0
WSW	19.97	0.66	0.52
W	126.49	-25.58	1.36
WNW	79.85	-14.29	0.81
NNW	52.07	-5.25	0.23
N	93.89	-11.12	0.48
NNE	56.54	-7.13	0.46

Table D.9: SAS analysis results at location 10

Direction	A_1	A_2	A_3
NE	55.65	1.97	0.0
ENE	90.10	-0.35	0.0
E	48.33	2.26	-0.50
ESE	5.26	10.01	-0.96
SSE	64.98	-15.63	1.44
S	40.71	-5.60	0.75
SSW	34.54	-2.94	0.71
SW	3.53	4.24	0.66
WSW	29.65	-0.88	0.55
W	131.97	-26.59	1.41
WNW	76.26	-9.76	0.30
NNW	79.63	-10.31	0.41
N	26.34	2.39	-0.03
NNE	26.33	3.25	0.0

Table D.10: SAS analysis results at location 11

Direction	A_1	A_2	A_3
NE	93.24	-0.17	0.0
ENE	132.18	-2.80	0.0
E	78.51	-7.88	0.33
ESE	51.21	-6.17	0.44
SSE	111.71	-29.92	2.61
S	93.59	-22.33	2.19
SSW	82.18	-17.42	2.17
SW	36.82	-3.34	1.51
WSW	88.88	-20.48	2.48
W	88.63	-13.01	0.71
WNW	94.0	-11.93	0.37
NNW	78.34	-8.84	0.34
N	4.72	8.88	-0.29
NNE	81.79	0.23	0.0

Table D.11: SAS analysis results at location 12

Direction	A_1	A_2	A_3
NE	58.32	4.11	-0.20
ENE	59.43	4.98	-0.26
E	70.30	-1.50	0.05
ESE	169.84	-48.30	4.22
SSE	255.64	-74.66	6.28
S	267.57	-75.40	6.33
SSW	233.90	-57.43	4.98
SW	150.00	-20.90	1.85
WSW	271.52	-73.60	6.42
W	50.78	4.40	-0.31
WNW	113.79	-9.81	0.13
NNW	58.48	-1.02	-0.02
N	54.42	3.09	-0.17
NNE	55.50	8.02	-0.43

Table D.12: SAS analysis results at location 13

Direction	A_1	A_2	A_3
NE	34.31	6.13	-0.22
ENE	31.88	6.16	-0.24
E	128.49	-22.67	1.55
ESE	118.45	-20.39	1.09
SSE	184.97	-50.93	4.02
S	158.39	-37.81	2.98
SSW	130.98	-22.88	1.75
SW	104.29	-13.74	1.04
WSW	137.12	-25.45	1.96
W	2.51	15.62	-0.86
WNW	157.74	-30.43	1.72
NNW	54.84	-2.89	-0.07
N	37.42	3.19	-0.13
NNE	31.13	11.07	-0.50

Table D.13: SAS analysis results at location 14

Direction	A_1	A_2	A_3
NE	71.13	6.04	-0.22
ENE	66.40	6.18	-0.25
E	228.53	-41.78	2.66
ESE	270.38	-66.74	4.66
SSE	301.36	-87.81	7.21
S	260.59	-64.07	4.96
SSW	224.96	-44.50	3.33
SW	182.51	-30.41	2.27
WSW	218.15	-41.56	3.05
W	40.62	15.16	-0.91
WNW	283.08	-58.75	3.36
NNW	95.73	-6.95	0.20
N	75.42	1.19	-0.08
NNE	71.10	11.20	-0.53

Table D.14: SAS analysis results at location 15

Direction	A_1	A_2	A_3
NE	88.72	2.88	-0.15
ENE	80.94	3.51	-0.18
E	246.00	-44.91	2.74
ESE	336.03	-88.96	6.34
SSE	365.55	-110.88	9.13
S	316.01	-81.78	6.28
SSW	277.03	-60.47	4.52
SW	244.68	-48.80	3.63
WSW	274.13	-59.37	4.41
W	72.41	8.07	-0.60
WNW	307.73	-64.42	3.63
NNW	109.87	-9.74	0.30
N	86.38	-0.70	-0.03
NNE	92.30	6.64	-0.38

Table D.15: SAS analysis results at location 16

Direction	A_1	A_2	A_3
NE	96.62	-6.82	0.14
ENE	104.70	-8.71	0.21
E	179.19	-35.31	2.08
ESE	244.52	-64.77	4.37
SSE	281.03	-88.62	7.20
S	238.13	-64.31	4.79
SSW	209.39	-48.24	3.39
SW	195.24	-43.53	3.03
WSW	210.48	-48.93	3.44
W	44.75	6.10	-0.54
WNW	211.33	-46.78	2.66
NNW	73.19	-7.60	0.22
N	79.58	-5.58	0.11
NNE	68.02	2.81	-0.31

Table D.16: SAS analysis results at location 17

Direction	A_1	A_2	A_3
NE	14.16	1.82	0.0
ENE	12.63	1.73	0.0
E	80.37	-22.37	1.70
ESE	97.46	-32.23	2.60
SSE	104.15	-35.53	3.08
S	95.13	-28.98	2.31
SSW	88.15	-25.24	2.00
SW	92.04	-26.18	2.07
WSW	27.71	0.49	0.0
W	71.75	-18.49	1.25
WNW	9.07	-0.34	0.05
NNW	11.06	1.23	0.0
N	35.97	1.16	0.0
NNE	68.02	2.81	-0.31

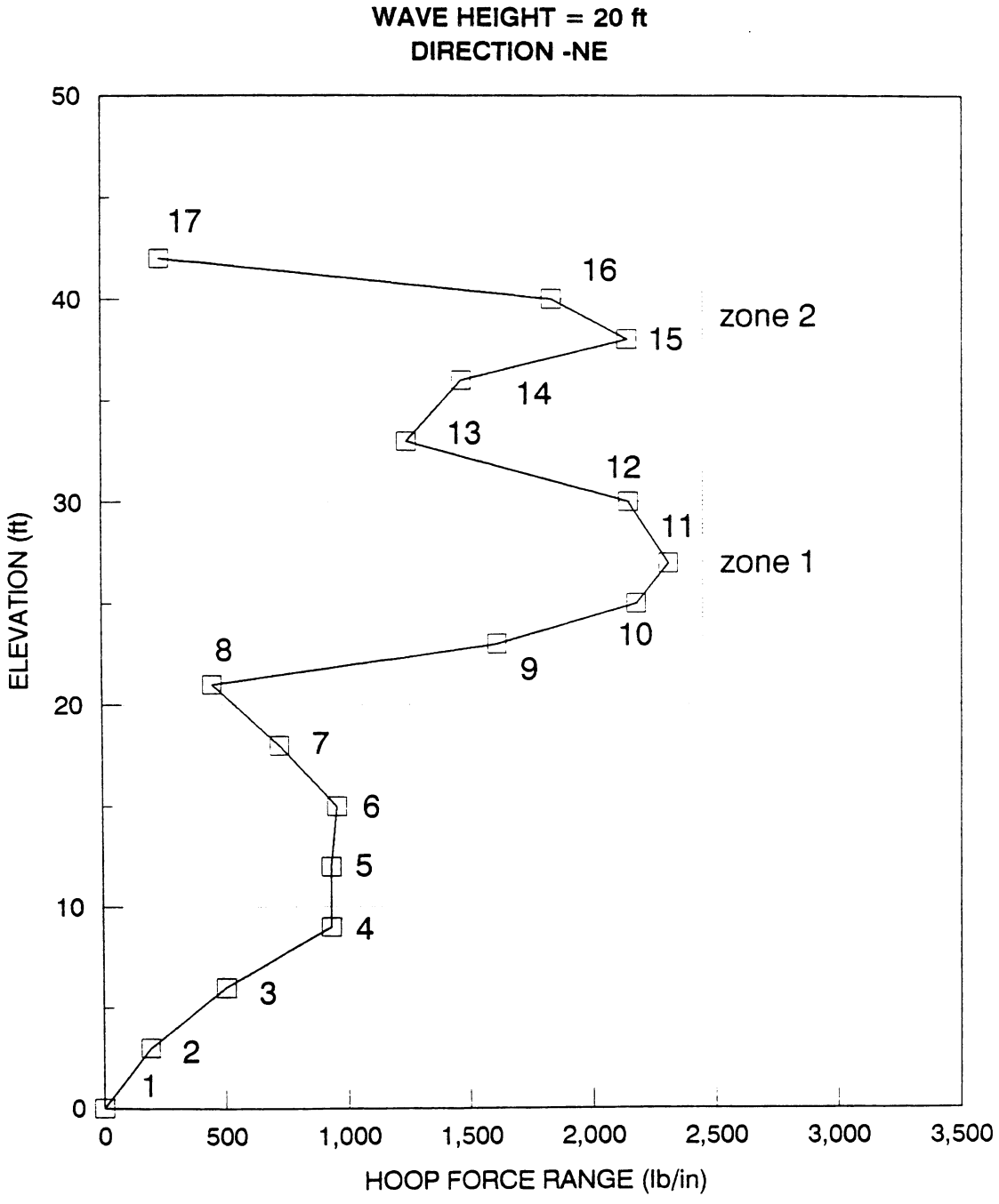

Fig. D.1 Variation of hoop-force ranges with elevation and identified critical failure zones

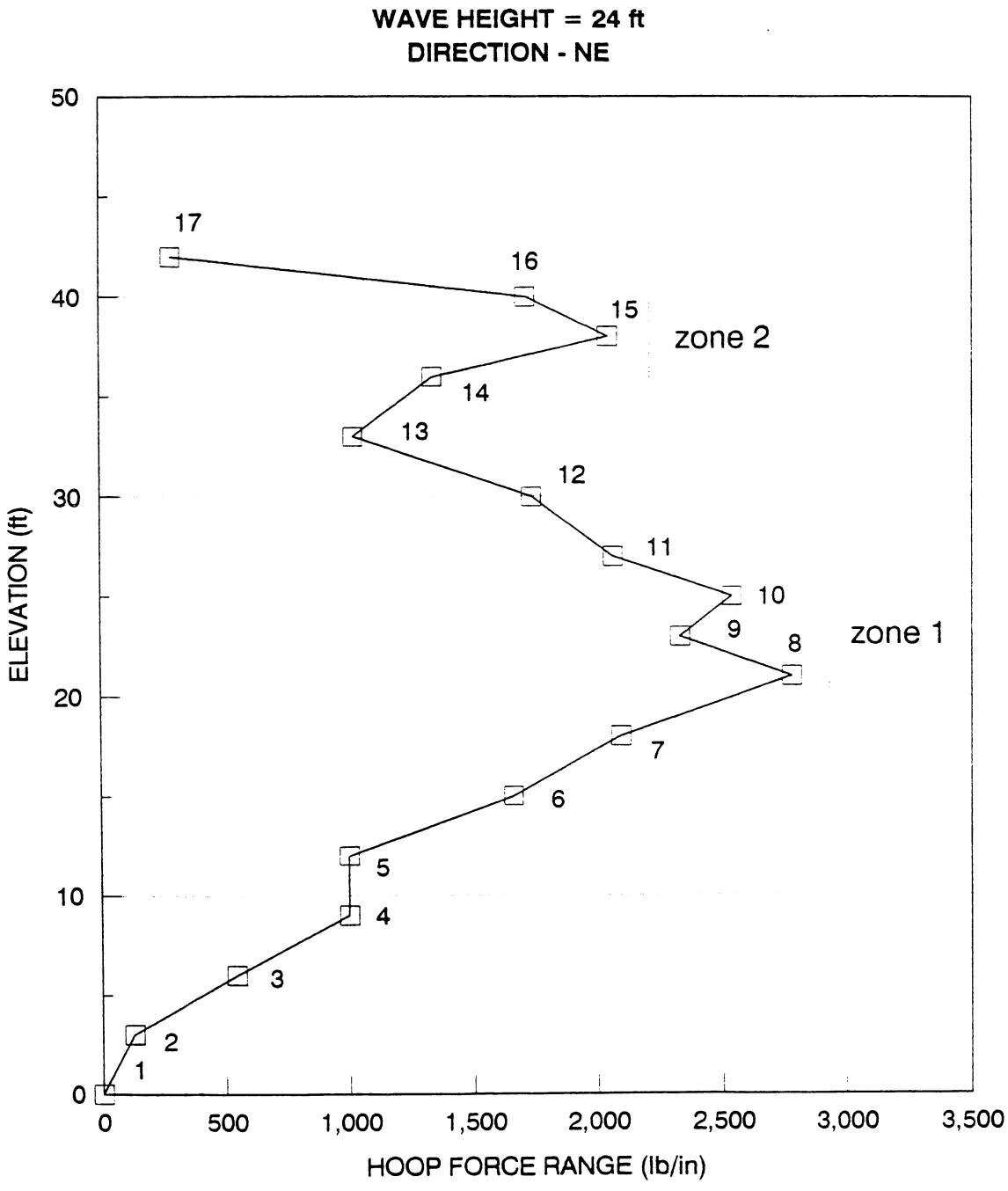

Fig. D.2 Variation of hoop-force ranges with elevation and identified critical failure zones

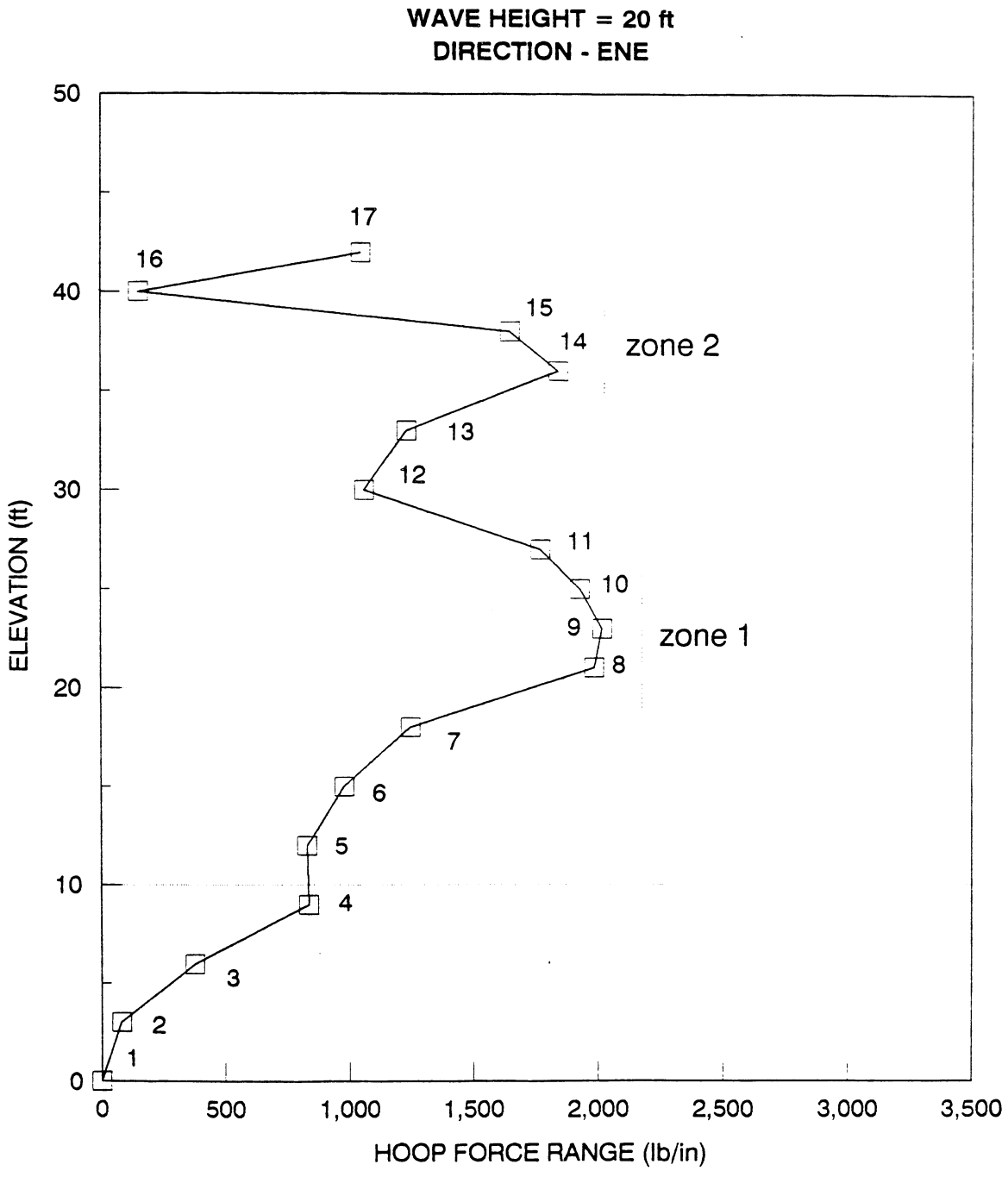

Fig. D.3 Variation of hoop-force ranges with elevation and identified critical failure zones

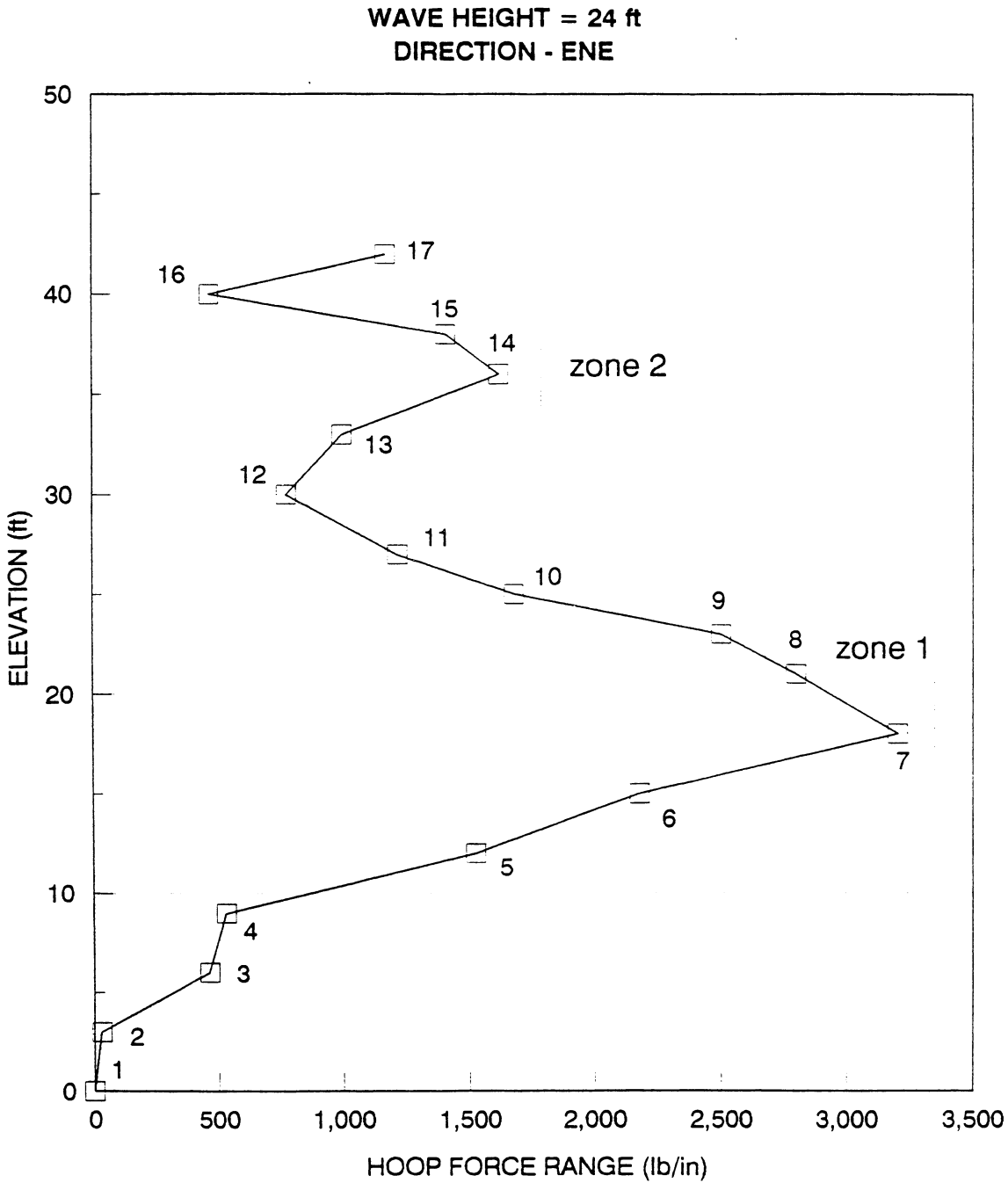

Fig. D.4 Variation of hoop-force ranges with elevation and identified critical failure zones

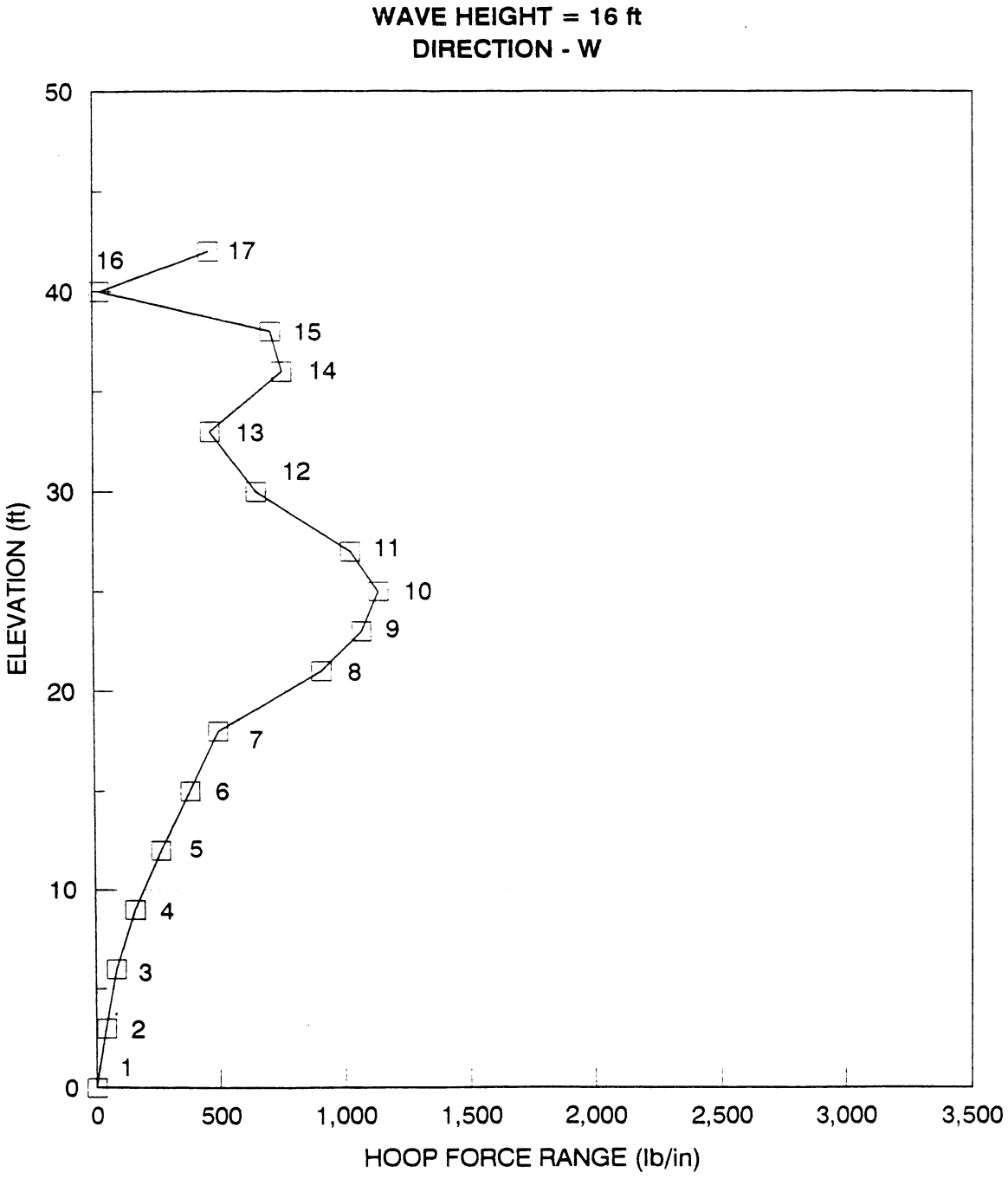

Fig. D.5 Variation of hoop-force ranges with elevation and identified critical failure zones

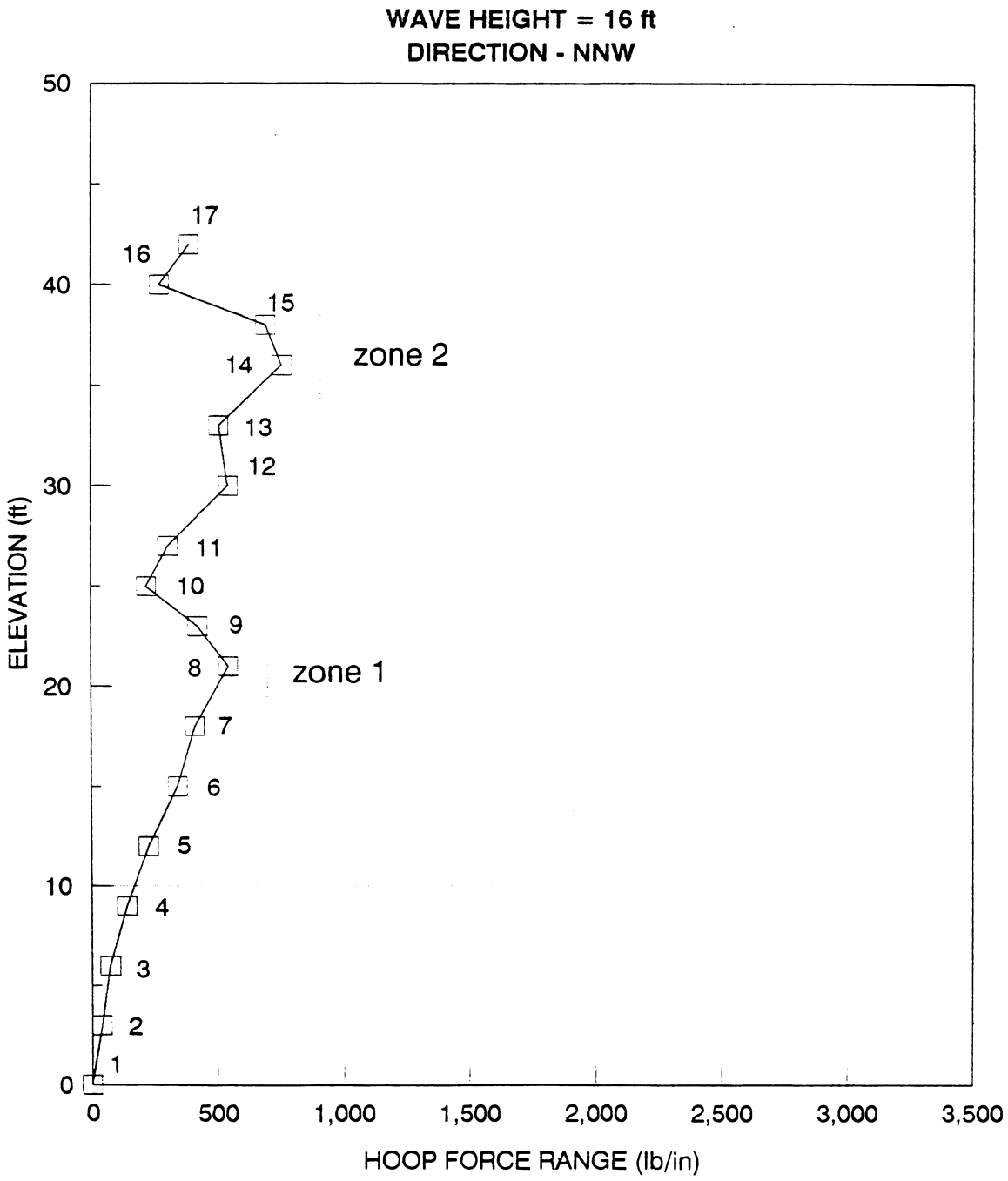

Fig. D.6 Variation of hoop-force ranges with elevation and identified critical failure zones

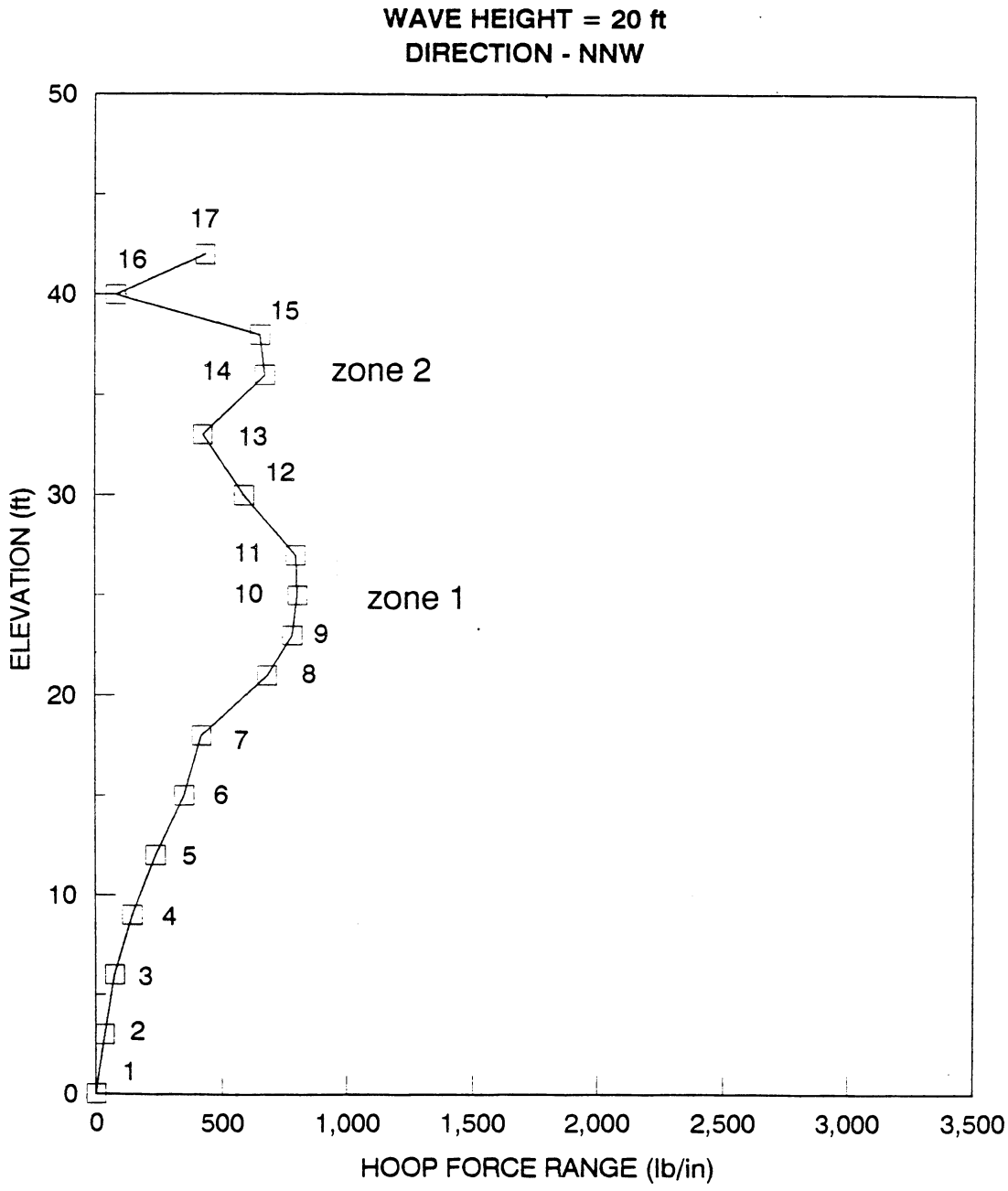

Fig. D.7 Variation of hoop-force ranges with elevation and identified critical failure zones

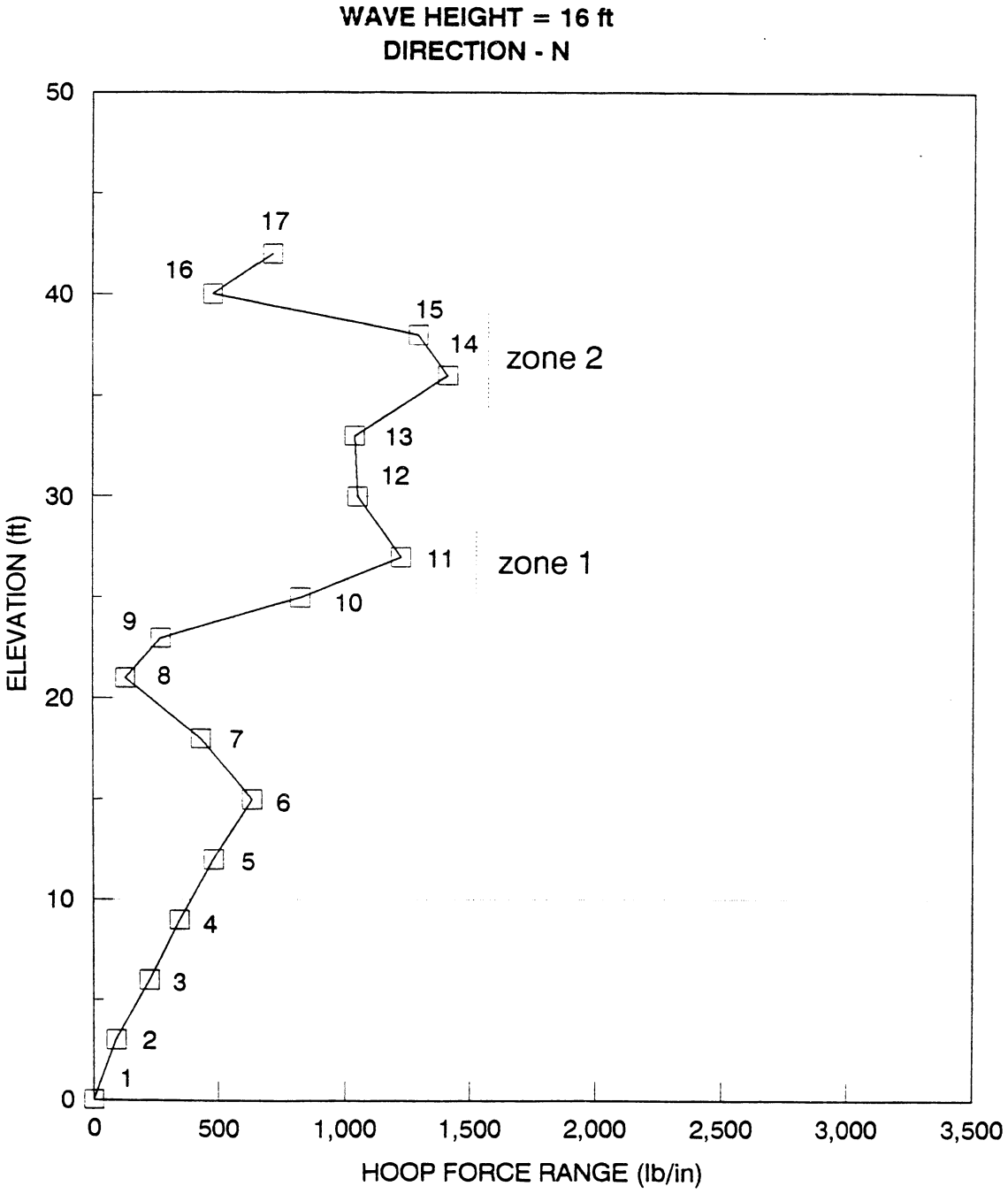

Fig. D.8 Variation of hoop-force ranges with elevation and identified critical failure zones

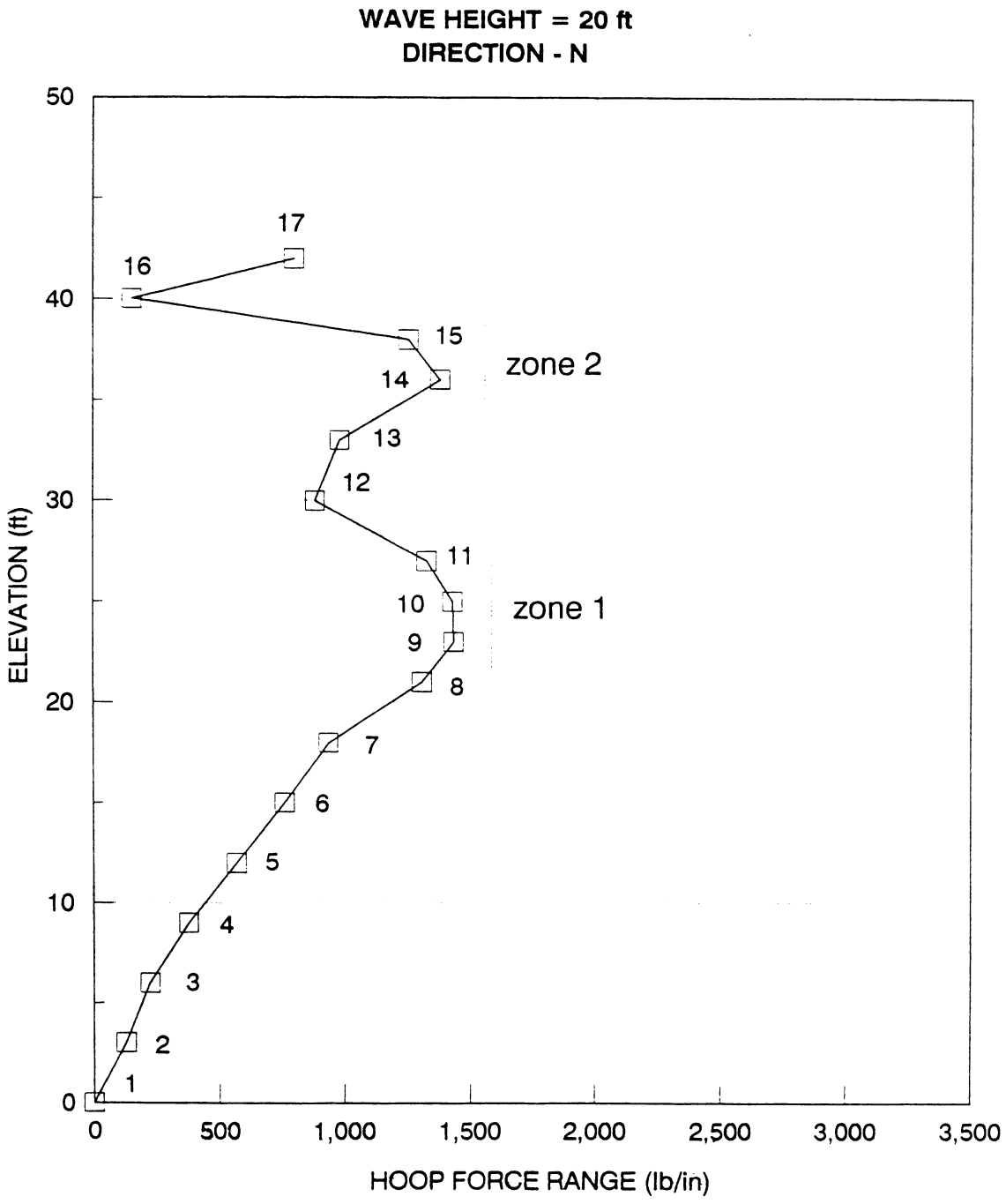

Fig. D.9 Variation of hoop-force ranges with elevation and identified critical failure zones

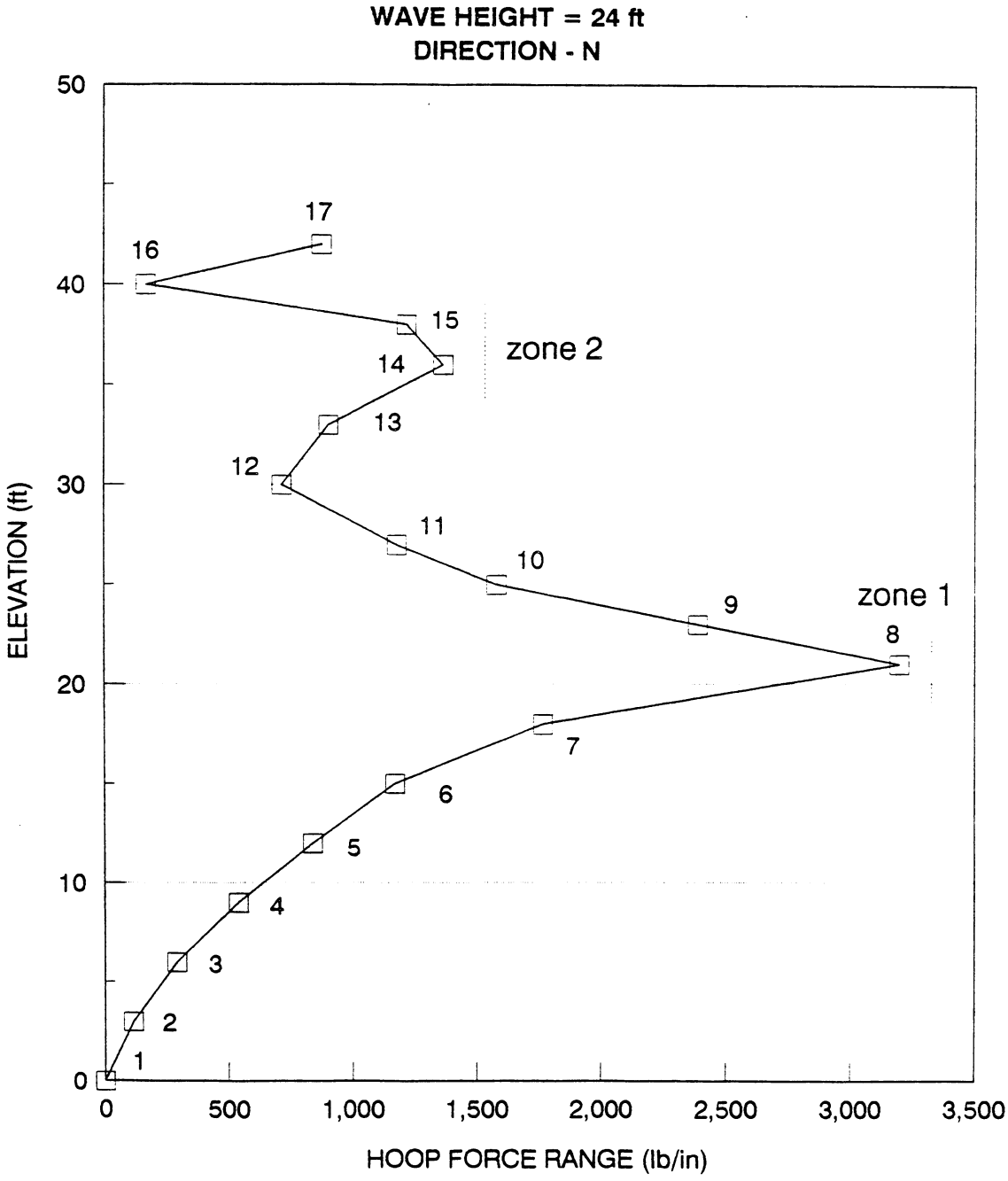

Fig. D.10 Variation of hoop-force ranges with elevation and identified critical failure zones

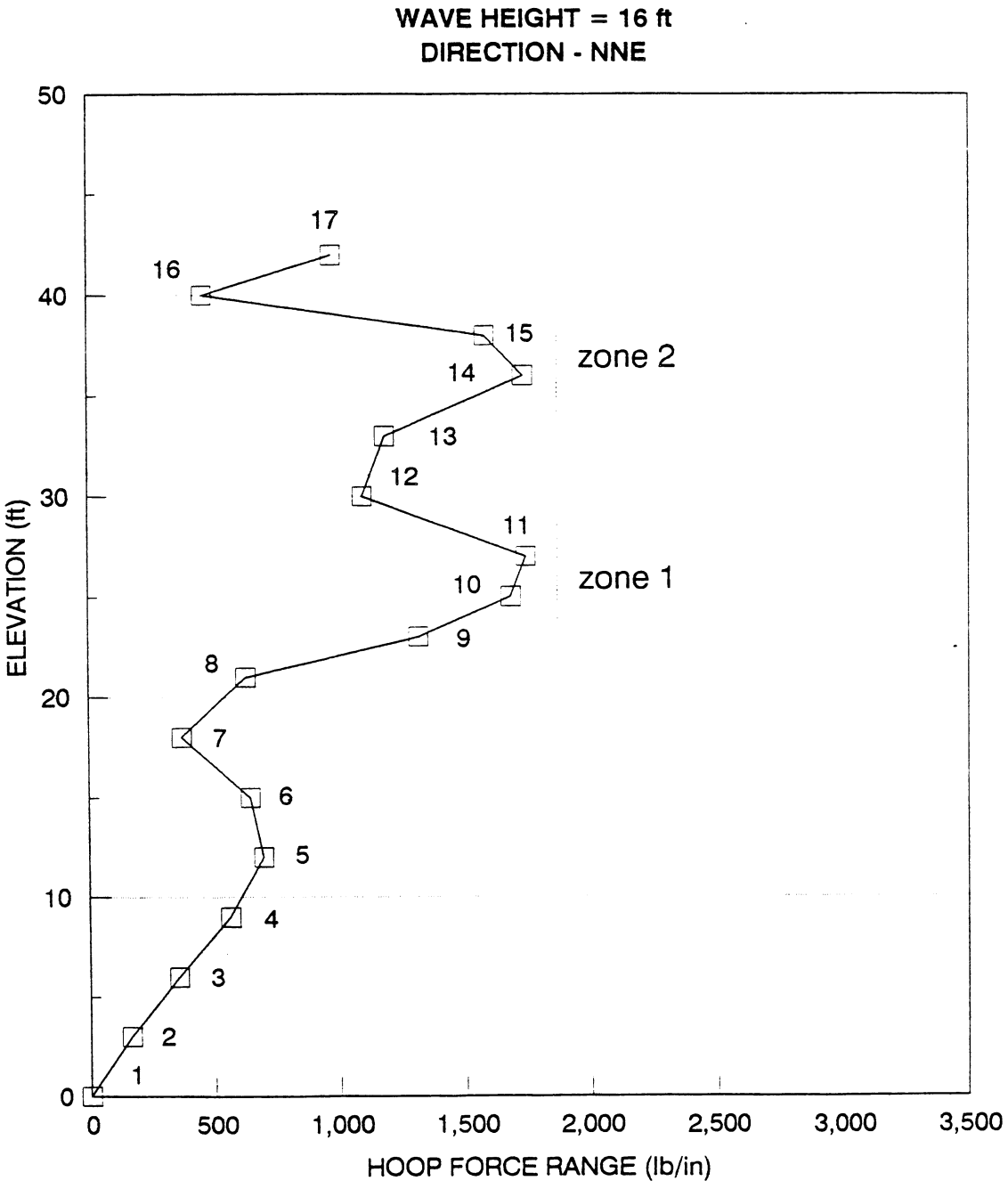

Fig. D.11 Variation of hoop-force ranges with elevation and identified critical failure zones

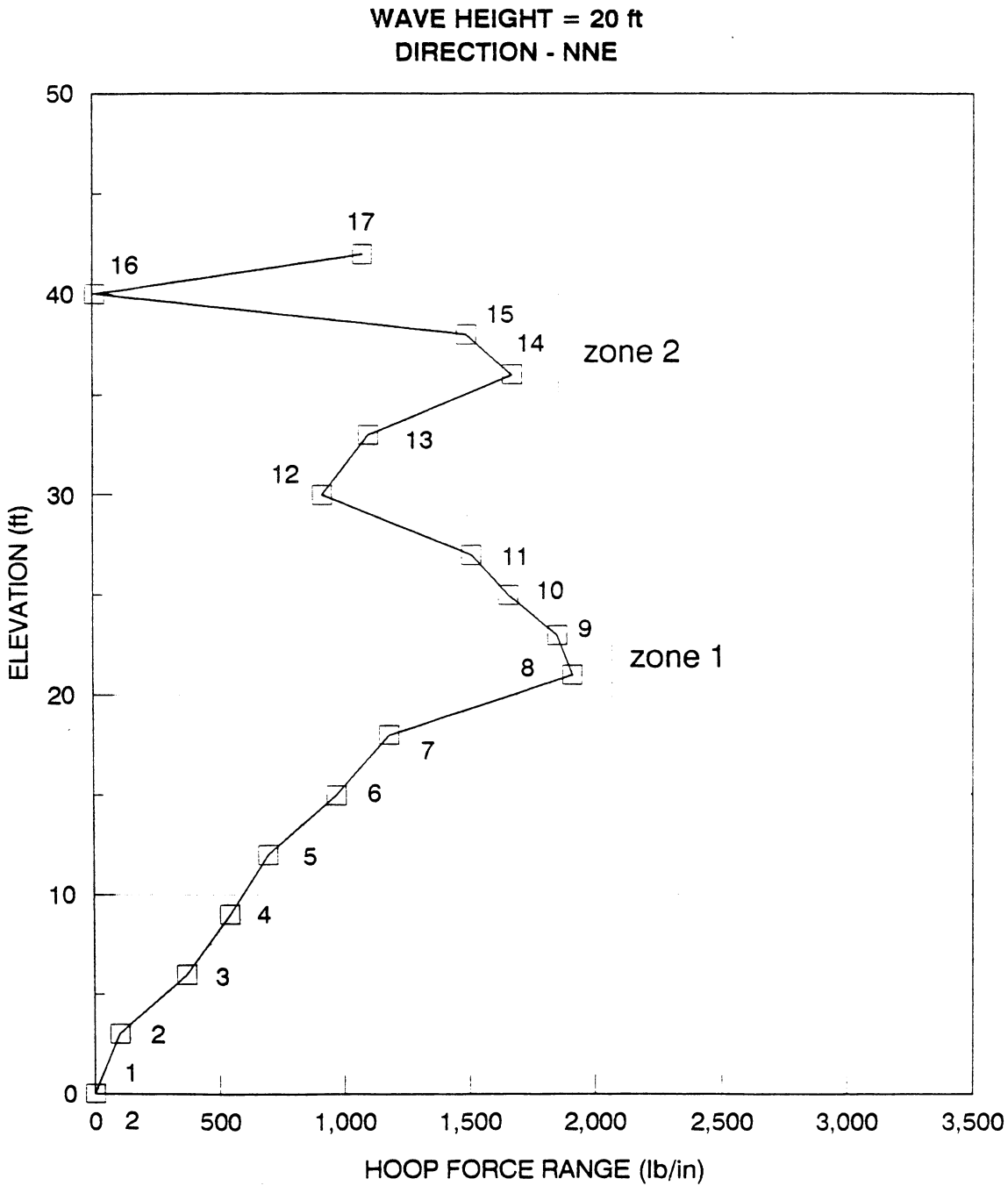

Fig. D.12 Variation of hoop-force ranges with elevation and identified critical failure zones

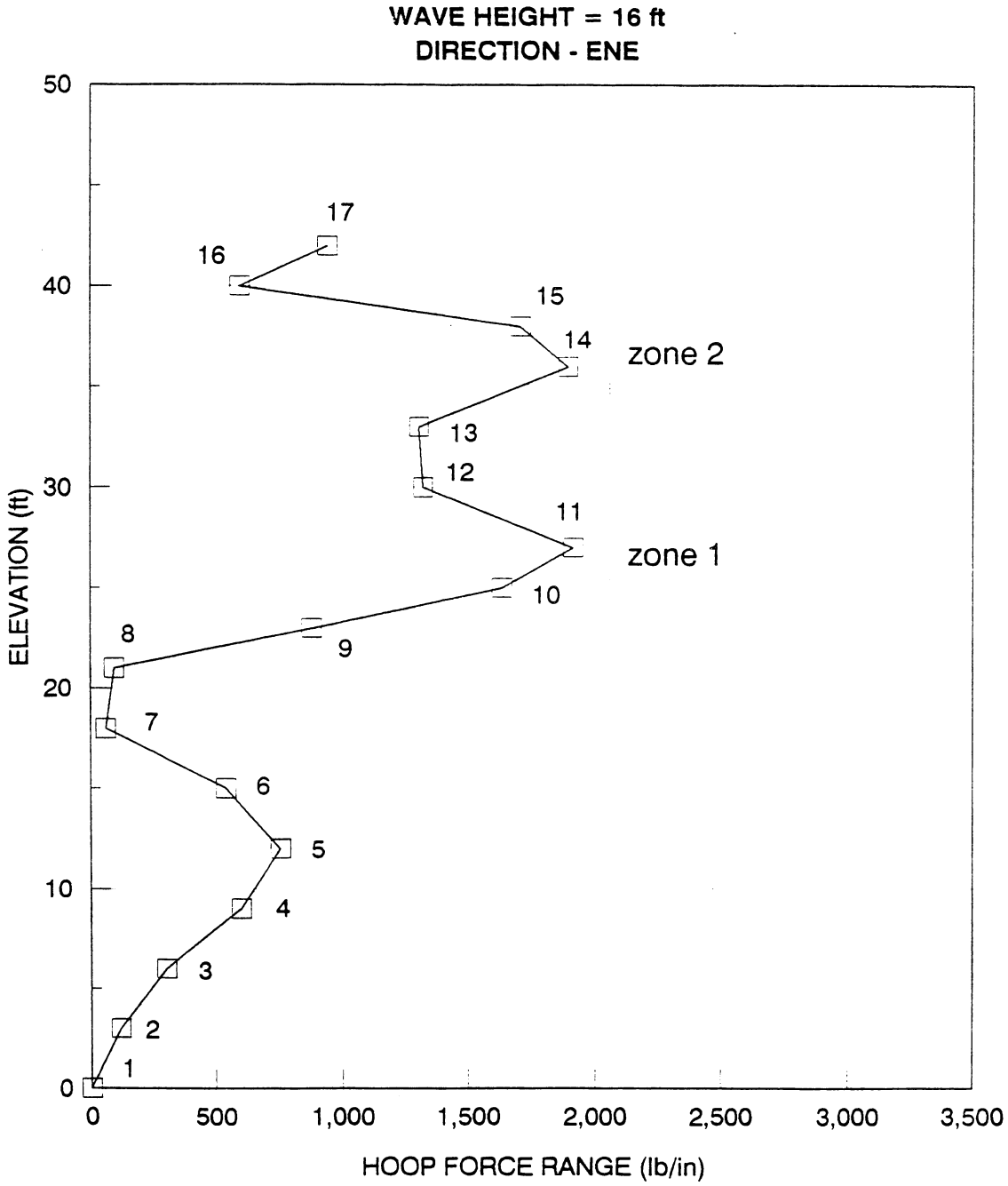

Fig. D.13 Variation of hoop-force ranges with elevation and identified critical failure zones

APPENDIX E

E.1 Computer Programs

This appendix outlines the various programs that have been written during the course of the project to handle large amounts of data. The objectives of the programs are stated. Only the important program files are listed. The computer programs developed basically cover five major areas. They are

1. regression analysis
2. pressure computation
3. post processing of the finite element results
4. determination of best-fit curves
5. damage evaluation

Of these 5 areas, No. 4 is created on the WYLBUR/HDS system at ISU. The other four are created on the VAX system. Regression analysis consisted of generation of wave height and wave period for different waves that exist in each direction. The directory for regression analysis is REGRESSION. The main regression algorithm exists in the file OMEGA.FOR. The computation flow chart is as shown in Fig. E.1. Other files that exist in the directory are LAMBDA.FOR for iterative calculation of wave length and NOWAVE.FOR and NOWAVE1.FOR for the calculation of the number of waves in a sea state. Subroutines in the file SUBMOD.FOR are used primarily for input and output access.

Pressure computations are made in a directory called PRESSURE. They are made using the programs PRESS5.FOR, CNOI.FOR and STAND1.FOR for the Stokes waves, Cnoidal waves and standing waves respectively. The programs are used in conjunction with the subroutines in the file SUB1.FOR. The input for pressure calculation consists of two parts, the file INPUT.DAT listing the coordinates and representative areas of the pressure points and nodes, and the interactive part consisting of interactive input for wave parameters. The computation flow chart is as shown in Fig. E.2. As shown in the figure, the output from the pressure computations consists of the pressure files and nodal force files. The nodal force files are in ANSYS File 23 format, ready for input into ANSYS finite element analysis program.

Post-processing of the finite element results is done in a directory called REDUCE. Within the directory are subdirectories for each direction, named after the direction, such as ENE, NNW, and the like. The data processing is done using the file DATA.FOR, which creates location-wise files consisting of the waves and associated hoop-force ranges.

Determination of the best-fit curves is done by using SAS, a general purpose statistical analyis program on the WYLBUR/HDS system. Regression is done by SAS, which is invoked by programs written in JCL (Job Control Language).

The output from SAS is stored in hard copy format. Output consists of best-fit curves and regression coefficients.

Damage evaluation is made in a subdirectory called DAMAGE of the directory REGRESSION. Damage evaluation is made primarily by using the program HAMOD.FOR. Input for damage evaluation is made in two parts, regression coefficients (SAS analysis) and the number of waves calculated. They are combined by the program ARRANGE.FOR as input to HAMOD.FOR. Damage evaluations for sensitivity analysis are done using the programs H1.FOR, H3.FOR, and the like.

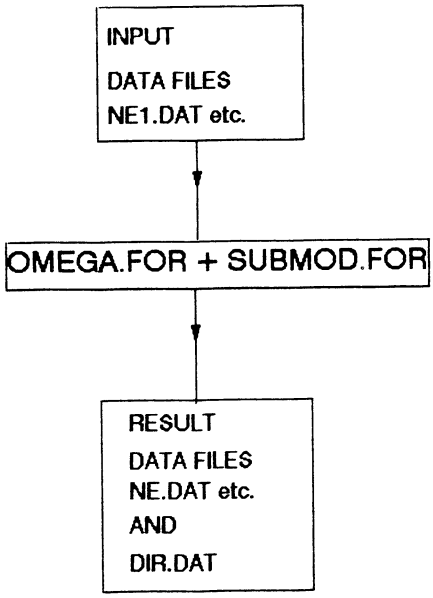

Fig. E.1 Computation flow chart for regression analysis

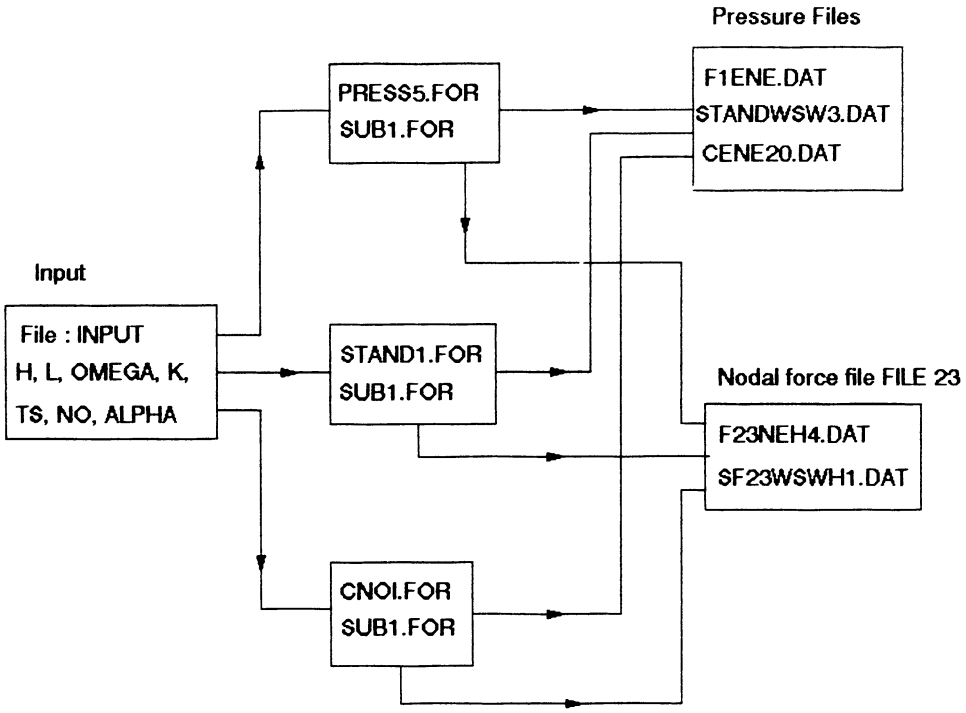

Fig. E.2 Computation flow chart for evaluation of pressures